Electrochemical studies of the kinetics and mechanism of aqueous iron reactions in mine-water

By

Mahmud Ashtewi Saleh Ashtewi

A thesis submitted in partial fulfilment of the requirements of the degree of Doctor of Philosophy

School of chemistry

Newcastle University

Newcastle Upon Tyne, UK

April 2013

Abstract

This work has been conducted to investigate the chemical processes involved in the remediation of acidic mine drainages (AMD) using electroanalytical methods to study the chemistry of Fe(III) in pure laboratory solutions and samples obtained from Shilbottle Colliery (Northumberland, UK), which are heavily contaminated with soluble Fe leached from the spoil heap. One method for remediation is to raise the pH of the waters and precipitate Fe(III) in an artificial wetland; however microelectrode voltammetry shows significant soluble Fe(III) remains.

The characterization of hydrolysed species of Fe(III) in pure laboratory solutions and Shilbottle samples has been studied using voltammetry, Raman spectroscopy, electrospray ionization - mass spectrometry (ESI-MS) and X-ray diffraction (XRD). The voltammetric and Raman studies show that, there is some similarity in square wave voltammograms and Raman spectra between Shilbottle solutions and aqueous laboratory Fe(III)-sulfate solutions. ESI-MS of laboratory Fe(III) solutions with non-coordinating, or weak coordinating anions such as perchlorate shows the presence of monomers, dimers, trimers and tetramers of soluble Fe(III) complexes. However no Fe-related peaks were observed in sulfate-containing media and the Shilbottle samples due to the presence of neutral species such as $FeSO_4OH$. XRD data shows formation of basic sulfate complexes in the case of Fe(III)-sulfate and no XRD peaks can be assigned to Fe(III) in perchlorate media.

Determination of soluble fractions of [Fe(III)/Fe(II)] and [SO_4^{2-}] in Shilbottle samples have been performed using developed voltammetric methods. The total soluble [Fe] varied between 281 and 446 ppm and soluble [SO_4^{2-}] between 3460 and 7400 ppm. A standard geochemical model (PHREEQC) has been used to study chemical speciation in AMD; a comparison of the model and our measurements indicates that the Shilbottle samples are clearly out-of-equilibrium.

Kinetic studies of hydrolysis of Fe(III) in pure laboratory solutions and Shilbottle samples have been performed using potentiometric, voltammetric and Raman spectroscopy techniques. The obtained data show that the hydrolysis of Fe(III) upon raising the pH by addition of NaOH is second order in [Fe]; the rate constants were measured and a mechanism which can rationalize the rate constants is proposed. Also,

effects of sulfate ions on the hydrolysis of Fe(III) in aqueous solutions have been investigated. The study shows that the SO_4^{2-} ions catalyse formation of soluble dimers, oligomers and basic sulfate complexes. Furthermore, $FeSO_4^{+}$ stays dissolved in the solution longer than simple Fe(III) species such as Fe^{3+}, $Fe(OH)^{2+}$ and $Fe(OH)_2^{+}$.

Dedication

To my parents (Mr Ashtewi Saleh & Mrs Khayria Ali), my wife, my brothers, my sisters, my lovely sons (Mohamed & Muadh) and to anyone who are waiting for my success, I dedicate this work.

Acknowledgments

I would like to express my sincere gratitude to my first supervisor Dr. Benjamin Richard Horrocks for encouraging and pushing me and for all his supports, advices and assistances. Also many thanks go to my second supervisor prof. Andrew Houlton for his encouragement and guidance, and also Prof. A.C.Aplin for his guidance in respect to geochemical information. A special acknowledgment goes to all staff and PhD students in Chemical Nanoscience laboratory for the spaciousness of their chests and their help. Many thanks go to all staff, postgraduate students and all employers at school of chemistry at Newcastle University.

I am deeply grateful to all my family (my father, mother, wife, brothers and sisters) that strongly supported me morally, as well as my government that supported me economically. Finally my respects and appreciative thanks go to all people in school of chemistry at Newcastle University.

Table of contents

List of tables

List of Figures

Abbreviations

E_p	peak potential
[O]	Concentration of oxidized species
[R]	Concentration of reduced species
{ }	Activity expression
ΔG	Gibbs free energy
A	electrode area
AAS	flame atomic absorption spectroscopy
AdSV	adsorptive stripping voltammetry
Ag/AgCl	silver chloride electrode
AMD	acidic mine drainage
A_p	area under peak
ARD	acidic rock drainage
ASV	anodic stripping voltammetry
C	coulomb
CCD	charge coupled device
CSV	cathodic stripping voltammetry
CV	cyclic voltammetry
D	diffusion coefficient
d	distance between the crystal planes
DCP	direct current plasma
DMO	direct metabolic oxidation
DO	dissolved oxygen
DPV	differential pulse voltammetry
E	Cell potential
E_f	Fermi energy level
Eh	Oxidation reduction potential [e^-]
ESI-MS	electrospray ionization-mass spectrometry
ETAAS	electrothermal atomization atomic absorption spectrometry
E^o	formal reduction potential
E^ϕ	standard reduction potential
F	Faraday constant

FTIR	Fourier transform infrared
GC-MS	gas chromatography-mass spectroscopy
GFAAS	graphite furnace atomic absorption spectrometry
HPLC-MS	high-performance liquid chromatography-mass spectroscopy
I	current density
I_0	exchange current density
I_A	anodic current density
I_C	cathodic current density
ICDD-PDF	international centre of diffraction data-powder diffraction file
ICP	inductively coupled plasma
ICP-AES	inductively coupled plasma atomic emission spectrometry
IMO	indirect metabolic oxidation
I_p	peak current density
ISEs	ion selective electrodes
J	joule
K	Thermodynamic equilibrium constant
K_c	apparent equilibrium constant
K	Kelvin
k	rate constant
k_0	rate constant at standard potential
k_A	rate constant for oxidation at electrode
k_c	rate constant for reduction at electrode
k_d	mass transfer coefficient
k_{obs}	observed rate constant
K_Υ	activity coefficient product
Lag.	lagoon
LC-MS	liquid chromatography-mass spectroscopy
LSV	linear sweep voltammetry
M	molar (mol L^{-1})
m	molality (mol kg^{-1})
m/z	mass-to-charge ratio
MIP	microwave induced plasma
mL	millilitre
mM	millimolar (mmol L^{-1})

mol	mole
MS	mass spectrometry
n	number of electrons
^{o}C	Celsius
^{o}F	Fahrenheit
pe	-log{e}
PHREEQC	PH REdox Equilibrium in the C programming language
ppm	part per million
PRB	permeable reactive barrier
R	gas constant
RAPS	reducing and alkalinity producing systems
SCE	saturated calomel electrode
SECM	scanning electrochemical microscopy
SEM	scanning electron microscopy
SHE	standard hydrogen electrode
SI	saturation indices
STM	scanning tunnelling microscopy
SWV	square wave voltammetry
T	temperature
t	time
TEM	transmission electron microscopy
TRXF	total reflection X-ray fluorescence
UME	ultramicroelectrode
UP	upper stream
USGS	U.S. Geological Survey
V	volt
XPS	X-ray photoelectron spectroscopy
XRD	X-Ray diffraction
α	transfer coefficient
α_A	anodic transfer coefficient
αc	cathodic transfer coefficient
ΔG^{ϕ}	standard Gibbs free energy
η	overpotential
θ	angle of incidence of X-Ray beam

λ	wavelength
$\mathcal{V}$	scan rate

Chapter 1: An introduction

1.1 Mine-water …. An overview

Mine-water is known as an acidic mine drainage (AMD) or acidic rock drainage (ARD) which naturally emanates from mine tailings, pits, mine waste rocks and underground working in the mining area. From the standpoint of the chemical description, AMD/ARD is characterized by high metal concentrations, toxic heavy metals and other toxic substances (such as cyanides), metalloids and low pH waters [1]. The major source of metals in AMD is sulfide minerals, which usually have a high concentration of iron and smaller amounts of nickel, gold, lead, copper and zinc depending on the constituent of local rock material in the site. Every site possesses a special composition and as a result the potential risks related to different sites varied from site-to-site, and the remediation methods are different [1, 2].

Mining industries are considered as a powerful economic source for numerous products, for instance production of precious metals (uranium and gold) and other artificial minerals which can be either fundamental or minor component of various manufactures [3, 4]. The seepage AMD of such abandoned sites persists for long periods of time after their use is discontinued up to hundreds of years in some cases [2, 4]. Accordingly, mining activities may cause serious threat for human health and other creatures on the earth's surface. The most dangerous and acute effect on human health is produced by cyanides resulting from gold mining operations. Other toxic elements which are released from mining processes can affect human health such as lead, cadmium and arsenic; such toxic substances reach the human body in different ways: water (groundwater and river waters affected by mines tailing), food (vegetable and fruits) and air (hydrogen cyanide). Hence, mining activities have direct effects on the environment in surrounding areas to mining sites, in turn it can be regarded as a real risk to human health when people consume polluted water and vegetables or inhale the polluted air [4-6].

1.2 Mine water and environment impacts

There is no doubt that mining operations are essential for numerous industries in many countries throughout the world. Such processes are widely regarded as a main source for

production of a large number of raw materials, in turn, they are involved in several industries, such as ceramics, paint, glass, plastics, metal and precious metals [3]. On the other hand, such mining activities have been taken into account as serious threat to the environment. The reasons for such a warning are related to release of wastewaters discharged from industrial mining sites, in particular, acidic mine drainage (AMD) which has been classified as real risk to the environment. The origin of AMD is usually oxidation of sulfide minerals especially pyrite (FeS_2) during exposure to oxygen and water. The oxidation of pyrite produces high concentrations of Fe^{2+} (which in turn converts to Fe^{3+}) and high sulfate concentrations, as shown by the following equations (1.1 – 1.3) [3, 7-9].

$$FeS_{2\,(s)} + \frac{7}{2}O_2 + H_2O \rightarrow Fe^{2+} + 2SO_4^{2-} + 2H^+ \quad \ldots\ldots\ldots\ldots\ldots(1.1)$$

$$Fe^{2+} + \frac{1}{4}O_2 + H^+ \rightarrow Fe^{3+} + \frac{1}{2}H_2O \quad \ldots\ldots\ldots\ldots\ldots(1.2)$$

$$Fe^{3+} + 3H_2O \rightarrow Fe(OH)_{3\,(S)}\ (\text{ochre}) + 3H^+ \quad \ldots\ldots\ldots\ldots\ldots(1.3)$$

Furthermore, mine tailings can contain significant concentrations of toxic metals such as Cd and Pb, also metalloids and other metals like Zn, Cu, Mn, Cr, Ti, V, Al and Hg. These elements are common metal contaminants in the environment [10]. Also, cyanides resulting from gold mining processes can be a serious danger to the environment at high concentrations, due to its poisons nature on the human health [11]. The presence of excessive concentrations of toxic metals, sulfates (as sulfuric acid, low pH) and cyanide lead to pollution of aquatic systems [12], degradation of soil quality [13], air pollution [4], wildlife mortality [14] and fishes [15] in land and natural waters surrounding the mining sites.

The pollution of aquatic systems in various areas throughout the world by AMD has been intensively studied [4, 12, 16-18]; different results have been obtained depending on whether the mine is high sulfide-bearing and consequently elevated concentrations of heavy metals or low sulfide content (e.g. gold mining). It has been established, for instance, that sediments and surface water were severely contaminated by toxic metals in the vicinity of a mining site in Spain (southwest of the Iberian Peninsula). This was attributed to high content of sulfide material in the tailings and spoil heaps by which the metal solutions can seep into sediments and surface water and cause water pollution [16].

While extraction of gold using cyanide in (Yanqul mine of Oman) showed that, the ground water content of cyanides were about 5 ppb which is below detection limit, this was attributed to the evaporation of CN (converted into hydrogen cyanide HCN) and deep water basins [4].

One of the significant environmental components is soil, which is not less damaged than aquatic systems in the areas near to mining activities. Contamination and degradation of such soils by waste waters and solid wastes have widely been investigated in many areas over the world [13, 18-20]. This is due to its direct association with agriculture (plants and food crops) and consequently with human and animal health. Several reports have established that soils in the vicinity of overburden sulfide tailing were affected, because these soils contain high levels of heavy metals, metalliferous deposits depending on the mine and the distance from the site, low pH values and high SO_4^{2-} concentration [18-20]. This leads to accumulation of such toxic elements in plants and food crops which grow and absorb their nutrients from contaminated soils and sediments. As a result the human and animals can be in risk due to consuming fruits or vegetables that were grown in such contaminated soils [5]. Furthermore, the presence of excessive amounts of heavy metals and sulfates with low pH (less than 3.0) or high pH (more than 9.0, Ca and Mg mines) can cause degradation of soil fertility, quality, porosity and reduce availability of main nutrients such as nitrogen and phosphorus [13].

In the UK, acidic mine drainages and spoil heap discharges markedly concern the environment in many areas, in particular in Northern England and Wales [21]. A considerable amount of investigations have been carried out on surface, ground water and soils in the affected districts by spoil heaps drainage, tailing and wastewaters [21-24]. The contamination of soils and aquatic basins were ascribed to presence of significant concentrations of metals such (Cu, Mn, Cd, Pb, Ni, As, Zn and Fe) as well as large amount of marcasite (white iron pyrite FeS_2) and pyrite (FeS_2) [22, 25].

The geographic distribution of abandoned metals mines in England and Wales have reported that the Cu, Zn, Pb and Cd are more abundant in Wales, while Fe which is often associated with Mn is the in Northeast of England (place of our study) and the southwest of Wales [25]. In comparison with other base metals in Wales and England, the total mass flux (in tonnes/year) of iron released into the water environment exceeds the flux of any other elements. It has been established that a significant portion of Fe release to environment arise from ironstone in which spoil heap is overburdened with

pyrite and marcasite [25]. The pyrite is oxidized either by dissolved oxygen with assistance of bacteria or by iron(III). This leads to production of Fe^{2+} and eventually this is oxidized to Fe^{3+} often by biological processes [7].

Iron(III) ions begin to hydrolyse via several stages to form complicated oligomers, polymers and eventually to precipitate as ochre, which is observed as a yellow coating of sands and river beds [26]. The oxidation of pyrite is the main source of sulfur and both soluble and solid complexes of iron in acid mine drainage (AMD) as well as other base and heavy metals. Such metals may be more abundant than iron in other sulfide ores (not pyrite) depending on the ore composition, such as copper mines [2, 10].

1.3 Chemistry of mine water formation

Extensive studies have been carried out to understand the chemistry of mine water formation [7, 27-31]. The studies have simply characterized AMD as waters in both phases fluid and solid. The fluid phase involves soluble ferrous, ferric, H^+, soluble SO_4^{2-} and soluble heavy metals ions, while the solid phase has mainly been characterized as ochre (as will be explained latter in this chapter). However, extra efforts have been devoted for further information related to formation of acid mine drainage, because it incorporates several oxidation-reduction reactions, hydrolytic equilibria states and complexation reactions. Compounding the matter is that not only chemical reactions create acid mine drainage but there are some biological processes which possess a critical role in catalysing and accelerating acid mine drainage formation [2]. Accordingly, the chemical reactions and biological processes act in parallel manner to generate contaminated drainages called acid mine water.

The major component of mine tailing disposal and waste rock dumps is metal sulfides. The most naturally abundant is pyrite (FeS_2), as well as other sulfide minerals such as marcasite (white pyrite FeS_2), sphalerite ($ZnS_{(s)}$), covellite ($CuS_{(s)}$), millerite ($NiS_{(s)}$), galena ($PbS_{(s)}$) and greenockite ($CdS_{(s)}$). All aforementioned sulfide minerals except pyrite release soluble metal ions during their exposure to the atmosphere or oxygenated water without the generation of H^+ ion. This can be major sources of heavy metals contamination, as shown in the simple chemical equations (1.4 – 1.8), ignoring for the moment the complications related to the detailed chemistry of acid mine drainage:

$$ZnS_{(s)} + 2O_{2\,(aq)} \rightarrow Zn^{2+} + SO_4^{2-} \qquad \text{……(1.4)}$$

$$CuS_{(s)} + 2O_{2\,(aq)} \rightarrow Cu^{2+} + SO_4^{2-} \quad \text{……(1.5)}$$

$$NiS_{(s)} + 2O_{2\,(aq)} \rightarrow Ni^{2+} + SO_4^{2-} \quad \text{……(1.6)}$$

$$PbS_{(s)} + 2O_{2\,(aq)} \rightarrow Pb^{2+} + SO_4^{2-} \quad \text{……(1.7)}$$

$$CdS_{(s)} + 2O_{2\,(aq)} \rightarrow Cd^{2+} + SO_4^{2-} \quad \text{……(1.8)}$$

Weathering of pyrite minerals releases soluble ferrous ion Fe^{2+} and hydrogen ions (H^+) as well as sulfate ions SO_4^{2-}, as illustrated in the equation (1.9):

$$FeS_{2(S)} + \frac{7}{2} O_2 + H_2O \rightarrow Fe^{2+} + 2SO_4^{2-} + 2H^+ \quad \text{……(1.9)}$$

The generated ferrous ions will be oxidized into ferric ions if a sufficient amount of dissolved oxygen is present or if the solution contacts with atmosphere. This process consumes protons from the solution, equation (1.10).

$$Fe^{2+} + \frac{1}{4}O_2 + H^+ \rightarrow Fe^{3+} + \frac{1}{2}H_2O \quad \text{……(1.10)}$$

Considerable increases in the net acidity are produced by two further reactions; the first is due to multiple hydrolysis steps of ferric ion (Fe^{3+}) to convert into iron oxyhydroxide (ochre) as illustrated in equation (1.11). The second reaction that generates extra protons (H^+) as well as ferrous ions and sulfate is the reaction of ferric ions (Fe^{3+}) with other pyrite minerals, as illustrated in equation (1.12).

$$Fe^{3+} + 3H_2O \rightarrow Fe(OH)_{3\,(S)} + 3H^+ \quad \text{……(1.11)}$$

$$7Fe^{3+} + \frac{1}{2}FeS_{2\,(S)} + 4H_2O \rightarrow SO_4^{2-} + \frac{15}{2}Fe^{2+} + 8H^+ \quad \text{……..(1.12)}$$

The cycle of reactions 1.10 – 1.12 can persist if sufficient dissolved oxygen is present and continue because of step (1.12). However, under anaerobic conditions ferrous ions (Fe^{2+}) will be predominant in acid mine drainages and reaction (1.12) may proceed toward completion [31, 32]. Accordingly, the fluids associated with aforementioned reactions exhibit low pH, high Oxidation reduction potential (Eh), high contents of heavy metals, ferrous, ferric and sulfate ions [1, 33].

The second part of AMD is fine particle solid phase (ochre), this has been characterized as iron(III) oxyhydroxide precipitate $Fe(OH)_{3(s)}$ (or misused synonym ferrihydrite). The

reactions by which this precipitate occurs, has been summarized in the simple manner as follows [27]:

$$4Fe^{2+} + O_2 + 4H^+ \xrightarrow{\text{Oxidation}} 4Fe^{3+} + 2H_2O \quad \text{.....(1.13)}$$

$$Fe^{3+} + 3H_2O \xrightarrow{\text{hydrolysis}} FeOOH + H_2O + 3H^+ \quad \text{.....(1.14)}$$

$$FeOOH + H_2O \rightarrow Fe(OH)_{3\ (ochre)} \quad \text{.....(1.15)}$$

However, this mechanism may be valid only at pH higher than 7.0, because at lower pH Schwertmannite ($Fe_8O_8(OH)_6SO_4$), jarosite (H, K, Na)$Fe_3(OH)_6(SO_4)_2$ and basic sulfate complexes have been reported to be formed in AMD at pH less than 6.5 [34-39].

1.4 Kinetics and mechanisms of pyrite oxidation in acidic mine drainages

Electron transfer from pyrite to dissolved oxygen (O_2) and ferric ions (Fe^{3+}) is the key reaction for releasing soluble sulfate ions (SO_4^{2-}), soluble ferrous ions (Fe^{2+}) and hydrogen ions (H^+) into solution. Therefore, studying the rate and mechanism of electron transfer from reducing agents to oxidizing agents is a major route to understanding role of such redox reactions in formation of acid mine drainages. Also, it can be the first step to identify more details about subsequent stages associated with formation of acid mine drainages.

For these reasons, the oxidation of pyrite (FeS_2) has received much attention in the fourth quarter of the last century. Numerous investigations have been performed to study the mechanisms of pyrite oxidation in aqueous solutions using spectroscopic techniques (such as X-ray photoelectron spectroscopy (XPS) [40-43], Raman spectroscopy [40, 44], Fourier transform infrared (FTIR) [45]) and electrochemical techniques (such as linear potential sweep voltammetry [46], cyclic voltammetry (CV), steady state voltammetry [47, 48], scanning tunnelling microscopy (STM) [42, 49-51]). The electrochemical techniques have advantages for analysing individual half reactions of pyrite oxidation; requiring less analysis time, smaller amount of pyrite material [47] and may provide detailed understanding of the atomic and electronic structure of pristine pyrite surfaces using in-situ STM [49, 50].

Three mechanisms have been suggested to explain the oxidation of pyrite by molecular oxygen and Fe^{3+}, namely, bacterial, chemical and electrochemical [31, 52-54].

1.5 Bacterial action on the rate and mechanism of pyrite oxidation

At the end of 1940s, the accepted thinking was that the role of acidophilic chemoautotrophic bacteria was to increase the rate of $Fe(OH)_3$ precipitation[7, 28, 55], but in 1953 it was established that *T. ferrooxidans* increases the rate of pyrite oxidation [30], and the oxidation rate of Fe^{2+} to Fe^{3+} by factor of 10^6 compared to the rate in their absence [7]. These bacteria harness the transferred electrons during redox processes as a source of energy for their growth and cell functions. Also, oxidation of sulfur and sulfide into sulfuric acid (H_2SO_4) can be accelerated by a bacterium from the same family called *T. thiooxidans* as shown in the following reactions [52, 53]:

$$S^0 + \frac{3}{2}O_2 + H_2O \rightarrow H_2SO_4 \qquad \text{……(1.16)}$$

$$S^{2-} + 2O_2 + 2H^+ \rightarrow H_2SO_4 \qquad \text{……(1.17)}$$

These bacteria can promote and enhance the oxidation, hydrolysis and precipitation of dissolved iron at pHs between 1.5 – 3.0 in which the bacteria thrive [27].

Despite that the comprehensive description of mechanisms and kinetics of pyrite oxidation by *Thiobacillus ferrooxidans* may not be straightforward. This is due to several variables which can influence the pyrite oxidation such as Eh, pH, oxidation medium, presence of certain bacteria and temperature. However, two mechanisms have been suggested to explain bacterial action on the pyrite oxidation process. The first is direct metabolic oxidation (DMO), and the second is indirect metabolic oxidation (IMO) [52, 53].

1.5.1 Direct metabolic oxidation (DMO)

In this mechanism, contact between bacteria and the pyrite surface is required and the overall reaction is:

$$FeS_2 + \frac{7}{2}O_2 + H_2O \xrightarrow{\text{bacteria}} Fe^{2+} + 2SO_4^{2-} + 2H^+ \qquad \text{……(1.18)}$$

Two steps were involved in the above reaction, the first is dissolution of FeS_2 to produce disulfide ion (S_2^{2-}), and the second is reaction of disulfide with oxygen to form sulfate ion (SO_4^{2-}), as illustrated in the following equations [53]:

$$FeS_2 \rightarrow Fe^{2+} + S_2^{2-} \quad \text{……(1.19)}$$

$$S_2^{2-} + 4O_2 \xrightarrow{\text{bacteria}} 2SO_4^{2-} \quad \text{....……(1.20)}$$

Two possible mechanisms for the behaviour of *T ferrooxidants* have been proposed, the first is that surface of pyrite is attacked by the bacteria by which the oxidation of sulfur (S) and iron (Fe) by oxygen (O_2) were catalysed, the reaction 1.21 is sum of all steps involved in this process [56]:

$$4FeS_2 + 15O_2 + 2H_2O \xrightarrow{\text{bacteria}} 2Fe_2(SO_4)_3 + 2H_2SO_4 \quad \text{……(1.21)}$$

The second proposed mechanism is that the *T. ferrooxidants* bacteria feed on pyritic sulfur which leads to its oxidation to sulphate as shown in equation (1.20) [53, 57].

1.5.2 Indirect metabolic oxidation (IMO)

In this mechanism, the direct contact between bacteria and pyrite surface is not required. However, the bacteria act to generate Fe(III) which act as the oxidizing agent instead of bacteria as shown in the following equations [53]:

$$FeS_2 + 7Fe_2(SO_4)_3 + 8H_2O \rightarrow 15FeSO_4 + 8H_2SO_4 \quad \text{…… (1.22)}$$

The Fe^{3+} used to oxidise the pyrite in previous reaction was generated by action of *T. ferrooxidants* on the produced ferrous ions and sulfur in the former equation as following equations:

$$4FeSO_4 + O_2 + 2H_2SO_4 \xrightarrow{\text{bacteria}} 2Fe_2(SO_4)_3 + 2H_2O \quad \text{……..(1.23)}$$

$$2S^0 + 3O_2 + 2H_2O \xrightarrow{\text{bacteria}} 2H_2SO_4 \quad \text{……..(1.24)}$$

1.6 Chemical mechanism of pyrite oxidation

The chemical mechanism of pyrite oxidation has been proposed to occur either by dissolved oxygen (DO) or by both dissolved oxygen (DO) and Fe(III) [58-61]. The former mechanism [60] has been suggested on the basis of direct contact between dissolved oxygen (DO) and partially protonated pyrite surfaces. This process occurs in several stages, the first is initiated by bonding the DO to the pyrite surface, followed by

a second step in which the double bond in dioxygen is broken and displaced by H_2O. Eventually, the sulfide is released as S_2OH^-, figure (1.1).

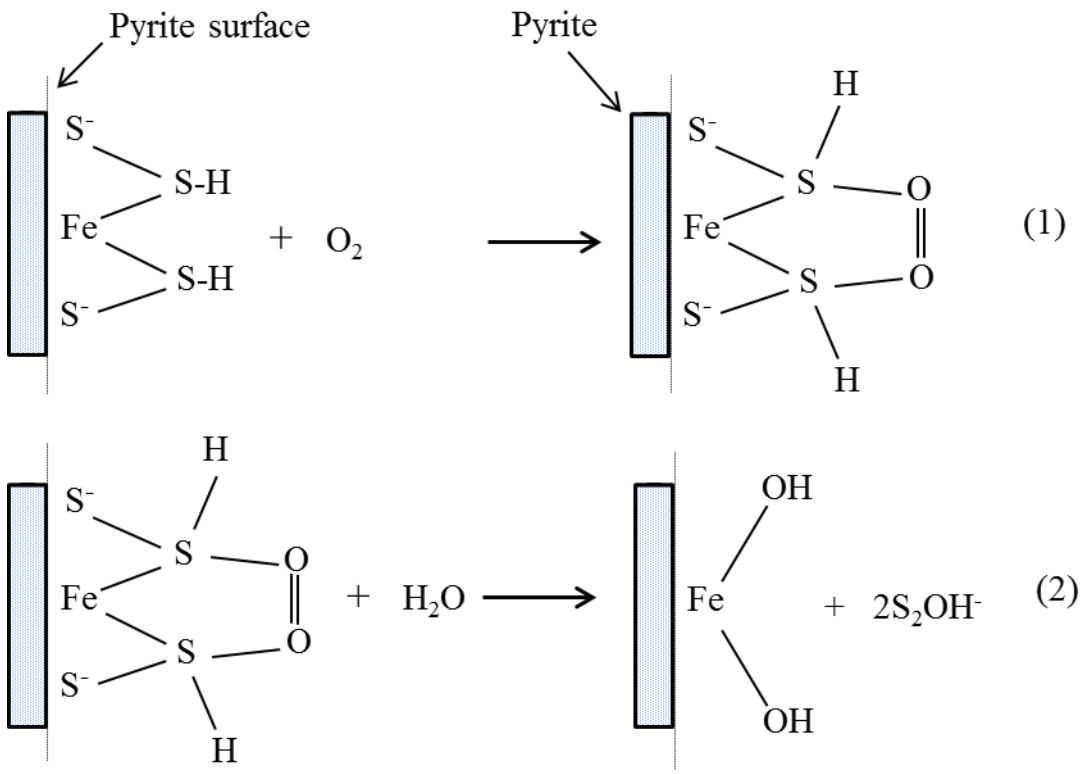

Figure 1.1: schemes (1) and (2) describe steps of pyrite oxidation by direct contact between pyrite surface and molecular oxygen (from [2], N. O. Egiebor and B. Oni, Acid rock drainage formation and treatment: a review. Asia-Pacific Journal of Chemical Engineering, 2007, **2**, 47-62).

The second mechanism involves electron transfer from adsorbed Fe(II) on the pyrite surface (FeS_2-Fe(II)) to (DO) to form FeS_2-Fe(III) in which Fe(III) is adsorbed on pyrite surface [59]. This step is followed by electron transfer from pyrite to adsorbed Fe(III) which leads to produce FeSSOH-Fe(II), in turn, it undergoes to further step of electron transfer to form $FeSSO_2H$-Fe(II), figure 1.2 (a and b). In this mechanism, the (DO) never directly reacts with pyrite, but the oxygen is reduced by acceptance of the electron from adsorbed Fe(II) on pyrite surface which leads to form Fe(III).

1.7 Electrochemical mechanism of pyrite oxidation

The electrochemical mechanism of pyrite oxidation has been described according to one or more of the following anodic and cathodic reactions occurring on the pyrite surface.

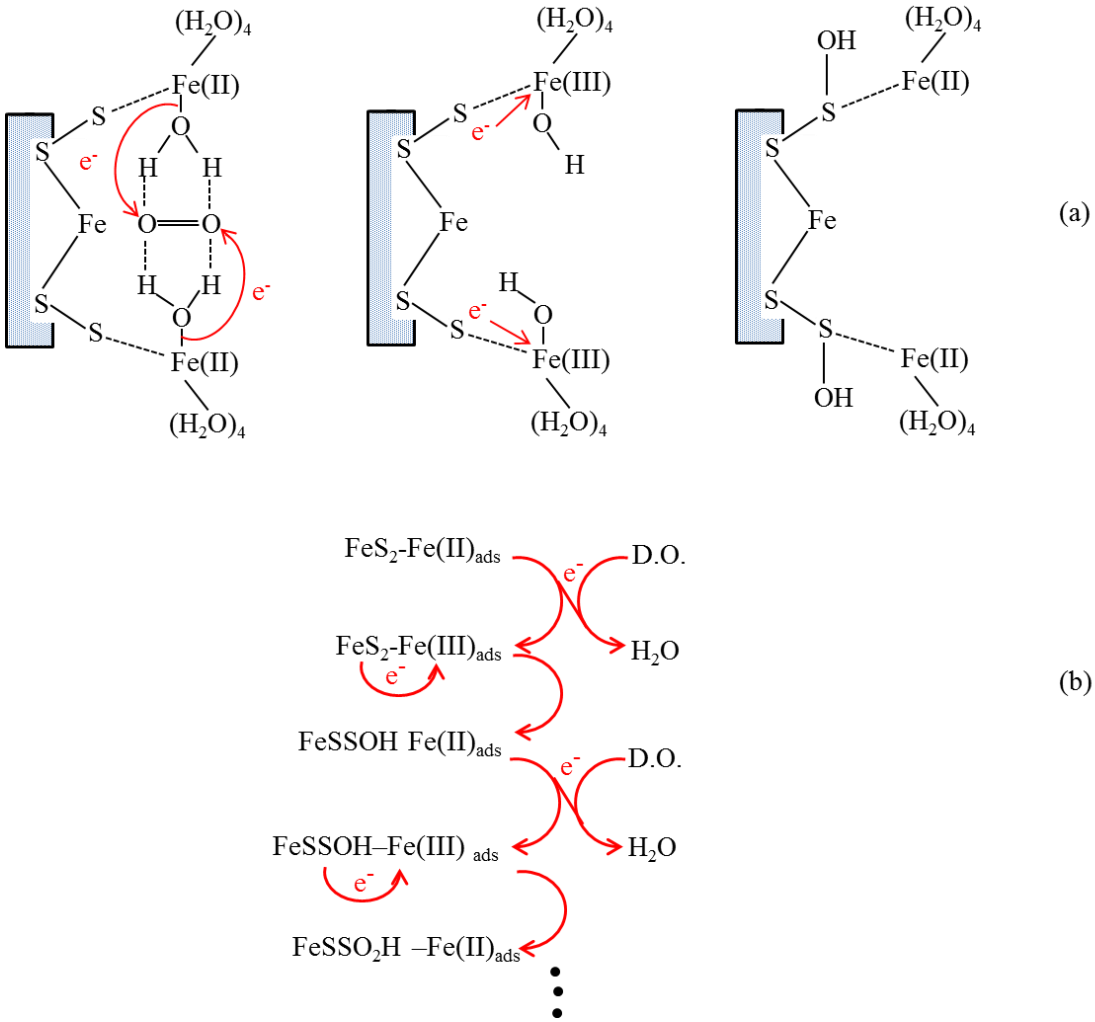

Figure 1.2: Schematic sequence of reaction steps for the oxidation of pyrite, (b) is a summary of (a), (note: The chemical reactions are not balanced in detail). (from [59] C. O. Moses and J. S. Herman, Pyrite oxidation at circumneutral pH. Geochimica Et Cosmochimica Acta, 1991, **55**, 471-482).

At the anode

$$FeS_2 + 8H_2O \rightarrow Fe^{3+} + 2SO_4^{2-} + 16H^+ + 15e^- \quad \text{.....(1.25)}$$

$$FeS_2 \rightarrow Fe^{2+} + 2S^0 + 2e^- \quad \text{.....(1.26)}$$

$$FeS_2 + 4H_2O \rightarrow Fe^{3+} + SO_4^{2-} + S^0 + 8H^+ + 9e^- \quad \text{.....(1.27)}$$

$$FeS_2 \rightarrow Fe^{3+} + 2S^0 + 3e^- \quad \text{.....(1.28)}$$

At the cathode

$$O_2 + 4H^+ + 4e^- \rightarrow 2H_2O \quad \text{.....(1.29)}$$

$Fe^{3+} + e^{-} \rightarrow Fe^{2+}$ ……(1.30)

The reaction (1.25) has been reported to follow the sulfate route (only sulfate and no sulfur element) and leads to produce Fe^{3+} and SO_4^{2-} [2, 62]. Reactions (1.25) and (1.26) have been observed to be controlled by the electrode potential; at high anodic potential SO_4^{2-} ions are produced, and at low anodic potential the elemental sulfur elements (S^0) has been observed to be the predominant as a solid component in the solution [2, 54].

According to above mechanisms, it has been understood that the oxidation of pyrite occurs as a result to electron transfer from pyrite into dissolved oxygen (DO) and soluble Fe^{3+}. The oxidation by (DO) has been suggested to occur via direct and indirect contact of (DO) to the pyrite surface in chemical mechanism. However, the oxidation of pyrite by bacteria can occur either by direct attachment to the pyrite surface or indirect microbial action in which Fe^{3+} is produced by bacterial oxidation of Fe^{2+}.

It has also been demonstrated that the rate of pyrite oxidation by Fe^{3+} (reaction 1.12) is more rapid than by (DO) (reaction 1.9). Therefore, the reaction (1.10) is rate-limiting step for overall pyrite weathering by Fe^{3+}. Reaction 1.10 is an abiotic reaction and its rate was observed to be increased at neutral pH because of the stabilising influence of hydroxyl ions (OH^-) on the higher oxidation state [7, 63]. However, the rate of the biotic reaction of pyrite weathering by Fe^{3+} was observed to be more rapid at low pH than at neutral pH. This variation in the rate of pyrite oxidation was attributed to two reasons. The first is the presence of acidophilic bacteria which catalyse production of Fe^{3+}. The second is the larger concentration of soluble species of Fe^{3+} at low pH, because $Fe(OH)_{3(s)}$ is protonated and forms more soluble species [32, 42].

1.8 Aqueous speciation of synthetic iron–sulfate–acid-water systems

It is well known that the first step of mineralogy and chemistry of acid mine drainages (AMD) is linked with low pH seepage, high content of sulfide minerals and high concentrations of soluble metals and sulfate. Oxidation of pyrite (FeS_2) has been established in numerous studies as the most significant source of soluble iron (Fe^{2+}), sulfate (SO_4^{2-}) and hydrogen ions (H^+) [29-31, 64]. Accordingly, understanding the behaviour and thermodynamic aspects of analogous synthetic soluble species of Fe^{3+}, Fe^{2+} and SO_4^{2-} in acidic solutions at high ionic strength is an important requirement. This may provide valuable information about chemical equilibria of such species to be

used in geochemical databases, which may lead to improvement of remediation strategies. Several studies have been conducted on synthetic systems of iron-sulfate-water in acidic solutions using geochemical models [65-69] and chemical techniques [34, 70-72].

The equilibrium constants of the speciation (e. g. $FeSO_4^+$, $FeHSO_4^{2+}$, $FeOHSO_4$ and $Fe(SO_4)_2^-$) in synthetic aqueous acid iron sulfate system (Fe(II)-Fe(III)-SO_4-H_2O) at 25 ^oC, ionic strength 0.35 mol kg^{-1} and pH varied between (1 and 4) has been verified using a speciation program and their values were recommended for incorporation into geochemical databases [65]. Further, the $Fe_2(SO_4)_3$–H_2SO_4–H_2O system has been investigated using Pitzer ion interaction model to obtain some thermodynamic parameters at solute molalities between 3 and 5.47 mol kg^{-1}, and high ionic strength up to 45 mol kg^{-1}. Although this model provides some thermodynamic properties of the system, a comparison of the obtained results with those derived from solubility products show that the solubility of some mineral-solution compositions in the $Fe_2(SO_4)_3$–H_2SO_4–H_2O system is not entirely understood [67]. Another study for modelling chemical equilibria of acid mine-drainage of the $FeSO_4$-H_2SO_4-H_2O system has been carried out using Pitzer formulation; the model provides useful thermodynamic parameterization of prediction of ferrous sulfate hydrate stability, phase transition points and solute activities over a temperature range of from 10 to 60 ^oC [68].

Chemical characterization using Raman spectroscopy has been conducted on two synthetic iron(III)-sulfate in sulfuric acid and water systems (Fe^{2+}–H_2SO_4–H_2O**)** and (Fe^{3+}–H_2SO_4–H_2O). These systems have been chosen to mimic AMD in the Rio Tinto (Spain) area. For the former system, the concentrations of the species $[SO_4^{2-}]$, $[HSO_4^-]$ and $[H^+]$ were measured, while thermodynamic information were obtained via calculation of activity coefficient product (K_Υ) which is essential for physico-chemical models. A Raman study of the system (Fe^{3+}–H_2SO_4–H_2O) has discovered that sulfate-iron(III) interaction occurs in both an inner-sphere and outer-sphere manner via hydrogen bonding [71, 72].

Further, synthetic systems (Fe^{2+}, Fe^{3+} and SO_4^{2-}) has been investigated using X-Ray absorption spectroscopy and Fourier transform infrared (FTIR). The reason for which the system was chosen is because of its similarity to AMD composition. The study concluded that the dominant soluble species in the system is Fe(III)-SO_4 complexes, these complexes are hydrogen-bonding interaction, and that the inner-sphere interaction

may not exceed 10% of the total sulfate. Also it has revealed that the Fe-sulfate interaction was similar in both aqueous solution and colloidal solid phase (e. g. schwertmannite). Further, it has found that the association of sulfate with Fe(II) can take place either only as an outer-sphere or it does not occur at all [34]. The observation that sulfate interacts with iron(III) not iron(II) is used in this study to determine sulfate from voltammetry peak shift.

1.9 Solid speciation of iron and sulfate in synthetic and natural precipitations

A subsequent step in AMD after producing soluble sulfate (SO_4^{2-}), H^+ and oxidation of Fe^{2+} into Fe^{3+} is precipitation of Fe^{3+} in solid phases called ochre as shown in equation (1.31), the nature of ochre depends on pH, sulfate concentration, other metals and different complexing ligands [35, 73].

$$Fe^{3+} + 3H_2O \rightleftharpoons Fe(OH)_{3\,(s)} + 3H^+ \qquad \text{.....(1.31)}$$

This process is called secondary iron(III) and sulfate minerals precipitation in acid mine drainages. Understanding the secondary iron(III) and sulfate deposition is valuable for predicting a possible pollution problem and exploring useful information about buried deposit. Further, it has been reported that the dominant solid phases may control the activity of major and minor soluble species in AMD which play a significant role in AMD remediation processes [39, 74].

The identification of the solid phase formed mainly from iron and sulfate in acid mine water has not fully been achieved, because of the complexity of such drainages. Therefore, several investigations have widely been conducted for both synthetic and natural specimens using geochemical models [35, 37, 75] and chemical characterization (X-Ray diffraction XRD [35, 37, 39], FTIR [37, 39], Mössbauer spectroscopy [39], scanning electron microscopy (SEM) and transmission electron microscopy (TEM) [76]. These studies have demonstrated that Jarosite ($K,Na,H_3O[Fe_3(OH)_6(SO_4)_2]$) can be formed at pH < 3 and at high sulfate concentration [SO_4^{2-}], while Schwertmannite ($Fe_8O_8(OH)_6SO_4$) can be the dominant deposit with pH range 3 - 4.5. At higher pH (pH > 6.5) ferrihydrite ($Fe_5HO_8.4H_2O$) and goethite (α-FeOOH) have been demonstrated to be the dominant compounds [35].

Other studies have identified presence of lepidocrocite (ϒ-FeOOH) [77], akaganeite (β-FeOOH) [78], Bianchite ($(Zn,Fe^{2+})(SO_4).6H_2O$), Botryogen ($MgFe^{3+}(SO_4)_2(OH).7H_2O$), Copiapite ($Fe^{2+}Fe_4^{3+}(SO_4)_6(OH)_2.20H_2O$) and Fibroferrite ($Fe^{3+}(SO_4)(OH).5H_2O$) [79] in acid mine drainages along with hematite and goethite, but they are less common. The most dominant mineral in sulfate-rich acidic mine drainages at moderate pH (pH of acid mine drainages) is schwertmannite. It is an iron(III) oxyhydroxysulfate with chemical formula ($Fe_8O_8(OH)_6SO_4$). It is a metastable phase, and it transforms to ferrihydrite, hematite and more stable goethite to release SO_4^{2-}, Fe and H^+ at pH > 4 as shown in equation (1.32) [80, 81], it also transforms to goethite and jarosite with low pH (pH < 2.5) [82].

$$Fe_8O_8(OH)_{5.5}(SO_4)_{1.25\,(s)} + \frac{5}{2}H_2O \rightleftharpoons 8FeOOH_{(s)} + \frac{5}{4}SO_4^{2-} + \frac{5}{2}H^+ \quad \text{.....(1.32)}$$

Different Fe(III) precipitates are known to play a significant role in treatment of AMD by attenuation of metal contaminants in the AMD. These precipitates have been utilized to adsorb metal ions from solution either by co-precipitation, sorption and formation of surface precipitate or a combination of all three. These processes have been found to be strongly pH-depended as they increase with increasing pH [83], SO_4^{2-} concentration [84] and the nature of the sorbent minerals whether it was naturally formed or synthetic [83, 84].

It has been established that adsorption of Cu, Pb, Cd and Zn on schwertmannite, ferrihydrite and goethite can be more adsorptive in environmental than synthetic solutions. This was attributed either to the formation of ternary complexes between the oxide surface, adsorbed SO_4^{2-} and the metal ion or bacteria-mediated formation of the AMD precipitate [84]. Also, the adsorption of Cu, Zn and Pd has been observed to be enhanced even at low pH in the case of presence of high concentration of SO_4^{2-} on ferrihydrite and goethite than its absence. Further, schwertmannite has been discovered to exhibit similar behaviour regarding Cu and Zn adsorption [84]. Therefore, understanding of secondary iron and sulfate minerals in AMD was key factor for developing effective remediation methods for AMD pollution.

1.10 Hydrolysis of iron(III) aqua complexes

The general concept of hydrolysis is simply the chemical reactions in which compounds are decomposed in water [85]. The hydrolysis of iron(III) is considered an important

reaction wherein the generated products possess several benefits in various fields including medicine, industry, corrosion, soil science and environmental chemistry [86]. Hydrolysis of iron(III) solutions can be accelerated by addition of base; initially, at low pH, a yellow solution appears in which mono and binuclear iron species are formed, but with an increase in the [OH^-/Fe^{3+}] ratio both polynuclear (either oxo or hydroxo complexes) are formed. Eventually, at [OH^-/Fe^{3+}] ratio equals to or exceeding 3.0 an amorphous precipitate is created which gradually transforms into a crystalline compound [86]. These hydrolysis stages and their kinetics are controlled by several variables such as the presence of different ligands (e. g. sulfate) [87-89], pH, iron(III) concentration and temperature [90, 91].

1.10.1 Effects of sulfate ions on hydrolysis-precipitation of iron(III)

Hydrolysis of iron(III) in aqueous solutions has been widely investigated [92-100], these studies have reported that at low pH the dominant complexes are iron(III) octahedral complex $[Fe(H_2O)_6]^{3+}$, $[Fe(OH)(H_2O)_5]^{2+}$, $[Fe(OH)_2(H_2O)_4]^{+}$, $[Fe_2(OH)_4(H_2O)_8]^{2+}$ and $[Fe_3(OH)_4(H2O)_{17}]^{5+}$. With increasing pH high molecular weight polymers (e. g. $[Fe_{12}(OH)_{34}]^{2+}$ are formed along with oxyhydroxide precipitates (e. g. goethite (α-FeOOH) and hematite (α-Fe_2O_3)). The foregoing complexes and their hydrolysis processes were obtained and occurred in direct manner in presence of weak coordinating ligands (e. g. nitrate (NO_3^-) and/or perchlorate (ClO_4^-)).

On the other hand, the presence of strongly coordinating ligands along with soluble iron(III) species leads to marked changes in the general pattern of hydrolysis processes (e.g. size of polymer, rate of hydrolysis and composition of precipitate). Because such ligands can occupy more than one coordination site in simple iron(III) species (e. g. $[Fe(H_2O)_6]^{3+}$), the resulting complexes hinder or catalyse different hydrolysis steps [101, 102].

The best example of the effect of strongly coordinating ligands with soluble iron(III) ion is sulfate ion (SO_4^{2-}). It has been established in various studies using spectrophotometry [103, 104], temperature-jump [105], continuous-flow techniques [106] and potentiometric [107] that, the hydrolysis of iron(III) in presence of sulfate produces different soluble species of iron(III)-sulfate depending on pH and [SO_4^{2-}]/[Fe^{3+}] ratio such as $[FeSO_4]^+$, $[FeHSO_4]^{2+}$ and $[Fe(SO_4)_2]^-$. The most significant component among these complexes is $FeSO_4^+$; it has been established from thermodynamic studies that the

stability of $FeSO_4^+$ is higher than other iron(III)-ligands complexes such as $FeCl^{2+}$ and $FeBr^{2+}$ complexes [108, 109].

Various studies using spectrophotometric, potentiometric, combined stopped-flow temperature jump techniques [107], Mössbauer spectroscopy [110], absorption spectra [111] and X-Ray diffraction (XRD) [112] have emphasized the role of $FeSO_4^+$ on the formation of basic sulfate complexes and other precipitates such as jarosite and/or hematite and/or goethite, depending on pH and $[SO_4^{2-}]/[Fe^{3+}]$ ratio. Further, $FeSO_4^+$ has been established to suppress the polymerization processes and catalyse the condensation of dimerization, basic sulfate-iron(III) and nucleation steps of iron(III) hydrolysis as shown the following scheme [111]:

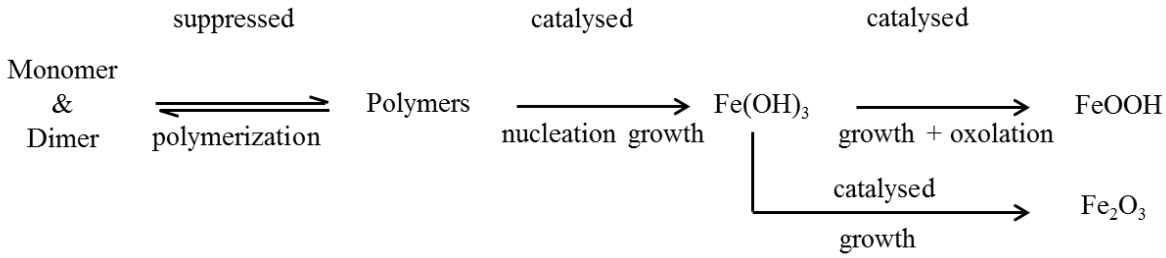

Accordingly, kinetic aspects of different steps of iron(III) hydrolysis in aqueous solution and in natural water such as mine water drainages should receive much attention, because this may lead to improve and develop best procedures for effective remediation methods which are the main object in our investigation.

1.11 Area of study and site description

The study was conducted on the Shilbottle Colliery site in Northumberland, in the north east of England. It is located about 30 miles north east of Newcastle upon Tyne and about 4 mile south east of Alnwick, figure 1.3. The history of this site can be traced back to the early 19^{th} century, where coal working was started on this site until 1982 when the site was closed and abandoned [113]. The major residues of these activities is a highly contaminated spoil heap, which is rich with a large amount of metal-sulfide especially pyrite. This, in turn, produces high concentrations of soluble metal ions such as Fe, Al and Mn as well as soluble SO_4^{2-} as rainwater leaches through the heap.

During the rainfall season the soluble metals-contaminated leachate from the spoil heap seep in to adjoining Tyelaw Burn, this in turn flows to the Coquet River causing

spectacular ochreous pollution. For these reasons several attempts have been adopted since the mid-1990s to reduce such severe environmental damage, including reed-beds and wetlands. These were constructed along with a permeable reactive barrier remediation system in 2003 [21, 113].

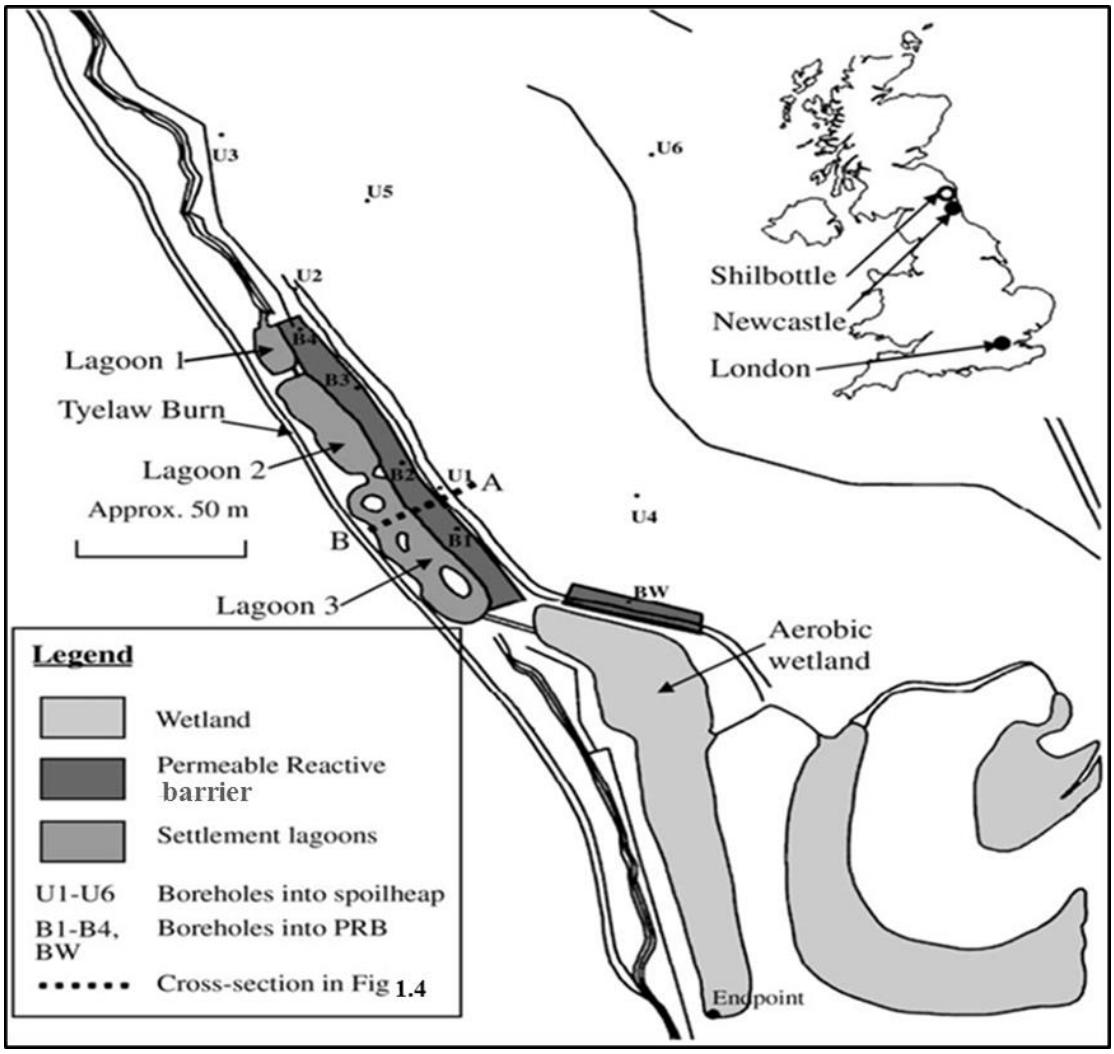

Figure 1.3: Schematic showing the location of study, and layout of plan at Shilbottle site settlement lagoons, emanating of pyrite from boreholes into spoil heap and PRB, (from[21] A P. Jarvis, A. Moustafa, P. H. A. Orme and P. L. Younger, Effective remediation of grossly polluted acidic, and metal-rich, spoil heap drainage using a novel, low-cost, permeable reactive barrier in Northumberland, UK. *Environ. Pollut.*, 2006, **143**, 261-268).

The steps through which the leachates discharge seeps from the spoil heap (locally termed as˝Brass heap˜) into Tyelaw Burn are illustrated in figure 1.4. Falling rain water on the spoil heap causes an increase in the seepage of soluble contaminants. Then the leachate is discharged through the constructed permeable reactive barrier (PRB) before entering settlement lagoons. Eventually, the decontaminated water can flow to Tyelaw Burn stream via reed-bed wetland.

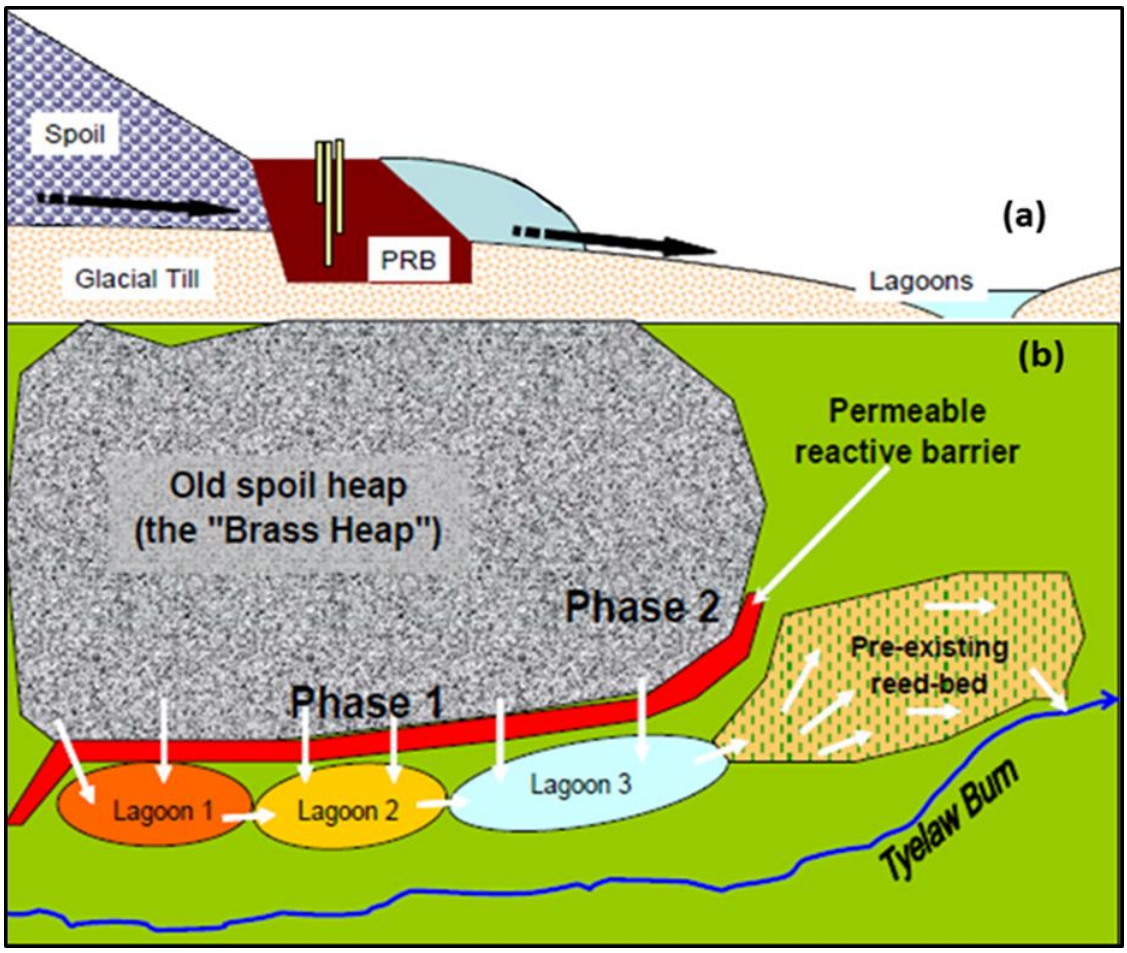

Figure 1.4: Schematic showing, (a) cross section and (b) longitudinal section (b) of the seepage of soluble contaminants into settlement lagoons and Tyelaw Burn. (From hydro- geological engineering research outreach (HERO) group at Newcastle University).

1.12 Study aims and objectives

There are two generic methods to treat mine water pollution, passive and active treatment systems. In the passive treatment technology, the improvement of mine water quality can be achieved using only naturally-available energy sources such as microbial metabolic energy and gravity. While in active treatment technology, the improvement of water quality require artificial energy (such as heat to change reaction rates, pressure to change gas-liquid exchange rates and electrical power for mixing or pumping), and/or biochemical regents such as sodium hydroxide NaOH, calcium hydroxide, organic polymers and less common pressurized gases. The main advantages which passive treatment has over active treatment are low operating costs, use of non-hazardous materials and the long term nature of the remediation process [32].

The most effective remediation technology that has been used to treat AMD in Northumberland coal sites (Shilbottle) in the last decade is the passive treatment system

[21, 114]. This technology included three options; (1) Permeable reactive barriers (PRB), (2) Reducing and alkalinity producing systems (PAPS) and (3) Compost wetlands [21]. For example, the PRB system was mainly constructed from carboniferous limestone mineral and less content of composted horse manure and green waste compost, as described in (Jarvis, et 2006) [21]. The significant objective of such technology is to rising up the pH which in turn encourages metal ions (e. g. iron and aluminium) to precipitate and reduce the mobility of metal contaminants [21, 113].

This remediation strategy (elevated pH and contaminated precipitation) has been established and used for AMD treatment for more than five years, but the pH of the Shilbottle site is still less than 4 and soluble iron species are still present up to a few mM. This may be attributed to kinetic considerations of condensation, polymerization and eventually precipitation of all soluble iron(III) species from the solution. For these reasons, this project aims to:

1- Develop electrochemical methods for measuring kinetic parameters of iron(III) hydrolysis.
2- Study the rate of hydrolysis, condensation and oligmerization processes of iron(III) aqueous solutions in both pure laboratory and environmental samples of Shilbottle AMD using electrochemical and spectroscopic techniques.
3- Study effects of sulfate on the rate of iron(III) hydrolysis and oligomerization using electrochemical techniques.
4- Identification and characterization of soluble iron and sulfate species in AMD using electrochemical and spectroscopic techniques, and comparing the obtained results with thermodynamic measurements using a geochemical model (PHREEQC).
5- Develop electrochemical methods for determination of soluble iron(II), iron(III) and sulfate concentrations in AMD.

Chapter 2: Analytical Techniques and Experiments

2.1 Electrochemical techniques / an introduction

The science of electrochemistry is the chemistry concerned with the interplay between the solution/electrode interfaces; such processes involve the changes of current, potential and charge as a function of chemical reactions. The advantages of electrochemical methods in comparison to other chemical techniques are high sensitivity, short analysis times (seconds), wide range of temperatures, use of many solvents and electrolytes, simultaneous analysis (more than one component in the same time), simplicity, moderate cost, portability and providing information about kinetics and thermodynamics [115-118].

Such techniques are classified into static methods (e.g. potentiometric) and dynamic methods (e. g. coulometric and voltammetric); such a classification is based on the fact that in static methods no current passes through the electrode-solution interface and the concentration of analyte species remains constant. In dynamic methods, a current flows across the electrode-solution interface and the concentration of species changes [119].

The dynamic methods are subdivided into two categories. Controlled-current methods include chronopotentiometry where the potential (E) is recorded as a function of time (t), coulostatic methods in which the potential (E) is recorded with time after a *charge-step* and a very short pulse of current flows to change the charge, and coulometry where the charge (Q) is measured as a function of time (t). The instrument used for these techniques is called a *galvanostat.* Controlled-potential methods encompass several subclasses of techniques depending on whether the potential is variable or fixed. The variable potential involves many common voltammetric techniques (linear potential, pulse and step potential, polarography and amperometry), while the fixed potential techniques involve the chronoamperometry and chronocoulometry, the equipment used for all voltammetric measurements is termed a *potentiostat* [115, 119]**.** The above classifications of electrochemical techniques are summarized in figure 2.1.

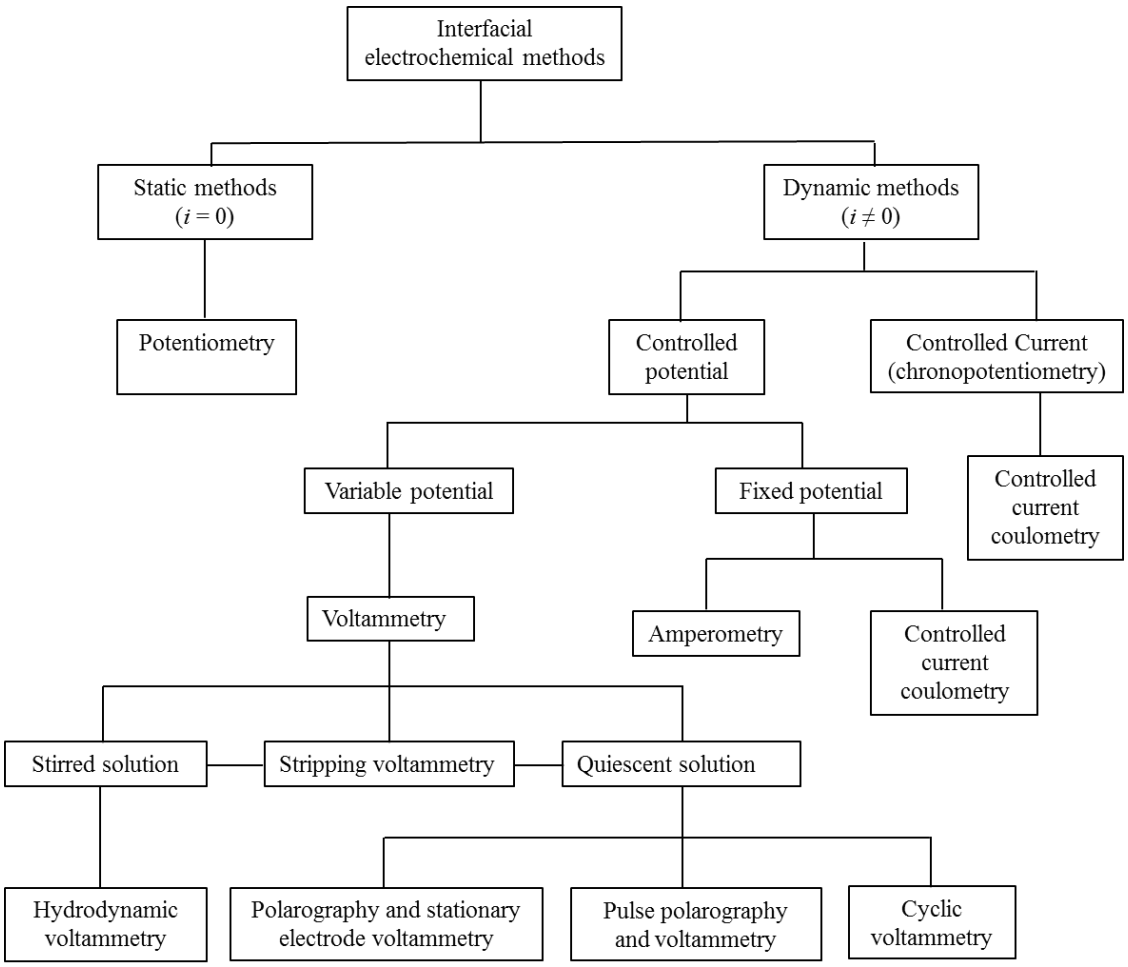

Figure 2.1: Classification of electrochemical techniques (Reprinted from [117] J. Wang, Analytical Electrochemistry, *By John Wiley, New Jersey*, 2006.).

2.2 Fundamentals and concepts of electrochemical analysis

This section will discuss the common principles of electrochemical analysis, as well as characterization of voltammograms obtained from different electrochemical experiments according to their reversibility. Furthermore, this section will review in some details potentiometric and voltammetric techniques which were used in this work e.g. ion selective electrode, chronopotentiometry, cyclic voltammetry (CV) and square wave voltammetry (SWV).

2.2.1 The composition of electrochemical cells

Electrochemical cells with low resistance can be investigated successfully using only two electrodes. However, the three electrode cell is preferred for electrochemical analysis especially at high cell resistance. The most interesting electrode among these

electrodes is the working (indicator) electrode, where the reaction between electroactive species in solution and electrode surface takes place. Then the potential is monitored relative to the reference electrode. Furthermore, at the working electrode full information can be acquired (e.g. thermodynamic and kinetics) depending on material of working electrode and applied potential.

The second electrode of electrochemical cell is the reference electrode in which the potential must remain as a constant value over the experiment duration, even with passing of the current across the reference electrode. Therefore, any changes in the electrochemical cell can be attributed to the processes occurring on the working electrode (either observed or controlled potential). The reference electrode should also be reversible and have a stable potential which may be calculated from the Nernst equation. There are many standard reference electrodes such as the standard hydrogen electrode (SHE) which is set by convention equal to 0.00 V, and standard silver chloride electrode (0.222V vs. SHE at 25 ^{o}C) and saturated calomel electrode SCE (0.242V vs. SHE at 25 ^{o}C).

The third electrode in the electrochemical cell is the counter (auxiliary) electrode; usually it can be platinum, tungsten or any inert wire. Since in cells comprising two-electrodes the current flows between both electrodes (working and reference), this may affect the potential of the reference electrode and consequently the cell potential, because the reference electrode serves simultaneously as auxiliary and reference electrode. In order to overcome on such problem a counter electrode should be used, and then the current will flow between working and counter electrodes instead of working and reference electrodes (figure 2.2) [115, 116].

The correlation between the potential and concentrations of electroactive species can be mathematically expressed by Nernst equation:

$$E=E^{\phi}+\frac{RT}{nF}\ln\frac{[O]}{[R]} \qquad \text{.....(2.1)}$$

Where E is cell potential (V), E^{ϕ} is standard electrode potential (V), R is the gas constant (8.3145 J mol^{-1} K^{-1}), F is Faraday's constant (1F= 96,485.3 C mol^{-1}), [O] is the activity of oxidized species and [R] is the activity of reduced species.

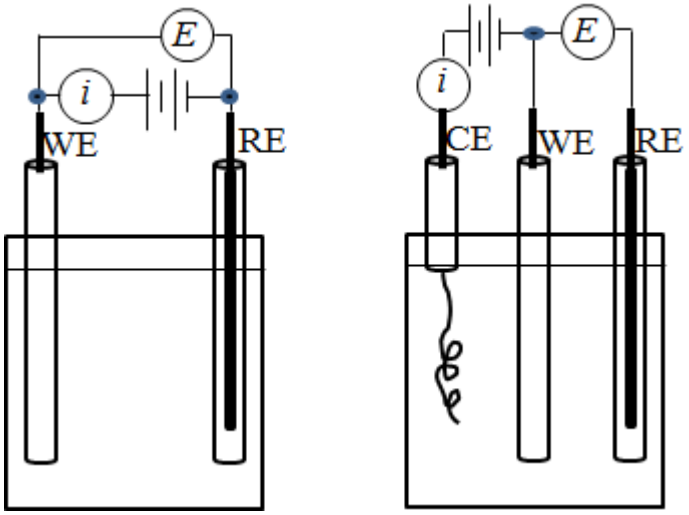

Figure 2.2: Schematic of two-electrode (left) and three-electrode (right) electrochemical cells. (from [116] Zoski. C. G., Handbook of Electrochemistry, *Elsevier*, 2007).

2.2.2 Potentials and Thermodynamics of Electrochemical cells

Conventionally, two electrochemical cells have been defined. Galvanic cells are those in which the reactions occur spontaneously and electrical energy is produced (i.e. free Gibbs energy is negative $\Delta G < 0$) when the electrodes are connected by an external conductor. The second type are the electrolytic cells in which an external applied potential is required to force reaction to occur (electrical energy is consumed) and the $\Delta G \geq 0$ [116]. The basic concept to derive a relation between the potential of electrochemical cells and activities of electroactive species is by thermodynamics at the half cell reaction. The relationship between free Gibbs energy and electroactive species can be given as:

$$\Delta G = \Delta G^{\emptyset} + RT \ln \frac{[R]}{[O]} \qquad \ldots\ldots\ldots\ldots\ldots\ldots (2.2)$$

Where ΔG is Gibbs free energy, ΔG^{ϕ} is a standard Gibbs free energy and n the number of electrons involved. The ratio between electroactive species can be changed by applying electrical current moving charge from one electrode to the other:

$$\Delta G = - nFE \qquad \ldots\ldots\ldots\ldots\ldots\ldots (2.3)$$

Where E/V is the cell potential at equilibrium (or at open circuit potential) at which no current passes through the cell. If the activities of {O} and {R} are unit activity, then E is equal to E^{ϕ} form Nernst equation:

$$\Delta G^{\phi} = - nFE^{\phi} \qquad \text{.....(2.4)}$$

Due to the negative sign in equation 2.4, standard potentials must be positive ($E^{\phi} > 0$) when ΔG^{0} is less than zero ($\Delta G^{0} < 0$), i.e. spontaneous reactions. The standard electrode potentials are calculated from the Nernst equation when the activities of redox species are unity. Cell potentials at open circuit can be calculated thermodynamically by subtracting the standard potentials of cathode and anode ($E^{\phi}_{cathode} - E^{\phi}_{anode}$), and the type of cell (Galvanic or Electrolytic) therefore will be known [116].

Thermodynamics in electrochemistry is usually defined for reversible processes, which in turn can be achieved only in systems at equilibrium. However, the term reversibility for redox reactions is used with three different meanings: (a) chemical reversibility when the reaction can proceed in both directions (forward and backward), (b) thermodynamic reversibility if the reaction can be at equilibrium at any time and (c) electrochemical reversibility when the concentrations of redox species at the electrode surface obey Nernst equation (equation 2.1) [120].

2.2.3 The nature of electrode reactions

It is well known that the electrode reaction process is sometimes complicated; it involves, in addition to simple electron transfer, several complicated processes (e.g. multiple electrons transfer, coupled chemical reactions, adsorption and phase formation). For the simple electron transfer reaction between two soluble and stable species of [O] and [R] there are three steps by which the current is maintained, the first is to supply reactants into electrode surface via mass transport process. The second is the electron transfer between the electrode surface and electroactive species which occurs via quantum mechanical tunnelling, and the third is the removal of products from the electrode surface to allow new reactants to reach the electrode also by mass transport. These can be recapitulated as follows [121]:

$$O_{bulk} \xrightarrow{\text{mass transport}} O_{electrode}$$

$$O_{electrode} \xrightarrow{\text{electron transfer}} R_{electrode}$$

$$R_{electrode} \xrightarrow{\text{mass transport}} R_{bulk}$$

2.2.4 Mass Transport

In electrochemistry there are three common types of mass transport. Figure 2.3 illustrates these three modes of mass transport [117, 121].

(a) Diffusion:

It is the spontaneous movement of analyte species to the electrode surface under concentration gradient whenever the concentrations of [O] and [R] are changed. During the electrochemical reaction is commenced at electrode surface, the concentration of [O] (for reaction O → R) starts to deplete with time in the region adjacent to the electrode surface, which is termed the diffusion layer (up to 10^{-2}cm thick).

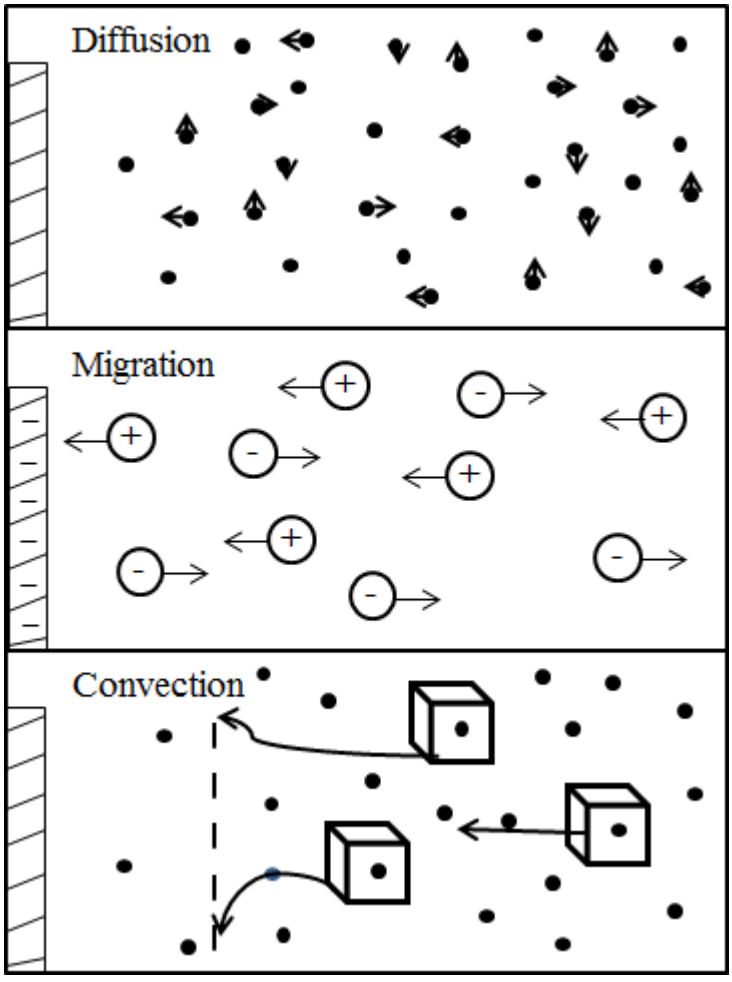

Figure 2.3: The three modes of mass transport (Modified version from [122] Maloy J. T., Factors affecting the shape of current-potential curves. *J. Chem. Educ.*, 1983, **60**, 285-289).

In contrast, the concentration of [R] starts to develop with time. Hence in order to maintain current flow during the experiment, O will diffuse toward the electrode, and R will diffuse away from the electrode or vice versa for an anodic reaction.

(b) Migration:

Migration is a movement of charged ions to the electrode surface by electrostatic force. The mechanism by which electrical charges pass through the electrolyte can be ascribed to the migration. However, such a mode of mass transport is uncommon for the analyte because the inert electrolyte screens the charge on the electrode and there is no electrical field outside the double layer (few nm).

(c) Convection:

Convection is the transport of material by movement of the liquid. It may be caused by thermal gradients or mechanical forces; it can occur either naturally by density gradients (unstirred solution) or mechanically via agitation, flow or vibration of the electrolyte (stirred solution). The most common system is the rotating disc electrode.

2.2.5 Electron Transfer

The key feature at the electrode-solution interface is the electron transfer process in which the electron moves from electrode to soluble species or vice versa. Such transfer corresponds to the difference between energies of electron orbitals in both the donor and acceptor. For the electrode (usually inert metal), this level is Fermi energy (E_f) which is equal to the highest filled orbital for a metal, and in the electroactive species is the valence orbital. Figure 2.4 shows flow of the electrons from the electrode to soluble species (reduction current), and from soluble species to electrode (oxidation current) [115, 123]. Elements can affect the velocity of electron transfer such as the electrode material and adsorbed anions e.g. Cl^-, Br^-, I^-, CN^- and S^{2-} [116].

Based on the foregoing, the reversibility is defined as situation when the concentrations at the electrode surface obey the Nernst equation. The mechanism of such process can be interpreted that the electron transfer process is very fast (i.e. the electroactive species undergoes the electron transfer as soon as it reaches the electrode surface), and the mass transport is considered to be the rate determining step as $k_0 >> k_d$ (k_0 is the rate constant at standard potential $E = E^{\phi}$ and k_d is the mass transfer coefficient). Therefore, the

current density (I) is high and the current is independent of overpotential (η). However, the current is very sensitive to changes in the agitaton or stirring of solution [121, 123].

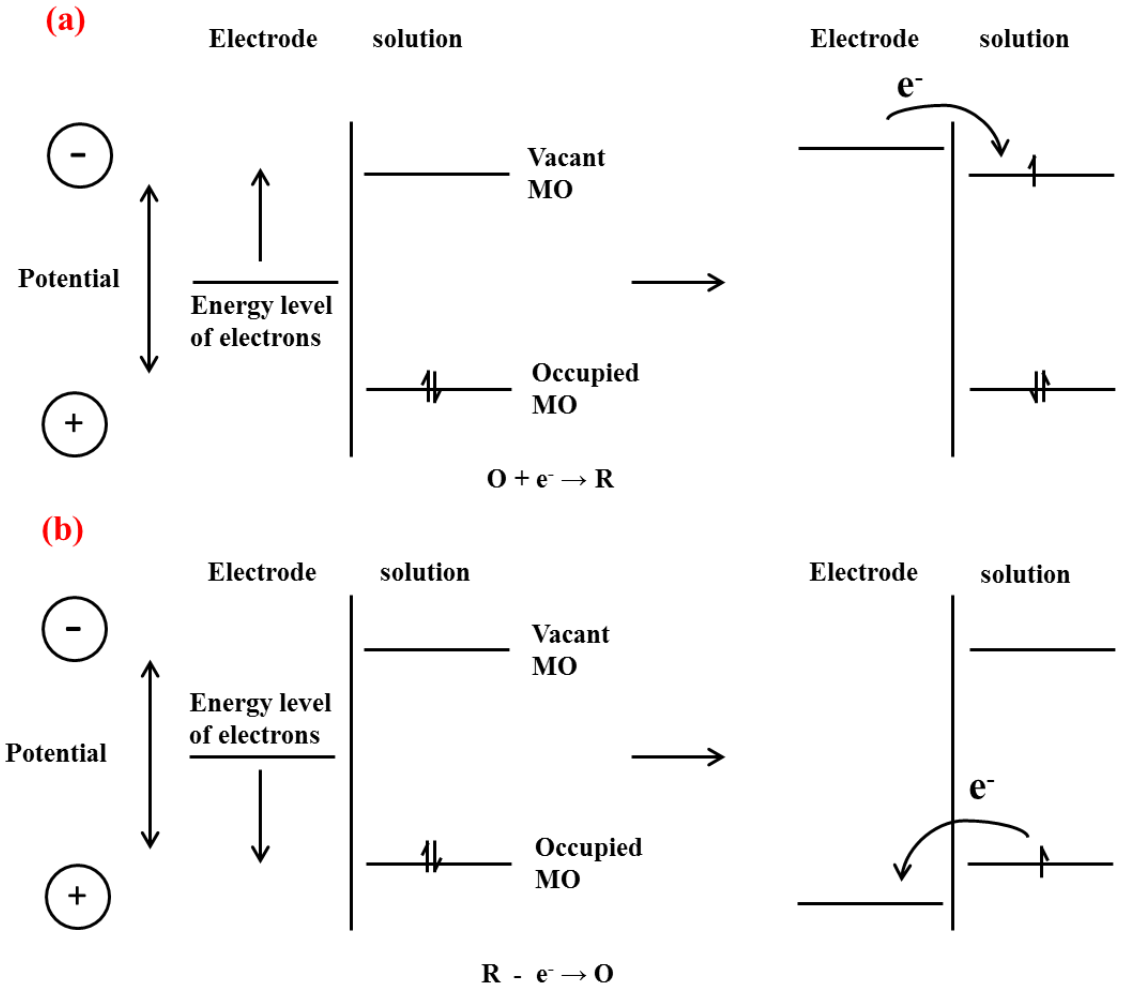

Figure 2.4: Representation of (a) reduction and (b) oxidation process of a species R and O in solution (from [115] Allen J. Bard and L.R. Faulkner, Electrochemical Methods Fundamental and Application, John Wiley, 2001).

2.3 Kinetics of electrode reactions

The electrochemical kinetics theory is related to the electron transfer process. As mentioned above there are some parameters which can perturb the electron transfer at the solution-electrode interface, such as electrode material, adsorbed species, multiple and consecutive electron transfer steps. If a high kinetic barrier occurs, this must be overcome by applying extra potential called overpotential, at this point the $k_0 << k_d$. The rate constant at the electrode varies with potential according to the following equations:

For a reduction reaction

$$k_C = k_0 \exp\left(\frac{-\propto_C nF(E-E^{\emptyset})}{RT}\right) \qquad \text{.....(2.5)}$$

For an oxidation reaction

$$k_A = k_0 \exp\left(\frac{\propto_A nF(E-E^{\emptyset})}{RT}\right) \qquad \text{.....(2.6)}$$

Where k_C is the rate constant for reduction at electrode, k_A is rate constant for oxidation at electrode; α_c and α_A are the cathodic and anodic transfer coefficients, respectively.

Also, there is another way to express the kinetics of electrode reaction by the Butler-Volmer equation; it shows that the current density depends on the exchange current density (I_0), transfer coefficients and overpotential.

$$I = I_0 \left[\exp\left(\frac{\propto_A nF\eta}{RT}\right) - \exp\left(\frac{-\propto_C nF\eta}{RT}\right) \right. \qquad \text{.....(2.7)}$$

From the equation (2.7) there are two cases either when $|I_A| >> |I_C|$

$$\log I = \log I_0 + \frac{\alpha_A nF\eta}{2.3RT} \qquad \text{.....(2.8)}$$

Or when $|I_A| << |I_C|$

$$\log I = \log I_0 - \frac{\alpha_C nF\eta}{2.3RT} \qquad \text{.....(2.9)}$$

The equations (2.8) and (2.9) are known as the Tafel equations by which the transfer coefficient (α) and exchange current density (I_0) can be obtained. Together these two parameters characterize the kinetics of a simple electrode reaction as shown in figure 2.5 [121, 123].

The case in which the electrode reaction can not be reversed by an infinitesimal potential change is called irreversibility. In such case, the rate of electron transfer is insufficient to maintain the equilibrium at electrode surface (Nernst equation is not obeyed). In an extreme case, the concentrations of [O] and [R] at electrode surface are not significantly varied relative to bulk concentrations. Therefore, the electron transfer step is the rate determining step.

Among the reversibility and irreversibility there is an intermediate process called quasi-reversibility in which the current is determined by a mixture of electron transfer and mass transport. In this situation, the concentrations of [O] and [R] at electrode surface deviate slightly from the Nernst equation and mass transport is important and also the overpotential can affect the process [121].

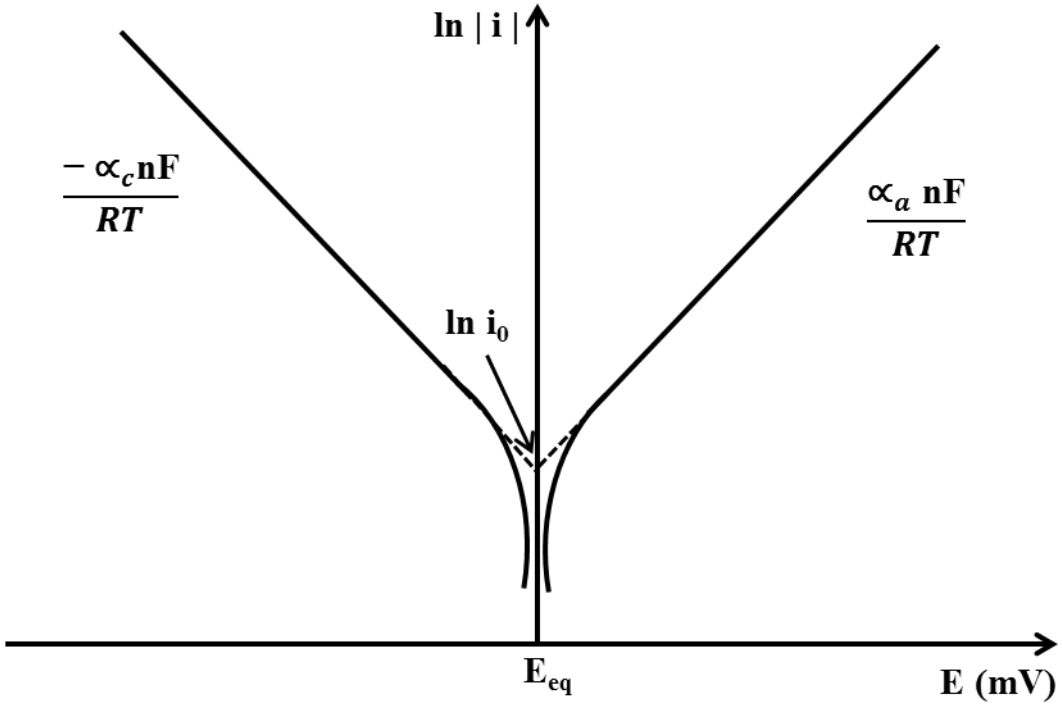

Figure 2.5: Experimental determination of kinetics constants I_0 and α, using the Tafel equation, (from [123] Christopher M. A. Brett and A.M.O. Brett, Electrochemistry Principles, Methods, and Applications, *Oxford University Press, United State, New York*, 1993.

2.4 Electrochemical Methods

This section will discuss some details of the electrochemical techniques used in this work. They encompass ion selective electrodes (chloride selective electrode and glass electrode) and chronopotentiometric measurements as potentiometric methods. Cyclic voltammetry and square wave voltammetry as voltammetric method, as well as some details about working electrode (material, preparation and cleaning) for voltammetric measurements.

2.4.1 Potentiometric method using ion selective electrode ISEs (chloride selective electrode and glass electrode)

Potentiometric analysis is based upon measuring the potential of the electrochemical cell when no current is applied. This method has been used for estimating the concentrations of numerous ions using ion selective electrodes [124].

2.4.2 Instrumentation/Equipment, sample preparation and analysis procedures for Potentiometric method

All potentiometric measurements at zero current (I = 0) were conducted using an electrometer (Keithely instrument, Inc., USA 6430 Sub-Femtoamp Remote sourceMeter®), controlled by an external PC with LabTracer 2.0 SourceMetrer® Integrated software. In the case of chloride selective electrode, the electrometer was connected with the Cole-Palmer combined chloride selective electrode. The electrode was made from glass; it was filled with 1 M of KNO_3. The electrode has a range of 2 to 12 pH, 0 to 80 ^oC (32 to 176 ^oF). The electrode was calibrated with standard solutions of NaCl rangeing from (10^{-7} – 10^{-1} M) in 0.1 M of Na_2SO_4 and cleaned with deionized water. The purpose of using 0.1 M of Na_2SO_4 is to match sulfate ion concentrations in Shilbottle samples and consequently calibrate for their effects on the electrode response.

A standard calibration curve (figure 4.8) was constructed and used to determine chloride concentrations in Shilbottle water samples. The chloride concentrations were measured for environmental samples (Shilbottle) by measuring the electrode potential for each sample. The cell consisted of ISE as a combined electrode (working and reference), it was immersed in the electrolytes/samples and Cl^- concentrations were estimated at laboratory temperatures between 17 ± 1 ^oC.

In the case of glass electrode, the electrometer was connected with HANNA HI 1130 combined glass electrode. The electrode was made from glass; it was filled with 3.5 M of KCl . The electrode measures pH in range of 0 to 13 and has a recommended operating range from 20 to 40 ^oC. The electrode was calibrated with two buffer solutions of pH 7.0 and 4.0, respectively. The $[H^+]$ in Shilbottle solutions was measured by immersing the electrode in the sample solution.

The environmental samples were collected in pre-washed (125 mL) polyethylene

bottles from the abandoned mining sites at Shilbottle. Pre-acidification was not used to avoid effects of acids on the hydrolysis. The pH values of these samples were immediately measured (within 2.0 hours). The purpose of this is step to record pH values to be analogous to actual mine water pH in the field, because hydrolysis of iron (III) leads to decrease pH with time. Also the samples were stored immediately in the fridge to minimize hydrolysis process of iron as much as possible.

2.4.3 Chronopotentiometric method

The chronopotentiometric method used in this work no current is applied between electrodes, and the potential is the dependent variable and is monitored as a function of time. One of the most common applications of chronopotentiometry is the monitoring of hydrogen concentration [H^+] as a function of time in inorganic aqueous solutions using a glass electrode (whose potential is a function of the hydrogen ion activity). The glass electrode is a combined electrode; it consisted of both working and reference electrodes in the same body [118, 125].

2.4.4 Sample preparation and analysis procedures for Chronopotentiometric method

The same equipment as in section 2.4.2 was used for chronopotentiometric measurements. The cell consisted of a pH electrode as a combined electrode (working and reference), the electrode was immersed in the electrolytes/samples. The hydrogen concentration was monitored every second for about 30 minutes. The resulting chronopotentiogram was processed by the PC (under Windows environment) attached to the electrochemical workstation. The chronopotentiogram measures the potential as a function of time, which is then converted to [H^+] and the order of hydrolysis reaction was identified by fitting a simple second order kinetics regression model to the chronopotentiometric data.

All chemicals were purchased from Aldrich and/or Alfa Aesar. Stock solutions of 0.030 M of iron(III) $FeClO_4.xH_2O$ and $Fe_2(SO_4)_3.5H_2O$ were prepared by dissolving the appropriate weight of Fe(III) salts in deionized water (18.2 MΩ cm). 0.2 M of $NaClO_4$ and Na_2SO_4 were prepared and used as a supporting electrolyte by dissolving appropriate weight of sodium salt in deionized water (18.2 MΩ cm). The sodium salts solutions were used as solvent to prepare iron(III) solutions. Also 0.1 M of NaOH was prepared by dissolving appropriate weight of sodium hydroxide in deionized water.

For kinetics studies 5.0 mL of 0.030 M of iron(III) perchlorate and/or iron(III) sulfate were placed in two different electrochemical cells. 5.0 ml of appropriate concentration of NaOH to achieve $[OH^-]/[Fe^{3+}]$ ratio 1.0 and 1.5 were added to the Fe(III) solution under vigorous stirring. The measurements were conducted immediately for the first 30 minutes. Kinetics information was obtained by monitoring the changes of $[H^+]$ with time. All Fe(III) solutions were prepared and analysed within 12 hours, with most intensive study during the first 3.0 hours to avoid effects of aging. The same procedures were followed in the case of 0.0025 M of iron perchlorate and sulfate (at the same $[OH^-]/[Fe^{3+}]$ ratios).

For Shilbottle samples, 5 mL of the solution was placed in an electrochemical cell, about 1 mL of different NaOH concentrations was added (all as one batch) to obtain $[OH^-]/[Fe^{3+}]$ ratios of approximately 1.0 or 1.5. The chronopotentiogram was recorded for measuring the rate constant of iron hydrolysis in Shilbottle solutions.

Note: This method was not applied for high iron(III) concentration about 0.25 M as used in Raman studies (as we will see latter section 2.6.10), because the change in $[H^+]$ was not well observed, this may be attributed to the long induction period at high concentrations [126].

2.4.5 Cyclic Voltammetry (CV) and steady state voltammetry measurements

Cyclic voltammetry is one of the most important and widely used methods among potential sweep techniques in particular and in voltammetry in general. It is not widely used for quantitative analysis; however it is extensively used for qualitative analysis. It is an attractive technique for the first electrochemical studies of new system, because it provides useful information about thermodynamic and kinetics of redox processes of electroactive species, adsorption and coupled chemical reactions. The obtained voltammogram in which the current is monitored as a function of applied potential is informative concerning the oxidation and reduction reactions from which the required information can be acquired [117, 118].

The potential-time waveform is based on sweeping potential at a constant rate between initial and final potentials (E_1 and E_2) which is known as the forward scan. Then the potential can be swept back to the initial potential (from E_2 to E_1) in the backward scan figure 2.6. Cyclic voltammetry is regarded as a reversal technique. Hence it can be

distinguished from linear sweep voltammetry (LSV), which strictly means only the forward sweep.

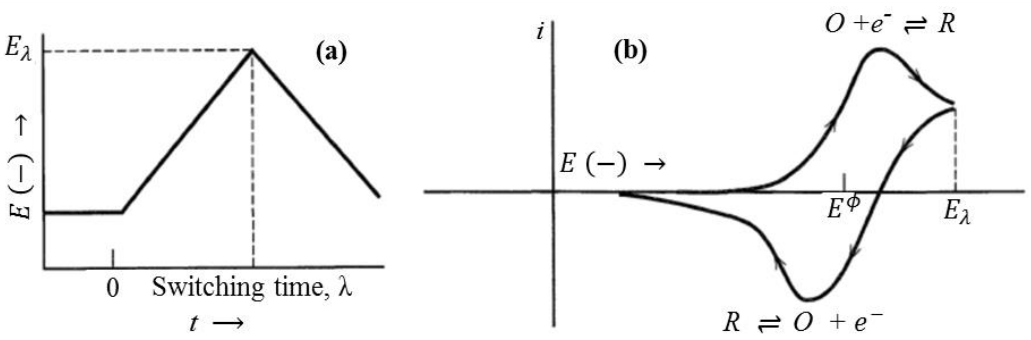

Figure 2.6: (a) cyclic potential sweep, (b) resulting cyclic voltammogram (from [115] Allen J. Bard and L.R. Faulkner, Electrochemical Methods Fundamental and Application, *John Wiley*, 2001)

Once the potential of the working electrode is swept to a value near the standard potential (the electrode potential is changed linearly with time between two values), the redox reaction will start at the electrode surface. For diffusion-controlled electron transfer reactions the concentrations of [O] and [R] will vary at the electrode surface and the current is proportional to the concentration gradient at the electrode surface. For example, if O species are present in bulk solution and [R] is zero in the bulk, when the potential is applied [O] will diminish with time at the electrode surface, while [R] will develop and a cyclic voltammogram is obtained (figure 2.7) [116].

The most characteristic parameters in the cyclic voltammogram are peak current (I_C and I_A) and peak potential (E_C and E_A) of the cathodic and anodic peaks, respectively. Such parameters vary in response to scan rate and the reactions at the electrode-solution interface. Therefore, in order to characterize the cyclic voltammogram of a simple electron transfer reaction three cases must be understood:

(a) Reversibility

According to electrochemical concepts, reversibility means that the Nernst equation is obeyed locally. This means that the ratio of $\frac{[O]}{[R]}$ at the electrode is given by the Nernst equation. Another way to express this is that the electron transfer process is fast and always maintains equilibrium at electrode-solution interface. In this case mass transport is important to maintain the concentrations [O] and [R] at the electrode surface constant

(concentration gradient), and is regarded as the rate determining step. For a planar diffusion-controlled case a key feature in cyclic voltammogram is the peak current which is given by equation 2.10):

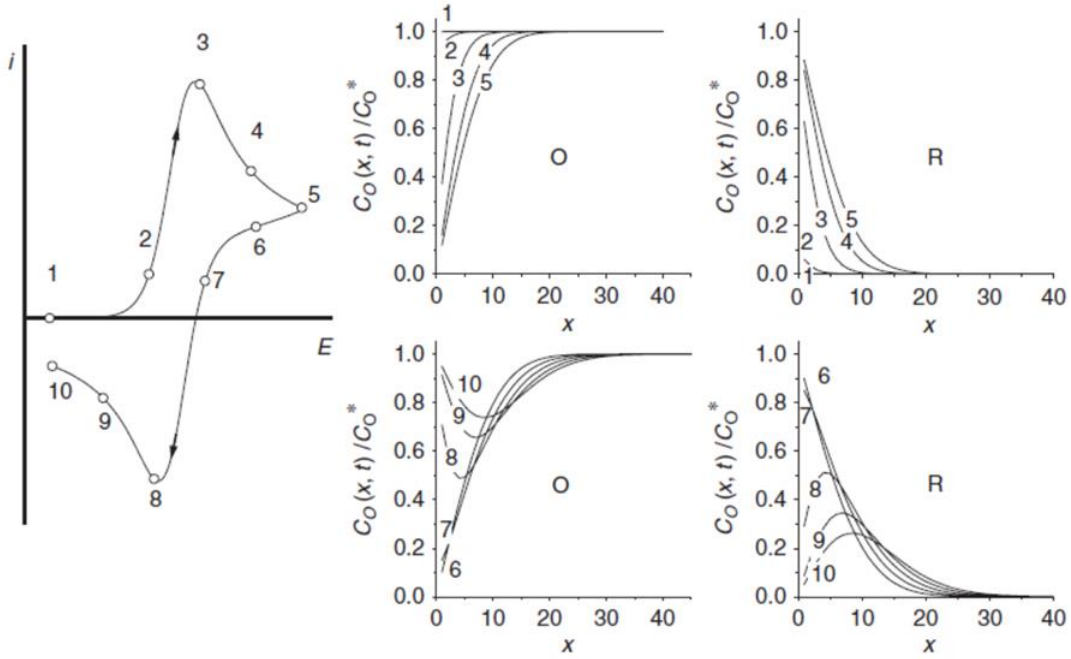

Figure 2.7: Cyclic voltammogram of O and R concentration profiles for diffusion to a planar electrode. Numbers on the concentration profiles correspond to the numbered points on the voltammogram (from [116] Zoski. C. G., Handbook of Electrochemistry, *Elsevier*, 2007).

$$i_p = \left(2.59 \times 10^5\right) n^{\frac{3}{2}} A D_o^{\frac{1}{2}} C_o^* \nu^{\frac{1}{2}} \qquad \text{.....(2.10)}$$

Where i_p is peak current in ampere, A is the electrode area (cm^2), D is diffusion coefficient ($cm^2\ s^{-1}$), C_o is the concentration in mol cm^{-3}, and ν is the scan rate in V s^{-1}. Based on equation 2.10, the peak current is proportional to the square root of scan rate as shown in figure 2.8. In order to diagnose the reversibility of a cyclic voltammogram, the following tests should be applied:

$$\Delta E = E_p^A - E_p^C = \frac{59}{n}\ mV$$

$$\left| E_p - E_{\frac{p}{2}} \right| = \frac{59}{n}\ mV$$

$$\left| \frac{I_p^A}{I_p^C} \right| = 1$$

$$I_p\ \alpha\ \nu^{\frac{1}{2}}$$

E_p is independent of $\mathcal{V}$

(b) Irreversibility

The opposite case of the reversibility is irreversibility; this means that rate of electron transfer is low. Thus the ratio of $\frac{[O]}{[R]}$ in Nernst equation at equilibrium is not obtained during the measurement.

The correlation between peak current and other parameters such as transfer coefficient (α), scan rate and concentration can be shown in the following equation:

$$i_p = \left(2.99 \times 10^5\right) \alpha^{\frac{1}{2}} A D_o^{\frac{1}{2}} C_o^* \mathcal{V}^{\frac{1}{2}} \quad \text{.....(2.11)}$$

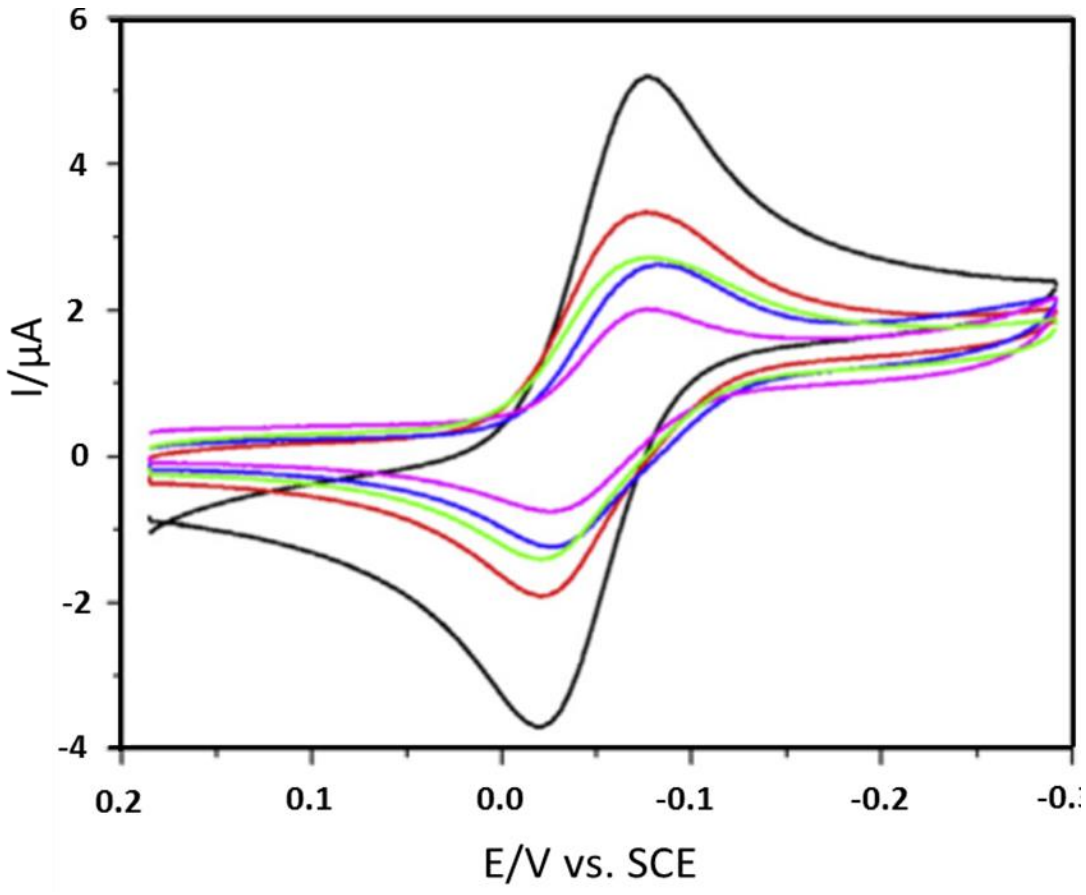

Figure 2.8: Cyclic voltammogram of reversible system, $O + e^- \rightarrow R$, (modified version from [121] Group S. E., Instrumental Methods in Electrochemistry, *Chichester, New York*, 1985).

From equation (2.11), it can be seen that the peak current is proportional to square root of scan rate and proportional to concentration. Also, E_p shifts about $\frac{30}{\alpha_c n_\alpha}$ mV for each decade increase in $\mathcal{V}$. The voltammograms in figure 2.9 are normalised

voltammogramms. In these voltammograms, the peak potential separation increases with increasing scan rate. Also, the height of current peak is slightly decreased compared with the peak current of a reversible voltammogram. The full diagnostic tests for irreversibility are as follows:

$$\left| E_p - E_{\frac{p}{2}} \right| = \frac{48}{\alpha_c n_\alpha} \text{ mV}$$

$$I_p^C \; \alpha \; \mathcal{V}^{\frac{1}{2}}$$

$$E_p^C \text{ shifts } -\frac{30}{\alpha_c n_\alpha} \text{ for each decade in } \mathcal{V}$$

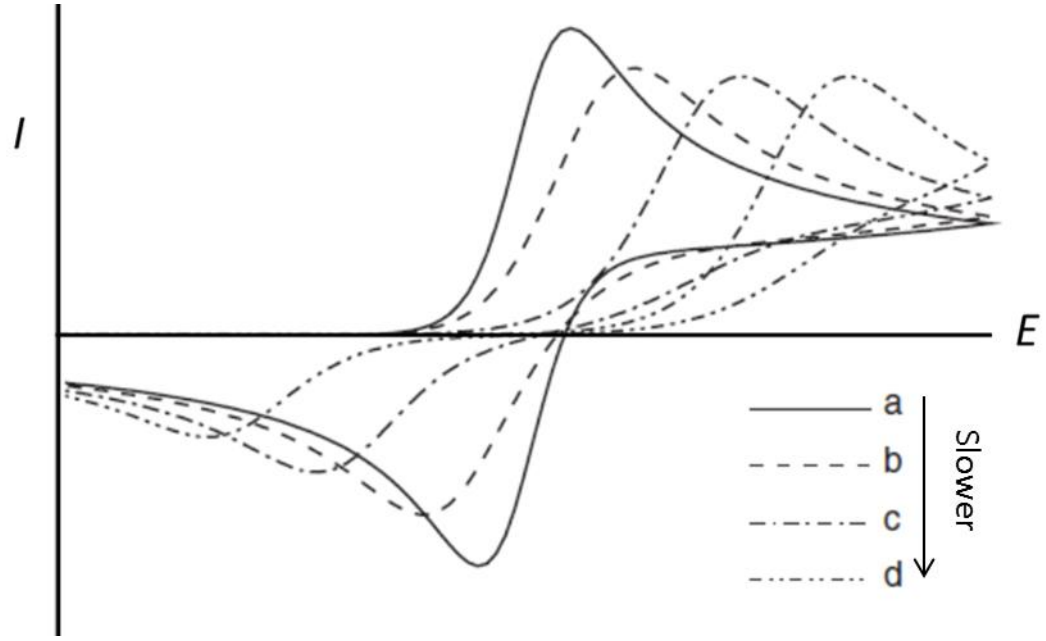

Figure 2.9: Cyclic voltammograms for irreversible process when only oxidized species are initially present in solution. (a) The mass transfer coefficient is smaller than the electron transfer rate constant. (b, c and d) The mass transfer coefficient is larger than the electron transfer rate constant. (from [116] Zoski C. G., Handbook of Electrochemistry, *Elsevier*, 2007).

(c) Quasi-reversibility

In cyclic voltammetry, many processes are reversible at low scan rates; however such processes may become irreversible at high scan rate. The intermediate case is known as quasi-reversible (voltammograms b and c in figure 2.9). Such processes can occur when the rate of electron transfer is insufficient to maintain Nernstian equilibrium, and mass transport is important to achieve Nernstian equilibrium at electrode surface. The quasi-reversible voltammogram can have both oxidation and reduction current peaks. The main diagnostic tests for quasi-reversible systems are as follows [115, 116, 121, 123]:

ΔE_p is greater than $\frac{59}{n}$ and increasing with $\mathcal{V}$

$\left| \frac{I_P^A}{I_p^C} \right| = 1$ provided $\alpha_C = \alpha_A = 0.5$

I_p increases with $\mathcal{V}^{\frac{1}{2}}$ but is not proportional to it

E_p^C shifts negatively with increasing $\mathcal{V}$

2.4.6 Instrumentation/Equipment for voltammetric measurements

All voltammetric measurements (CV and SWV) were performed using the potentiostat of a CH-instruments scanning electrochemical microscope CHI 900, CH Instruments, Inc., USA; the electrochemical equipment was supplied with software to control the experiment via a PC. A conventional three-electrode system was used for recording voltammograms of cyclic voltammetry (CV) and square wave voltammetry (SWV). The working electrode was a 1 mm radius platinum electrode; the counter electrode was a 0.25 mm radius tungsten wire and the reference electrode was a silver/ silver chloride reference electrode (Ag/AgCl) bridged by a saturated KCl (3.7 mol dm^{-3}) solution. For steady state measurements a platinum ultramicroelectrode of a 50 µm radius was used. The scan parameters were adjusted depending on the type of experiment performed (normal cyclic voltammetry or steady state voltammetry).

The measurements were conducted in a 50 mL electroanalytical glass cell with three electrodes working, counter and reference electrode. The three electrodes (connected to a scanning electrochemical spectroscope workstation) were immersed in the sample solution. The resulting voltammogram was processed by the PC (under a Windows environment) attached to the scanning electrochemical microscope workstation which measures the current as a function of applied voltage.

2.4.7 Analysis procedures of electrochemical characterization (Kinetic studies of electrode-solution interface) using CV

For CV studies 5.0 mL of 0.01 M of iron(III) perchlorate and/or iron(III) sulfate solutions were placed in two different electrochemical cells, and the solutions were degassed under N_2 for 10 minutes. The scan parameters were as follows (initial E = 1.0 V, high E = 1.0 V, low E = 0.3 V, scan rate = 0.01, 0.05, 0.10, 0.15, 0.20 and 0.25 V s^{-1},

sample interval 0.001 V, quiet time = 2.0 s and sensitivity = 1.0×10^{-5} A/V). For Shilbottle samples, 5 mL of environmental solution were placed in electrochemical cell and same scan parameters were applied. The resulting cyclic voltammograms were recorded and saved for analysis and interpretation.

2.4.8 Analysis procedures for measuring iron concentrations using steady state voltammetry

An ultramicroelectrode technique was used for measuring the dissolved fractions of Fe(II) and Fe(III) in Shilbottle samples using a standard addition method. 5 aliquots of 5 mL of Shilbottle solutions were placed in 5 different electrochemical cells. 5 different standard concentrations of iron(III) sulfate solutions (2, 4, 6, 8 and 10 mM) were prepared and added to the Shilbottle samples. Cyclic voltammograms were recorded for each aliquot according to the following scan parameters (initial E = 0.80 V, high E = 0.80 V, low E = 0.50 V, scan rate = 0.1 V s^{-1}, sample interval 0.001 V, quie t time = 2.0 s and sensitivity = 1.0×10^{-8} A/V).

The Fe(III) concentration was calculated from the diffusion limited cathodic current by standard addition. The concentration of Fe(II) was calculated from the anodic diffusion limited current under the assumption that the diffusion coefficients of Fe(II) and Fe(III) are the same. (Note: the same workstation used for CV was used for square wave voltammetry (section 2.4.9). Also all chemicals were the same as discussed in (section 2.4.4).

2.4.9 Square Wave Voltammetry

Square wave voltammetry (SWV) has more sensitivity and less charging current background than differential pulse voltammetry (DPV). Square wave voltammetry offers a combination of the best aspects of other pulse voltammetric methods and has the diagnostic value of normal pulse voltammetry and the background suppression of differential pulse voltammetry. Also it can offer a wider range of time scales than other pulse techniques. SWV can provide useful mechanistic information in a manner similar to CV, because SWV is also a reversal technique. SWV has some advantages over CV; it can detect concentrations lower than detected by CV, with less distortion due to lower background current and consequently the fitting of theoretical models can be carried out with higher accuracy. The sensitivity of SWV for quantitative measurements at trace

levels is higher than many other voltammetric and some spectroscopic techniques (e.g. molecular or atomic absorption spectroscopy or liquid chromatography) [115, 118].

SWV is a rapid technique in which the analysis time can be only few seconds to record a complete voltammogram; this is due to fast scan rate, unlike DPV which typically takes 2-3 minutes. Therefore, SWV is an effective technique to study kinetics parameters of the electrode and chemical kinetics [117]. The basic of pulse voltammetry is that charging current decay exponentially like ($e^{-\frac{t}{RC}}$), the faradaic current decays more slowly like ($t^{-\frac{1}{2}}$). By sampling the current after a delay the faradaic current is maximised, as illustrated in Figure 2.10.

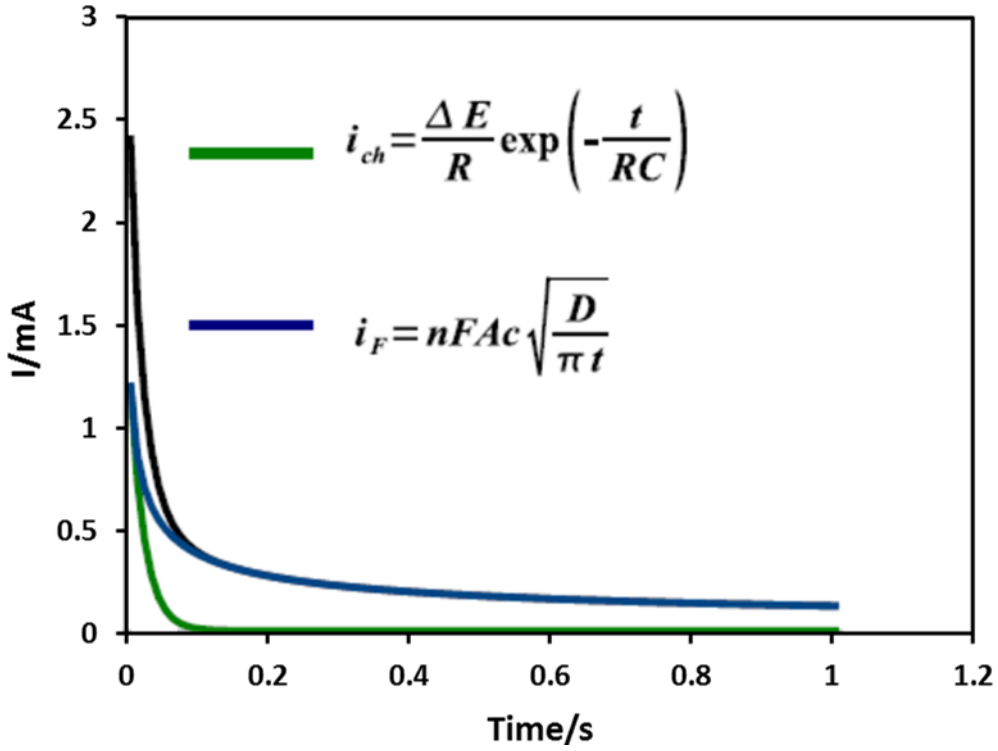

Figure 2.10: Diagram showing the decay of faradaic and charging currents in pulse voltammetic techniques. The blue curve shows the faradaic current, the green curve is the charging current and the total current is represented by the black line.

SWV is carried out at a stationary electrode. Its waveform consists of many cycles in which each tread of a staircase scan has superimposed a symmetrical double pulse, one of which is in the forward direction and another is reversed as illustrated in figure 2.11. This scheme shows that the background current is suppressed, because the forward and reverse current are sampled at the end of each pulse, where the charging current is negligible compared to the Faradaic current.

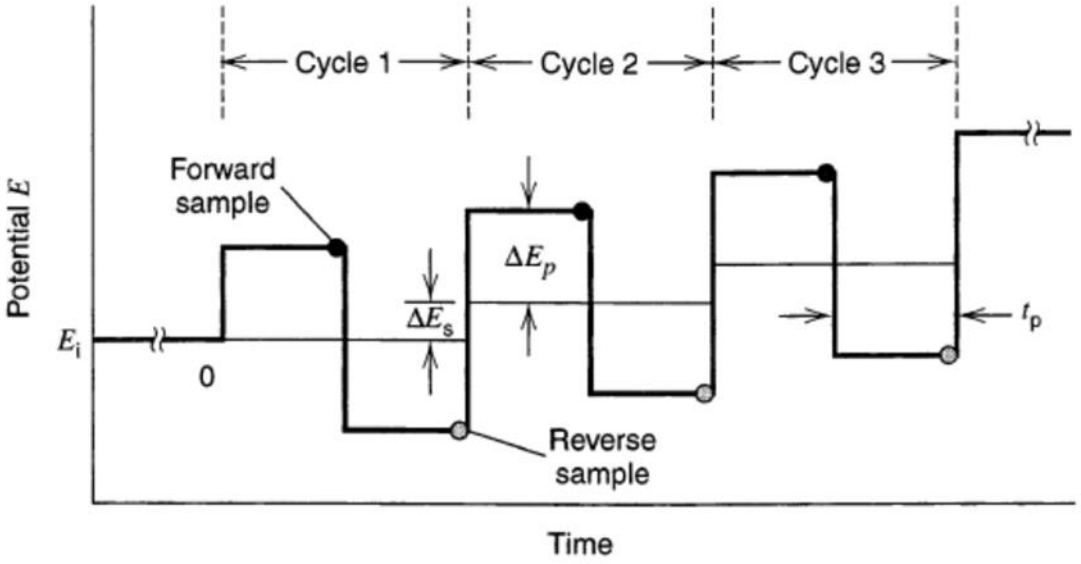

Figure 2.11: Waveform and measurement scheme for square wave voltammetry (from [115] Allen J. Bard and L.R. Faulkner, Electrochemical Methods Fundamental and Application, *John Wiley*, 2001).

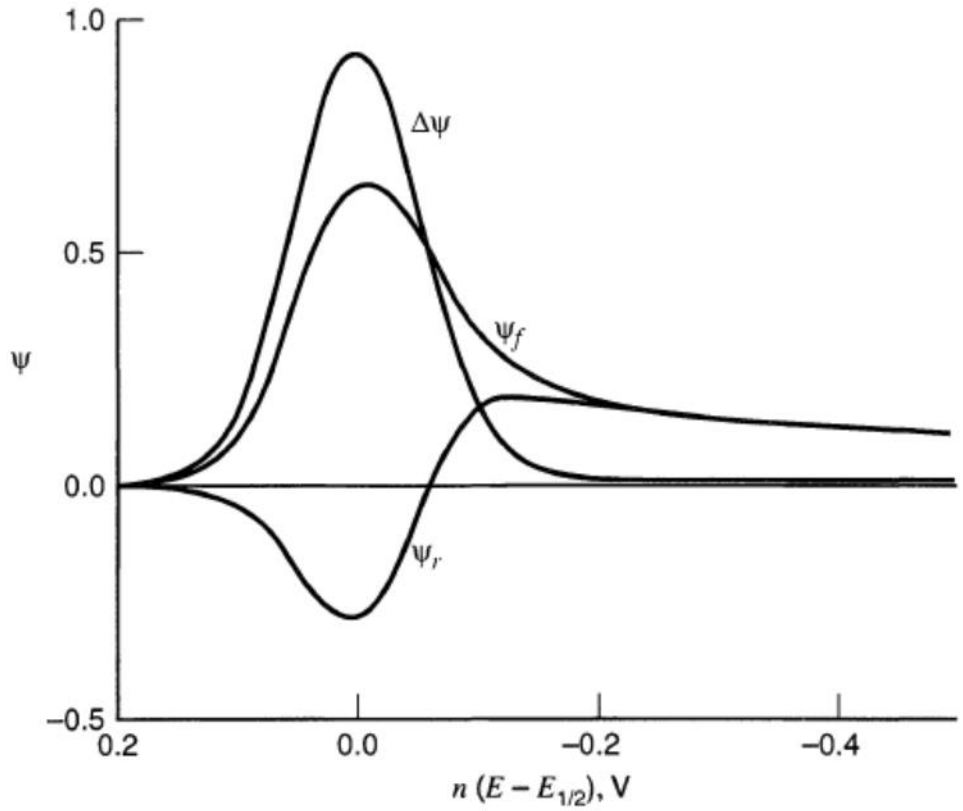

Figure 2.12: Dimensionless square wave voltammograms for the reversible O/R case with R absent from the bulk. nΔEp = 50 mV and nΔEs = 10 mV. Forward currents (ψf), reverse currents (ψr), and difference currents (Δψ). (from[115] Allen J. Bard and L.R. Faulkner, Electrochemical Methods Fundamental and Application, John Wiley, 2001).

The voltammograms usually display the difference current obtained by subtracting the forward and reverse currents which were sampled at two different time points. A

reversible square wave voltammogram (i-E) in figure 2.12 is obtained with a symmetrical bell shapes. The difference current is larger than forward current or reverse current and the current peak is higher than in DPV by a factor of 4. The obtained peak current is proportional to the concentration of electroactive species in solution [115, 117].

2.4.10 Analysis procedures for qualitative characterization using SWV

Characterization of two different species was conducted using SWV. The first was characterization of simple soluble species of Fe(III) and soluble Fe(III) oligomers. 5.0 mL of 0.030 M of iron(III) perchlorate and/or iron(III) sulfate in 0.2 M of sodium perchlorate and/or sodium sulfate were placed in two different electrochemical cells. 5 mL of different concentrations of NaOH (all as one batch) were added to obtain $[OH^-]/[Fe^{3+}]$ ratios of 1.5. The scan parameters were as follows (initial E = 1.0 V, low E = -0.4 V, amplitude = 0.025 V, frequency = 15 Hz, sample interval 0.004 V, quiet time = 2.0 s and sensitivity =1.0×10^{-5} A/V). The resulting voltammograms were recorded before and after NaOH addition and saved for analysis. Similar procedures were followed for Shilbottle samples.

The second part was characterization of the peak due to reduction of hydrogen ions. 5 mL of 0.015 M of iron(III) sulfate $Fe_2(SO_4)_3.9H_2O$ was placed in electrochemical cell. SWV voltammogram were recorded on carbon electrode as a working electrode. Another two solutions were prepared from 0.05 M of NaOH and H_2SO_4 in 0.2 M of Na_2SO_4. The SWV voltammograms of last two solutions were recorded on platinum as a working electrode. The scan parameters of second part were as follows (initial E = 1.0 V, low E = - 0.3 V, amplitude = 0.025 V, frequency = 15 Hz, sample interval 0.004 V, quiet time = 2.0 s and sensitivity = 1.0×10^{-5} A/V).

2.4.11 Procedures for kinetic studies using SWV

Kinetic studies were carried out by the following procedures. 5 mL of 0.030 M of iron(III) perchlorate and/or iron(III) sulfate were placed in two different electrochemical cells, 5 mL of different concentrations of NaOH (all as one batch) were added to obtain $[OH^-]/[Fe^{3+}]$ ratios of 1.0 and 1.5. Square wave voltammograms for each case were recorded at 1, 5, 10, 15, 20, 30, 60, 120, 180 minutes according to the following scan parameters (initial E = 1.0 V, low E = 0.0 V, amplitude = 0.025 V, frequency = 15 Hz,

sample interval 0.004 V, quiet time = 2.0 s and sensitivity = 1.0×10^{-5} A/V) and saved for analysis and interpretation. The voltammetric measurements were conducted immediately for the first 180 minutes (the period where the hydrolysis process occurs). All iron(III) solutions were prepared and analysed within 12 hours, with most intensive study during the first 3.0 hours to avoid aging effects.

2.4.12 Analysis procedures for depletion of soluble species of iron(III) using SWV

5 mL of 0.030 M of iron(III) perchlorate and/or iron(III) sulfate were placed in two different electrochemical cells, 5 mL of different concentrations of NaOH (all as one batch) were added to each solution to obtain $[OH^-]/[Fe^{3+}]$ ratios of 1.0, 1.5, 1.9, 2.1, 2.3 and 2.4 for iron(III) sulfate solutions, and to obtain $[OH^-]/[Fe^{3+}]$ ratios of 1.0, 1.5, 1.9 and 2.1 for iron(III) perchlorate. Square wave voltammograms for each case were recorded according to the following scan parameters (initial E = 1.0 V, low E = 0.2 V, amplitude = 0.025 V, frequency = 15 Hz, sample interval 0.004 V, quiet time = 2.0 s and sensitivity = 1.0×10^{-5} A/V), and saved for analysis.

2.4.13 Procedures for measuring soluble iron concentrations suing SWV

SWV technique was used for measuring total dissolved iron species in Shilbottle samples using a standard addition method. 5 aliquots of 5 mL of Shilbottle solutions were placed in 5 different electrochemical cells. 5 different standard concentrations of iron(III) sulfate solutions (2, 4, 6, 8 and 10 mM) were prepared and added to Shilbottle solutions. Square wave voltammograms were recorded according to the following scan parameters (initial E = 0.9 V, low E = 0.4 V, amplitude = 0.025 V, frequency = 15 Hz, sample interval 0.004 V, quiet time = 2.0 s and sensitivity = 1.0×10^{-5} A/V) and saved for analysis.

Total iron concentration of samples from five settlement lagoons was determined by plotting peak current (I_p) versus standard concentrations of Fe(III) (more details in chapter 4).

2.4.14 Procedures for measuring soluble sulfate concentrations using SWV

5 aliquots of 5 mL of 0.010 M of $Fe(ClO_4)_3.xH_2O$ were placed in 5 different electrochemical cells (solutions 1, 2, 3, 4 and 5). 5 mL of 5 different concentrations of

Na_2SO_4 (0.0, 0.02, 0.10, 0.20 and 1.0 M) were added to the 5 aliquots in solutions 1, 2, 3, 4 and 5, respectively to obtain final solutions with 0.005 M of Fe^{3+} and (0.0, 0.01, 0.05, 0.10 and 0.5 M of SO_4^{2-}). Three series of these solutions with the same compositions were prepared, but with different pHs, the pH of first series was adjusted to pH 2.25, the second was adjusted to pH of 2.75 and the third series was adjusted to pH 3.25. The pH was adjusted by addition of an appropriate small volume of NaOH or H_2SO_4. Square wave voltammograms were recorded according to the following scan parameters (initial E = 0.9 V, low E = 0.4 V, amplitude = 0.025 V, frequency = 15 Hz, sample interval 0.004 V, quiet time = 2.0 s and sensitivity = 1.0×10^{-5} A/V) and saved for analysis.

2.5 Working electrode (materials, preparation and cleaning)

2.5.1 *Working electrode materials*

In voltammetric measurements, the quality of the results is strongly influenced by the working electrode where the redox reactions take place. Therefore for precise measurements, the material of working electrode is important. The optimum working electrode should be inert toward solvent and solution components (sample), possess high signal-to-noise characteristics, reproducible response, low background over the potential range and be smooth (geometry and mass transport are better defined) [117, 121].

The mercury electrode possesses a high overpotential for H^+ reduction and has a very smooth surface compared to the solid electrodes. The latter electrodes have several characteristics such as: chemical and electrochemical stability, electrical conductivity, and rapid electron transfer for a wide variety of redox systems. The most common of solid electrodes are noble metals, carbon, semi-conductors (metals oxides) and conducting organic salts.

Carbon electrodes are widely used for several chemical and electrochemical applications, because these possess low background current, high active surfaces, chemical inertness, a broad potential window and low cost. Metal electrodes exhibit fast electron transfer kinetics, so they are usually preferred for studying kinetics and mechanisms, and also studying thermodynamic quantities [116, 123].

Compared with carbon electrodes the metal electrodes (platinum and gold are mostly used) are more sensitive to adsorption of anions on their surfaces, such anions (Cl^-, Br^-, I^-, CN^-, S^{2-}). Oxygen and hydrogen evolution also have lower overpotentials on metal electrodes surfaces compared to carbon electrodes. Therefore, in order to improve the efficiency of working electrodes and consequently rapid electron transfer kinetics, cleaning and polishing the working electrode are important [116].

2.5.2 Preparation and polishing processes of working electrode

The solid electrodes are in the form of either wire or rod insulated by either epoxy resins or plastic sheath. It is essential to ensure that crevices between sheath and electrode do not occur, which may allow the solution to penetrate into the electrode body and cause corrosion and other artefacts. Due to the difference of the expansion coefficient between metals and plastic (sheath), their surfaces may not be coplanar and the care in their polishing is required [123].

As mentioned above, when a thin film is formed on the electrode surface as a result of adsorbed anions, solvent decomposition and oxides or complex formation, then polishing the electrode surface is necessary in order to ensure rapid electron transfer and favourable characteristics. There are several methods by which the cleaning of electrode surface can be carried out. These approaches are: mechanical polishing, heat treatment, solvent cleaning, electrochemical polarization and laser activation. The two approaches used in this work are mechanical polishing and electrochemical polarization (electrochemical pre-treatment) [116].

The electrodes employed were platinum (radius = 1.0 mm) and to a lesser extent glassy carbon (radius = 1.0 mm). A similar mechanical polishing process was followed with both electrodes. Fine grade alumina (particle size 0.1 down to 0.05 μm) was used; the alumina was spread on smooth glass plate and then slurried in deionized water to form a paste. The electrode was polished many times by circular motions or in the form of figure 8 (or horizontal motion ∞). Eventually, the electrode was carefully cleaned primarily by rinsing with deionized water followed by alcohol or acetone. Finally it was dipped in deionized water for period of time (about 3.0 min) and dried by N_2 gas. After all these procedures the electrode was assessed by recording a voltammogram of blank solution (e. g. 0.1 M H_2SO_4) before use. If the voltammogram exhibited a repeatable features after 10 cycles and very low background current, this meant that the working

electrode was successfully polished, if not the electrode was re-polished. For best results the electrode prefers to be used immediately after polishing.

Another polishing method was the electrochemical pre-treatment which is best for electrode surface activation than mechanical method. For platinum electrode the potential cycling using cyclic voltammetry between -0.2 to 1.5 V vs Ag/AgCl in 0.1 M H_2SO_4 was carried out for 20 cycles, the purpose of such process was to oxidize the contaminations formed on the electrode surface such as metal oxides or absorbed species. Then the electrode was removed and immersed in deionized water for about 3.0 min, dried by blowing with N_2 gas, assessed by recording a blank mixture solution of 0.1 M H_2SO_4.

In respect to glassy carbon electrodes, cyclic voltammetry was performed at potentials between -1.0 to 1.5 V vs Ag/AgCl in 0.1 M $HClO_4$ for 20 cycles. Then the electrode was removed and immersed in deionized water for period of time (about 3.0 min), dried by N_2 gas, assessed by recoding a blank voltammogram in 0.1 M H_2SO_4, and then it was ready for use [116].

The purpose of using of the aforementioned cleaning steps in this work was to obtain a smooth, brilliant surface because:

1- The environmental samples (Shilbottle), especially unfiltered samples, contain considerable amounts of organic matter and colloidal materials that can adsorb on the electrode and affect the results.

2- Studies of iron (Fe) oligomerization are complicated because the oligomers and polymers can precipitate and adsorb on the electrode surface.

2.6 Spectroscopic techniques

In addition to electrochemical techniques, in this work some spectroscopic and diffraction techniques such as, mass spectrometry (MS), inductively coupled plasma (ICP), X-ray diffraction (XRD) and Raman spectroscopy were used. The goal of such measurements is to support the data that have been obtained using electrochemical techniques, also to provide extra information about components of the samples under study (characterization and measurement).

2.6.1 Mass spectrometry

Mass spectrometry techniques were designed by physicists since the beginning of last century on the basis that measurements of the mass to charge ratio (*m/z*) of charged species can be obtained via their behaviour in electric and magnetic fields. It has been utilized in many applications in biochemical, inorganic, organic and enzyme analysis. The main components of most mass spectrometry techniques are sample inlet, ion source, mass analyser, detector and data system as illustrated in figure 2.13.

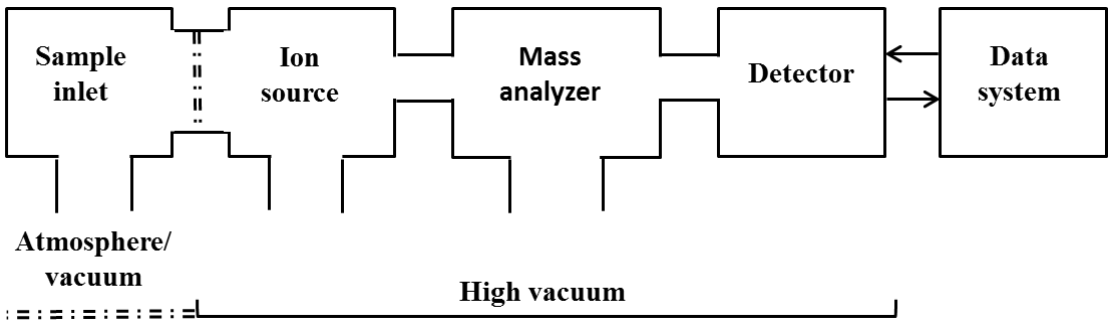

Figure 2.13: The components of a mass spectrometer (from [127] Pavia D. L., Lampman G. M., Kriz G. S. and Vyvyan J. R., Introduction to spectroscopy, *Brooks/code Thomson learning*, 2001).

(a)- Sample introduction by which the samples can be introduced into the ionization chamber. Since the samples may be gas, liquid and solid, they must be converted into volatile components in order that a stream of molecules is obtained and can flow to the ionization chamber. There are some less volatile substances for which special systems have been designed with an oven to convert the sample into vapour. The recent types of mass spectrometry techniques are connected with chromatography, such as gas chromatography-mass spectroscopy (GC-MS), liquid chromatography-mass spectroscopy (LC-MS) and high-performance liquid chromatography-mass spectroscopy (HPLC-MS) in which the sample is automatically separated. Hence each component can be analysed indiviually. However, the main disadvantage of the said methods are that, they need rapid scanning by the mass spectrometer in order that it can determine the spectrum of the preceeding component before the next one arrives in the mass spectrometer.

(b)- Ionization process in which the molecules are transformed into charged species; this can be achieved in four ways: electron ionization, chemical ionization, electrospray ionization and desorption ionization techniques. The method used in this work is the electrospray ionization (2.6.3), because it is suitable for studying both large

biomolecules and small molecules in range of 100 – 1500 m/z in aqueous solution. Further, it is useful for both volatile and non-volatile compounds e. g. iron(III) complexes.

In such methods the solution is sprayed out through a capillary (the capillary was placed between high voltage potential) into a heated chamber. Charged droplets are obtained and expelled into the ionizer chamber. During the passing process, they face a counter flow of dry gas, which evaporates the solvent from the droplets. Thus, these droplets are broken down into small drops via some electrostatic processes. Eventually, the samples species are left as a gas phase ions and solvent-free.

(c)- Mass analyser is the equipment of the spectrometer where the charged ions are split depending on their mass-to-charge ratio (*m/z*) relative to their behaviour in electric and magnetic field. This process can be carried out via several types of analysers according to (m/z) range, the velocity of charged ions and the resolution property e.g. magnetic sector, double-focusing, quadruple and time-of-flight mass analysers.

(d)- Detector by which the current (caused by number of ions which strike the detector) can be measured. The electrical current is recorded as a signal by data systems consequently such signals are eventually presented as mass spectrum from which analytical information can be acquired [118, 127].

2.6.2 Mass spectrum

The spectrum is a plot of ion abundance (density) versus mass-to-charge ratio (*m/z*). In the ionization chamber the largest ion formed usually possesses the tallest peak on the spectrum, this called the base peak. Accordingly, the abundances of other ions and consequently their peaks are plotted relative to the base peak. In mass spectrometry the positive molecular ions M^+ can be generated by removing electron from the formed molecule, which is the same molecular weight of the original molecule after removing the electron. By identifying of ion molecular weight, the molecular weight of unknown substances can be determined.

The preferred method for determination of the molecular formula employs the isotopic pattern; it is based on the fact that the majority of elements atoms have more than one or two stable isotopes. In most elements the heavier isotope has lower abundance (e.g. H_2 occurs largely as ^1H and about 0.02% is as ^2H), with the exception of fluorine and few

other elements. Therefore, this kind of mass spectrometry has been designed to distinguish each element by the relative abundance of the isotopes. Occasionally, the isotopes show one or two mass units above the normal atoms (mostly M^+ +1 and M^+ +2). Therefore, determination of molecular formula by isotopic pattern analysis may need additional attempts to recognize the formula [127, 128].

2.6.3 Electrospray ionization-mass spectrometry (ESI-MS)

The electrospray ionization technique has become a powerful tool for characterization of anionic and cationic species especially for inorganic complexes in aqueous solutions (coordination compounds). The characterization of aqueous solutions via other types of mass spectrometry can be less precise or may be impossible [129].

In ESI-MS, the ESI source is a stainless steel capillary tube which serves as a source of generated ions. Solvents are passed through the capillary tube via an injection needle. A strong electrostatic field is created by applying high voltage to the tip of the stainless capillary tube; the purpose of this is to convert the solvent into small charged droplets. Once these droplets become small enough, the electrostatic energy of the charge density on their surfaces becomes higher than their surface tension (i.e. they reach the Rayleigh instability limit). Then the repulsive forces will split the droplets into smaller size. The electric field of such droplets will be developed at the surface of smaller droplets until the point at which the electric field is strong enough for ions to be evaporated. The ions are passed through the nozzle into a region in which the neutral species are removed via auxiliary pumping. Eventually, the free ions will enter into the mass analyser and other analysis steps, as illustrated in figure 2.14 [118].

For precise measurements, several parameters must be governed such as conductivity, flow rate and surface tension to which significant influences on the spray and ionization of the sample solvents can be ascribed. The favourite solvents for electrospray are polar such as acetone, methanol, acetonitrile and less desirable water (because water has high surface tension). In respect of the conductivity, solvents with conductivities from 10^{-13} Ω^{-1} cm^{-1} to 10^{-5} Ω^{-1} cm^{-1} are easy to electrospray [118].

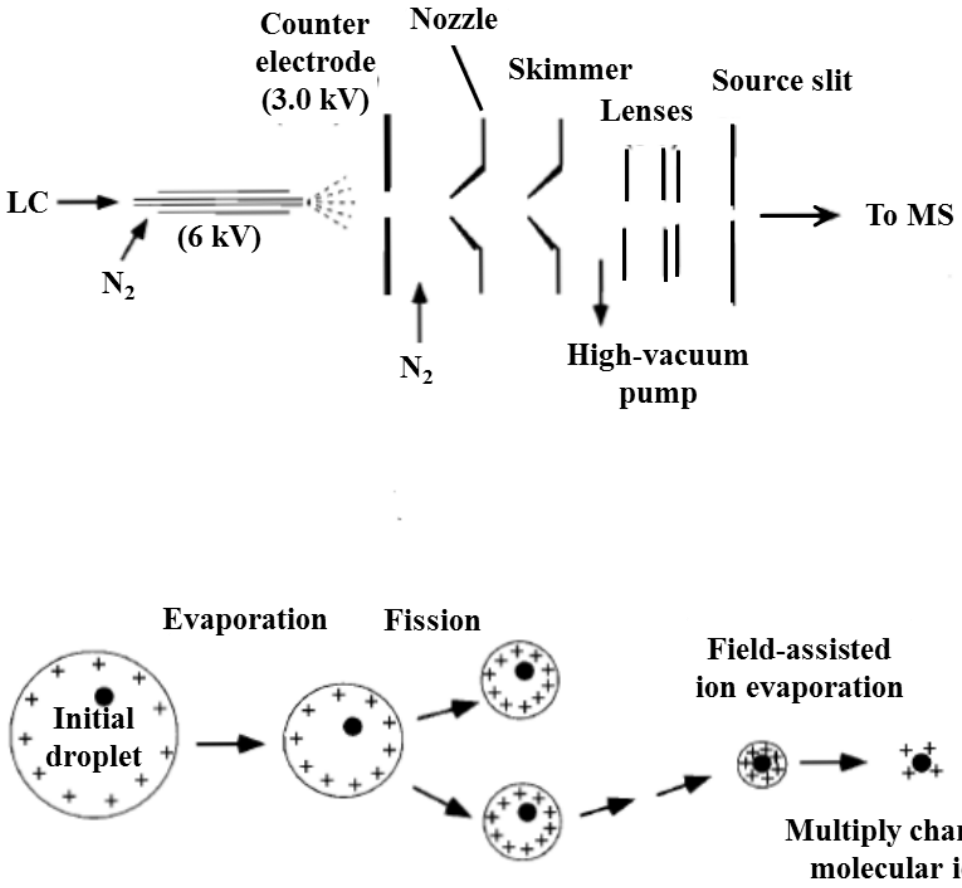

Figure 2.14: The sample steps through mass-spectrometer and the droplets fission in ESI-MS (from [118] Settle F. A., Handbook of Instrumental Techniques for Analytical Chemistry, By Prentice Hall PTR, *New Jersey*, 1997).

2.6.4 Instrumentation/Equipment, sample preparation and analysis procedures for ESI-MS measurements

The electrospray mass spectra obtained in this work were recorded by a micro mass LCT (Waters Inc. Premier) mass spectrometer equipped with a Z-spray electrospray interface. The sample injection into the spectrometer was by Harvard apparatus model 11 syringe pump at a flow-rate of 20 µL min^{-1}. The operation conditions were as follows: capillary voltage (3000 V), sample cone voltage (80 and 120 V), desolvation temperature (250 ^{o}C), source temperature (100 ^{o}C), cone gas flow-rate (30 L h^{-1}), desolvation gas flow-rate (500 L h^{-1}), sample flow-rate (20 µL min^{-1}) and the mass range (*m/z*) (50-2000). The positive modes of mass spectrum were acquired using Masslynx NT software (version 4.1).

The samples were divided into two aliquots, one of which is laboratory sample and another is environmental sample (Shilbottle site). First, stock solutions of 0.03 M of

iron(III) $FeClO_4.nH_2O$ and $Fe_2(SO_4)_3.5H_2O$ were prepared by dissolving the appropriate weight of iron salts in 0.2 M of sodium salts ($NaClO_4$ and Na_2SO_4) using deionized water (18.2 MΩ cm). Diluted solutions (10^{-4}M) were prepared from stock solution for each Fe(III) salt, because the suitable sample concentration for ESI-MS analysis is about 10^{-4} M or less.

The environmental samples were filtrated through a 0.45 μm size cellulose nitrate filter paper and diluted by a factor of twenty (5%). Both samples (laboratory and environmental) were injected into the mass spectrometer and the spectrum were recorded for each case and saved for analysis and interpretation.

2.6.5 Inductively coupled plasma atomic emission spectrometry (ICP-AES)

(ICP-AES) is an advanced tool compared with counterparts in optical atomic emission spectrometry in which the atomization and excitation are carried out by one of three sources (flame, arc and spark). The flame emission technique is utilized only for determination of easily excited metals such as Na, K, Ca and Li, but determination of other metals (refractory metals) using a flame as an atomizer is impossible because the flame temperature is about 3150 ^oC which is not sufficient to excite such metals. In the 1940s the electric arc and electric spark were used as excitation sources for qualitative and quantitative determinations of multi-elements (about 70-80 elements). These techniques are not ideal for elemental analysis, because they have some drawbacks such as complex spectra, background effects, lack of reproducibility, not well suited to measure liquid solutions and lower temperature than ICP [118, 124, 130].

Since the 1970s the emission spectrometry based on plasma has been widely used as a reliable technique for quantitative and qualitative analysis of almost all elements in the periodic table. Further, it can determine non-metals elements such as bromine, chlorine and sulfur. The main advantage of the plasma is its ability to provide a high temperature up to 6500 K by which most atoms convert to ions. The emission lines from ions are more sensitive than those from atoms. The ionic and atomic lines are very sharp (line width typically less than 5 pm) which are easier to identity and interference is uncommon. ICP-AES has become a powerful tool in many fields such as geochemistry, environmental science, biology and medicine [118].

There are three types of plasma sources: inductively coupled plasma ICP, direct current plasma DCP and microwave induced plasma MIP. Using the ICP technique has several advantages: for example, low detection limit, rich emission lines, high stability, and low noise [118, 124].

Since the plasma is the basic component in the ICP technique, an important question is: what is the plasma? The plasma is an electrically conducting gaseous mixture composed of electrons, ions and neutral particles. The most common gas employed in the plasma is argon (Ar) from which a higher gas temperature is achieved and less reactive chemical species than in flames. The argon ions are capable to maintain a high temperature in order to sustain ionization, because Ar^+ ions are able to absorb sufficient power from an external source [124, 130].

The typical inductively coupled plasma torch consists of three overlapping quartz tubes through which a stream of inert gas (usually argon) passes. The outer tube is the largest tube; its diameter is about 2.5 cm. It is surrounded on the top by a water-cooled induction coil which is energized by a radio-frequency generator. The temperature is generated by ionization of argon gas ions and electrons will interact with the magnetic field, and these ions and electrons will move in a closed circuit inside the coil. The resistance of the flowing ions and electrons to such movement leads to ohmic heating and raises the temperature.

Due to the high temperature of the plasma, thermal isolation for the internal side of the outer tube is required. In order to achieve this tangential flow cooling is carried out through the middle tube. The sample is introduced into argon flow as aerosol or vapour via central tube. A typical inductively coupled plasma torch and also a typical block diagram of ICP-AES are shown in figure 2.15 (a and b) [124].

2.6.6 Instrumentation/equipment, sample preparation and analysis procedures for ICP-AES measurements

The instrument used in this work was a UNICAM 701 ICP-OES (Unicam Instruments, Cambridge, England), quartz aqueous torch with glass spray chamber. RF power was 1 kW, coolant flow (13 L min^{-1}), nebuliser pressure (42 psi), auxiliary flow (0.4 L min^{-1}) and sample uptake (1.3 mL min^{-1}). The nebuliser is a standard V-groove PFA micro-flow (produces a fine aerosol).

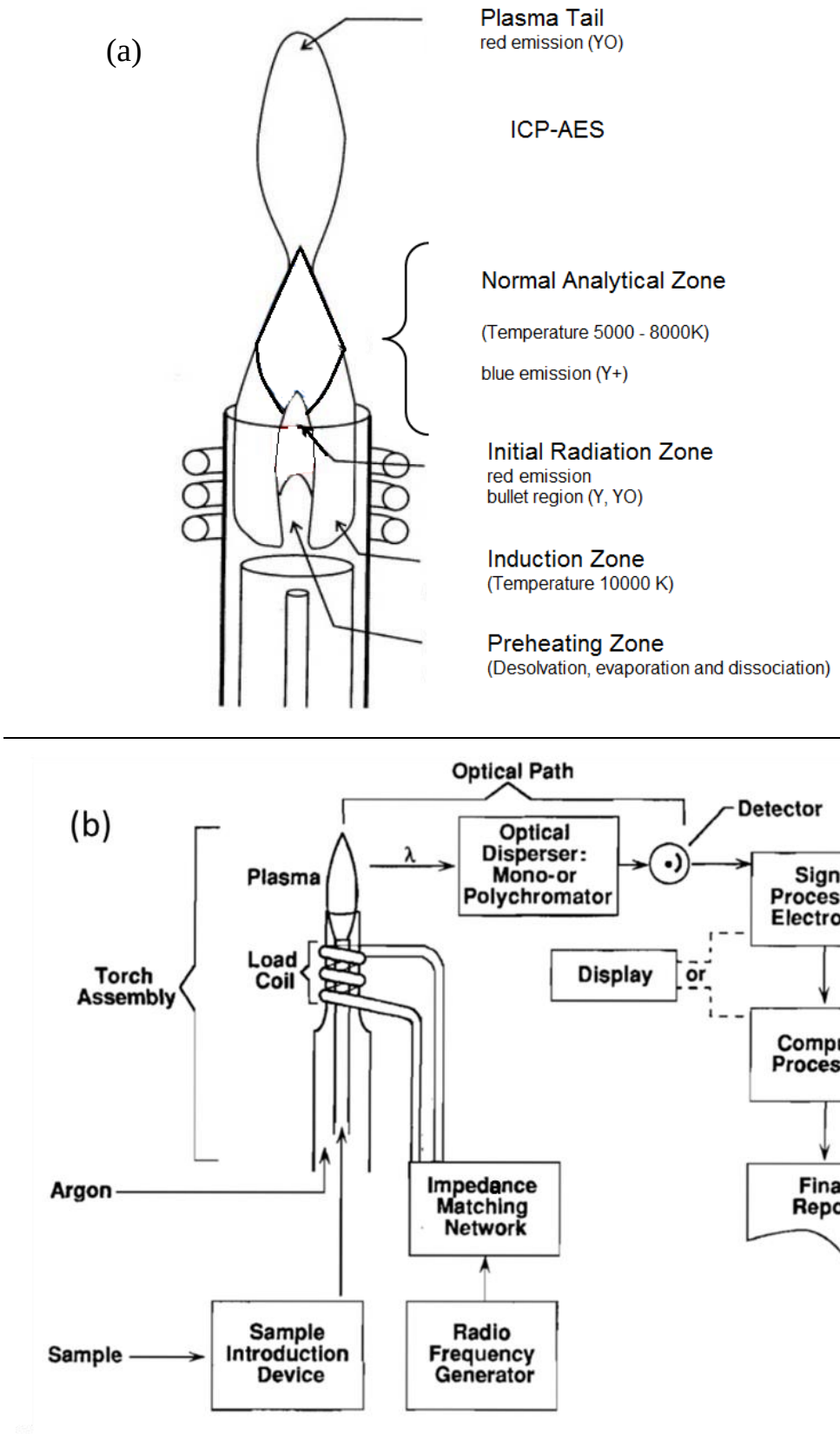

Figure 2.15: (a) typical inductively coupled plasma, (b) typical block diagram of ICP-AES (from[118, 124] Settle F. A., Handbook of Instrumental Techniques for Analytical Chemistry, By Prentice Hall PTR, New Jersey, 1997) & Holler F. J. and Nieman T. A. Skoog D. A., The principles of instrumental analysis, Brooks/code Thomson Learning, 1998

1000 ppm of stock standard solutions were prepared for the determined elements, these elements were (S, Mg, Ca, Mn, Na, K, Fe, Al, Zn, P, Sn, Cu, As, Pb, and Hg). Chemicals were purchased from Sigma-Aldrich. Grade 'A' glass volumetric flasks were used for preparation processes using deionized water (18.2 MΩ cm). Standard calibration curves were prepared by which the concentration of each element was estimated.

The environmental samples were filtrated through a 0.45 μm size cellulose nitrate filter paper; dilutions were conducted for elements with high concentration (e. g. Ca, Mg and S). The samples were injected into the equipment with flow rate 1.3 mL $min^{-1}$and concentrations of all the foregoing elements were estimated in Shilbottle solutions.

2.5.7 Raman spectroscopy

Raman scattering and infrared absorption are regarded as the main spectroscopic techniques to characterize chemical substances according to the vibration modes in molecules. Raman spectroscopy was discovered in 1928s by Indian physicist C.V. Raman; however it was not widely used for many years due to some drawbacks in respect of sample fluorescence and degradation. In the 1960s once lasers became available, Raman spectroscopy has become an important analytical tool. The main advantages of Raman spectroscopy over infrared spectroscopy are; its ability to analyse aqueous solutions, its ability to employ glass and quartz cells by which the atmospherically unstable materials (e. g. sodium chloride plates) can be avoided. The main interferences are fluorescence of impurities [124, 131].

In the infrared technique the absorption arises when the frequency of incident light is sufficient to promote vibrational of the molecule from ground state to a vibrational excited state. However, the principle of Raman scattering is based on the inelastic scattering of a single frequency of light by the sample. One vibrational unit of energy different from the incident beam (scattered photons from molecules) is collected and detected. The incident beam interacts with molecular vibrations and transfers energy to these vibration modes [131]. This inelastic process is inherently weak and only one photon in every 10^6 – 10^8 photons undergoes to Raman scattering. Thus, this process requires a very high power density to very small amount of sample which can be delivered by the laser. In recent Raman equipment the source of light are usually lasers, because they produce sufficient intensity with reasonable single-to-noise ratio [131].

Despite both techniques (Raman scattering and infrared absorption) showing similar principles in respect of molecular vibrations, they differ in their selection rules. Infrared absorption involves change in dipole moment and charge distribution. Whereas Raman scattering causes momentary distortion (polarization) of the cloud of electrons in a molecule after which reemission of the radiation occurs as the molecule enters a new vibrational state. For example, homonuclear molecules such as chlorine, hydrogen and nitrogen, which have no dipole moment and no transition dipole for the stretching vibration (by which the distance between two nuclei is changed), nevertheless polarize, and can show Raman scattering and the wave number of the vibration mode can be obtained [124].

The major three components of modern Raman spectroscopy are: a laser source, sample preparation system and spectrograph, which are illustrated in block diagram of Raman spectrometer in figure 2.16. The source of light in recent Raman equipment is usually a laser. The different common lasers are listed in table (2.1) [124]:

Laser source	Wavelength / nm
Argon ion	488.0 or 514.5
Krypton ion	530.9 or 647.1
Helium/Neon	632.8
Diode laser	782 or 830
Nd/YAG	1064

Table 2.1: Some common laser sources for Raman spectroscopy

In Raman spectroscopy the sample handling is easier than in infrared spectroscopy because only visible light is used, thus glass, lenses and fiber-optic can be used. In contrast infrared spectroscopy requires unstable crystalline halides which are IR transparent. For example, an ordinary glass melting-point capillary is used for non-absorbing liquid samples. The samples can be analysed in different physical states such as liquid and solid. The major advantage of Raman compared with infrared is that, Raman scattering samples in water can be carried out because water shows weak Raman scattering, while it is a strong absorber of infrared radiation. As it employs visible light, Raman spectroscopy is often carried out in a confocal microscope and this allows imaging [124]. Figure 2.17 illustrates diagram of Laser-Raman Spectroscopic system based on a confocal microscope.

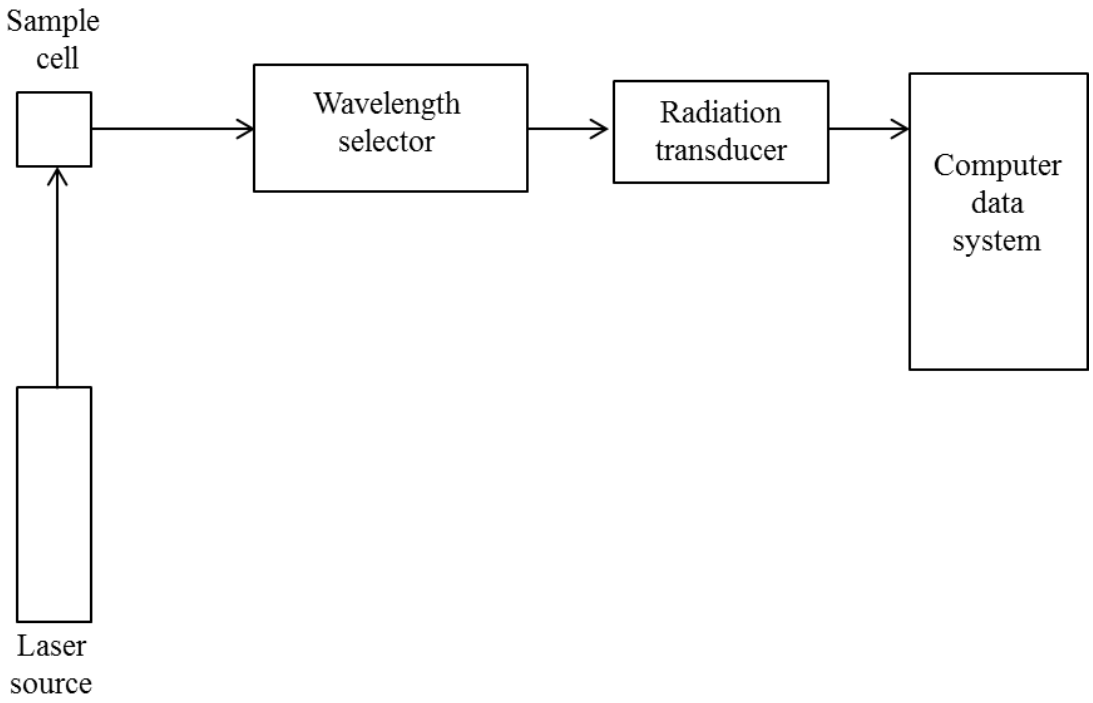

Figure 2.16: A block diagram of a Raman spectrometer. (From [124] Holler F. J. and Nieman T. A. Skoog D. A., The principles of instrumental analysis, *Brooks/code Thomson Learning*, 1998).

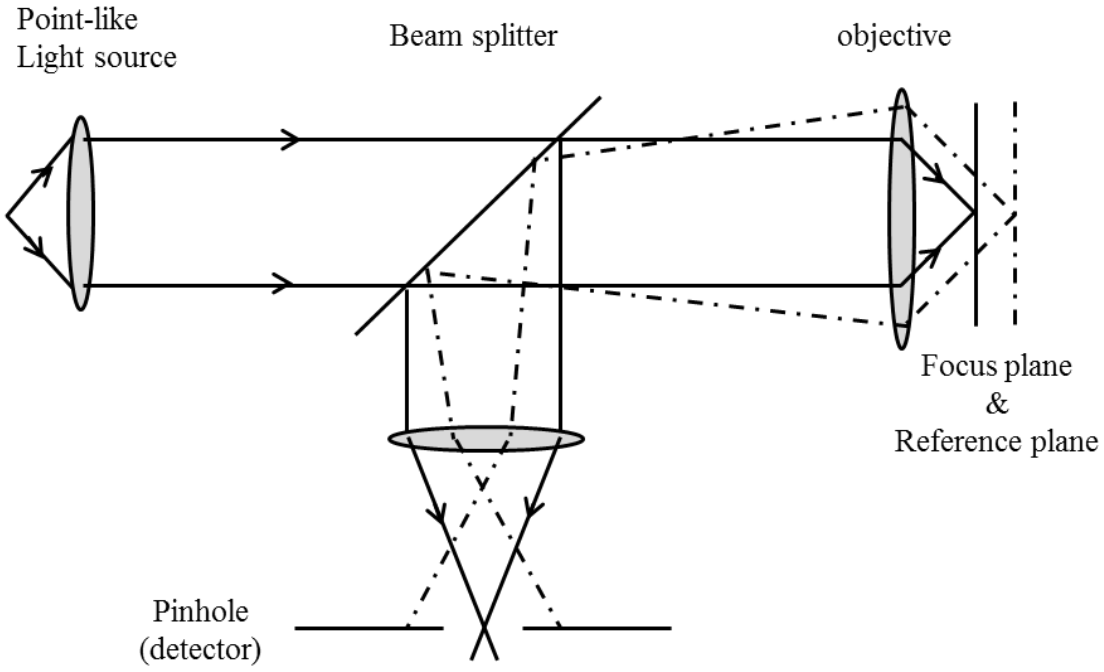

Figure 2.17: Principal setup of a confocal microscope (from [132] Dieing T, Hollricher Oand Toporski J., Confocal Raman Microscopy, *Springer, New york*, 2011).

2.6.8 Instrumentation/equipment for Raman measurements

All Raman measurements were conducted using confocal microspectroscopy (WiTec confocal Raman microscope model CRM, 200, Ulm, Germany). The 488 nm line of argon ion laser (Melles-Griot) was used as the excitation source with output 35 mW. The experiments were performed at an integration time 30 s of 0.1s/pixel. Peltier-cooled charge coupled device (CCD) detector was used to detect and analyse the collected spectrum.

2.6.9 Analysis procedures of characterization studies using Raman spectroscopy

Dried and evaporated solutions of 0.03 M of iron(III) perchlorate and iron(III) sulfate dissolved in 0.2 M of $NaClO_4$ and Na_2SO_4 were prepared on glass coverslips. Also dried samples of Shilbottle waters were prepared in the same way. The 488 nm line of an argon ion laser was used as the excitation source. Raman spectra were collected at room temperature (around 17 ± 1 ^oC) for both environmental and laboratory dried samples. The spectra were collected within a range of 150 and 1350 cm^{-1} in Raman shift.

2.6.10 Procedures for kinetic studies using Raman spectroscopy

Kinetic studies of high concentrations 0.25 M of $Fe_2(SO_4)_3.5H_2O$ and $Fe(ClO_4).xH_2O$ solutions were carried out. The solution in sulfate media was (0.50 M of Fe^{3+} dissolved in 0.2 M of Na_2SO_4), while the solution in perchlorate media was (0.50 M of Fe^{3+} dissolved in 0.2 M of $NaClO_4$). Enough amount of NaOH was added to each solution to achieve an $[OH^-]/[Fe^{3+}]$ ratio of 1.0, after 1 minute (from NaOH addition) the Raman spectrum was recorded every minute for about 60 minutes (intensity versus time). All spectra were acquired under ambient conditions and at room temperature (around 17 ± 1 ^oC) within spectral range 150 and 1500 cm^{-1} in Raman shift.

2.6.11 X-Ray diffraction (XRD)

X-Ray diffraction is a powerful technique for examining and analysing crystalline solid materials. It is able to provide the actual crystal structure for single crystals and sometimes for mixtures of crystalline powders. In addition, XRD is a unique method for providing qualitative identification and quantitative information in a mixture of two

compounds. For instance, XRD is able to estimate the percentage of NaCl and KBr in a solid crystalline mixture. Other analytical techniques e. g. ICP-MS often measure only the percentages of K^+, Na^+, Br^+ and Cl^- of a solid mixture [124, 133].

XRD is based upon the unique diffraction pattern of electromagnetic radiation for each crystalline substance. Once X-Ray radiation collides with a crystal lattice surface (the crystal lattice is a group of atoms, molecules and ions arranged in a periodic three dimensional 3D pattern) as shown in figure 2.18. The incident beams will scatter and form a reflected beam. If the reflected beams from each of the planes of the crystal are in phase with each other, the intensity is increased. Such constructive interference is the base of the diffraction pattern. However, if the reflected beams are completely out of phase with each other, destructive interference will occur and no intensity will be detected [133].

The operative equation in X-Ray diffraction is the Bragg equation which gives scattering angles for which constructive interference occur, equation (2.12):

$$n\lambda = 2d \sin\theta \qquad \ldots\ldots\ldots\ldots\ldots\ldots\ldots\ldots (2.12)$$

Where θ is the angle of incidence beam of X-Ray, d is the distance between the crystal planes, *n* the order of reflection and λ the wavelengths.

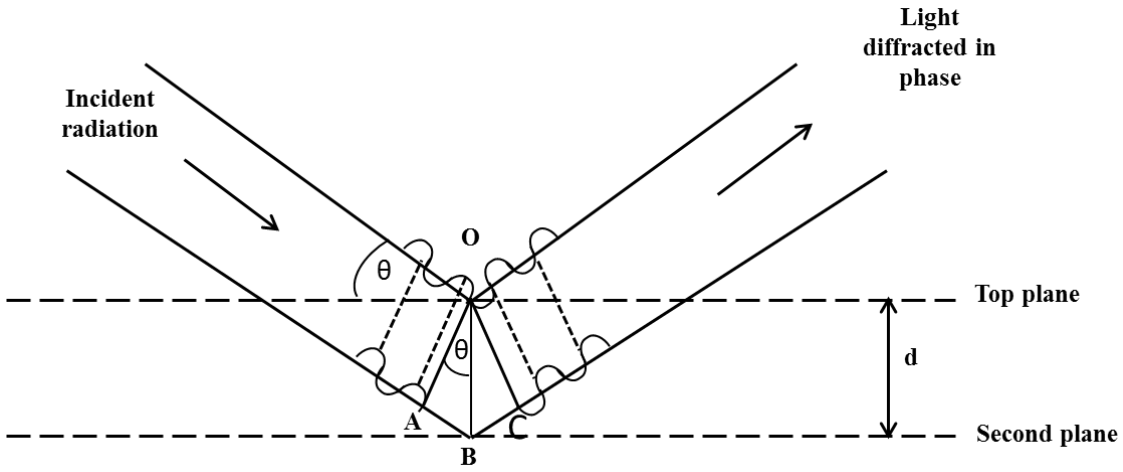

Figure 2.18: Reflection of X-rays from top and second planes of atoms in a solid lattice.

The diffraction angle 2θ is calculated from the distance between the two crystal planes, which is denoted d. Thus, the position of diffraction peak depends on the separation of the crystal planes and also on the wavelength of the incident beam of X-rays. The

intensity of diffraction peak also depends on the type and number of atoms and also on the locations of the atoms in the crystal planes [134].

2.6.12 Instrumentation/equipment, sample preparation and analysis procedures for XRD method

The instrument used for XRD measurements was a PANalytical X'Pert Pro MPD, powered by a Philips PW3040/60 X-ray generator and fitted with an X'Celerator detector. Diffraction data was acquired by exposing powder samples to Cu-Kα X-ray radiation, which has a characteristic wavelength (λ) of 1.5418 Å. X-rays were generated from a Cu anode supplied with 40 kV and a current of 40 mA.

The data were collected over a range of 5-90^{o} (2θ) with a step size of 0.0334^{o} (2θ) and nominal time per step of 200 seconds, using the scanning X'Celerator detector (hence the longer effective counting time). Fixed anti-scatter and divergence slits of 1/4^{o} were used together with a beam mask of 10 mm and all scans were carried out in 'continuous' mode. Phase identification was carried out by means of the X'Pert accompanying software program PANalytical high score plus in conjunction with the ICDD Powder Diffraction.

Samples of solid precipitates of 0.5 M iron(III) perchlorate and iron(III) sulfate dissolved in 0.2 M of $NaClO_4$ and Na_2SO_4 were prepared by addition enough amounts of NaOH. Three solid samples were prepared, the first was by addition of 2 mL of 1 M NaOH to 2 mL of 0.5 M $Fe_2(SO_4)_3$ (final concentration 0.25 M) to achieve $[OH^-]/[Fe^{3+}]$ ratio equal to 1.0 (for all samples NaOH was added as one batch). The second was by adding of 2 mL of 2 M NaOH to 2 mL of 0.5 M $Fe_2(SO_4)_3$ to achieve $[OH^-]/[Fe^{3+}]$ ratio equal to 2.0. The third was by addition of 2 mL of 1.0 M NaOH to 2 mL of 0.5 M $Fe(ClO_4)_3$ to achieve $[OH^-]/[Fe^{3+}]$ ratio of 2.0. These solutions were dried in room temperature (20 ± 3 ^{o}C) for approximately 40 days. The resulting solid was ground using a mortar and pestle to obtain a fine homogenous powder. The XRD diffraction patterns for solid samples were taken and analysed by X'Pert accompanying software program PANalytical high score plus in conjunction with the international centre of diffraction data-powder diffraction file (ICDD-PDF) database.

Chapter 3: Electrochemical and spectroscopic characterization of iron(III) species

3.1 Introduction

It is well known that iron(III) has a strong tendency to hydrolyse in aqueous solutions; this hydrolysis process depends on numerous conditions e.g. concentration, pH, temperature, aging time and anions [102, 135-137]. It has been reported that in acidic solutions the hydrolysis is simple and soluble species of Fe^{3+}, $Fe(OH)^{2+}$, $Fe(OH)_2^{+}$ and $Fe_2(OH)_2^{4+}$ are formed. The equilibrium between mononuclear species has been established to be rapid [137-139]. However, in mildly acidic media the hydrolysis process is slow and achieving the equilibrium state may take a long time; furthermore the formed complexes are complicated compared with acidic solutions, because dimer, trimer, high oligomer and polymers are expected to be formed [86, 140-142].

Characterization of soluble hydrolysed species of iron(III) in aqueous solutions may not therefore be possible using voltammetric techniques especially at fairly elevated pH values (3 – 4). However, there are a few studies which have been published concerning this matter [143, 144]. In this work we have performed detailed studies using voltammetric techniques (SWV) to identify soluble species of iron(III) species, even oligomer species with inorganic ligands (e.g. ClO_4^- and SO_4^{2-}).

On the other hand, detailed kinetic studies of ferric/ferrous couple in inorganic media (e.g. ClO_4^-, Cl^- and SO_4^{2-}) on solid electrodes have been performed [145-147]. It has been observed that, the presence of coordinated inorganic ligands with iron(III) enhances the electron transfer between the redox couple Fe(III)/Fe(II) and the electrode surface, while in non-coordinating or very weak coordinating media such as ClO_4^- the electrode kinetics are slower than in chloride, bromide or sulfate media [146, 148]. Sulfate anions have less effect on the electron transfer kinetics than halide ions. Such behaviour was ascribed to adsorption of coordinated anions on the platinum electrode surface, which serve as a bridge for faster electron transfer [146, 148].

For these reasons we conducted some experiments to study the voltammetric behaviour on laboratory samples in order to compare the obtained results with environmental samples, as mine water samples are very complicated and they contain a significant

amount of potentially adsorbing species. The simple voltammetric characterization (reversibility, quasi-reversibility and irreversibility) of these solutions were examined in this work. In addition, the characterization of soluble and solid iron(III) compounds of laboratory samples were carried out using Raman spectroscopy, mass spectroscopy and X-ray diffraction.

3.2 Results and discussion

3.3 Electrochemical characterization

There are two different classes of characterization using voltammetric techniques. The first is related to electron transfer kinetics, and another is to recognize and distinguish soluble species in sample solution.

3.4 Kinetic studies of electrode-solution interface

Using cyclic voltammetry, it is possible to classify the electrode reaction for these samples into reversible, quasi-reversible or irreversible categories depending on the rate of electron transfer at the electron-solution interface. Whenever the rate of electron transfer is fast, it can maintain the equilibrium at electrode surface and the Nernst equation is obeyed locally. The situation is the opposite with irreversible reactions. In this work, we studied the voltammetric behaviour of three different solutions of iron(III), the first is laboratory iron(III) sulfate, second is also laboratory iron(III) perchlorate (a weakly coordinating anion) and the third is an environmental sample (Shilbottle sample), which contains a substantial concentration of sulfate.

3.4.1 Iron(III) sulfate

Figure 3.1 illustrates cyclic voltammograms of 0.005 M of $Fe_2(SO_4)_3.5H_2O$ in 0.2 M of Na_2SO_4 at different scan rates**:** (a) 0.01, (b) 0.05, (c) 0.10, (d) 0.15 and (e) 0.20 V s^{-1}, respectively. On the voltammogram two peaks were observed; these peaks are for reduction and oxidation of monomer species of iron(III) (as we will see latter in this chapter section 3.5). The potential difference between these peaks (oxidation and reduction) varied between 142 and 316 mV at scan rates 0.01 and 0.25 V s^{-1}, respectively. The cathodic peak potential E_p^C depends on scan rate (ν) and it shifted to negative potential with increasing scan rate. The I_p^A/I_p^C ratio is less than 1.0 at all the

different scan rates. The peak current increases with increasing square root of scan rate ($\nu^{\frac{1}{2}}$), but it is not proportional to it as shown figure 3.2.

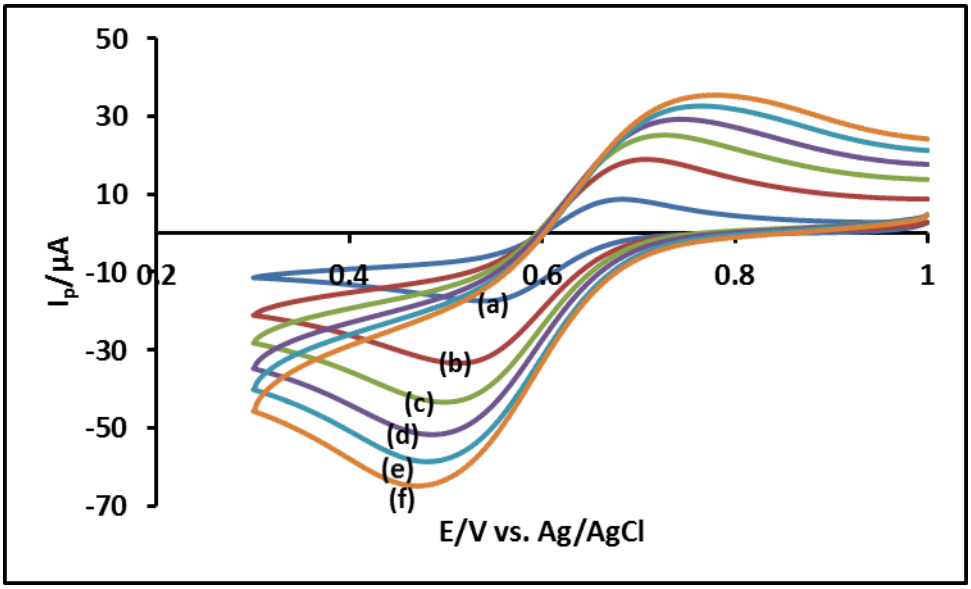

Figure 3.1: Cyclic voltammograms 0.010 M of $Fe_2(SO_4)_3.5H_2O$ in 0.2 M of Na_2SO_4 at different scan rate**:** (a) 0.01, (b) 0.05, (c) 0.10, (d) 0.15, (e) 0.20 and (f) 0.25 V s^{-1}, respectively. (Initial E = 1.0 V, high E = 1.0 V, low E = 0.3 V, segment = 2.0, sample interval 0.001 V, quiet time = 2.0 sec and sensitivity = 1.0 × 10^{-5} A/V), the working electrode was a 1 mm radius platinum electrode; the reference electrode was Ag/AgCl. The solution was degassed under nitrogen for 10 minutes.

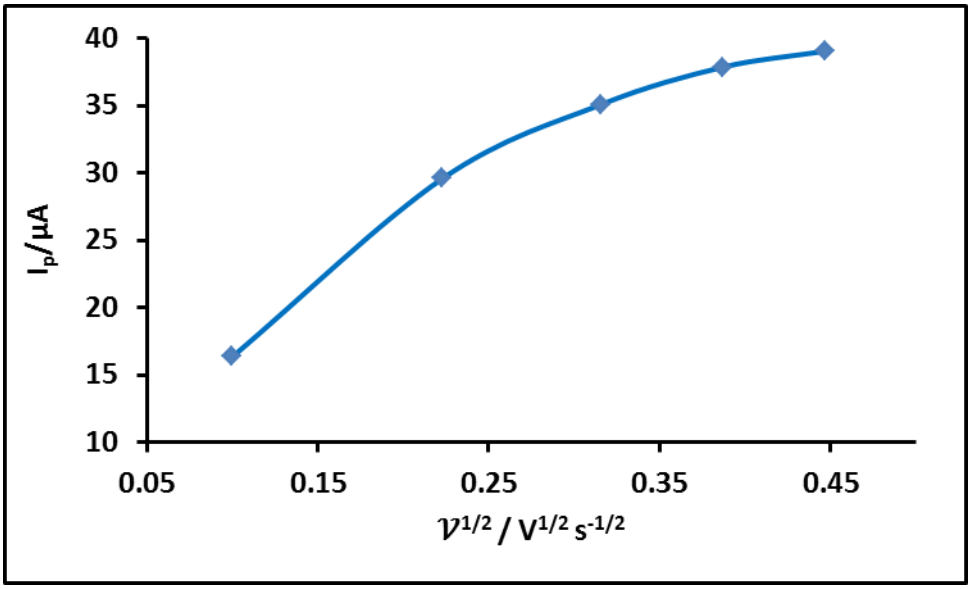

Figure 3.2: I_p vs. $\nu^{\frac{1}{2}}$ of 0.005 M of $Fe_2(SO_4)_3.5H_2O$ in 0.2 M of Na_2SO_4

According to all aforementioned parameters (illustrated in table 3.1), the oxidation-reduction system of monomeric species of iron(III) in sulfate media shows quasi-reversible one-electron reduction characteristic under our experimental conditions which are: platinum electrode diameter 1.0 mm, the range of scan rate is between 0.01 –

0.25 V s^{-1} and the concentration of supporting electrolyte is about 0.2 M of Na_2SO_4 to reduce effects of uncompensated resistance iR_u (which can be considered to be neglected in our case).

ν	$\Delta E_p = E_p^A - E_p^C$ (mV)	I_p^A/I_p^C	E_p^C (V)	I_p (A)
0.01	142	0.83	0.540	1.709×10^{-5}
0.05	194	0.77	0.513	3.073×10^{-5}
0.10	229	0.74	0.497	3.726×10^{-5}
0.15	256	0.73	0.484	4.024×10^{-5}
0.20	289	0.73	0.479	4.167×10^{-5}
0.25	316	0.71	0.471	4.219×10^{-5}

Table 3.1: Diagnostic parameters from the cyclic voltammograms of monomeric soluble iron(III) sulfate species.

3.4.2 Iron(III) perchlorate

According to variables in table 3.2 and voltammograms in figure 3.3, the cyclic voltammogram of soluble aqueous species of iron(III) in perchlorate solution exhibits also quasi-reversible one-electron reduction character under our experimental conditions. Such a classification was based on the diagnostic criteria for cyclic voltammograms of quasi-reversible systems [121].

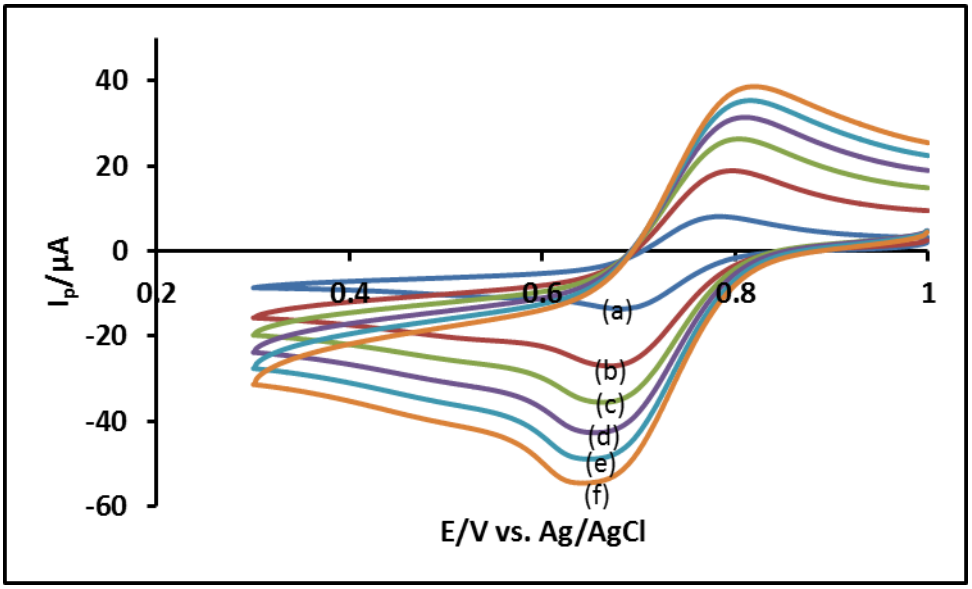

Figure 3.3: Cyclic voltammograms 0.010 M of $Fe(ClO_4)_3.xH_2O$ in 0.2 M of $NaClO_4$ at different scan rate**:** (a) 0.01, (b) 0.05, (c) 0.10, (d) 0.15, (e) 0.20 and (f) 0.25 V s^{-1}, respectively. (Initial E = 1.0 V, high E = 1.0 V, low E = 0.3 V, segment = 2.0, sample interval 0.001 V, quiet time = 2.0 sec and sensitivity = 1.0×10^{-5} A/V), the working electrode was a 1 mm radius platinum electrode; the reference electrode was Ag/AgCl. The solution was degassed under nitrogen for 10 minutes.

For example, peak potential separation (ΔE_p) was 101 mV at scan rate 0.01 V s^{-1}, and it increased to reach 178 mV at scan rate 0.25 V s^{-1}. The I_p^A/I_p^C ratio is very close to 1.0 at different scan rate. Peak current increases with increasing square root of scan rate ($\nu^{\frac{1}{2}}$), such increase seems to be not proportional to $\nu^{\frac{1}{2}}$ (figure 3.4). Reduction peak shifted to the negative potential whenever the scan rate is increased about 21 mV for 10 fold increasing of ν. All these aspects indicate that the electron transfer in this system is not fast enough to maintain the equilibrium at electrode surface, and the Nernst equation is not satisfied at the electrode surface. Therefore kinetic processes should be considered in this case.

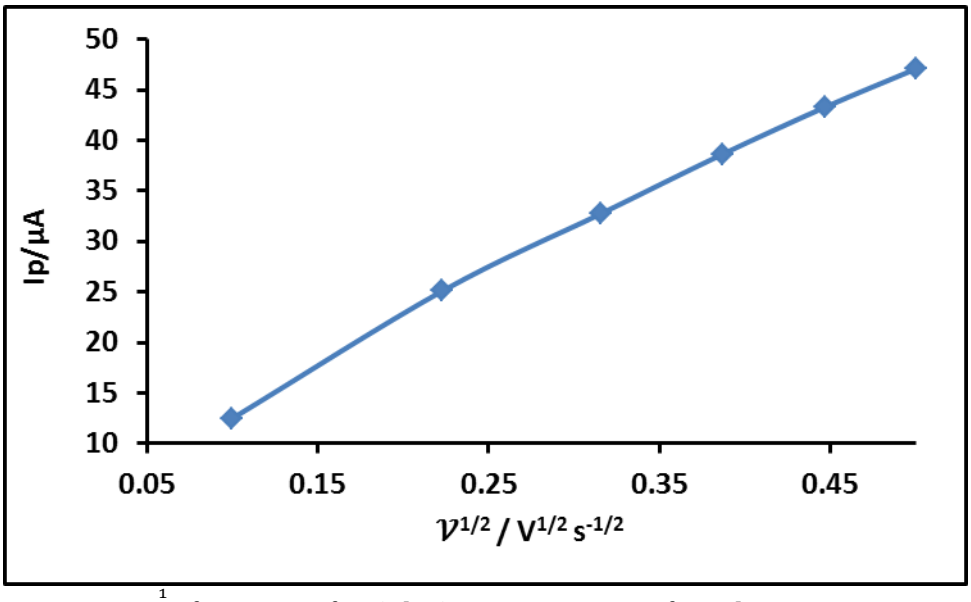

Figure 3.4: I_p vs. $\nu^{\frac{1}{2}}$ of 0.010 M of $Fe(ClO_4)_3.xH_2O$ in 0.2 M of $NaClO_4$

ν	$\Delta E_p = E_p^A - E_p^C$ (mV)	I_p^A/I_p^C	E_p^C (V)	I_p (A)
0.01	101	0.94	0.682	1.177×10^{-5}
0.05	127	0.93	0.670	2.33×10^{-5}
0.10	144	0.94	0.661	3.10×10^{-5}
0.15	155	0.94	0.655	3.62×10^{-5}
0.20	165	0.93	0.650	4.01×10^{-5}
0.25	178	0.92	0.640	4.34×10^{-5}

Table 3.2: Diagnostic parameters from the cyclic voltammograms of monomeric soluble iron(III) perchlorate species

3.4.3 Environmental samples (Shilbottle site)

The soluble species of iron(III) in Shilbottle samples exhibit quasi-reversible one-electron reduction process in most diagnostic tests. For example, the oxidation-

reduction peak separation was 100 mV at a scan rate of 0.01 V s^{-1}, and about 196 mV at a scan rate of 0.25 V s^{-1} (table 3.3). Also the reduction peak shifted to negative potential with increasing ν, peak current increased with increasing ν, but it is not proportional to $\nu^{\frac{1}{2}}$ (figure 3.6). Again, the voltammetric parameters indicate that the process may be described as quasi-reversible. However, the environmental samples are complex and the assignment of the cyclic voltammogram is a simple quasi-reversible process omits some details, because it includes numerous redox species (e.g. organic compounds, inorganic metals and other complex material). One example of such a complication that, one can observe on the Shilbottle cyclic voltammograms that the I_p^A/I_p^C ratio exceeds 1.0 and the ratio varied between 1.29 and 1.45, which indicates that other redox active species may be involved. The shape of cathodic peak is different to the laboratory samples especially sulfate, and there appears to be an additional broad peak near 0.5 V. In addition, the current is non-zero at 1.0 V (the beginning of the scan) which suggests that there is substantial iron(II) present. Accordingly the kinetic characterization of Shilbottle samples must be considered tentative.

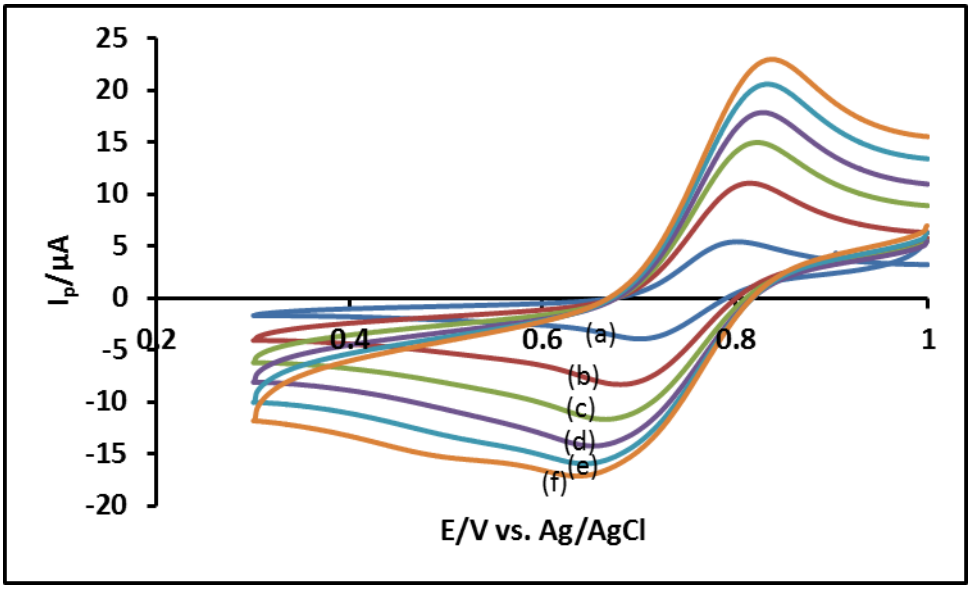

Figure 3.5: Cyclic voltammograms of Shilbottle sample (settlement lagoons) in which the concentration of soluble iron(III) species is about 0.007 M at different scan rate**:** (a) 0.01, (b) 0.05, (c) 0.10, (d) 0.15, (e) 0.20 and (f) 0.25 V s^{-1}, respectively. (Initial E = 1.0 V, high E = 1.0 V, low E = 0.3 V, segment = 2.0, sample interval 0.001 V, quiet time = 2.0 sec and sensitivity = 1.0×10^{-5} A/V), the working electrode was a 1 mm radius platinum electrode; the reference electrode was Ag/AgCl. The solution was degassed under nitrogen for 10 minutes.

It can be concluded from the results above (peak separations), in respect to the rate of electron transfer at the electrode-solution interface that, monomeric species of iron(III) in sulfate media are rather slower than monomeric iron(III) in perchlorate media. This may be in disagreement with previous studies [146, 147], but such difference may be

attributed to the fact that the heterogeneous rate constant of Fe(III)/Fe(II) in sulfate media decreases with increasing pH, due to formation of different iron(III)-sulfate complexes at pH higher than 1.0 [143, 149]. A comparison of Shilbottle samples with laboratory solutions (iron(III) in sulfate or perchlorate media) is rather hard, because of the complex composition of mine waters.

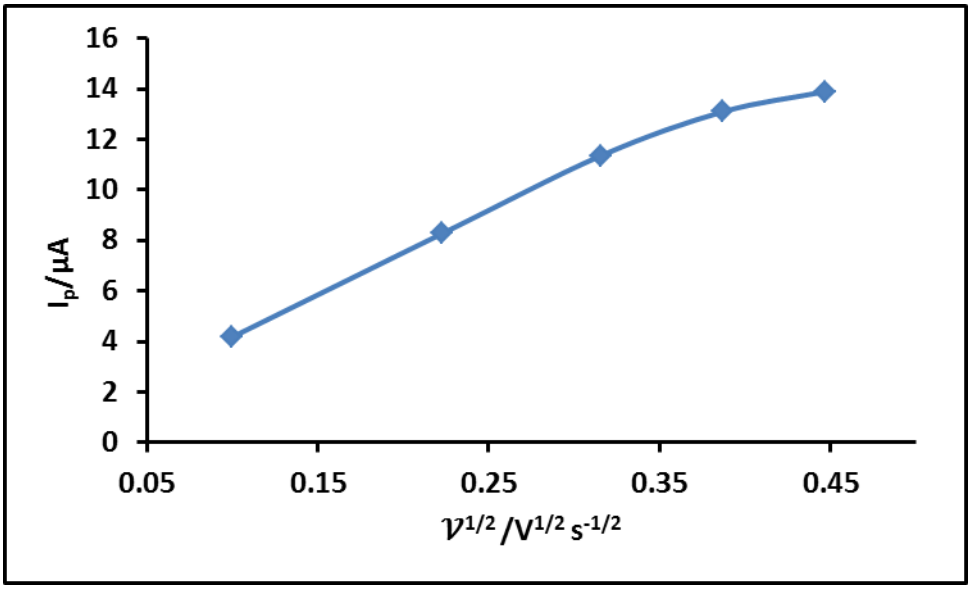

Figure 3.6: I_p vs. $\nu^{\frac{1}{2}}$ of Shilbottle sample (settlement lagoons)

ν	$\Delta E_p = E_p^A - E_p^C$ (mV)	I_p^A/I_p^C	E_p^C (V)	I_p (A)
0.01	100	1.29	0.702	5.42×10^{-6}
0.05	135	1.30	0.681	1.08×10^{-5}
0.10	158	1.27	0.665	1.44×10^{-5}
0.15	177	1.29	0.653	1.70×10^{-5}
0.20	179	1.33	0.644	1.87×10^{-5}
0.25	196	1.45	0.640	2.03×10^{-5}

Table 3.3: Diagnostic parameters from the cyclic voltammograms of monomeric soluble species of iron in Shilbottle sample (settlement lagoons).

3.5 Qualitative characterization

The second part of the characterization of hydrolysed species of iron(III) in aqueous solution is qualitative analysis by which identification of some species can be achieved using voltammetry. SWV was used because the charging current background is very low compared with CV. Three different solutions were investigated, soluble iron(III) solutions in sulfate and perchlorate media, and also environmental solutions.

3.5.1 Iron(III) sulfate

Figure 3.7 illustrates square wave voltammograms of 0.015 M of $Fe_2(SO_4)_3.5H_2O$ in an aqueous solution of 0.2 M of Na_2SO_4 with and without NaOH. On the voltammogram, two reduction peaks were observed when no NaOH was added to the solution, while three peaks were observed after addition of NaOH. As has been previously reported, in aqueous iron(III)-sulfate $FeSO_4^+$, $Fe(SO_4)_2^-$ and $FeHSO_4^{2+}$ are the dominant species at high sulfate concentration and for pH range between 0 - 4 [143, 150]. Therefore the most positive peak (i) at about 0.636 V (figure 3.7: voltammogram 1, line blue) can be ascribed to one-electron reduction of monomer iron(III)-sulfate complexes ($FeSO_4^+$ and / or $Fe(SO_4)_2^-$) according to the following equations (3.1 – 3.13):

$$FeSO_4^+ + e^- \rightleftharpoons Fe^{2+} + SO_4^{2-} \qquad \text{……(3.1)}$$

$$Fe(SO_4)_2^- + e^- \rightleftharpoons Fe^{2+} + 2SO_4^{2-} \qquad \text{……(3.2)}$$

The formation constants of $FeSO_4^+$ and $Fe(SO_4)_2^-$ (K_1 and K_2) have previously been measured and their values are 263 M^{-1} and 2089 M^{-2}, respectively [109, 111]. In the following calculations we used K_c instead of K (thermodynamic formation constant) because the formal potential (E^o) is known from our voltammetric measurements not the standard potential (E^ϕ). The Nernst equation for Fe^{3+} in aqueous solution is:

$$E = E^o_{Fe^{3+}/Fe^{2+}} + \frac{RT}{F}\ln\frac{[Fe^{3+}]}{[Fe^{2+}]} \qquad \text{……..(3.3)}$$

And for $FeSO_4^+$ and $Fe(SO_4)_2^-$ the Nernst equation are as shown in equations 3.1 and 3.2, respectively:

$$E = E^o_{FeSO_4^+/Fe^{2+}} + \frac{RT}{F}\ln\frac{[FeSO_4^+]}{[Fe^{2+}][SO_4^{2-}]} \qquad \text{……..(3.4)}$$

$$E = E^o_{Fe(SO_4)_2^-/Fe^{2+}} + \frac{RT}{F}\ln\frac{[Fe(SO_4)_2^-]}{[Fe^{2+}][SO_4^{2-}]^2} \qquad \text{……..(3.5)}$$

If we multiple the fraction $\frac{[Fe^{3+}]}{[Fe^{3+}]}$ into $\frac{[FeSO_4^+]}{[Fe^{2+}][SO_4^{2-}]}$ both sides are equal as shown in the equation (3.6):

$$\frac{[FeSO_4^{+}]}{[Fe^{2+}][SO_4^{2-}]} = \frac{[Fe^{3+}]}{[Fe^{3+}]} \cdot \frac{[FeSO_4^{+}]}{[Fe^{2+}][SO_4^{2-}]} \qquad \text{……..(3.6)}$$

Rearrangement the equation 3.6, we will obtain equation (3.7)

$$\frac{[Fe^{3+}]}{[Fe^{2+}]} = \frac{[FeSO_4^{+}]}{[Fe^{2+}][SO_4^{2-}]} \cdot \frac{[Fe^{3+}][SO_4^{2-}]}{[FeSO_4^{+}]} \qquad \text{……..(3.7)}$$

Substituting $\frac{[Fe^{3+}]}{[Fe^{2+}]}$ in (3.7) and equivalent expression into equation (3.3), we obtain equation (3.8):

$$E=E^{o}_{Fe^{3+}/Fe^{2+}} + \frac{RT}{F} \ln \frac{[FeSO_4^{+}]}{[Fe^{2+}][SO_4^{2-}]} + \frac{RT}{F} \ln \frac{[Fe^{3+}][SO_4^{2-}]}{[FeSO_4^{+}]} \qquad \text{…….(3.8)}$$

In a similar way we can obtain equation (3.9):

$$E= E^{o}_{Fe^{3+}/Fe^{2+}} + \frac{RT}{F} \ln \frac{[Fe(SO_4)_2^{-}]}{[Fe^{2+}][SO_4^{2-}]^2} + \frac{RT}{F} \ln \frac{[Fe^{3+}][SO_4^{2-}]^2}{[Fe(SO_4)_2^{-}]} \qquad \text{…….(3.9)}$$

According to equilibrium (3.10), the formation constant K_1 of $FeSO_4^{+}$ is:

$$Fe^{3+} + SO_4^{2-} \rightleftharpoons FeSO_4^{+} \qquad K_1 \qquad \text{……(3.10)}$$

$$K_1 = \frac{[FeSO_4^{+}]}{[Fe^{3+}][SO_4^{2-}]} \qquad \text{……(3.11)}$$

And from equilibrium (3.12), the formation constant K_2 of $Fe(SO_4)_2^{-}$ is:

$$Fe^{3+} + 2SO_4^{2-} \rightleftharpoons Fe(SO_4)_2^{-} \qquad K_2 \qquad \text{……..(3.12)}$$

$$K_2 = \frac{[Fe(SO_4)_2^{-}]}{[Fe^{3+}][SO_4^{2-}]^2} \qquad \text{……(3.13)}$$

Therefore the Nernst equations (3.8) and (3.9) can be rewritten as follows for both species:

$$E= E^{o}_{Fe^{3+}/Fe^{2+}} + \frac{RT}{F} \ln \frac{[FeSO_4^{+}]}{[Fe^{2+}][SO_4^{2-}]} - \frac{RT}{F} \ln K_1 \qquad \text{…….(3.14)}$$

And

$$E = E^{o}_{Fe^{3+}/Fe^{2+}} + \frac{RT}{F}\ln\frac{[Fe(SO_4)_2^{-}]}{[Fe^{2+}][SO_4^{2-}]^2} - \frac{RT}{F}\ln K_2 \qquad \text{.....(3.15)}$$

This means that the reduction peak potential of iron(III) in sulfate media ($FeSO_4^+$ or $Fe(SO_4)_2^-$) shifts negative by an amount of ($-\frac{RT}{F}\ln K_1$ or $-\frac{RT}{F}\ln K_2$) compared with $[Fe(H_2O)_6]^{3+}$, as the $[Fe(H_2O)_6]^{3+}$ complex is thought to be the predominant species in iron(III) perchlorate solution. K_1 and K_2 values have previously been measured and their values are 263 and 2089, respectively [109, 111]. The peak shifts by amount of 143 mV in case of $FeSO_4^+$, and about of 196 mV for $Fe(SO_4)_2^-$.

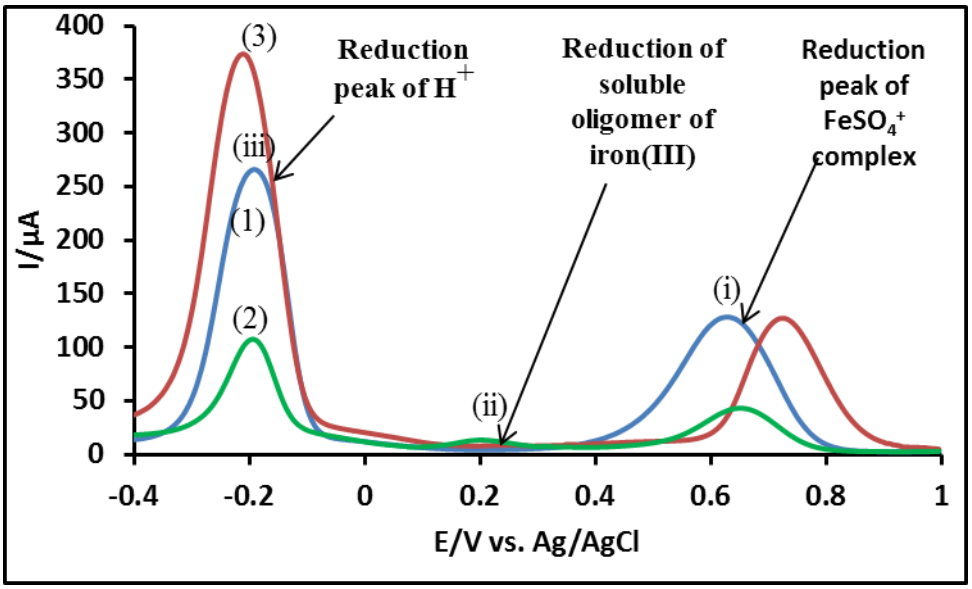

Figure 3.7: Square wave voltammograms of 0.015 M of $Fe_2(SO_4)_3.5H_2O$ in 0.2 M of Na_2SO_4, (1) without NaOH, (2) with NaOH ratio 1.5 and (3) 0.015 M of $Fe(ClO_4)_3.xH_2O$ in 0.2 M of $NaClO_4$. (Initial E = 1.0 V, low E = - 0.4 V, amplitude = 0.025 V, frequency = 15 Hz, sample interval 0.004 V, quiet time = 2.0 s and sensitivity = 1.0×10^{-5} A/V). The working electrode was a 1 mm radius platinum electrode; the reference electrode was Ag/AgCl. The solution was not degassed. The red voltammogram (3, $Fe(ClO_4)_3$) is shown to demonstrate the shift of the reduction peak of the soluble monomer species of iron(III) in sulfate media compared to that in perchlorate media.

From figures 3.7, the reduction peak of soluble iron(III)-sulfate shifted negative by 112 mV compared to hexaqueous iron(III) complex $[Fe(H_2O)_6]^{3+}$. The measured shift is closer to the value calculated for $FeSO_4^+$ than $Fe(SO_4)_2^-$, therefore we assign the peak to the reduction of $FeSO_4^+$ and any species in rapid proton-transfer equilibrium with it such as ($FeHSO_4^{2+}$ or $FeSO_4OH$) (i.e. $[Fe^{3+}] : [SO_4^{2-}] = 1:1$). These observations are in good agreement with previous studies [143, 151]

The peak labelled (ii) in figure 3.7 (green voltammogram) at about 0.20 V can be attributed to the one-electron reduction of soluble oligomer of iron(III). The reason why we do not attribute this peak to the dimer; trimer or even tetramer soluble iron(III) species is because, it is not observed on the voltammogram (1) which is a SWV voltammogram of 0.015 M of iron(III) without NaOH. Such species (dimer, trimer and tetramer) have been reported to exist in 0.1 – 20 mM iron(III) aqueous solutions even without NaOH [135, 136]. However, the oligomer reduction peak observed in the voltammogram (2) appear only on increasing the ratio of $[OH^-]/[Fe^{3+}]$ with addition of NaOH. It has been established that oligomers and polymers can be formed more rapidly with increasing $[OH^-]/[Fe^{3+}]$ ratio [142]. Also it is worth noting that in our experiments, the reduction peak of such oligomers was not observed in up to 0.025 M of iron(III) in the absence of NaOH.

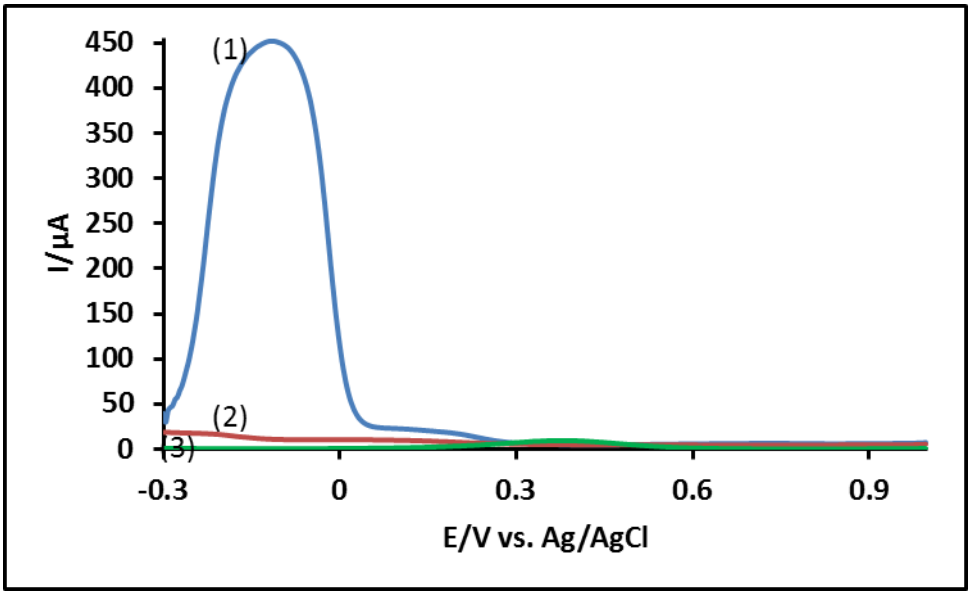

Figure 3.8: Square wave voltammograms of (1) 0.05 M of H_2SO_4 in 0.2 M of Na_2SO_4 on Pt electrode, (2) 0.05 NaOH in 0.2 M of Na_2SO_4 on the Pt electrode, (3) 0.015 M of $Fe_2(SO_4)_3.5H_2O$ in 0.2 M of Na_2SO_4 on the carbon electrode. (Initial E = 1.0 V, low E = - 0.3 V, amplitude = 0.025 V, frequency = 15 Hz, sample interval 0.004 V, quiet time = 2.0 s and sensitivity = 1.0×10^{-5} A/V).

The peak at about -0.180 V (labelled (iii) in figure 3.7) corresponds to reduction of hydrogen ion in the solution. This was supported with additional experiments such as (1) performing SWV for 0.05 M of H_2SO_4 in 0.2 M of Na_2SO_4 at a Pt electrode, (2) 0.05 NaOH in 0.2 M of Na_2SO_4 on the Pt electrode and (3) 0.015 M of iron(III) in 0.2 M of Na_2SO_4 at a glassy carbon electrode as shown in figure 3.8. From the figure, it is clear that the reduction peak at about -0.180 V is markedly increased in the presence of added H^+ (voltammogram 1), whereas it is absent in the presence of OH^- (voltammogram 2).

Also it is not detectable at a carbon electrode (voltammogram 3); carbon electrodes are known to have high overpotential for oxygen or hydrogen reduction in comparison with metal electrodes (e.g. platinum) [116]. Extra evidence to support the assignment of the peak to H^+ reduction is given in figure (3.9). I_p decreased with increasing the $[OH^-]/[Fe^{3+}]$ ratio (addition NaOH into the solution).

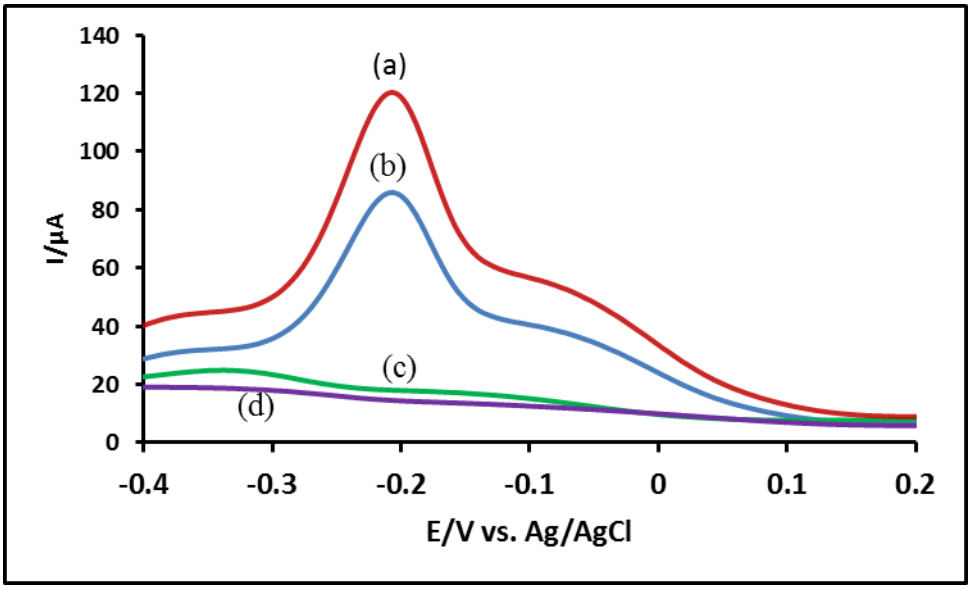

Figure 3.9: Square wave voltammograms of 5×10^{-3} M of $Fe(ClO_4)_3.xH_2O$ in 0.2 M of $NaClO_4$ on Pt electrode, (a) $[OH^-]/[Fe^{3+}] = 1.0$, (b) $[OH^-]/[Fe^{3+}] = 1.1$, (c) $[OH^-]/[Fe^{3+}] = 1.7$ and (d) $[OH^-]/[Fe^{3+}] = 2.0$. (Initial E = 0.2 V, low E = - 0.4 V, amplitude = 0.025 V, frequency = 15 Hz, sample interval 0.004 V, quiet time = 2.0 s and sensitivity = 1.0×10^{-5} A/V). The working electrode was a 1 mm radius platinum electrode; the reference electrode was Ag/AgCl. The solution was not degassed.

3.5.2 Iron(III) perchlorate

The SWV voltammogram of 0.015 M of iron(III) in perchlorate media is shown in figure 3.10. Three reduction peaks were observed on the voltammogram at about 0.748, 0.20 and -0.180 V, respectively. The most positive peak labelled (i) at about 0.748 V corresponds to reduction of hexaqueous of iron(III) (Fe^{3+}), because it is near to standard reduction potential of redox couple of (Fe^{3+}/Fe^{2+} at SHE) according to the following equation:

$$Fe(H_2O)_6^{3+} + e^- \rightleftharpoons Fe(H_2O)_6^{2+} \qquad \text{.....(3.16)}$$

However, such peak may also be ascribed to the reduction of both Fe^{3+} and $FeOH^{2+}$ as a single peak, because proton transfer to the oxygen of coordinated water is extremely fast in comparison with the time scale of SWV. Therefore, both species Fe^{3+} and $FeOH^{2+}$ are

in rapid equilibrium with each other, and they appear as one reduction peak in a SWV voltammogram [144].

In respect to the other two peaks at 0.20 and -0.180 V labelled (ii) and (iii) on the SWV voltammogram in figure 3.10; they correspond to the reduction peak of soluble oligomers of iron(III), and to reduction of H^+ respectively, as explained in the previous section (3.5.1).

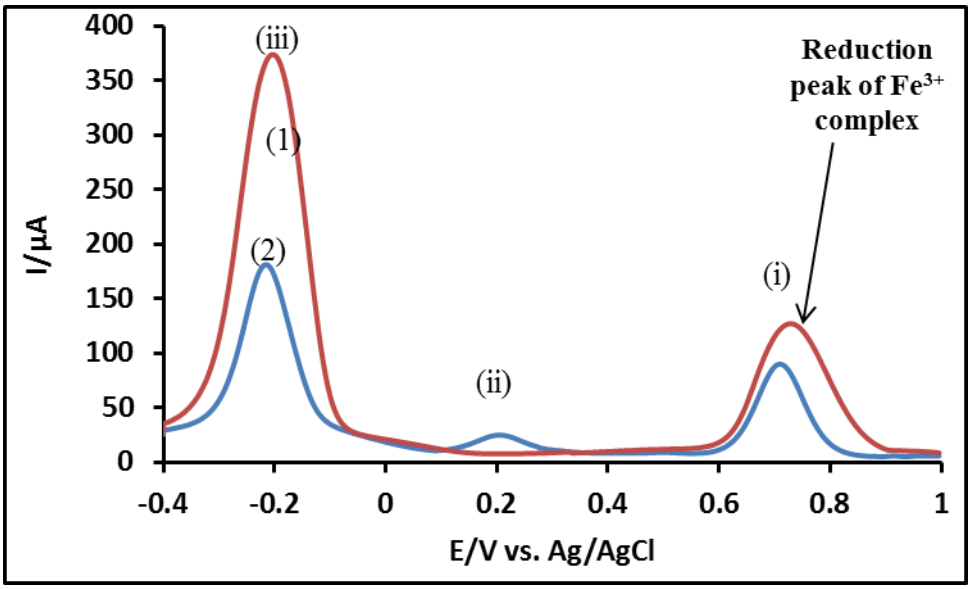

Figure 3.10: Square wave voltammogram of 0.015M of $Fe(ClO_4)_3.xH_2O$ in 0.2 M of $NaClO_4$, (1) without NaOH, (2) with NaOH ratio 1.5, (initial E = 1.0 V, low E = - 0.4 V, amplitude = 0.025 V, frequency = 15 Hz, sample interval 0.004 V, quiet time = 2.0 s and sensitivity = 1.0×10^{-5} A/V). The working electrode was a 1 mm radius platinum electrode and the reference electrode was Ag/AgCl. The solution was not degassed.

3.5.3 Environmental sample (Shilbottle site)

The chemistry of mine water is highly complex; it includes extensive hydrolysis reactions, oxidation-reduction reactions and solid-solution equilibria, as well as some biological processes. Accordingly, the qualitative characterization of mine water solutions using voltammetry is not easy to accomplish. However, simple SWV voltammograms obtained in this work for soluble redox species in mine water from Shilbottle samples are illustrated in figure 3.11.

There are three reduction peaks on the voltammogram (2), such peaks can be characterized in analogous manner to section 3.5.1. Because Shilbottle solutions contain a considerable amount of soluble species of iron and sulfate, therefore the most positive peak labelled (i) at about 0.660 V can be ascribed to one-electron reduction of $FeSO_4^+$,

it is shifted to negative potential by about 112 mV relative to $[Fe(H_2O)_6]^{3+}$ in weakly coordinating media e.g. iron(III) perchlorate solution. According to Nernst equation (3.14), the peak is expected to shift by about 143 mV according to the formation constant of $FeSO_4^+$ K_1. The exact shift, in turns, depends on numerous parameters e.g. temperature, sulfate concentrations and ionic strength. However, the observed shift is clearly closer to the expected for $FeSO_4^+$ than $Fe(SO_4)_2^-$.

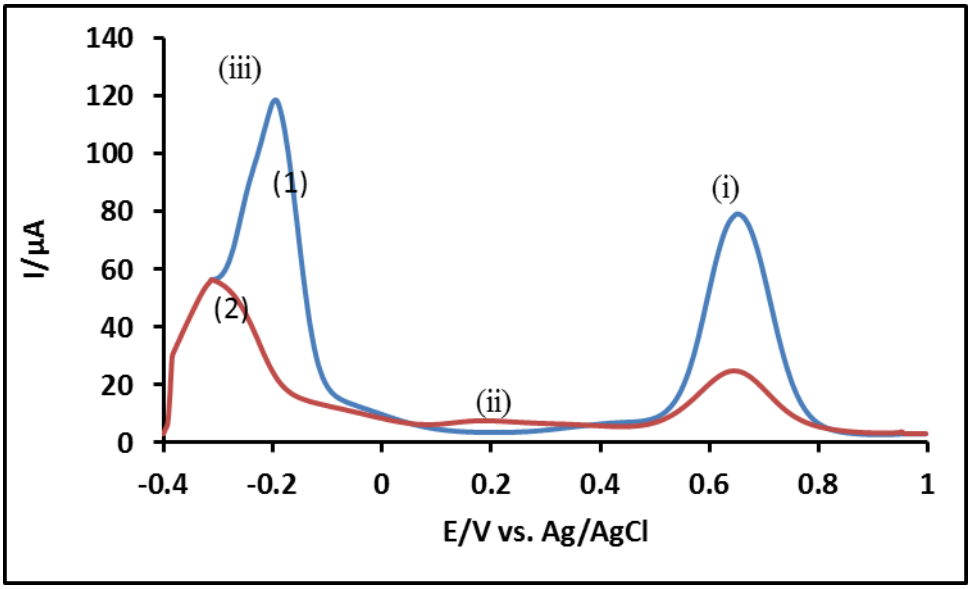

Figure 3.11: Square wave voltammogram of Shilbottle sample (settlement lagoons) in which the concentration of soluble iron(III) species is about 0.004M, (1) without NaOH, (2) with NaOH ratio 1.5, (initial E = 1.0 V, low E = - 0.4 V, amplitude = 0.025 V, frequency = 15 Hz, sample interval 0.004 V, quiet time = 2.0 s and sensitivity = 1.0×10^{-5} A/V), the working electrode was 1 mm platinum electrode; the reference electrode was Ag/AgCl. The solution was not degassed.

In respect to other two peaks labelled (ii) and (iii) at about 0.20 and -0.180 V, there are analogous to the peaks that have been characterized in sections (3.5.1 and 3.5.2). Such peaks were ascribed to reduction of oligomer of soluble iron(III) and H^+, respectively. Although, peak (iii) seems to be asymmetrical and also it is not entirely identical, this may due to adsorption of organic compounds and other material on the electrode surface.

3.6 Spectroscopic characterization

Two different spectroscopic techniques were used to characterize both environmental and standard laboratory solutions. They are Raman spectroscopy and electrospray ionization mass spectroscopy (ESI-MS). Also diffraction technique X-ray diffraction (XRD) was used.

3.7 Raman spectroscopy characterization

Raman spectroscopy was used to characterize the speciation of iron(III) in sulfate and perchlorate media, and also for AMD samples. In this section an appropriate amount of sample solution was evaporated and dried on a glass coverslip, then it was analysed as a solid residual on the coverslip. Characterization of iron(III) complexes by means of Raman spectroscopy is based on the determination of molecular vibration modes. An informative spectrum can be rapidly obtained. Raman measurements do not require chemical or digestion pre-preparation of the samples prior to Raman spectrum acquisition; therefore it can be considered as a powerful technique for environmental samples such as AMD [72].

3.7.1 Iron(III) sulfate

Raman spectra of dried aqueous solutions of dissolved 0.03 M of $Fe_2(SO_4)_3.5H_2O$ in 0.2 M of Na_2SO_4 were analysed between 150 and 1500 cm^{-1}. The main bands in Raman spectra of such sample are attributed to the vibration modes of tetrahedral SO_4^{2-} in Fe-sulfate, also to two other bands which can be attributed to metal oxygen stretching vibrations. It has been pointed out that, the four bands of SO_4^{2-} tetrahedral exhibit symmetric stretching (v_1) and bending (v_2) modes, and asymmetric stretching (v_3) and bending (v_4) modes at 983, 450, 1150 and 611 cm^{-1}, respectively figure 3.12 [152, 153].

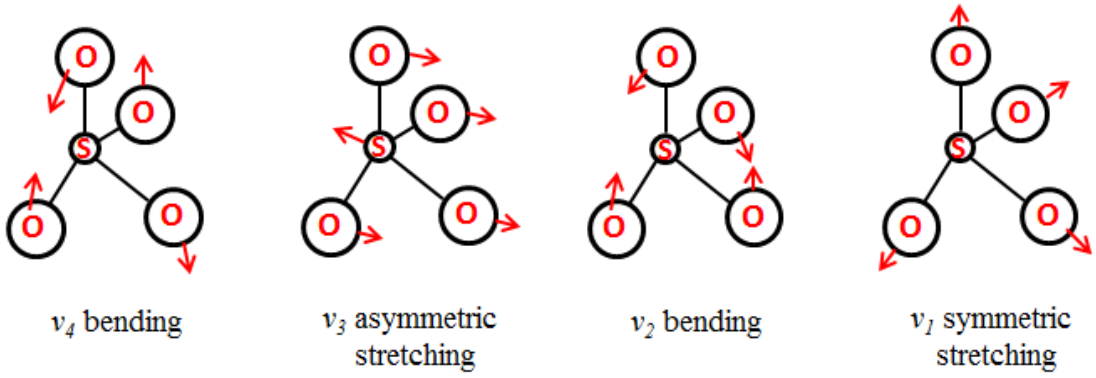

Figure 3.12: Four normal modes of tetrahedral molecules such as SO_4^{2-}, modes *v*1 and *v*2 are only Raman active, while modes *v*3 and *v*4 are both IR and Raman active.

The symmetric vibration bands exhibit a higher intensity than asymmetric bands. In Figure 3.13, the bands at 989 and 1089 cm^{-1} correspond to the v_1 and v_3 symmetric and asymmetric stretching modes of sulfate, respectively [153]. Iron(III) sulfate exhibits a strong peak near 990 cm^{-1}, which makes this region useful for identification of iron(III)

sulfate from mixed spectra [152]. While the broad band with two small centres at 578 and 620 cm^{-1} belongs to asymmetric bending v_4 SO_4^{2-} modes; such band splitting indicates that a reduction of the symmetry of the sulfate anions may occur [154]. The band centred at 450 cm^{-1} can be assigned to symmetric bending v_2 SO_4^{2-} modes [154].

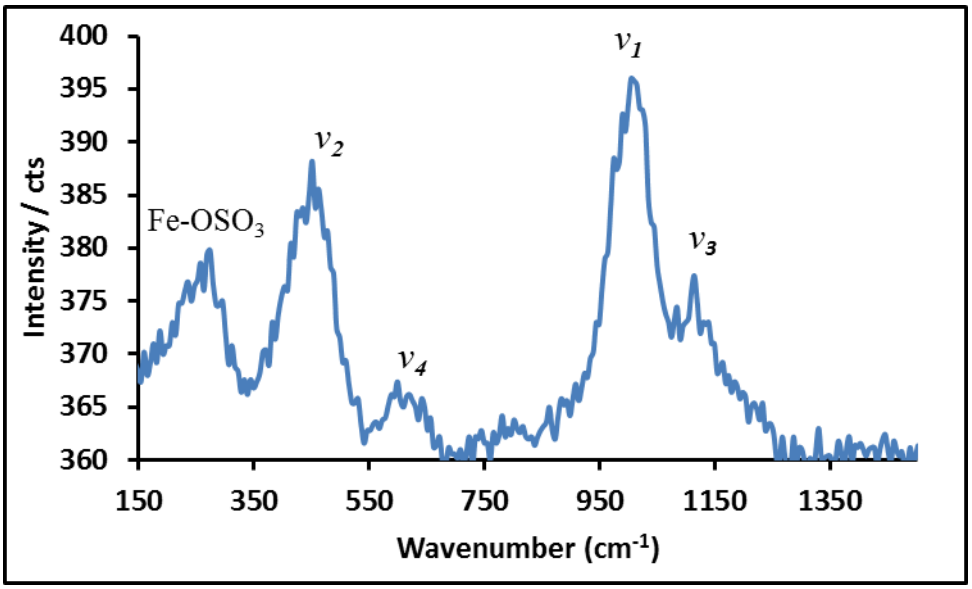

Figure 3.13: Raman spectrum of a dried aqueous solution of dissolved 0.03 M of $Fe_2(SO_4)_3.5H_2O$ in 0.2 M of Na_2SO_4, an integration time 30 s and excitation wavelength λ_{exc} = 488 nm.

When coordinated ligands like sulfate are present in the solution, marked difference may occur in the Raman spectrum, due to replacement of water molecules by sulfate ligands in inner sphere coordination. Accordingly, a vibration band may appear at low wavelength (200 to 300 cm^{-1}) such that observed at 247 cm^{-1} on figure 3.13 can be ascribed to Fe-OSO_3 vibrations [155]. Such a band was not observed in iron(III) with perchlorate where the metal-ligand interaction is very weak (section 3.7.2).

3.7.2 Iron(III) perchlorate

Raman spectra of dried aqueous solutions of dissolved 0.03 M of $Fe(ClO_4)_3.xH_2O$ in 0.2 M of $NaClO_4$ were taken between 150 and 1500 cm^{-1}. The spectrum exhibits a marked similarity with the spectrum of iron(III) sulfate; such analogous properties can be attributed to the similarity of vibration modes for ClO_4^- and SO_4^{2-}, both of which exhibit fundamental tetrahedral vibration modes in Raman region figure 3.12. Accordingly in figure 3.14, the v_1 at 929 cm^{-1} is symmetric stretching mode of ClO_4^-. While v_3 was broad peak centred at 1080 cm^{-1}, such peak is ascribed to the asymmetric stretching modes of ClO_4^-. Also the v_4 and v_2 at 604 and 477 cm^{-1} are assigned to asymmetric and

symmetric bending modes of ClO_4^-, respectively [156]. The band near 435 cm^{-1} can be assigned to Fe-O stretching mode in hexa-aqua complex $[M(H_2O)_6]^{n+}$ [157, 158], this peak was not observed in iron(III)-sulfate which may be incorporated with symmetric bending modes of SO_4^{2-} (v_2). No band was observed in the wavenumber range (200 – 300 cm^{-1}) as observed in iron(III) sulfate solution. This is because the iron(III)-perchlorate bond is weak compared with iron(III)-sulfate.

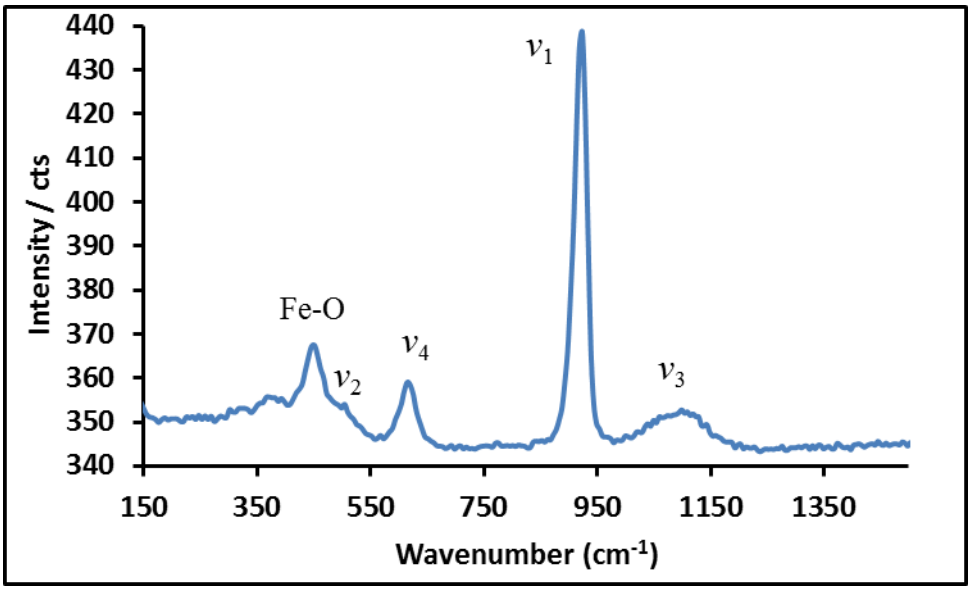

Figure 3.14: Raman spectrum of a dried aqueous solution of dissolved 0.03 M of $Fe(ClO_4)_3.xH_2O$ in 0.2 M of $NaClO_4$, an integration time 30 sec and excitation wavelength (λ_{exc}) = 488 nm.

3.7.3 Raman spectra of environmental solution (Shilbottle site)

It has been reported that Shilbottle solution comprises of high amount of sulfate and iron [21], therefore most Raman spectra bands were identical to vibration of sulfate. Figure 3.15 shows a Raman spectrum of environmental solution. It is clear that the spectrum seems to be rather complicated compared to the standard laboratory samples of iron(III) sulfate with a broad feature at low wavenumber that may represent many overlapping bands. However, it is possible to distinguish several bands belonging to vibrations of SO_4^{2-} and the stretching mode Fe-O. The two peaks assigned at 921 and 1007 correspond to the v_1 symmetric stretching modes of sulfate and bisulfate. The implication of the multiple bands of the v_1 mode is that, the sulfate units are not equivalent in the sample structure (AMD) [154]. The differences in the wavenumbers of the bands are ascribed to size polarity of the cations which may incorporate with acid mine minerals [154].

Also peaks assigned at 1086 and 1136 cm^{-1} can be attributed to the v_3 asymmetric stretching modes of sulfate. Such multiple asymmetric bands imply that the symmetry of sulfate anions in acid mine water structure is reduced form T_d to C_{2v}. There are two peaks observed of low-intensity at 806 and 768 cm^{-1}, such peaks can be attributed to water librational mode and FeOH deformation vibration, respectively [154]. The symmetric bending v_4 SO_4^{2-} mode is assigned at 610 cm^{-1}, while it is hard to differentiate the symmetric bending v_2 SO_4^{2-} modes in the wavelength range between 400 and 500 cm^{-1}, this may be due to incorporating with other peaks such as Fe-O stretching mode in hexa-aqua complex at 435 cm^{-1}.

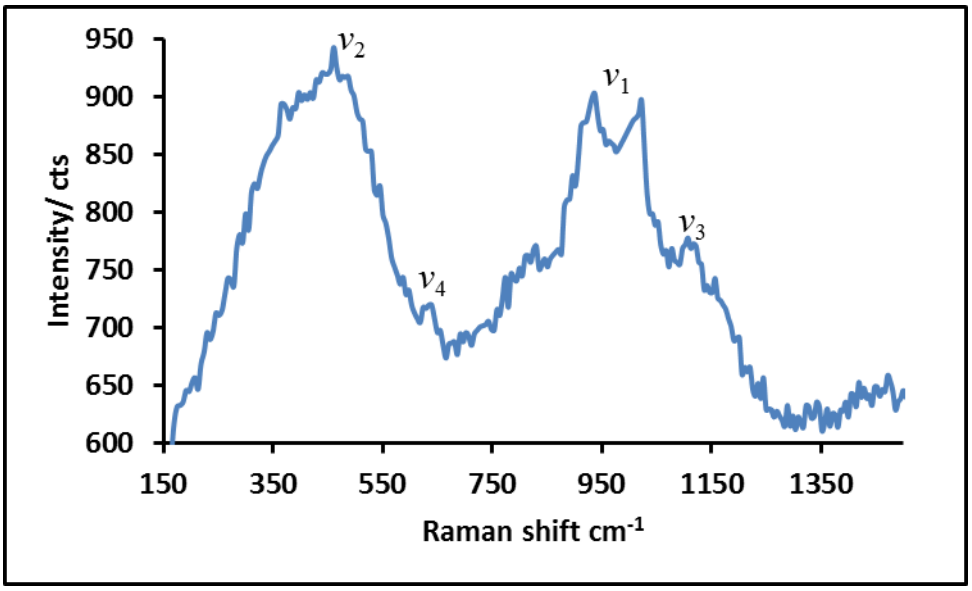

Figure 3.15: Raman spectrum of dried aqueous solution of Shilbottle site (settlement lagoons), an integration time = 30 sec and the excitation wavelength λ_{exc} = 488 nm.

3.8 Mass spectroscopy studies

Electrospray ionization mass spectroscopy ESI-MS was used to attempt to identify the hydrolysis products of iron(III) sulfate and perchlorate, and also AMD solutions. It is an effective technique to explore the chemistry of iron speciation in aqueous solution. In this study, we did not intend to characterize the exact structure of iron(III) species in such solutions, because the composition of AMD solutions is too complex. However, our aim was to investigate and prove the formation of iron(III) dimers, trimers or tetramers in perchlorate media or to detect any iron(III) species in sulfate media and AMD solutions. Therefore, aqueous iron(III) with sulfate and perchlorate ligands was studied, and also AMD solutions using ESI-MS.

3.8.1 Mass spectroscopy of aqueous iron(III) perchlorate solution

Figure 3.16 shows the mass spectrum of 10^{-4} M of iron(III) perchlorate in aqueous solution (preparation and dilution procedures were described in section 2.6.4). It shows a considerable number of clusters in positive ion mode at different values of *m/z* ranged between 450 and 1800. In this solution, the main elements are Fe, Cl, O, H, Na. Masslynx NT software (version 4.1) was used to study the isotopic distribution pattern of these elements. The significant isotopes of iron are ^{54}Fe, ^{56}Fe and ^{57}Fe and their abundances are 5.82, 91.66 and 2.19%, respectively. For chloride the more abundant isotopes are ^{35}Cl and ^{37}Cl with natural abundances of 75.87 and 24.22%, respectively. ^{23}Na, ^{16}O and ^{1}H possess only one significant isotope, because of the low abundance of the other isotopes compared with the main isotope.

Analysing such clusters via their isotopic distribution patterns enabled us to determine the peaks number which are due to formation of monomers, dimers, trimers or tetramers species of iron(III). For example the signals assigned at *m/z* 1486, 1488, 1489, 1490, 1491, 1492, 1493, 1494, 1495, 1496 and 1498 are ascribed to tetramer iron(III) species; this can be affirmed by comparing both simulated and recorded spectra on the spectrum in figure 3.16.

Also signals assigned mainly at 634, 1224, 1246 and 1614 were identified as monomer, dimer, trimer and tetramer iron(III) complexes, respectively. It is noted that each cluster increments the former one by an *m/z* value of about 122 which is the molecular weight of $NaClO_4$, this means that the sodium perchlorate is clustered around iron atoms in either coordinated or non-coordinated manner. However, several peaks can be assigned only for sodium perchlorate and water fragments without iron(III) species.

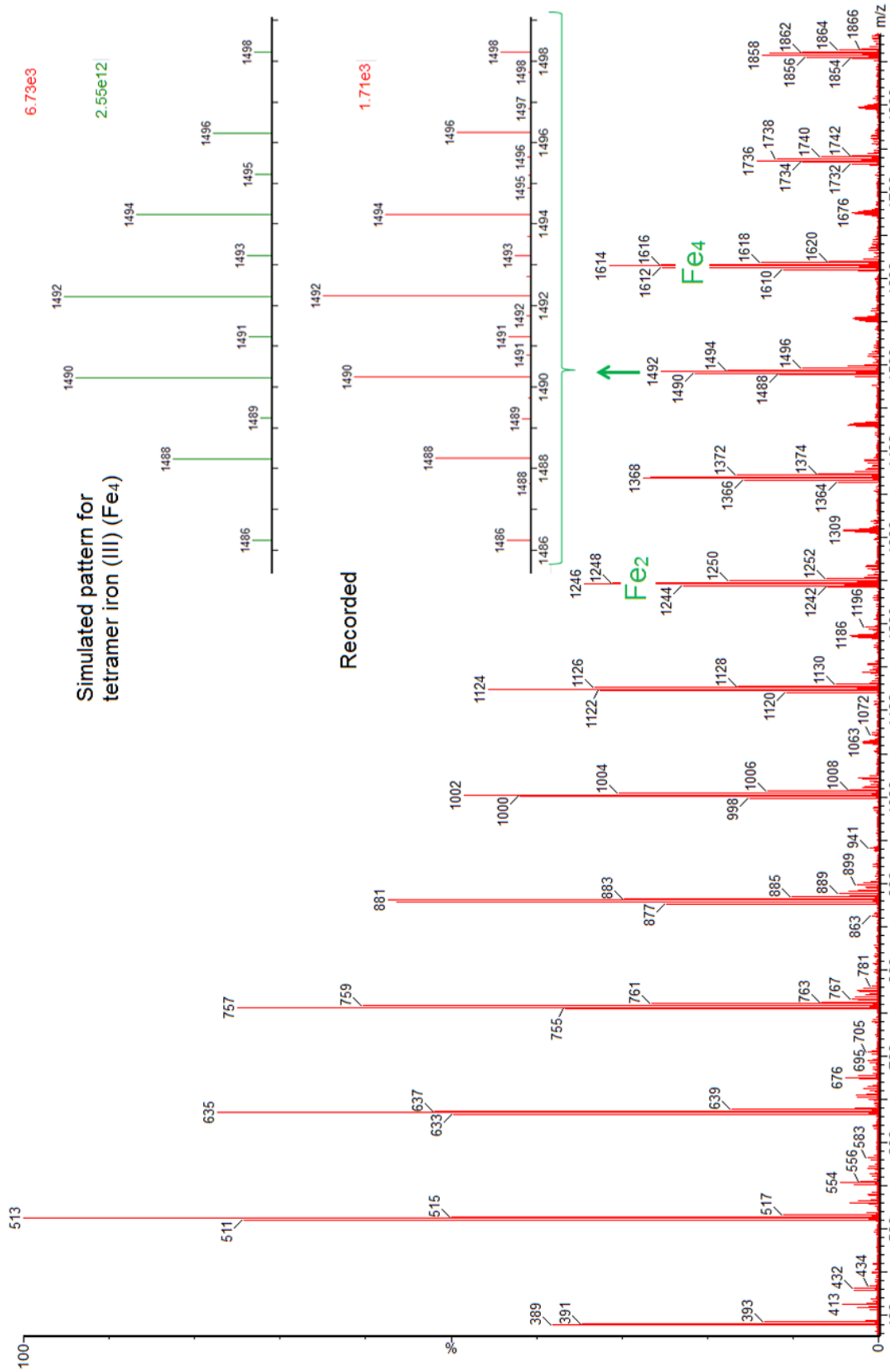

Figure 3.16: Mass spectrum (positive ion mode) of 10^{-4} M of $Fe(ClO_4)_3.xH_2O$.

3.8.2 Mass spectroscopy of aqueous iron(III) sulfate solution

The mass spectrum of 10^{-4} M of iron(III) sulfate (preparation and dilution procedures were described in section 2.6.4) is depicted in figure 3.17. The spectrum was analysed for its isotopic distribution pattern using Masslynx NT software (version 4.1) in positive ion mode at m/z range between 100 – 1000, after this range no signals were observed. Sulfur (S) has three significant isotopes patterns ^{32}S, ^{33}S and ^{34}S with natural abundances of 95.02%, 0.75% and 4.21%, respectively. Also isotope patterns of other elements involved in this solution such as Fe, Na, O and H were considered. Most signals were attributed to fragments of Na_2SO_4.

This can be observed by the step in m/z value of 142 which is the molecular weight of sodium sulfate, as well as fragments of S and H_2O.

No signals have been detected for either $FeSO_4^+$ or for any iron(III) complexes. A possible explanation for that is the formation of neutral iron(III) sulfate complexes such as $Fe(OH)SO_4$, $Fe_2O(SO_4)_2$, $Fe_3(SO_4)_2(OH)_5.2H_2O$ and $Fe_4(SO_4)(OH)_{10}$ in presence of sulfate [112, 159] and ESI-MS is unable to measure neutral species.

A simple example is the equilibrium:

$$[Fe(H_2O)_5SO_4]^+ \overset{K_a}{\rightleftharpoons} [Fe(H_2O)_4(OH)SO_4] + H^+ \qquad \text{.....(3.17)}$$

$$K_a = \frac{[Fe(H_2O)_4(OH)SO_4][H^+]}{[Fe(H_2O)_5SO_4]^+} \qquad \text{.....(3.18)}$$

Such equilibrium is markedly dependent on the pH and pK_a of the solution. Since the pK_a of this equilibrium has not been experimentally measured, we estimated it theoretically according to the following scheme:

$$FeSO_4^+ \overset{pK_a}{\rightleftharpoons} Fe(OH)SO_4 + H^+$$

$$pK_1 \downarrow\uparrow \qquad\qquad pK_3 1\downarrow$$

$$Fe^{3+} + SO_4^{2-} \overset{pK_2}{\rightleftharpoons} Fe(OH)^{2+} + SO_4^{2-} + H^+$$

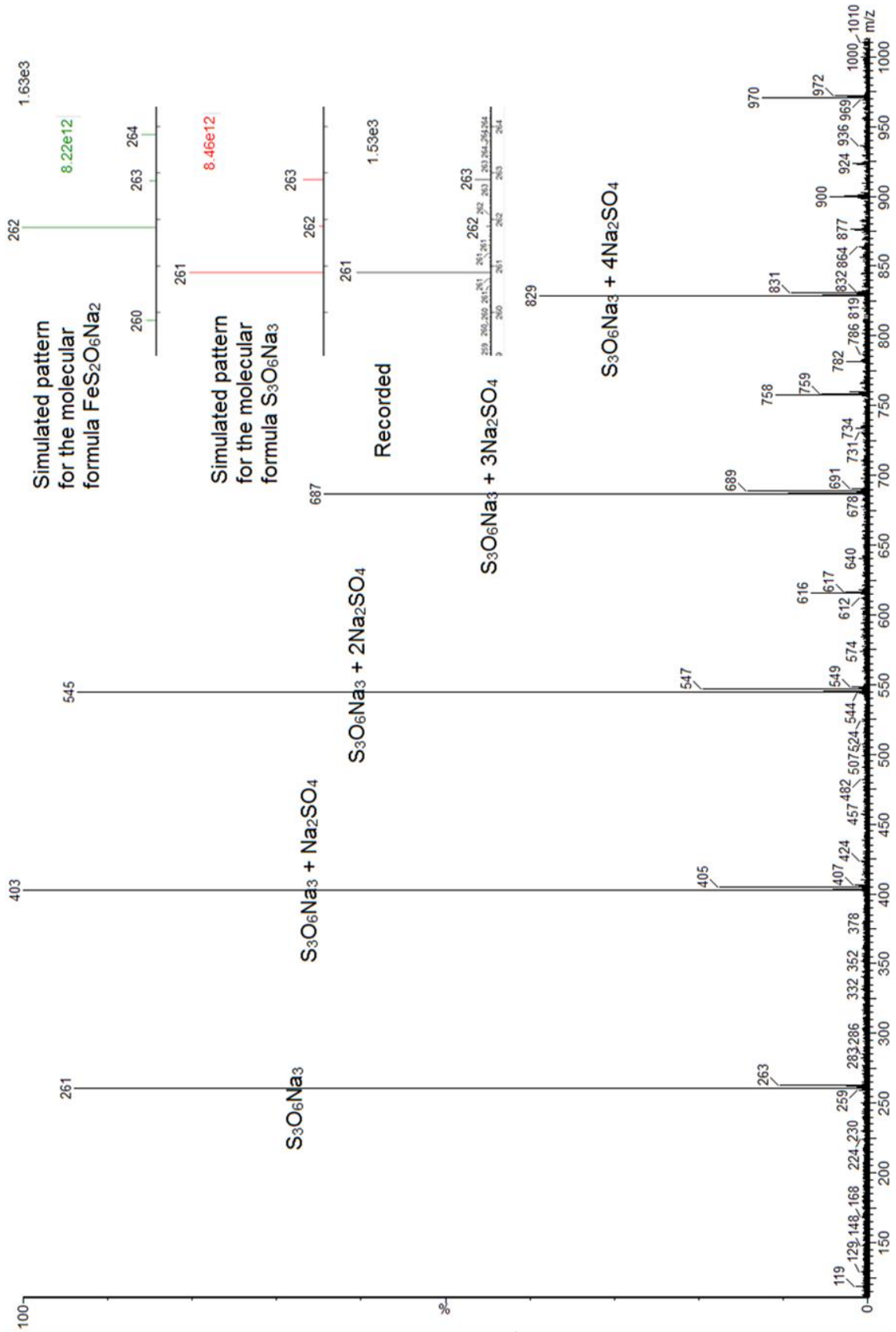

Figure 3.17: Mass spectrum (positive ion mode) of 10^{-4} M of $Fe_2(SO_4)_3.5H_2O$

Thermodynamic constants (using activity coefficient) pK_1, pK_2 and pK_3 have been previously potentiometrically measured with theoretical estimates of the activity coefficient at ionic strength 1.0 M, 1.0 M and 3.0 M and their values are 4.04 ± 0.10, 2.77 ± 0.03 and 2.56 ± 0.08, respectively [65, 109, 160, 161]. Also, pK_3 was estimated by comparison with other metal-hydroxide complexes at zero added ionic strength [65] and its value is 2.30. Therefore, pK_3 is calculated to be the average of these two values with uncertainty equal to 2.43 ± 0.13 and the p*K*a value has been estimated in this work according to the above scheme:

$$pK_a = pK_1 + pK_2 - pK_3$$

$$= 4.04 \pm 0.10 + 2.77 \pm 0.03 - 2.43 \pm 0.13 = 4.38 \pm 0.16$$

Accordingly, in the case of pH > pK_a by a value of 1.0, then the ratio of concentration of the $Fe(OH)SO_4$ complex to the concentration of $FeSO_4^+$ increases by factor of 10, and vice versa. Due to the required sample concentration for ESI-MS analysis being limited to about 10^{-4} M or less, then the pH of such aqueous solution exceeds 4.0. In this case, we suspect that the most dominant species may be $Fe(OH)SO_4$ which can not be detected by ESI- MS. Whereas in Shilbottle sites the $FeSO_4^+$ (where the pH in such sites is about 3.5 which is less than pK_a) can be the dominant species. For these reasons, we could not detect any signals related to iron in the spectrum of iron(III) aqueous solutions containing sulfate. All the signals which can be seen in the spectrum can be attributed to clusters of sulfate ions with sodium ions and water, and also the fragments of such clusters.

3.8.3 Mass spectroscopy of environmental solution (Shilbottle site)

As shown in figure (3.18), the mass spectrum of diluted acid mine water solution is very complicated (dilution procedures were described in section 2.6.4), therefore analysing such a spectrum using ESI-MS is an ambitious goal, because the AMD is a mixture of metallic, non-metallic elements and organic compounds. However, again no signals related to iron were detected in this spectrum; this can be attributed to presence of high concentrations of sulfate which in turn form neutral complexes with iron(III) as discussed in section (3.8.2). The only detected signals at *m/z* 545, 546, 547, 548 and 549 were ascribed to clusters of sulfate, such cluster may be incorporated with several elements in which isotopic distribution pattern is inactive such as Na, Mn, Al, O, H and C.

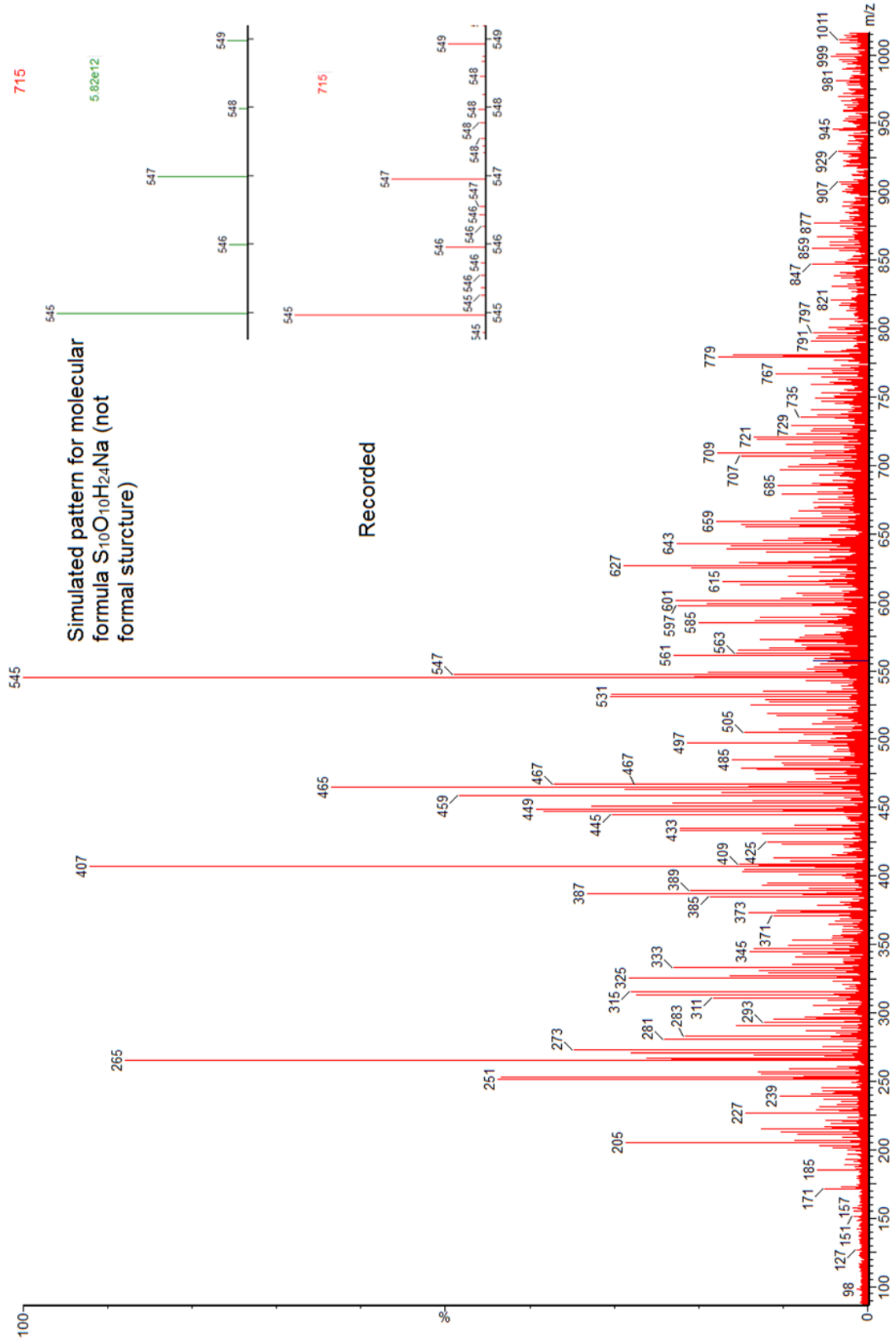

Figure 3.18: Mass spectrum (positive ion mode) of diluted solution (5%) of Shilbottle site (settlement lagoons).

The meaning of inactive isotopic distribution is that the natural abundance of some isotopes is very low compared to the main isotope, therefore such isotopes can be ignored, for example oxygen has three isotopes O^{16}, O^{17} and O^{18}, their abundances are 99.76, 0.04 and 0.20 %, respectively. Hence isotopic distribution of O^{17} and O^{18} can be ignored when compared with O^{16}, because they are not significant in isotopic distribution pattern. Accordingly, the elements of Na, Mn, Al, O, H and C have no effects on the isotopic distribution pattern, because they have only one significant isotope. Such elements are supposed to be incorporated with sulfate cluster in AMD spectrum. Also there are numerous patterns in the spectrum that can not be interpreted; these may be related to metals such as Ca, Mg, K and Zn which are present in such samples as shown by ICP-AES analysis (section 4.6).

3.9 X-Ray diffraction characterization

Diffraction identification studies of solid samples using X-Ray powder methods are based on the fact that an X-Ray diffraction pattern is unique for each crystalline material.

Accordingly, it is necessary for the analyte to be in crystalline form for XRD analysis to obtain useful diffraction data. One of the limitations of the XRD technique is its inability to identify amorphous substances. In this study, solid samples of 0.25 M of iron(III) perchlorate and iron(III) sulfate with NaOH were prepared and analysed by XRD (procedures were described in section 2.6.12).

3.9.1 Iron(III) sulfate

Figure 3.19 depicts XRD patterns of solid sample of 0.25 M iron(III) sulfate with $[OH^-]/[Fe^{3+}]$ ratios of (a) 1.0 and (b) 2.0, respectively. From the figure, it is apparent that only sodium iron sulfate hydroxide hydrate (metasiderontrite $Na_4Fe_2(SO_4)_2(OH)_2.3H_2O$) and iron(III) sulfate hydrate ($Fe_2O_3.2SO_3.5H_2O$ or $2Fe(OH)SO_4$) crystals were identified as basic iron(III) sulfate complex in both ratios. Otherwise no iron(III) compounds were identified as solid crystals in both samples. This is mainly because iron(III) crystals such as goethite (α-FeOOH) and hematite (α-Fe_2O_3) were not formed under our experiment conditions. It has been established that formation of solid phase of amorphous iron(III) hydroxide hydrate (ferrihydride) and its transformation into crystalline compounds (commonly goethite and hematite) depends on pH [162, 163],

temperature [162, 164], nature of anions [99, 111, 165] and aging time [165, 166]. The crystals of iron(III) can be formed at pH above 10 [162, 163] and temperature exceeds 65 ^{o}C [110, 111, 162, 164].

Our experiment temperature was about 20 ± 3 ^{o}C and the pH was (≤ 4) in both cases. Therefore, the probability of formation of iron(III) crystals is low compared with above studies; this was confirmed with XRD results in which XRD peaks for iron(III) crystals were not observed with exception of sodium iron sulfate hydroxide hydrate ($Na_4Fe_2(SO_4)_2(OH)_2.3H_2O$) and iron(III) sulfate hydrate ($Fe_2O_3.2SO_3.5H_2O$ or $2Fe(OH)SO_4$). As well as XRD data identified crystals related to sodium sulfate (Na_2SO_4).

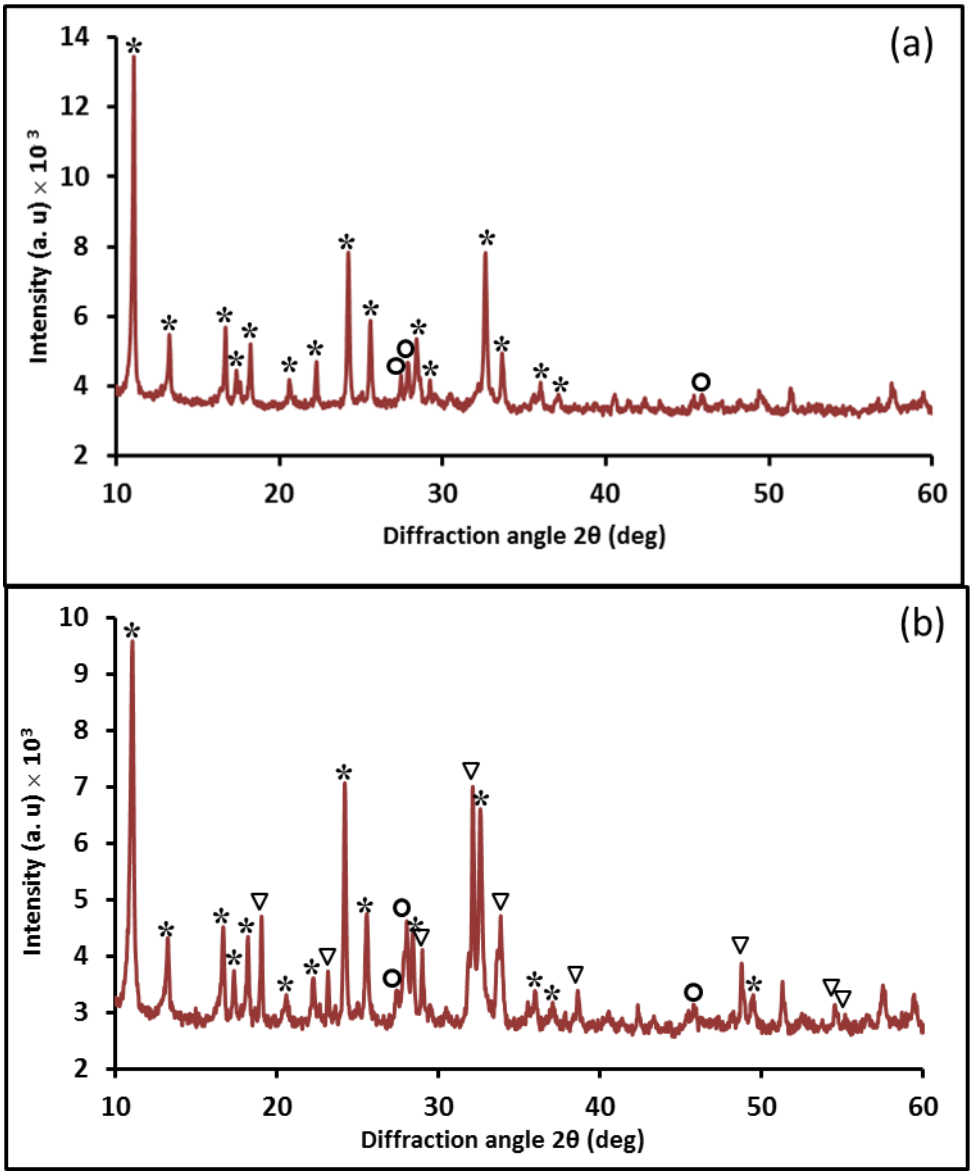

Figure 3.19: XRD patterns of solid phase of 0.25 M $Fe_2(SO_4)_3.5H_2O$ in 0.2 M Na_2SO_4 with $[OH^-]/[Fe^{3+}]$ ratio (a) 1.0 and (b) 2.0. (∗) sodium iron sulfate hydroxide hydrate (O) iron sulfate hydrate $Fe_2O_3.2SO_3.H_2O$ or $2Fe(OH)SO_4$ and (∇) sodium sulfate Na_2SO_4.

The crystalline phase identification of XRD lines for the above crystals were matched from the international centre of diffraction data-powder diffraction file (ICDD-PDF) database and were overlaid to diffraction patterns. XRD peaks are assigned at 2θ values of 10.98, 13.24, 16.37, 16.68, 17.31, 20.64, 22.26, 24.16, 25.50, 28.31, 32.55, 33.60, 35.90 and 37.10, which correspond to 020, 110, 120, 021, 101, 121, 040, 200, 041, 141, 132, 060, 142 and 310 of Miller indices values, respectively. These signals coincided with the reference spectrum for sodium iron sulfate hydroxide hydrate (card number of 00-029-1219). While XRD peaks at 2θ values of 27.33, 27.76 and 49.72, which correspond to Miller indices values of 200, 120 and 040, respectively. These peaks coincided with the reference spectrum for iron(III) sulfate hydroxide $Fe_2O_3.2SO_3.H_2O$ or $2Fe(OH)SO_4$ (card number 00-021-0428). Also, XRD peaks of sodium sulfate (Na_2SO_4) were observed only at $[OH^-]/[Fe^{3+}]$ ratio 2.0 at 2θ values 19.04, 23.15, 28.03, 28.99, 32.12, 38.62, 48.78 and 54.55, which correspond to 111, 220, 131, 040, 311, 222, 351 and 062 of Miller indices values, respectively. These patterns were matched to sodium sulfate (card number 00-024-1132).

3.9.2 Iron(III) perchlorate

Figure 3.20 illustrates XRD patterns of iron(III) perchlorate with $[OH^-]/[Fe^{3+}]$ ratio equal to 2.0. It was obvious that, the observed XRD peaks were only related to crystals of sodium perchlorate ($NaClO_4$) and sodium perchlorate hydrate ($NaClO_4.2H_2O$). While XRD peaks related to crystal phases of iron(III) were not observed due to formation of amorphous phases of iron(III) instead of iron(III) crystal because the above mentioned reasons (preparation conditions e. g. pH and temperature).

XRD peaks assigned at 2θ values of 17.10, 24.38, 25.84, 32.36, 40.89, 53.08 and 53.15, which correspond to -110, 310, -312, -204, 420, 006 and – 606 of Miller indices values, respectively were ascribed to crystals of sodium perchlorate hydrate ($NaClO_4.2H_2O$) [167]. While XRD peaks assigned at 2θ values 22.38, 25.14, 30.17, 37.44 and 47.65, which correspond to 111, 020, 102, 022 and 302 of Miller indices values, respectively were attributed to crystals of sodium perchlorate ($NaClO_4$) [168]. The crystalline phase identification was carried out with aid of ICDD-PDF. As the former patterns are matched with sodium perchlorate hydrate $NaClO_4.2H_2O$ (card number of 00-031-1287), the second patterns are matched to sodium perchlorate $NaClO_4$ (card number of 00-008-

0494). The reason for choosing such experiment conditions in this work is to be similar to the conditions of kinetics studies which were carried out using Raman spectroscopy.

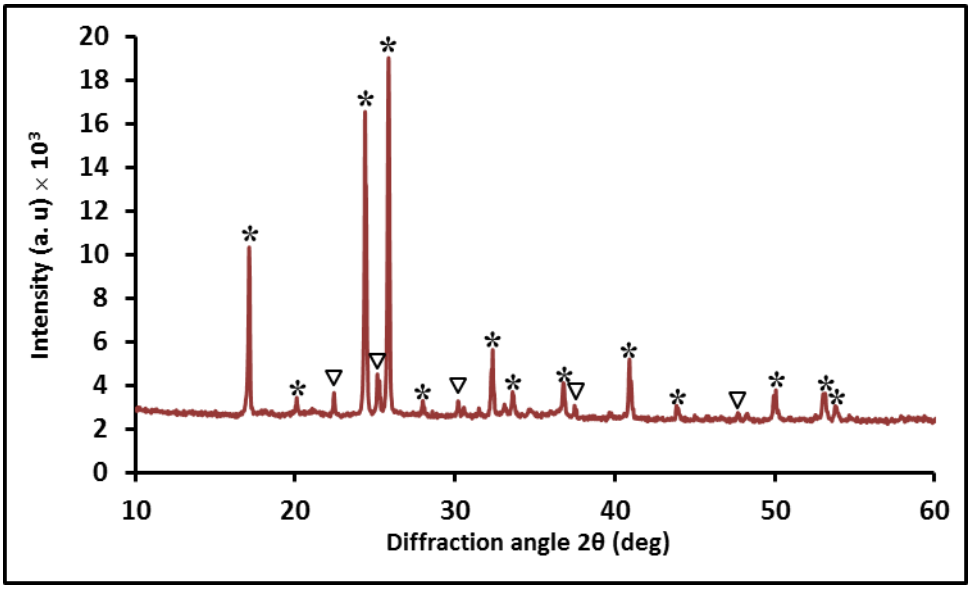

Figure 3.20: XRD patterns of solid phase of 0.25 M $Fe(ClO_4)_3.xH_2O$ in 0.2 M $NaClO_4$ with $[OH^-]/[Fe^{3+}]$ ratio of (2.0). (∗) sodium perchlorate hydrate $NaClO_4.H_2O$ and (∇) sodium perchlorate $NaClO_4$.

It can be concluded from this chapter that, the laboratory solutions of iron(III) perchlorate, iron(III) sulfate and environmental Shilbottle solutions exhibit simple one-electron reduction quasi-reversible characteristic under the experimental conditions. However, the rate of electron transfer in electrode-solution interface was slightly faster in the case of iron(III) perchlorate solution over the other two solutions. Also, Shilbottle solutions showed simple one-electron reduction quasi-reversible behaviour, but with some unexpected variations such as I_p^A/I_p^C ratios exceeding 1.0, the ratio varied between 1.29 and 1.45, and the current was non-zero at the beginning of the scan which indicate that there is substantial iron(II) present in these solutions.

A reduction peaks for simple soluble, oligomer soluble species of iron and hydrogen ions were observed in both laboratory and Shilbottle solutions using SWV. Raman spectra showed similar vibration in respect to sulfate modes between Shilbottle and standard iron(III)-sulfate samples. However, the Raman spectrum of Shilbottle samples was slightly complicated. While in perchlorate media these vibrations were assigned to vibration modes of perchlorate.

Further, ESI-MS spectra did not show any signals related to soluble simple species of iron and sulfate [e. g. $FeSO_4^+$, $FeH(SO_4)^{2+}$ and $Fe(SO_4)_2^-$] in Shilbottle solutions and

standard iron(III)-sulfate, this was ascribed to formation of neutral species at pH ≥ 4, while MS spectra of iron(III) perchlorate solution detected signals related to charged monomers, dimers, trimers and tetramers of iron(III). XRD data exhibit crystals only for iron(III) basic sulfate complexes, Na_2SO_4 and $NaClO_4$ in two laboratory samples (iron(III)-sulfate and iron(III) perchlorate, respectively).

Chapter 4: Electrochemical and spectroscopic techniques for measuring elemental concentrations in acid mine drainages (AMD)

4.1 Introduction

It has been established in several studies that AMD in the north east of England contains high concentrations of SO_4^{2-}, Fe, Ca, Mn, and Al, and lower concentrations of other metals such as Ni, Zn, Cd and Cu depending on the mine rock composition [21, 23]. The concentrations of such elements were measured using inductively coupled plasma optical emission spectroscopy ICP-AES. Iron and sulfate are the main components in such waters due to oxidation of pyrite (FeS_2) to produce soluble iron species and sulfate.

Several techniques and methods have been used for determination of iron in aqueous solutions, for example flame atomic absorption spectroscopy (AAS) [169], graphite furnace atomic absorption spectrometry (GFAAS) [170], electrothermal atomization atomic absorption spectrometry (ETAAS) [171], inductively coupled plasma mass spectroscopy (ICP-MS) [172] and total reflection X-ray fluorescence (TRXF) [173]. All these techniques can only measure total iron concentrations from which insufficient information about mobility and bio-availability of soluble iron can be provided.

Although some electroanalytical techniques (e.g. anodic stripping voltammetry (ASV), cathodic stripping voltammetry (CSV) and adsorptive stripping voltammetry (AdSV)) can be used to measure both total concentration and dissolved speciation of iron. However, such techniques often do not differentiate between Fe(III) and Fe(II); the only method which has been widely used for such purpose is based on colorimetric measurements by using complexation agents [170, 174]. For example 5-sulfosalicylic acid dehydrate forms a red ferric-sulfosalicylate complex at low pH, and with increasing pH by adding ammonia it forms yellow colour with total iron in the solution [174]. This method may not have high precision due to the sensibility to the interferences with other transition metals especially in complicated samples such as mine water.

On the other hand, the SO_4^{2-} concentration has been widely determined using various direct and indirect methods (e.g. colorimetric [175], gravimetric [176], inductively coupled plasma atomic emission spectrophotometry (ICP-AES) [177], turbidimetric [178] and ion chromatography (IC) [179]. The colorimetric and gravimetric methods are

not widely used because they require special skills and are time consuming. Also ICP-AES is rarely used for SO_4^{2-} analysis because it depends on the assumption that formation of non-sulfate sulfur species (sulfides and sulfites) is negligible. The turbidimetric and ion chromatography techniques are widely used in determining sulfate concentration in many fields. However, these methods are fairly time consuming as they require a sample pre-preparation process to improve their accuracy and precision, for example to improve the stability of $BaSO_4$ in turbidimetric analysis different ligands have to be added. Also they require low sulfate concentration to be measured (limited range).

For these reasons, we developed electrochemical methods for determination of soluble iron species and soluble sulfate in AMD using voltammetry by which we may attempt to facilitate determination of soluble iron and sulfate with high accuracy, because this method is not affected by the same interferences in such complicated environmental samples as the methods mentioned above. We also determined the concentrations of Fe(II) and Fe (III) in the dissolved fraction of AMD using a simple ultramicroelectrode technique. We performed extra measurements such as Eh, $[H^+]$ and $[Cl^-]$ in AMD using a potentiometric method, and estimated the oxidation-reduction potential of AMD solutions (Eh) using voltammetric and potententiometric methods. The obtained results were inserted into geochemical models; the purpose of which is to compare the predicted Fe species in AMD using thermodynamic models with voltammetric measurements. Finally, we determined concentrations of some elements such Fe, Mg, Ca, K, Mn, Al, Na, Cu, Pb, Sn, As, Hg, Zn, P and S using ICP-AES.

4.2 Results and discussion

4.3 Electrochemical techniques

Two kinds of electrochemical techniques were used, voltammetry and potentiometry.

4.4 Voltammetric studies

SWV was used to determine total soluble species of iron, soluble sulfate and oxidation-reduction potential of AMD solutions, while steady state voltammetry was used to quantify the ratio between Fe(II) and Fe(III) fractions.

4.4.1 Determination of soluble iron species in acid mine drainages using SWV

The concentrations of soluble species of Fe(III) in Shilbottle samples were electrochemically estimated by a standard addition method using square wave voltammetry technique SWV; due to the complexity of the samples, the standard addition method is preferred. Different volumes of solutions containing known concentrations of Fe(III) (2.0, 4.0, 6.0 and 8.0 mM) were added to the same volumes of unknown samples. Therefore, the cathodic peak current (I_p^C) of soluble Fe(III) species increases with increasing amounts of [Fe^{3+}] in solution (figure 4.1). Plotting cathodic peak current versus standard added concentration of Fe(III) is illustrated in (Fig. 4.2).

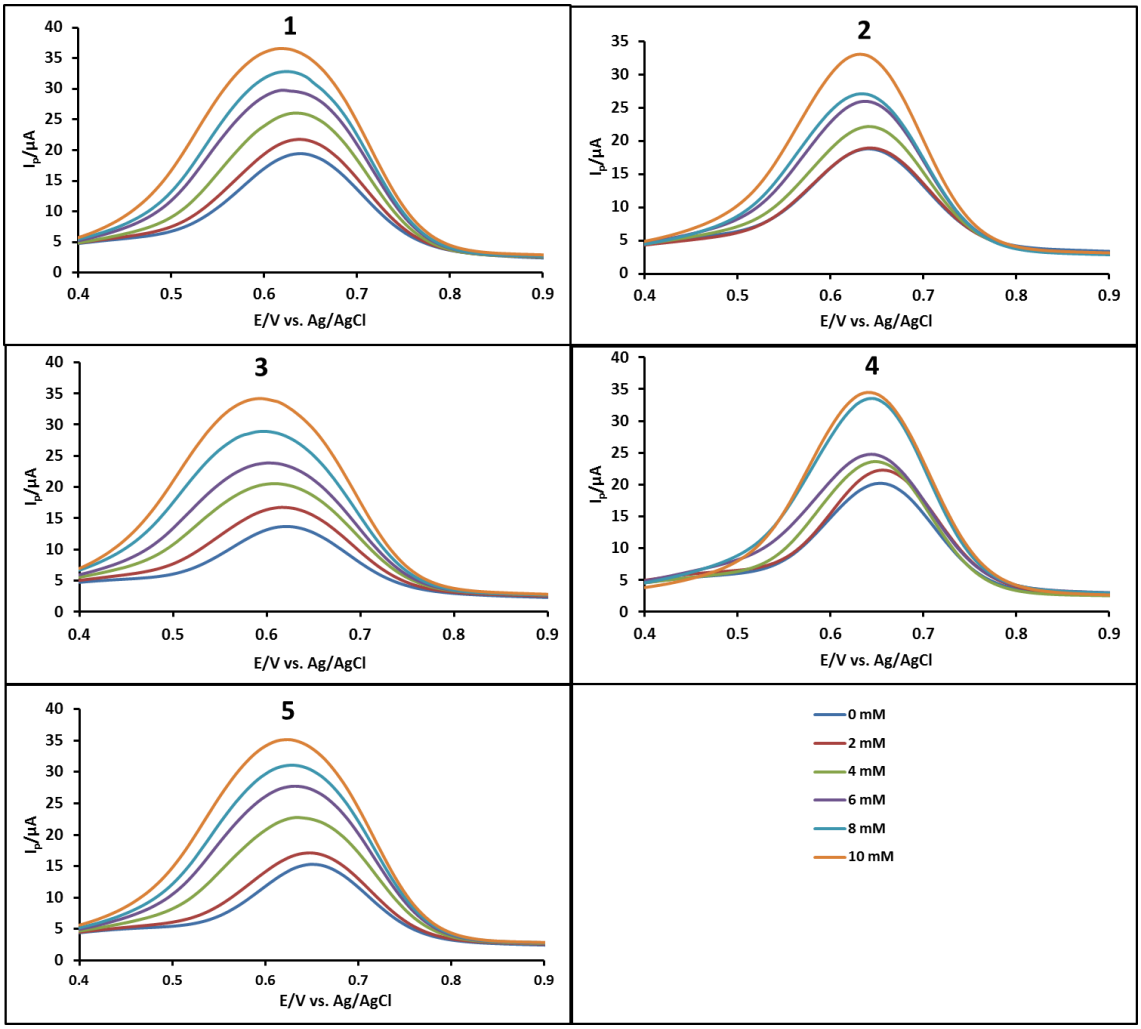

Figure 4.1: The reduction peak current of iron vs. standard iron concentration in environmental samples using SWV, (1) upper stream (2) lagoon 01, (3) lagoon 02, (4) lagoon 03A and (4) lagoon 03B. (Initial E = 0.9 V, low E = 0.4 V, amplitude = 0.025 V, frequency = 15 Hz, sample interval 0.004 V, quiet time = 2.0 s and sensitivity = 1.0×10^{-5} A/V), the working electrode was 1 mm of platinum; the reference electrode was Ag/AgCl. The solution was not degassed.

Linear regression of the calibration line with uncertainty measurements was performed, and the parameters of a simple linear regression model were obtained (equation 4.1).

$$Y = (m \pm \Delta m)X + (b \pm \Delta b) \quad \ldots\ldots\ldots\ldots\ldots\ldots\ldots\ldots (4.1)$$

Where (m) is the slope, (b) is the y-intercept and (Δm and Δb are uncertainty of the slope and the intercept, respectively). The iron concentrations of five settlement lagoons of Shilbottle samples were calculated (Table 4.1).

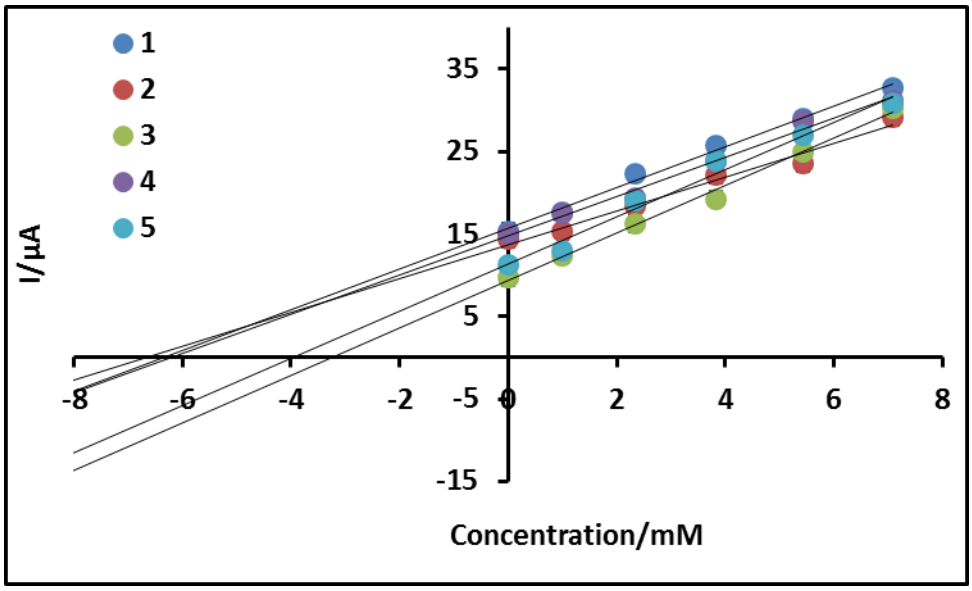

Figure 4.2: Determination of total soluble iron concentration in environmental samples by SWV, (1) upper stream (2) lagoon 01, (3) lagoon 02, (4) lagoon 03A and (5) lagoon 03B.

The findings show that the soluble Fe concentrations varied between 182 ± 15 and 373 ± 46 mg L^{-1} (ppm) with average of 296 mg L^{-1} in five settlement lagoons of the site (Upper stream UP, lag. 01, lag.02, lag.03A and lag. 3B, respectively). These results were compared with measurements obtained from ICP-AES for the same samples (as we will see latter in this section 4.6). It was observed that, the iron concentration measured by SWV was significantly higher than obtained by ICP-AES by a factor up to 5 times; this is mainly attributed to matrix effects in ICP-AES measurements in such kind of environmental samples.

Sample name	**UP**	**Lag. 01**	**Lag. 02**	**Lag. 03A**	**Lag. 3B**
Total iron concentration	Iron concentration /ppm				
	355 ± 26	373 ± 46	182 ± 15	346 ± 31	222 ± 31

Table 4.1: Soluble iron concentrations (in mg L^{-1}) of five different settlement lagoons in Shilbottle site (NE of England) were calculated by voltammetric technique SWV using Pt electrode, (the values are the intercept ± standard error of mean)

Such matrix effects (called non-spectroscopic interferences) are caused by presence of high concentrations of easily ionized elements such as K, Na, Ca Mg and also from Al

and Mn in AMD [180]. Unlike spectroscopic interferences where the analyte emission signal is enhanced by interference from other elements, non-spectroscopic interferences cause suppression or enhancement to the analytical signal depending on the volatility of the analyte compared with the matrix, if the analyte is more volatile than the matrix the signal will be more intense, and vice versa [181]. It has been stated that the signal intensity of 50 ppm of iron in complex samples consisting of several salts (AMD) may decrease 10 times compared to that in pure sample solution due to the matrix effects. Therefore, in order to minimize such problem, several pre-treatment steps have to be made which can be time consuming [181].

Despite that ICP-AES is a preferred tool for determination of elements in environmental samples because of its capability to measure simultaneously multiple elements in a mixture. SWV can be a better choice for accurate determination of iron concentration in AMD samples where the interferences with different elements are expected. It measures soluble concentrations of iron in the solution by measuring the reduction peak current (I_p) of iron, which is unique for soluble iron species which can provide the real concentration.

Our results were of a similar order of magnitude, but slightly higher than obtained in previous work [21] in which the total iron concentration was up to 223 mg L^{-1} with a mean of 110 mg L^{-1}. Also unpublished work in which the dissolved iron concentration for sample collected in February 2007 were 149, 109 and 126 mg L^{-1} for lagoons 01, 02 and 03, respectively. These differences in iron concentrations may be due to matrix effects in the environmental solution, and may also be because of seasonal variation and changing flow conditions as a result of rainfall.

4.4.2 Determination of soluble dissolved fractions of iron(II) and iron(III) in acid mine drainages using ultramicroelectrode voltammetry

A standard addition method was used to determine concentrations of Fe(II) and Fe(III) in Shilbottle samples with an ultramicroelectrode technique. Figure 4.3 illustrates that the diffusion-limited reduction current of Fe(III) is proportional to Fe(III) concentration. Therefore, plotting cathodic limiting current versus added standard iron(III) concentrations is shown in figure 4.4 for which a linear regression was performed to obtain straight line equation (equation 4.1) and determine the Fe(III) concentration in the sample.

Fe(II) concentrations were estimated with the assumption that the diffusion coefficient (D) of Fe(II) is equal to that of Fe(III). Accordingly, the figure 4.3 shows the proportion of anodic to cathodic limiting currents which represent the concentrations of Fe(II) and Fe(III) in 5 samples from different locations in the Shilbottle site. The obtained results were shown in table 4.2.

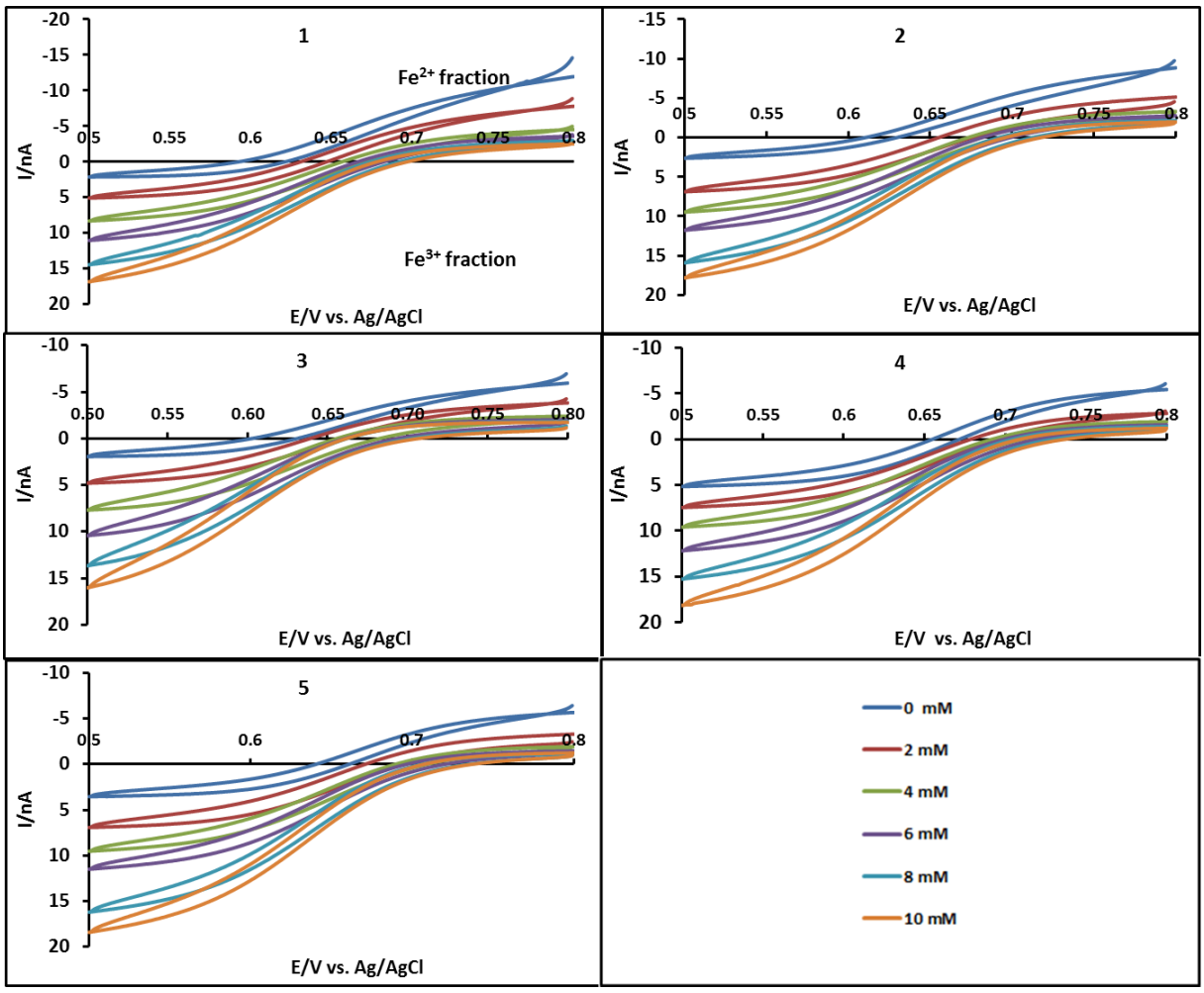

Figure 4.3: Steady state ultramicroelectrode voltammograms vs. standard iron(III) concentration in environmental sample; (1) upper stream (2) lagoon 01, (3) lagoon 02, (4) lagoon 03A and (4) lagoon 03B. (initial E = 0.80 V, high E = 0.80 V, low E = 0.50 V, scan rate = 0.005 V/sec, sample interval 0.001 V, quiet time = 2.0 sec and sensitivity = 1.0×10^{-8} A/V), the working electrode was ultramicroelectrode a 50 µm radius platinum; the reference electrode was Ag/AgCl. The solution was not degassed.

It can be concluded that there were good agreement between two different electrochemical techniques in comparison with ICP-AES conducted in this work. This is shown in tables (4.2 & 4.3) where the iron concentration measured by UME (mean value = 310 ppm) was higher than measured by ICP-AES (mean value = 64 ppm). Such a marked difference between UME and ICP-AES techniques can be attributed to matrix effects in case of ICP-AES as discussed earlier (section 4.4.1).

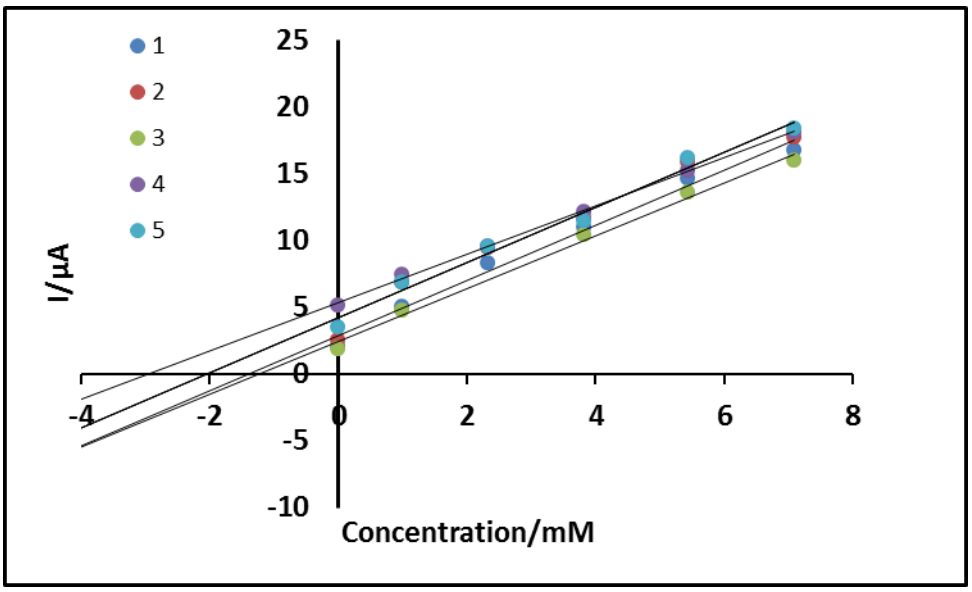

Figure 4.4: Determination of the soluble fractions of Fe(II) and Fe(III) in environmental samples using ultramicroelectrode voltammetry; (1) upper stream (2) lagoon 01, (3) lagoon 02, (4) lagoon 03A and (4) lagoon 03B.

Sample Name	UP	Lag. 01	Lag. 02	Lag. 03A	Lag. 3B
	Iron concentration /ppm				
[Fe(III)]	77 ± 17	106 ± 28	69 ± 12	166 ± 4	114 ± 21
[Fe(II)/Fe(III)]	0.79	0.56	0.51	0.18	0.32
[Fe(II)]	369 ± 17	237 ± 28	138 ± 12	202 ± 4	167 ± 21
Total conc.	446 ± 34	343 ± 56	207 ± 24	368 ± 8	281 ± 42

Table 4.2: Fe(III) and Fe(II) concentrations (in mg L^{-1}) of five different settlement lagoons in Shilbottle site (NE of England) were calculated by ultamicroelectrode voltammetric technique. UP denotes to upper stream of the site, Lag. denotes to settlement lagoons 1, 2, 3A and 3b, respectively. (the values are the intercept ± standard error of mean)

From the table 4.2, it is clear that the fraction of Fe(II) is higher than Fe(III) in all samples. The ratio of Fe(II)/Fe(III) has a maximum value at upper part of the stream and it decreases gradually from lagoon upper stream to lagoons 02. This may be because increasing the amount of dissolved oxygen at the end of these lagoons compared to their beginning (i. e. waters in upper stream flows immediately to lagoons 01 and 02, figure 1.3) which increases the exposure to the air in lagoon 02 compared to upper stream sample. The remediation process in the settlement lagoons at Shilbottle is clearly decreasing the soluble Fe content, but does not remove it entirely.

Analytical method	Upper stream	Lagoon 02	Lagoon 3B
	Iron concentration /ppm		
UME	446 ± 34	207 ± 24	281 ± 42
SWV	355 ± 26	182 ± 15	222 ± 31
ICP-AES	104.1 ± 0.5	37.8 ± 0.8	49.1 ± 0.7

Table 4.3: iron concentrations of three samples of Shilbottle using different methods, SWV, UME and ICP-AES. (SWV and UME values are the intercept ± standard error of mean, and ICP values are the mean ± standard deviation of 3 replicates).

4.4.3 Determination oxidation-reduction potential Eh and pe of electroactive redox iron species in Shilbottle samples using voltammetry and potentiometry

The oxidation-reduction potential (Eh) is a measure of the chemical potential of electrons in solutions. Its utility in describing solution chemical equilibria depends on relevant reactions attaining equilibrium. It is necessary for the electron transfer process at the indicator electrode to be at equilibrium. Eh has been commonly used as a master variable to describe redox reactions in aqueous solutions and mine water drainages in geochemical models. It has been used to evaluate geochemical speciation models for suboxic and anoxic ground water systems, to characterize oxidation-reduction status of surface environments and to predict whether the system is overall reductive or oxidizing. It can be measured by simple potentiometry with an inert metallic indicator electrode. Eh may also be determined experimentally and /or calculated from Nernst equation by measuring the redox couples present in the system.

The former method can be carried out using potentiometry with an inert indicator electrode (e.g. Pt) and reference electrode (e. g. SCE or Ag/AgCl). However, the potentiometric methods have encountered several problems that can affect the precision of Eh measurements. These problems can be related to both technical difficulties in the measurements and to interpretations of acquired data. It has been reported that mixed potentials [182, 183], electrode poisoning [183, 184] and disequilibrium of the system [183, 185] may arise during the measurements due to low concentration of electroactive species ($\leq 10^{-5}$ M) and changing electron transfer rates owing to fouling of the electrode surface [186].

On the other hand, in order to calculate Eh using Nernst equations, the concentrations and or activities of electroactive species must be known. The determination of Fe^{2+} and Fe^{3+} concentrations in the sample solution using colorimetric or using geochemical modelling has been measured. However, these measurements can be time consuming,

subject to inferences and may have less accuracy especially at elevated pH values [174, 187, 188]. In this work, the concentrations and therefore activities of the dominant soluble species in acid mine drainages of Shilbottle samples ([$FeSO_4^+$], [Fe^{2+}] and [SO_4^{2-}]) were determined using simple ultramicroelectrode and SWV methods. Accordingly, Eh for {$FeSO_4^+$}/{Fe^{2+}}{SO_4^{2-}} system was calculated using Nernst equation, and 0.534 V versus SHE was used as standard reduction potential for $FeSO_4^+/Fe^{2+}$ system.

$$E = E^{\phi}_{FeSO_4^+/Fe^{2+}} + \frac{RT}{nF} \ln \frac{\{FeSO_4^+\}}{\{Fe^{2+}\}\{SO_4^{2-}\}} \qquad \text{……(4.2)}$$

Where

E = the reduction potential of the reaction

E^{ϕ} = the standard reduction potential of $FeSO_4^+/Fe^{2+}$ couple (0.534 V)

R = general gas constant 8.31 J/mol .K

T = temperature in Kelvin

F = Faraday constant 96485 C/mol

n= number of the electrons (1 electron)

The Eh can be expressed as pe in analogous way to pH:

$$pe = \frac{Eh\ F}{2.303\ RT} \qquad \text{……(4.3)}$$

Where e = electron (transferred electron between $FeSO_4^+/Fe^{2+}$ couple).

The iron concentration in Shilbottle samples is low compared to other soluble concentration e. g. [SO_4^{2-}]. Activities of soluble iron are needed because it takes in to account the interaction energies of ions in the solutions. Debye Huckel equation (4.4) was used for estimation activity coefficient (γ_i).

$$-\log\gamma_i = \frac{AZ_i^2\sqrt{I}}{1+Ba_i\sqrt{I}} \qquad \text{……(4.4)}$$

Where γ_i is activity coefficient, a_i is ionic radius, I is ionic strength, Z_i is the charge of ion species *i* and A and B are temperature dependent constants (at 25 ^oC 0.51 and 0.328, respectively).

The equation (4.4) was used in our measurements, because simple Debye-Hückel equation ($\log \gamma_i = -A\ Zi^2 \sqrt{I}$) is useful only when ionic strength concentration is about 0.001 M or less. In our case, soluble sulfate concentration is in the range (0.11 – 0.23 M, section 4.4.4); therefore the simple Debye-Hückel equation can not be applied in our solutions. The values of Eh and pe for Shilbottle were electrochemically determined by both potentiometric and voltammetric and they are illustrated in table 4.4

Sample Name/Method	UP	Lag. 01	Lag. 02	Lag. 03A	Lag. 3B
Eh (V) (Vol.)	0.615	0.638	0.643	0.652	0.654
pe	10.51	10.90	10.97	11.14	11.16
Eh (V) (pot.)	0.858	0.875	0.911	0.925	0.891
pe	14.66	14.94	15.56	15.80	15.22

Table 4.4: Oxidation-reduction potentials (Eh) and pe of five different settlement lagoons in shilbottle site (NE of England) using voltammetry (vol.) and potentiometry (pot.) All values of Eh are versus SHE.

From the table, it can be observed that Eh and therefore pe values are different in the two methods. This may be ascribed to that the system in the potentiometric method is probably not at redox equilibrium which may be attributed to the mixed potential effects at the Pt electrode. These results indicate the use of straightforward potentiometry to determine pe in AMD is unlikely to be reliable. The pe values obtained by voltammetric methods will be introduced as an input to a geochemical speciation model for thermodynamic calculation (as we will see in section 4.7).

4.4.4 Determination of soluble sulfate concentration in acid mine drainages using SWV

An electrochemical approach that has not been applied before in geochemical measurements was developed to determine concentrations of soluble sulfate ions in Shilbottle samples using a voltammetric technique (SWV). A calibration plot of formal potential against $\log[SO_4^{2-}]$ for various ratios of sulfate to iron at different pH values (Figure 4.5) was prepared. Cathdic peak potential (E_{pc}) of soluble species of $FeSO_4^+$ was plotted versus $\log[SO_4^{2-}]$ for 0.005 M of $Fe(ClO_4)_3$ with different concentrations of Na_2SO_4 (0.00, 0.01, 0.05, 0.10 and 0.5 M). Multiple linear regressions of the data at three different pHs (pH_s = 2.25, 2.75 and 3.25) were made, and the resulting equation (4.5) was used to calculate soluble sulfate concentration in Shilbottle samples:

$$E_p = 0.754 - 0.046\ pH + 0.053\ pSO_4^{2-} \quad \text{.....(4.5)}$$

Where E_{pc} is formal cathodic peak potential; this was measured for each environmental sample using square wave voltammetry as shown in figure 4.6. The pH was measured using a glass electrode. On the basis of Nernst equation without any consideration of activity coefficients, the coefficients of pH and pSO_4^{2-} terms are expected to be -0.059 and +0.059, respectively. The differences from the value observed in the regression analysis are quite small and are likely due to activity coefficient effects.

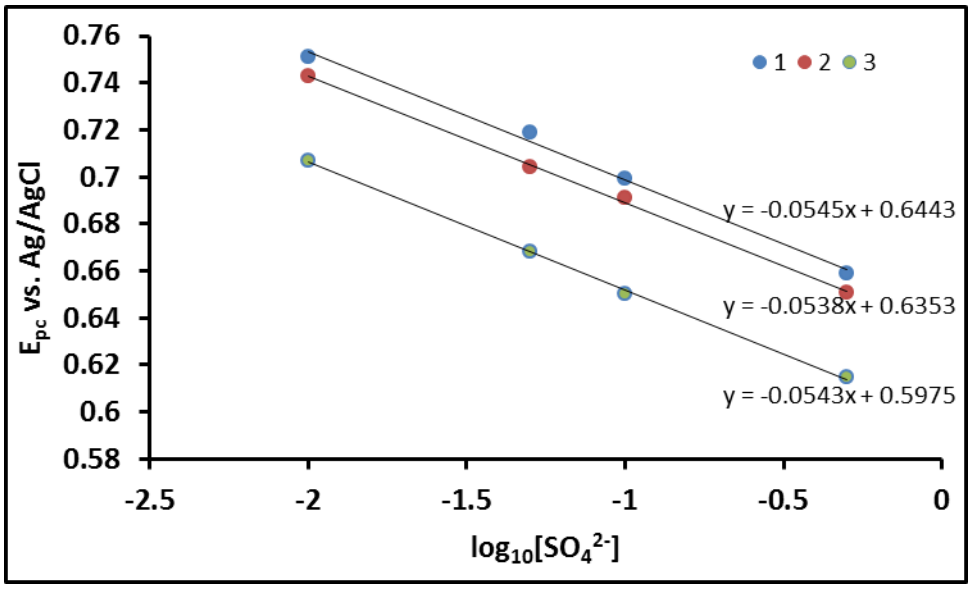

Figure 4.5: Plot of cathodic peak potential versus $\log_{10}[SO_4^{2-}]$ (for 0.005 M of $Fe(ClO_4)_3$ and 0.00, 0.01, 0.05, 0.1 and 0.5 M of Na_2SO_4, respectively) at 3 different pH values (1) 2.25, (2) 2.75, (3) and (3) 3.25.

Using the regression equation, the concentrations of soluble sulfate in Shilbottle samples were determined by measuring the cathodic peak potential. These data are presented in table 4.5, the sulfate concentration ranged between 3460 ± 105 mg L^{-1} in lagoon 3B and 7400 ± 220 mg L^{-1} in the Upper stream of the site with average of about 5330 ± 150 mg L^{-1}. These results were slightly less than that obtained in previous work [21] in which the sulfate concentration was around 6400 mg L^{-1} using ICP-AES. This also may be mainly attributed to seasonal variations. In this work, we compared the results obtained by voltammetric technique (SWV) with other obtained using ICP-AES for the same samples; this is an indirect way to measure sulfate using ICP-AES, as ICP-AES only measures total sulfur concentration, and the conversion of S and SO_4^{2-} is based on the following equation:

1 mg/L of S = (96.056/32.06) mg/L of SO_4^{2-}

= 2.996 mg/L of SO_4^{2-}

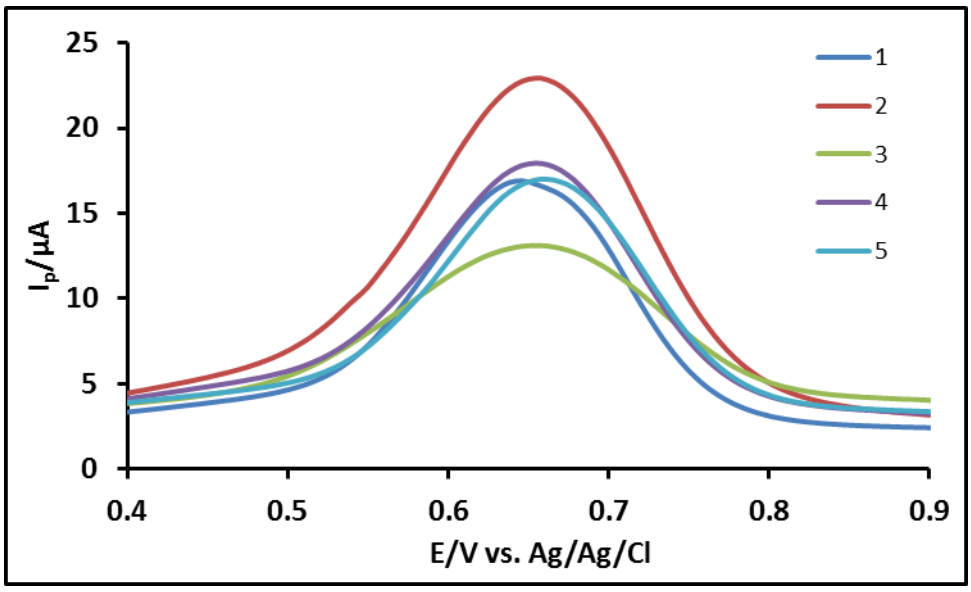

Figure 4.6: The cathodic peak potential of soluble species of $FeSO_4^+$ in Shilbottle solution on SWV voltammogram, (1) upper stream (2) lagoon 01, (3) lagoon 02, (4) lagoon 03A and (5) lagoon 03B. (Initial E = 0.9 V, low E = 0.4 V, amplitude = 0.025 V, frequency = 15 Hz, sample interval 0.004 V, quiet time = 2.0 s and sensitivity = 1.0×10^{-5} A/V), the working electrode was a 1 mm radius platinum electrode; the reference electrode was Ag/AgCl. The solution was not degassed.

Sample Name	UP	Lag. 01	Lag. 02	Lag. 03A	Lag. 3B
Soluble sulfate concentrations	ppm				
	7400 ± 220	5190 ± 125	4630 ± 140	5970 ± 180	3460 ± 105

Table 4.5: Sulfate [SO_4^{2-}] concentrations of five different settlement lagoons in Shilbottle site (NE of England) were calculated by square wave voltammetry technique in (mg L^{-1}), (the values are the slope of cathodic peak versus $\log_{10}[SO_4^{2-}]$ ± standard error of mean).

Sample Name	UP	Lag. 02	Lag. 3B
Soluble sulfate concentrations	ppm		
	4416 ± 9	4035 ± 20	4415 ± 10

Table 4.6: Sulfate [SO_4^{2-}] concentrations of three different settlement lagoons in Shilbottle site (NE of England) were calculated by ICP-AES in (mg L^{-1}), (the values are the mean ± standard deviation of 3 replicates)

The obtained results were presented in the table 4.6. The results were slightly less than determined by SWV, this may be attributed to that the matrix effects interference [189]. The diagram in (Figure 4.5) was designed on the principle of the Nernst equation for the reaction (4.6):

$$FeSO_4^+ + e^- \rightleftharpoons Fe^{2+} + SO_4^{2-} \qquad \text{……(4.6)}$$

The Nernst equation will be:

$$E = E^{o}_{FeSO_4^{+}/Fe^{2+}} + \frac{RT}{nF} \ln \frac{[FeSO_4^{+}]}{[Fe^{2+}][SO_4^{2-}]} \qquad \text{……..(4.7)}$$

Or

$$E = E^{o}_{FeSO_4^{+}/Fe^{2+}} + \frac{RT}{F} \ln \frac{[FeSO_4^{+}]}{[Fe^{2+}]} - \frac{RT}{F} \ln [SO_4^{2-}] \qquad \text{…….(4.8)}$$

Rearrangment of the equation (4.8) and ($-\log_{10}[SO_4^{2-}] = pSO_4$):

$$E = E^{o}_{FeSO_4^{+}/Fe^{2+}} + \frac{RT}{F} \ln \frac{[FeSO_4^{+}]}{[Fe^{2+}]} + \frac{2.303\ RT}{F} pSO_4^{2-} \qquad \text{…….(4.9)}$$

When $E = E^{o}$ on square wave voltammogram, the $[FeSO_4^{+}] = [Fe^{2+}]$, then:

$$E = E^{o}_{FeSO_4^{+}/Fe^{2+}} + \frac{2.303\ RT}{F} pSO_4^{2-} \qquad \text{…….(4.10)}$$

The plot of reduction peak potential of soluble species of $FeSO_4^{+}$ (E_{pc}) versus $\log_{10}[SO_4^{2-}]$ will be a straight line of slope about −0.059V if the complex is $[FeSO_4^{+}]$ or equal to -0.18V if the complex has two sulfate ions which are release on reduction, e.g. $[Fe(SO_4)_2^{-}]$. Sulfate is known to coordinate very weakly to Fe(II) [34].

Therefore, if we have the following equilibrium:

$$Fe^{3+} + SO_4^{2-} \rightleftharpoons FeSO_4^{+} \qquad K_1 \qquad \text{…….(4.11)}$$

$$K_1 = \frac{[FeSO_4^{+}]}{[Fe^{3+}][SO_4^{2-}]} \qquad \text{…….(4.12)}$$

If we follow the same procedures in section (3.5.1), then equation 4.13 become:

$$E = E^{o}_{Fe^{3+}/Fe^{2+}} + \frac{RT}{F} \ln \frac{[FeSO_4^{+}]}{[Fe^{2+}][SO_4^{2-}]} + \frac{RT}{F} \ln \frac{[Fe^{3+}][SO_4^{2-}]}{[FeSO_4^{+}]} \qquad \text{….(4.13)}$$

This can be rearranged to:

$$E = E^{o}_{Fe^{3+}/Fe^{2+}} + \frac{RT}{F} \ln \frac{[FeSO_4^{+}]}{[Fe^{2+}][SO_4^{2-}]} - \frac{RT}{F} \ln K_1 \qquad \text{…….(4.14)}$$

The peak potential in SWV will be different for aqueous solutions of $Fe(ClO_4)_3$ and $Fe_2(SO_4)_3$ by an amount equal to $(-\frac{RT}{F}\ln K)$, For example, according to equation (4.14), the value of K_1 has been measured and it is 263 M^{-1} [109, 111] then the peak potential will shift by 0.143 V to negative potential. The peak for Fe^{3+} reduction in aqueous solution of $Fe(ClO_4)_3$ will also shift to negative potentials by amount of - 2.3 RT/F ≈ 0.059 V with a tenfold increase of SO_4^{2-} (figure 4.7), which can be attributed to formation of $FeSO_4^+$. Also, it can be observed from figure 4.7 that reduction peak current decreases with increasing $[SO_4^{2-}]$, this is because the dilution effects for adjusting pH by adding NaOH and HCl.

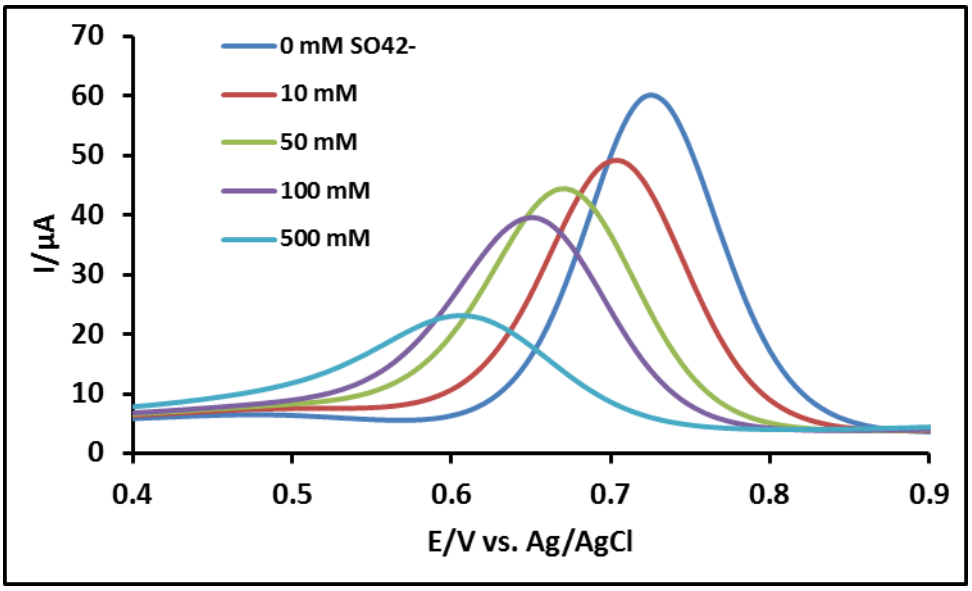

Figure 4.7: Showing the cathodic peak $[Fe(H_2O)_6]^{3+}$ reduction shifting to the negative with increasing sulfate concentration, (a) 0.0, (b) 0.01, (c) 0.05, (d) 0.1 and (e) 0.5 M of $[SO_4^{2-}]$. (Initial E = 1.09 V, low E = 0.4 V, amplitude = 0.025 V, frequency = 15 Hz, sample interval 0.004 V, quiet time = 2.0 sec and sensitivity = 1.0×10^{-5} A/V), the working electrode was a 1 mm radius platinum electrode; the reference electrode was Ag/AgCl. The solution was not degassed.

From the these results (4.4.1) and (4.4.4), it can be concluded that, the dominant soluble species in Shilbottle samples can be one of $FeSO_4^+$, $FeHSO_4^{2+}$ or $FeSO_4OH$ depending on the pH. In other words, the ratio of $[Fe^{3+}]$:$[SO_4^{2-}]$ is 1:1. This can be supported by observing that, the cathodic peak potential (E_{pc}) of Shilbottle samples shifts into the negative potential to about 0.660 V vs. Ag/AgCl as shown in Figure 4.6. This is in good agreement with our results obtained in (section 3.5.1).

4.5 Potentiometry

Two potentiometric experiments were conducted to measure hydrogen and chloride ion concentrations in Shilbottle samples using ion selective electrodes.

4.5.1- Determination of [H^+] concentrations in acid mine drainages

Measuring [H^+] can be carried out using a potentiometric technique in which the potential difference between two sides of membrane of glass electrode is measured. This potential difference is related to the variation of [H^+] between outer and inner sides of the membrane (i. e. the difference between analyte solution and the solution in the electrode itself).

Measuring pH is crucial in numerous fields such as geology, hydrology, and biologcal processes, one of which is mine water system. It has been regarded as a master variable for mobility of contaminants in acid mine drainages, due to the sulfide minerals which are dissolved in water; the released metal ions can be dissolved or they can precipitate as oxyhydroxides. This depends on the pH of the stream, at circumneutral pH most metals and sulfides precipitate and accumulate within pathways of the stream, while at low pH these metals will dissolve and move with the water flow [32]. For these reasons, raising the pH of acid mine drainages was established as one of the most powerful methods for remediation.

In this work, we measured the pH of Shilbottle samples immediately (within 2.0 hours), the purpose of this step is to record pH values representative of actual mine water pH in the field, and also to avoid changes from the expected hydrolysis steps of iron(III) which in turn leads to decrease of pH. The values of pH for Shilbottle were electrochemically determined and they are illustrated in table 4.7

Sample Name	**UP**	**Lag. 01**	**Lag. 02**	**Lag. 03A**	**Lag. 3B**
pH	3.50	3.59	3.56	3.52	3.62

Table 4.7: pH values of five different settlement lagoons in Shilbottle site (NE of England) using potentiometry

The pH data shows that pH values of Shilbottle systems varied between 3.50 and 3.62. According to the geochemical study in [190] at such pH values, many metals of interest in AMD should remain in solution. It has been established that 90% of iron, aluminium,

copper, zinc, and manganese are precipitated at pH values above (4.05), (4.0 – 5.5), (4.49 – 6.11), (5.5 – 7.23) and (5.5 – 9.98), respectively [191]. Therefore, soluble species of such metals and also sulfate can be present in Shilbottle samples.

4.5.2 Determination of [Cl^-] concentrations in acid mine drainages

There are numerous rapid, robust and selective methods widely used to measure chloride concentration in aqueous solutions such as Volhard titration [192], spectrophotometry [193], ion chromatography [194] and indirect determination of chloride using X-ray fluorescence and atomic absorption [195, 196]. However, these methods require chemical reagents for a complexation and precipitation process [193, 195, 196], are time consuming [192] and some have a high cost of equipment [196].

Potentiometry with ion selective electrodes (ISEs) can be the favoured choice, because it possesses several advantages. It can be specific for chloride only and no matrix effects are involved, it is rapid, it has a low running cost and simple equipment. ISEs of course respond to activity rather than concentration, whereas spectroscopic techniques usually determine concentrations. ISEs will also not determine adsorbed or complexed species, but for our purposes, which are to provide input data for a thermodynamic speciation model, the concentration of freely dissolved ions is the important quantity. Therefore, the concentration of soluble chloride concentration [Cl^-] in Shilbottle solutions was determined using a chloride ion selective electrode.

It has been established in several studies [197, 198] that the chloride ions coordinate with iron(III) to form soluble complexes of [$FeCl^{2+}$, $FeCl_2^+$, $FeCl_3$ and $FeCl_4^-$], this depends on pH and chloride concentrations. The purpose of measuring soluble chloride concentrations in Shilbottle samples is to determine if sufficient chloride is available for the formation of soluble [$FeCl_n^{+3-n}$] complexes in acid mine drainages. The presence of such species would affect the rate at which soluble iron is removed by remediation. The measurements obtained here are used as input data for geochemical model based on the code (PHREEQC-(USGS)) (see latter in this chapter, section 4.7).

All procedures for electrode calibration and sample preparation were discusses in (chapter 2). Standard calibration curves were prepared by plotting electrode potential (E) vs. $\log_{10}$[Cl] for different [Cl^-] concentrations (10^{-7} – 10^{-1} M), figure (4.8). From the

slope, the chloride concentrations can be estimated according to the following equations (4.15 – 4.17):

$$\text{Slope} = \frac{dy}{dx} = \frac{-2.303\ RT}{F} \qquad \text{.....(4.15)}$$

From Nernst equation:

$$E = E^{\emptyset}\ (\text{constant}) - \frac{2.303\ RT}{F} \log [Cl^-] \qquad \text{.....(4.16)}$$

$$[Cl^-] = 10^{-\frac{(E - E^{\phi})\ F}{2.303\ RT}} \qquad \text{.....(4.17)}$$

As E^{ϕ} is the standard potential of internal reference electrode (constant value).

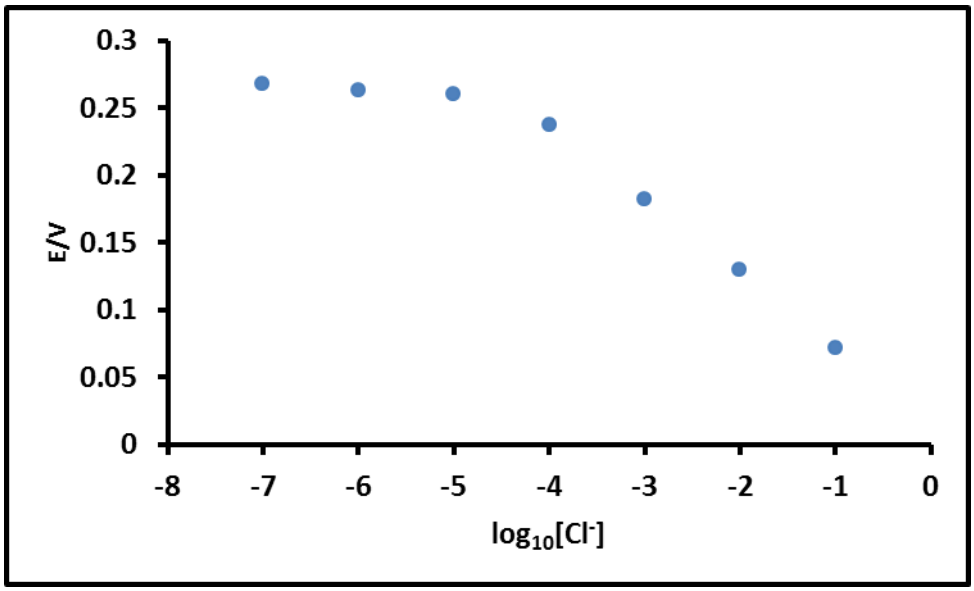

Figure 4.8: Graph of E/V vs. $\log_{10}[Cl^-]$ for different concentration standard solutions of NaCl (10^{-7} – 10^{-1} M)

The obtained chloride concentrations in Shilbottle system are shown in table 4.8. The results show that, the chloride concentrations were low compared with other soluble components e. g. iron and sulfate. Accordingly, the contributions of soluble complexes of $[FeCl_n^{+3-n}]$ in acid mine drainages are likely to be negligible in comparison with other soluble iron complexes e. g. $FeSO_4^+$. This will be confirmed using geochemical model based on the code PHREEQC-(USGS).

Sample Name	UP	Lag. 01	Lag. 02	Lag. 03A	Lag. 3B
[Cl^-] in ppm	2.70 ± 0.03	1.98 ± 0.03	2.51 ± 0.03	0.77 ± 0.03	1.64 ± 0.03

Table 4.8: Showing [Cl^-] of five different settlement lagoons in the Shilbottle site (NE of England) using potentiometry (chloride selective electrode). (the values are the mean ± standard error of mean).

4.6 Multi-elements analysis by ICP - AES

Inductively coupled plasma atomic emission spectroscopy (ICP-AES) was used to determine the total concentrations of Fe, Mg, Ca, K, Mn, Al, Na, Cu, Pb, Sn, As, Hg, Zn, P and S in three environmental samples. The results are presented in table 4.9. It is clear that, the AMD in Shilbottle samples contain high concentrations of S, Mg, Ca, Fe, Al and Mn, these concentrations are close to or smaller than the results obtained in 2005 [21] for the same site with a few variations, which can be ascribed to either effective remediation processes in the last 5 years or to seasonal variation due to changing flow conditions. The sulfate concentration was calculated from sulfur concentration determined by ICP-AES according to following equation [177]:

1 mg/L of S = (96.056/32.06) mg/L of SO_4^{2-}

= 2.996 mg/L of SO_4^{2-}

This is simply equivalent to the assumption that all sulfur is present as sulfate. Calibration curves were prepared by measuring 5 standard solutions for measured element, the standard curve was installed in the instrument. The unknown concentration of the element was calculated automatically from the instrument. The accuracy of the instrument is for 4 significant figures. The obtained results are presented in the table 4.9. The concentrations of Fe and SO_4^{2-} were compared with results obtained by the electrochemical techniques which were used in this work. The concentrations determined using ICP-AES were slightly smaller, which were attributed to matrix effects accompanied with ICP-AES measurements especially in the case of iron. The matrix effects are caused by the presence of considerable concentrations of elements such as Ca, Mg, Al and S in Shilbottle samples which affect the analyte signal. As it has been reported that the matrix effects (called non-spectroscopic interferences) are caused by presence of high concentrations of easily ionized elements such as K, Na, Ca Mg and also from Al and Mn in AMD [180]. In the spectroscopic interferences the analyte emission signal is enhanced by interfering with other elements, whereas non-spectroscopic interferences may cause suppression or enhancement to the analytical

signal [181].

Element	Upper stream	Lagoon 02	Lagoon 3B
	ppm		
Fe	104.1 ± 0.5	37.84 ± 0.79	49.14 ± 0.75
Mg	835.0 ± 14.8	523.1 ± 3.5	596.2 ± 1.3
Ca	244.0 ± 1.3	202.5 ± 2.6	230.2 ± 2.5
K	26.43 ± 1.66	24.55 ± 1.51	20.30 ± 1.58
Na	98.19 ± 2.10	53.43 ± 1.06	61.68 ± 0.47
Mn	83.77 ± 0.12	56.49 ± 0.31	59.39 ± 0.22
Al	207.9 ± 2.1	80.14 ± 0.57	87.80 ± 2.72
Cu	0.1307 ± 0.0004	0.1839 ± 0.0025	0.1323 ± 0.0008
Pb	0.0818 ± 0.0019	0.0216 ± 0.0074	0.0100 ± 0.0040
As	2.340 ± 0.079	1.303 ± 0.049	1.236 ± 0.073
Sn	0.8734 ± 0.0324	0.5979 ± 0.0310	0.5147 ± 0.0639
Zn	2.186 ± 0.013	1.490 ± 0.006	1.696 ± 0.007
Hg	0.4880 ± 0.0073	0.3112 ± 0.0193	0.3313 ± 0.0178
P	1.362 ± 0.020	1.037 ± 0.031	1.280 ± 0.076
S	1474 ± 9	1622 ± 20	1347 ± 10
SO_4^{2-}	4416 ± 9	4860 ± 20	4036 ± 10

Table 4.9: Showing concentrations of Fe, Mg, Ca, K, Mn, Al, Na, Cu, Pb, Sn, As, Hg, Zn, P, SO_4^{2-} and S of three settlement lagoons in shilbottle site (NE of England) using Inductively coupled plasma atomic emission spectroscopy (ICP-AES), (the values are the mean ± standard deviation of 3 replicates).

4.7 Thermodynamic speciation calculation using a geochemical model

Geochemical models have been developed for numerous environmental applications including equilibrium between minerals and water, surface complexation, solid solutions, ion exchange and gas phase reactions. Modelling of non-equilibrium dissolution and precipitation, decomposition of organic compounds and microbial reactions has also been simulated by geochemical models using general kinetic formulations. One of the most popular geochemical codes used for this sort of modelling is PHREEQC which is acronym for PH REdox EQuilibrium in the C programming language. It is a computer program that is designed to perform a wide variety of low-temperature aqueous geochemical calculations. It is made available by the U.S. Geological Survey (USGS) and has been widely used as a geochemical calculation module in other software programs.

PHREEQC is able to calculate concentrations of elements, molalities and activities of aqueous species, pe, pH, mole transfers of phases to achieve equilibrium as a function of specified reversible and irreversible geochemical reactions and saturation indices. It has been used to generate predominance diagrams [199], and as geochemical models for

reactive-transport environments such as acid mine water [200]. In addition, it has been used as a method for speciation calculations in which it provides both the concentrations and activities of dissolved metals in aqueous solution [201, 202]. The Pitzer ion-interaction equation has been incorporated in PHREEQC to provide high accuracy for activity coefficients even in solutions with high ionic strength [199].

In this work, PHREEQC was applied to identify the distribution of aqueous soluble species in acidic mine drainages with respect to the iron and sulfate so that we can compare the speciation determined by PHREEQC results with experimental results which we have obtained using electrochemical and spectroscopic techniques (chapter 3), and also to determine mineral saturation indices (SI). The saturation indices can be applied to determine the capability of the solution to precipitate minerals as a solid phase. This is important in AMD treatment because precipitation of metals in artificial wetlands at Shilbottle is part of the remediation strategy.

$$SI = \log \frac{IAP}{K_s} \qquad \text{……..(4.18)}$$

Where IAP is the ion activity product and K_s is the solid solubility product. Positive, negative and zero SI values indicate that the solution is supersaturated, undersaturated and saturated, respectively with respect to the particular solid phase.

All required parameters for the speciation model determined in this chapter are the total concentration of soluble species of iron, sulfur, chloride, hydrogen ion and also pe and the temperature in ^{o}C. The pe values obtained by the voltammetric method are introduced as an input to a geochemical model instead of those obtained by potentiometry, because of the mixed potential effects observed at the Pt indicator electrode. These parameters were used as input to calculate the distribution of aqueous species and saturation indices for important solid phases (SI). The output of calculation includes both activities and concentrations (molality). All these calculations ignored heterogeneous reactions at the solid/liquid and liquid/gas interfaces.

The obtained results of upper stream of Shilbottle site are presented in table 4.10. For simplicity we only present the output of one sample (upper stream) as the rest of samples (lagoon 01, lagoon 02, lagoon 03A and lagoon 03B) exhibit analogous data with few differences which are presented in table 4.11. Such differences include only the predominant species of iron(III) such as $FeSO_4^+$, $Fe(OH)^{2+}$, $Fe(SO_4)_2^-$ and $Fe(OH)_2^+$

which depend on the solution components such as sulfur, iron concentrations and pH of the solution.

Table 4.10: The inputs and the outputs parameters of upper stream sample

Use PHREEQC to calculate the distribution of aqueous species and saturation indices for solid phases (SI).

SOLUTION 1 the inputs parameters for Upper stream sample

pH	03.50	
Pe	10.51	
Fe	06.33 mM	(measured by voltammetry in this work)
Cl	0.076 mM	(measured by potentiometry in this work)
S(6)	25.70 mM	(measured by voltammetry in this work)
temp	16.00 ^{0}C	

----------Description of solution----------

pH	=	3.500
pe	=	10.510
Specific Conductance (uS/cm, 16 °C)	=	2407
Density (g/cm^3)	=	1.00140
Activity of water	=	0.999
Ionic strength	=	5.235×10^{-002}
Mass of water (kg)	=	1.000×10^{000}
Total alkalinity (eq/kg)	=	-1.620×10^{-003}
Total carbon (mol/kg)	=	$0.000\times10^{+000}$
Total CO_2 (mol/kg)	=	$0.000\times10^{+000}$
Temperature (°C)	=	16.000
Electrical balance (eq)	=	-3.773×10^{-002}
Percent error, 100*(Cat-|An|)/(Cat+|An|)	=	-71.27
Iterations	=	5
Total H	=	$1.110133\times10^{+002}$
Total O	=	$5.560916\times10^{+001}$

The outputs of solution 1 (Upper stream sample)

----------Distribution of species----------

Species	Molality	Activity	Log Molality	Log Activity	Log Gamma(log γ_i)
H^+	3.704×10^{-004}	3.162×10^{-004}	-3.431	-3.500	-0.069
OH^-	1.910×10^{-011}	1.549×10^{-011}	-10.719	-10.810	-0.091
H2O	$5.551\times10^{+001}$	9.995×10^{-001}	1.744	-0.000	0.000
Cl	7.600×10^{-005}				
Cl^-	7.582×10^{-005}	6.160×10^{-005}	-4.120	-4.210	-0.090
$FeCl^+$	1.662×10^{-007}	1.365×10^{-007}	-6.779	-6.865	-0.086
$FeCl^{+2}$	9.094×10^{-009}	4.134×10^{-009}	-8.041	-8.384	-0.342
$FeCl_2^+$	1.859×10^{-012}	1.527×10^{-012}	-11.731	-11.816	-0.086
$FeCl^3$	9.292×10^{-018}	9.404×10^{-018}	-17.032	-17.027	0.005
Fe(2)	5.797×10^{-003}				
Fe^{+2}	3.331×10^{-003}	1.605×10^{-003}	-2.477	-2.795	-0.317
$FeSO_4$	2.460×10^{-003}	2.490×10^{-003}	-2.609	-2.604	0.005
$FeHSO_4^+$	6.183×10^{-006}	5.077×10^{-006}	-5.209	-5.294	-0.086
$FeCl^+$	1.662×10^{-007}	1.365×10^{-007}	-6.779	-6.865	-0.086
$FeOH^+$	9.765×10^{-010}	8.018×10^{-010}	-9.010	-9.096	-0.086
Fe(3)	5.330×10^{-004}				
$FeSO_4^+$	3.353×10^{-004}	2.753×10^{-004}	-3.475	-3.560	-0.086
$FeOH^{+2}$	7.752×10^{-005}	3.525×10^{-005}	-4.111	-4.453	-0.342
$Fe(SO_4)_2^-$	7.313×10^{-005}	6.005×10^{-005}	-4.136	-4.222	-0.086

$Fe(OH)_2^+$	3.159×10^{-005}	2.594×10^{-005}	-4.500	-4.586	-0.086
Fe^{+3}	1.237×10^{-005}	2.983×10^{-006}	-4.908	-5.525	-0.618
$Fe_2(OH)_2^{+4}$	1.148×10^{-006}	4.906×10^{-008}	-5.940	-7.309	-1.369
$FeHSO_4^{+2}$	5.213×10^{-007}	2.370×10^{-007}	-6.283	-6.625	-0.342
$Fe_3(OH)_4^{+5}$	8.633×10^{-008}	6.262×10^{-010}	-7.064	-9.203	-2.139
$FeCl^{+2}$	9.094×10^{-009}	4.134×10^{-009}	-8.041	-8.384	-0.342
$Fe(OH)_3$	6.965×10^{-009}	7.049×10^{-009}	-8.157	-8.152	0.005
$FeCl_2^+$	1.859×10^{-012}	1.527×10^{-012}	-11.731	-11.816	-0.086
$Fe(OH)_4^-$	1.704×10^{-014}	1.399×10^{-014}	-13.768	-13.854	-0.086
$FeCl_3$	9.292×10^{-018}	9.404×10^{-018}	-17.032	-17.027	0.005
H(0)	1.465×10^{-031}				
H_2	7.326×10^{-032}	7.415×10^{-032}	-31.135	-31.130	0.005
O(0)	1.514×10^{-033}				
O_2	7.571×10^{-034}	7.663×10^{-034}	-33.121	-33.116	0.005
S(6)	2.570×10^{-002}				
SO_4^{-2}	2.243×10^{-002}	$1.034e^{-002}$	-1.649	-1.986	-0.336
$FeSO_4$	2.460×10^{-003}	2.490×10^{-003}	-2.609	-2.604	0.005
$FeSO_4^+$	3.353×10^{-004}	2.753×10^{-004}	-3.475	-3.560	-0.086
HSO_4^-	3.204×10^{-004}	2.631×10^{-004}	-3.494	-3.580	-0.086
$Fe(SO_4)^{2-}$	7.313×10^{-005}	6.005×10^{-005}	-4.136	-4.222	-0.086
$FeHSO_4^+$	6.183×10^{-006}	5.077×10^{-006}	-5.209	-5.294	-0.086
$FeHSO_4^{+2}$	5.213×10^{-007}	2.370×10^{-007}	-6.283	-6.625	-0.342

----------Saturation indices----------

Phase	SI	log IAP	log KT	
$Fe(OH)_3(a)$	0.08	4.97	4.89	$Fe(OH)_3$
Goethite	5.64	4.97	-0.67	FeOOH
$H_2(g)$	-28.02	-31.13	-3.11	H_2
$H_2O(g)$	-1.75	-0.00	1.75	H_2O
Hematite	13.25	9.95	-3.30	Fe_2O_3
Melanterite	-2.46	-4.78	-2.32	$FeSO_4:7H_2O$
$O_2(g)$	-30.29	-33.12	-2.82	O_2

End of simulation.

The thermodynamic data obtained from PHREEQC showed that the predominant soluble iron(III) complex in acid mine drainages is $FeSO_4^+$ by (2- 4) fold over the following soluble species $FeOH^{2+}$ through the five settlement lagoons. These results are in good agreements with our electrochemical studies, as the SWV indicated that the ratio between Fe^{3+} : SO_4^{2-} is (1:1) in Shilbottle waters. However, SWV was not able to distinguish whether these complexes are $FeHSO_4^{2+}$, $FeSO_4^+$ or $FeOHSO_4$ depending on the pH of the solution.

Accordingly, depending on the equilibrium constants (K_a) between these complexes, at very low pH (< 1.0) the predominant complex is $FeHSO_4^{2+}$, at pH ranging between (1.0 and 4.0) the predominant complex is $FeSO_4^+$ [143], while at pHs exceeding 4.0 (> 4.0) a considerable amount of $FeOHSO_4$ could be predominant in the solution. The equilibrium constant between $FeOHSO_4$ and $FeSO_4^+$ (equation 4.19) has not been

experimentally measured. However, we estimated it theoretically as discussed (in chapter 3) and it is equal to 4.38 ± 0.16. The PHREEQC database does not include the equilibrium constant (*K*) between $FeOHSO_4$ and $FeSO_4^+$ because it has not previously been measured; the model can be tested by raising the pH in the input file. Even at pH=8.0, the species $FeOHSO_4$ were not seen in outputs of PHREEQC results. $Fe(OH)_3$ and $Fe(OH)_4^-$ were seen instead.

$$[Fe(H_2O)_5SO_4]^+ \rightleftharpoons [Fe(H_2O)_4OHSO_4] + H^+ \qquad K \qquad \text{.....(4.19)}$$

The results obtained from electrochemistry, mass spectroscopy and PHREEQC indicate that the predominant soluble species in respect to iron and sulfate in Shilbottle sample in which pH is around 3.6 is $FeSO_4^+$, but under the conditions required for ESI-MS where pH > 4, it is very likely that neutral $FeOHSO_4$ dominates and this explains the lack of success ESI-MS for AMD analysis.

Soluble iron species	**Concentration (m)**				
	Upper stream	Lagoon 01	Lagoon 02	Lagoon 03A	Lagoon 03B
$FeSO_4^+$	3.35×10^{-4}	6.57×10^{-4}	3.72×10^{-4}	1.00×10^{-3}	5.41×10^{-4}
$Fe(OH)^{2+}$	7.75×10^{-5}	2.41×10^{-4}	1.24×10^{-4}	2.82×10^{-4}	2.61×10^{-4}
$Fe(OH)_2^+$	3.16×10^{-5}	1.29×10^{-4}	6.35×10^{-5}	1.26×10^{-4}	1.61×10^{-4}
$Fe(SO_4)_2^-$	7.31×10^{-5}	1.04×10^{-4}	5.92×10^{-5}	1.80×10^{-4}	6.50×10^{-5}

Table 4.11: Major soluble components in five samples of Shilbottle solutions according to PHREEQC

The saturation indices (SI) values of Shibottle solutions are presented in table 4.12, they indicate that supersaturation with respect to $Fe(OH)_{3(s)}$, goethite and hematite are expected. SI > 0 implies the solutions are supersaturated and therefore it is out-of-equilibrium. For this reason, studying AMD using only PHREEQC may not be comprehensive because the Fe(III) solutions in AMD are out-of-equilibrium. This is an important motivation for studying kinetic aspects of such natural waters.

Solid phase	**SI**				
	Upper stream	Lagoon 01	Lagoon 02	Lagoon 03A	Lagoon 03B
$Fe(OH)_{3(s)}$	0.08	0.79	0.46	0.71	0.93
goethite	5.64	6.35	6.02	6.27	6.49
hematite	13.25	14.67	14.01	14.51	14.95

Table 4.12: SI values of five samples of Shilbottle solutions according to PHREEQC

It can be concluded from this chapter that, the concentrations of soluble species of Fe^{3+}, Fe^{2+}, total iron, soluble sulfate were measured using voltammetry in Shilbottle samples, the results showed that the concentration of soluble sulfate and iron were varied between (4630 and 7400 ppm) and (182 and 355 ppm) for sulfate and iron, respectively. Also Fe, SO_4^{2-}, Mg, Ca, K, Mn, Al, Na, Cu, Pb, Sn, As, Hg, Zn and P were measured by ICP-AES. Other electrochemical measurements were carried out such as pH, $[Cl^-]$ and Eh.

Electrochemical studies indicated that soluble species in AMD (Shilbottle) in respect to iron and sulfate are $FeSO_4^+$, $FeHSO_4^{2+}$ or $FeSO_4OH$. These observations were in good agreement with thermodynamic calculations (geochemical models, except in the case of $FeSO_4OH$ for reasons related to the internal database of the model) which, in turn, showed that the predominant iron(III) soluble species in Shilbottle site is $FeSO_4^+$. Also, the geochemical models showed that the solutions are supersaturated with respect to $Fe(OH)_{3(s)}$, goethite and hematite and therefore they may be out-of-equilibrium.

Chapter 5: Kinetic studies and sulfate effects on the hydrolysis and precipitation of iron(III) in aqueous solutions

5.1 Introduction

Iron(III) is thermodynamically unstable in aqueous solutions; it undergoes several hydrolysis processes to entirely precipitate in a range of different solid forms e. g. amorphous or crystalline in response to changing in temperature, pH, ageing time [135, 137, 203-205]. Such behaviour makes it of wide interest among scientists and engineers. For agricultural and biogeochemists, the information about the availability of soluble iron(III) in sea water and soils for example are required. Because it is capable to give indication how microorganisms, living organisms and plants can obtain soluble iron from ambient (e.g water and soil) especially at circumneutral pH where most of the iron(III) is in solid form [206-208]. For engineers and geochemists, the precipitation of iron(III) is a crucial issue for environmental treatment. The precipitation of soluble species of iron by rising the pH is one of the most common remediation process used for acid mine drainage systems. As natural water systems are complex, due to their reactions are commonly simultaneous reactions [1, 21, 208, 209].

Thermodynamic principles can be used as powerful manner to calculate chemical speciation and to determine the changing in chemical distribution in environmental systems using geochemical modelling. The geochemical models are usually purely based on thermodynamic equilibria, because large databases of thermodynamic information are available. They have been widely used to predict solubility and distribution of iron species in acidic mine drainages [210-212], sulfate [65] and trace metal speciation in natural waters [213-215].

However, the kinetics of several chemical reactions (hydrolysis and precipitation processes in acidic mine drainages) may be slow, and they require extra time to reach the equilibrium state. A good example is Fe(III)-SO_4(II)-H_2O system where different iron(III) solid phases can be formed depending on hydrolysis conditions. The solid phases formed can be basic sulfate complexes, hematite, goethite, ferrihydrite, jarosite, schwertmannite or amorphous hydrous ferric oxide depending on temperature, pH and solution composition [87-89].

Also it has been established that SO_4^{2-} ions can catalyze the initial condensation and nucleation steps and suppress formation of high polymers of iron oxyhydorxide [108, 111], (depending on these studies we propose a scheme figure 5.1 to give a clear picture for our following interpretations). Therefore, the kinetics of hydrolysis and precipitation processes of iron(III) in presence of sulfate has to be taken in to account, and the thermodynamic calculations have to be used with appropriate caution.

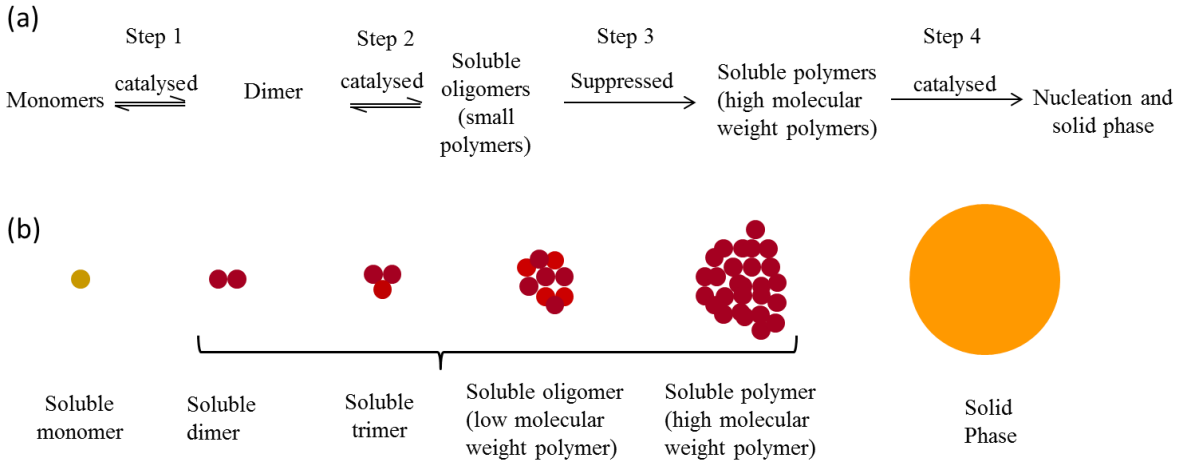

Figure 5.1: Effects of sulfate on hydrolysis process of iron(III) (a), and the terms used in this work for soluble hydrolysed iron(III) species and solid phase (b). The colours in (b) are chosen to approximate the colours of the actual solutions or precipitates.

Numerous studies have investigated the kinetics of hydrolysis and precipitation of iron(III) in sea water [216] and laboratory aqueous solutions at pH (6.0 – 9.0) [217, 218]. At low pH (pH < 4) the first order rate constant of iron(III) chloride precipitation was measured using a potentiometric technique (Ross combination electrode) on the basis that dissolved iron(III) species $Fe(OH)_{3(eq)}$ are lost from the solution by two steps; a slow initial polymerization step, followed by a rapid crystalline growth step. The drawback of this method is that Fe^{3+} ions decrease the rate of crystalline growth due to either incorporation of Fe^{3+} in the structure of the precipitate or by adsorbing on active sites of precipitate [219]. These studies have found that the precipitation process is first order with respect to dissolved $Fe(OH)_{3(aq)}$.

Kinetic studies of the hydrolysis of iron(III) monomers and dimers in diluted solutions in the presence and absence of sulfate ions have been performed using the stopped-flow technique [220], and pressure-jump relaxation kinetic technique [105, 139, 221]. These studies have concluded that the first hydrolysis of iron(III) [$Fe^{3+} \rightleftharpoons Fe(OH)^{2+} + H^+$] reached the equilibrium very rapidly and kinetic information was not obtained. This is in line with the usual expectation that proton transfer to oxygen is faster than the time

scale of CV or SWV experiments used in this work.

The second hydrolysis reaction (k_2) was found to be a first order reaction, while the formation of iron(III)-monosulfate and dimer formation were found to be second order reactions. The rate constants of these reactions were measured depending on ionic strength and temperature; they are summarized in table (5.1). One of the aforementioned studies also reported that the presence of sulfate speeds up the formation of iron(III) dimer [108].

Reaction	Rate constant	units	*n*	μ/M	T/^{o}C	Ref.
$Fe(OH)^{2+} \overset{k_2}{\rightleftharpoons} Fe(OH)_2^{+} + H^{+}$	6.1×10^4	s^{-1}	1	0.0003	25	[139]
$Fe^{3+} + SO_4^{2-} \overset{k_1}{\rightleftharpoons} FeSO_4^{+}$	4.6×10^3	$M^{-1} s^{-1}$	2	0.5	25	[105]
$2Fe(OH)^{2+} \overset{k_{12}}{\rightleftharpoons} Fe_2(OH)_2^{4+}$	4.5×10^2	$M^{-1} s^{-1}$	2	0.5	25	[108]

Table 5.1: Rate constants of hydrolysis of monomers and dimer formation of iron(III), *n* is order of reaction, μ is ionic strength and T is temperature

In this work we used a simple electrochemical method to study the kinetics of hydrolysis of iron(III) solutions at (pH > 4) to include wide range of hydrolysis steps starting from monomers, dimers, trimer, …., and oligomer of soluble iron(III) species by monitoring the release of H^+ ions. This method avoids possible errors resulting from adsorption or incorporation of soluble iron(III) species on or in solid precipitates [219]. In addition, we developed a spectroscopic technique using Raman spectroscopy to study the kinetics of the hydrolysis of iron(III) perchlorate and iron(III) sulfate in concentrated aqueous solution. Also, we studied the effects of SO_4^{2-} ions on the kinetics of precipitation of soluble iron(III) species using square wave voltammetry (SWV).

5.2 Results and discussion

5.3 Kinetic studies of iron(III) hydrolysis in laboratory and environmental samples using a chronopotentiometric technique

$[H^+]$ vs. time curves of iron(III) perchlorate, iron(III) sulfate and Shilbottle solutions are shown in figures 5.2, 5.3 and 5.4. The principle of the curve was designed on the basis that, the hydrolysis of iron(III) in aqueous solutions releases hydrogen ions (H^+) into the solution, and these ions were monitored versus time using a glass electrode and

useful kinetic information can be acquired. It has been established in several studies [90, 91, 94, 126] that after dissolving iron(III) salts in water, the pH of such solutions decreases with time depending on the iron concentrations.

Previous study [126] has concluded that the solutions with low iron(III) concentrations (0.0002 – 0.001 M) immediately reached the supersaturation state with respect to amorphous iron(III) hydroxide, and that the supersaturation decreases with increasing iron(III) concentrations because of pH effects. In other words, in the case of diluted solutions, a large number of nuclei were formed immediately after dissociation, these go on to form polymers and leave a small fraction of monomers for further hydrolysis processes. While at high iron concentrations (conc. > 0.004 M) the degree of supersaturation decreased and a large number iron(III) monomers were available to continue hydrolysis. Also, the study has pointed out that the addition of NaOH can enhance the polymerization and nucleation process of iron(III) by which the supersaturation state is rapidly achieved.

Therefore, it can be clear that the major source for H^+ ions in such solutions is from condensation of simple species of iron(III) followed by agglomeration of the formed species to form oligomers and higher molecular weight polymers. Such decreases in pH may be attributed to the hydrolysis of iron(III) salts in aqueous solutions which releases (H^+) ions according to the following reactions (5.1 – 5.4) as well as to other higher polymer equilibria:

$$2[Fe(H_2O)_6]^{3+} \rightleftharpoons [Fe_2(H_2O)_{10}(OH)_2]^{4+} + 2H^+ \quad \text{.....(5.1)}$$

$$[Fe(H_2O)_6]^{3+} + [Fe(H_2O)_5(OH)]^{2+} \rightleftharpoons [Fe_2(H_2O)_{10}(OH)_2]^{4+} + H^+ \quad \text{.....(5.2)}$$

$$3[Fe(H_2O)_5(OH)]^{2+} \rightleftharpoons [Fe_3(H_2O)_{14}(OH)_4]^{5+} + H^+ \quad \text{.....(5.3)}$$

$$[Fe(H_2O)_5(OH)]^{2+} + [Fe(H_2O)_5(OH)]^{2+} \rightleftharpoons [Fe_2(H_2O)_9(OH)_3]^{3+} + H^+ \quad \text{..(5.4)}$$

The released H^+ was measured potentiometrically by observing the variation with time of the potential of the glass electrode after addition of a certain amount of NaOH (aq).

A theoretical model for a simple second order reaction was fitted to the experimental data according to equations (5.5). The curves exhibited evident identity between experimental and theoretical data.

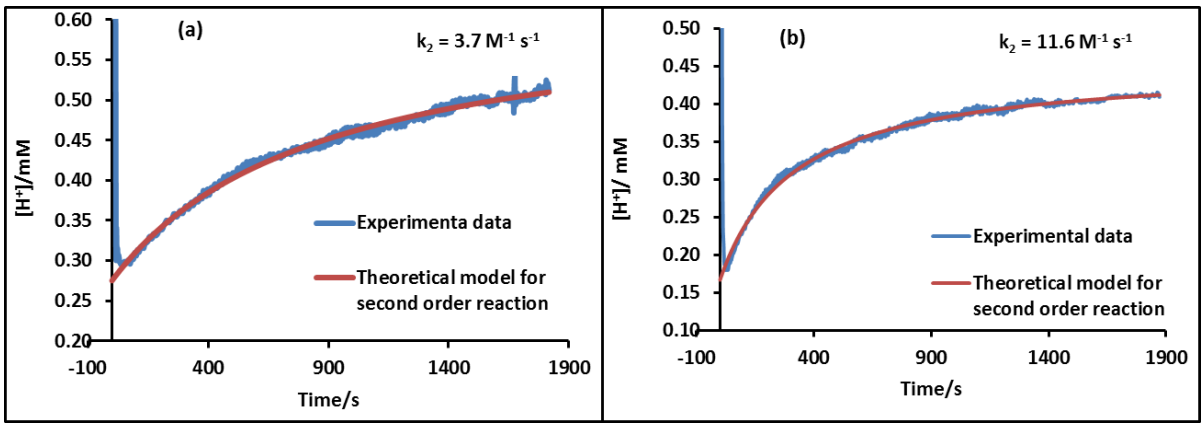

Figure 5.2: $[H^+]$ vs. time curves of 0.015 M of iron(III) perchlorate solution at $[OH^-]/[Fe^{3+}]$ ratios (a)= 1.0, (b)=1.5), theoretical model of simple second order reaction was fitted to the experimental data.

$$[H^+]_{tot.} = [H^+]_{pro.}\left[1- \frac{1}{1+kt\,[H^+]_{pro.}}\right] + [H^+]_{int.} \qquad \text{.....(5.5)}$$

Where $[H^+]_{int.}$ denotes the initial concentration of hydrogen ion at (t = 0), $[H^+]_{pro.}$ denotes the concentration of hydrogen ion produced by the reaction at completion, $[H^+]_{tot}$ denotes the total hydrogen concentration at any time (t), t is the time and k is the rate constant.

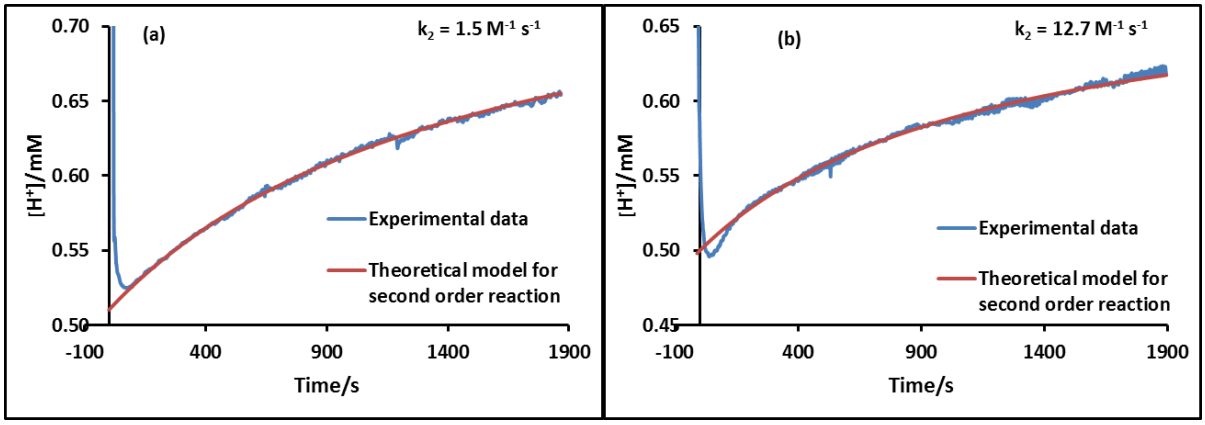

Figure 5.3: $[H^+]$ vs. time curves of 0.015 M of iron(III) sulfate solution at $[OH^-]/[Fe^{3+}]$ ratios (a)= 1.0, (b)=1.5), theoretical model of simple second order reaction was fitted to the experimental data.

Simple mechanisms can be suggested to rationalize the condensation of monomer species to form dimers and also to rationalize the condensation of dimers and trimers to form high oligomers as shown in the following mechanisms (1 and 2):

Mechanism (1)

$$2[Fe(H_2O)_5(OH)]^{2+} \xrightarrow{k_2^*} [Fe_2(H_2O)_{10}(OH)_2]^{4+} \quad \text{.....(reaction 1)}$$

$$[Fe(H_2O)_6]^{3+} + [Fe(H_2O)_5(OH)]^{2+} \xrightarrow{k_2} [Fe_2(H_2O)_{10}(OH)_2]^{4+} + H^+ \quad \text{....(reaction 2)}$$

$$[Fe(H_2O)_6]^{3+} \underset{}{\overset{K_1}{\rightleftharpoons}} [Fe(H_2O)_5(OH)]^{2+} + H^+ \quad \text{.....(reaction 3)}$$

$$v = 2k_2^* \left([Fe(H_2O)_5(OH)]^{2+} \right)^2 + k_2 \left([Fe(H_2O)_6]^{3+} \right) \left([Fe(H_2O)_5(OH)]^{2+} \right)$$

$$= \frac{2k_2^* K_1^2 + k_2 K_1 [H^+]}{[H^+]^2} \left([Fe(H_2O)_6]^{3+} \right)^2$$

$$= k_{obs} \left([Fe(H_2O)_6]^{3+} \right)^2 \quad \text{.....(5.6)}$$

Where k_2^* and k_2 are rate constants for reactions (1) and (2), respectively. K_1 is equilibrium constant for reaction (3), and $k_{obs.}$ is the observed rate constant.

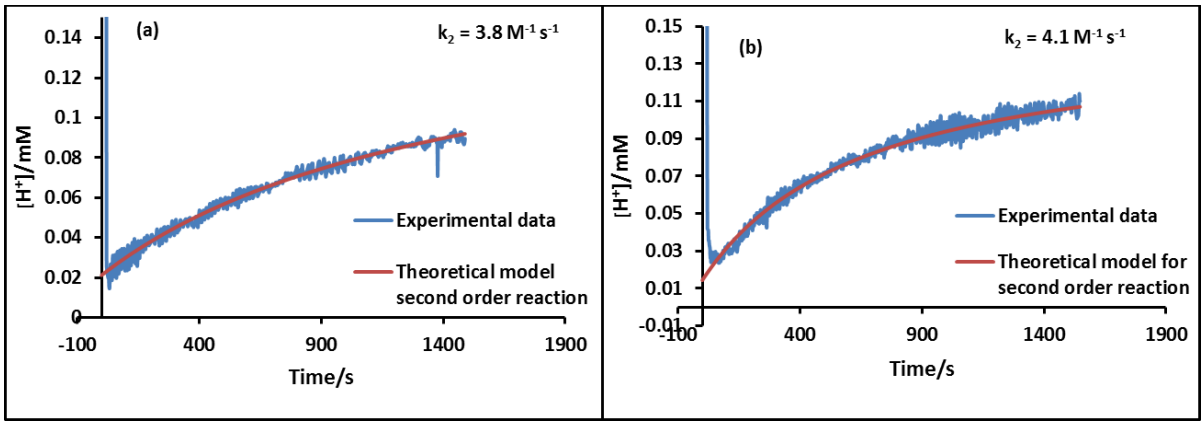

Figure 5.4: $[H^+]$ vs. time curves of two settlement lagoons of Shilbottle samples (a) lagoon 01 and (b) lagoon 03 after addition certain amount of NaOH, theoretical model of simple second order reaction was fitted to experimental data.

Mechanism (2)

$$2[Fe_2(H_2O)_{10}(OH)_2]^{4+} \xrightarrow{k_2^*} [Fe_3(H_2O)_{14}(OH)_4]^{5+} + [Fe(H_2O)_5(OH)]^{2+} + H^+$$

$$2[Fe(H_2O)_5(OH)]^{2+} + [Fe_2(H_2O)_{10}(OH)_2]^{4+} \xrightarrow{k_2} [Fe_4(H_2O)_{18}(OH)_6]^{6+} + 2H^+$$

$$2[Fe(H_2O)_5(OH)]^{2+} \underset{}{\overset{K_1}{\rightleftharpoons}} [Fe_2(H_2O)_{10}(OH)_2]^{4+}$$

$$v = k_2^* \left([Fe_2(H_2O)_{10}(OH)_2]^{4+}\right)^2 + 2k_2\left([Fe(H_2O)_5(OH)]^{2+}\right)^2 \left([Fe_2(H_2O)_{10}(OH)_2]^{4+}\right)$$

$$= k_2^* \left([Fe_2(H_2O)_{10}(OH)_2]^{4+}\right)^2 + 2k_2 \left[\left(\frac{[Fe_2(H_2O)_{10}(OH)_2]^{4+}}{K_1}\right)^{\frac{1}{2}}\right]^2 [Fe_2(H_2O)_{10}(OH)_2]^{4+}$$

$$= k_2^* \left([Fe_2(H_2O)_{10}(OH)_2]^{4+}\right)^2 + \frac{2k_2}{K_1} \left([Fe_2(H_2O)_{10}(OH)_2]^{4+}\right)^2$$

$$= \frac{k_2^* K_1 + 2k_2}{K_1} \left([Fe_2(H_2O)_{10}(OH)_2]^{4+}\right)^2$$

$$= k_{obs} \left([Fe_2(H_2O)_{10}(OH)_2]^{4+}\right)^2 \qquad \text{……..(5.7)}$$

A simple scheme can be drawn to generalise these mechanisms as follows:

$$[Fe_m(H_2O)_a]^{x+} + [Fe_n(H_2O)_b]^{y+} \rightarrow [Fe_{m+n}(H_2O)_{a+b-z}(OH)_z]^{(x+y-z)+} + zH^+$$

Where $[Fe_m(H_2O)_a]^{x+}$ and $[Fe_n(H_2O)_b]^{y+}$ are different soluble species of iron(III), (m and n are numbers = 1, 2, 3, ….., etc.), and H^+ is hydrogen ions released as a result to hydrolysis process.

These mechanisms (5.6 and 5.7) predict that the reaction is second order with respect to soluble iron species. Also, it is apparent that the dimerization process as well as various other condensation steps (trimer and high oligomers) can be regarded as a main source for H^+ ions. This is in good agreement with a previous study [126] in which the H^+ ions were released into the solution as a result of condensation processes of monomer iron(III) species to form dimers, trimer and high polymers.

The rate constant k_{obs} was estimated for two iron(III) concentrations (0.0025 and 0.015 M) in sulfate and perchlorate media with two different $[OH^-]/[Fe^{3+}]$ ratios (1.0 and 1.5) and for three settlement lagoons of Shilbottle samples. The values obtained are presented in tables 5.2 and 5.3, respectively.

From table 5.2 it can be observed that the rate constants appear to be similar for (0.0025 and 0.015 M) of both iron(III) salts (perchlorate and sulfate) at $[OH^-]/[Fe^{3+}]$ ratio 1.5. However, the rate constants are slightly less at $[OH^-]/[Fe^{3+}]$ ratios 1.0 than 1.5

especially in the case of 0.015 M of iron(III) by factor of 3 and 8 for iron(III) and perchlorate and sulfate, respectively.

Iron salt	$Fe(ClO_4)_3$		$Fe_2(SO_4)_3$	
Iron concentration / M	0.0025	0.015	0.0025	0.015
$[Fe^{3+}]/[OH^-]$ ratio	Rate constant / M^{-1} s^{-1}			
1.0	6.6	3.6	8.1	1.5
1.5	9.6	11.6	11.2	12.7

Table 5.2: Rate constants (k_{obs}) for two iron(III) concentrations (0.0025 and 0.015 M) in perchlorate and sulfate media with two different $[OH^-]/[Fe^{3+}]$ ratios (1.0 and 1.5).

A possible interpretation which can be made according to [126] is that, at a concentration of 0.015 M of iron(III), the supersaturation of the solution in respect to amorphous iron(III) hydroxide is low because the pH is low and a considerable amount of soluble iron(III) monomers are present in the solution. Therefore, in such high concentrated solutions where the pH is rather low (pH ≈ 2.5), the supersaturation can be achieved only with high ratio of $[OH^-]/[Fe^{3+}]$ in order that the dimerization and subsequent condensation processes can take place in the solution. In turn, they also release H^+ ions into the solution.

Also, it can be observed that, the rate constants in sulfate media were close to their counterparts in perchlorate media, despite the fact that sulfate has been reported to speed up the condensation of hydrolysed species of ion(III) to form dimers. In turn, it can affect the kinetics of the hydrolysis [108]. It has also been pointed out that the induction time (the time between addition of base and the start of the pH decrease) decreases with increasing pH, but it increases with increasing sulfate concentrations [222].

Our results were in agreements with above findings in respect to effects of pH on the hydrolysis kinetics, while they did not exhibit marked effects of sulfate on the kinetics of hydrolysis in respect to the induction time and release of hydrogen ions. There are two possible reasons which may be valid to interpret the observed results. The first (which is for induction time) may be due to using NaOH instead of $NaHCO_3$, which was used in previous study [222] since NaOH is a stronger base than $NaHCO_3$. Accordingly, the replacement of OH^- with SO_4^{2-} ligands during base addition to form simple iron(III)-hydroxo species such as Fe^{3+}, $(Fe(OH)^{2+}$ and $Fe(OH)_2^+$ along with

iron(III)-sulfate species ($FeSO_4^+$) is more likely than in the case of $NaHCO_3$, as it has been pointed out in previous studies that, the sulfate can be replaced by OH^- with increasing pH [89, 222, 223].

Furthermore, The rate (k_{ex}/s^{-1}) for exchange of water molecules as a ligands in the octahedral aqua complex of iron(III) $Fe(H_2O)_6^{3+}$ is about 10^3 s^{-1}, this indicates that iron(III) possesses rapid ligand exchange [224]. Accordingly, the formed iron(III)-hydroxo species ($Fe(OH)^{2+}$ and $Fe(OH)_2^+$) after addition NaOH may behave in similar manner in the case of iron(III) perchlorate in respect of decrease of induction time.

The second possibility (which is for releasing hydrogen ions) is that, the overall processes of iron(III) hydrolysis responsible for releasing H^+ ions may be equal in sulfate solution to that in perchlorate. In other words, the mount of released hydrogen ions resulting from simultaneous processes such as dimerization, oligomerization and/or polymerization and nucleation in both solutions may be equal. It is well known that all iron(III) hydrolysis processes occur simultaneously and they release H^+ ions into the solution. Sulfate ions have been established to suppress formation of higher polymers and catalyse dimerization, oligomerization and nucleation processes [108, 111]. Therefore, the overall rate of such different effects in sulfate solutions may be close in respect to releasing H^+ to that in perchlorate solution where the rate of polymerization and nucleation were not influenced by perchlorate. This leads to that iron(III) in perchlorate and sulfate solutions exhibit fairly analogous behaviour in respect to the rate and the amount of H^+ released.

It can be concluded that, the rate of hydrolysis and condensation of simple soluble species of iron(III) in aqueous solutions depend mainly on the amount of added base. It was observed that rate constants at $[OH^-]/[Fe^{3+}]$ ratio 1.5 were higher than their counterparts with $[OH^-]/[Fe^{3+}]$ ratio 1.0.

Analogous observations were observed in environmental samples in respect of increasing hydrogen concentrations after addition of NaOH. However, the rate constant values were slightly smaller than observed in laboratory solutions. This may be due to, the lower concentration of iron(III) in Shilbottle solution compared to iron(II). It has been established that, the hydrolysis constants (pK_a) of iron(II) species in aqueous solutions are 9.4, 20.5 and 29 for $[Fe(H_2O)_6]^{2+}$, $[Fe(H_2O)_5(OH)]^+$ and

$[Fe(H_2O)_4(OH)_2]^{4+}$, respectively. Accordingly, iron(II) species start to hydrolyse at pH > 8.0 which is much higher than the pHs studied in this work [225].

Sample name	Lagoon 01	Lagoon 02	Lagoon 03
Rate constant / $M^{-1}s^{-1}$	3.8	6.0	4.1

Table 5.3: Rate constants (k_{obs}) for three environmental samples: lagoon 01, lagoon 02 and lagoon 03.

Finally, the obtained rate constants for hydrolysis of iron(III) in laboratory solution were considerably less than obtained for iron(III) dimer formation, according to following equation:

$$2[Fe(H_2O)_5(OH)]^{2+} \underset{k_{21}}{\overset{k_{12}}{\rightleftharpoons}} [Fe_2(H_2O)_{10}(OH)_2]^{4+} \qquad \text{.....(5.8)}$$

As it has been reported in [108] that k_{12} was 450 M^{-1} s^{-1} at 25 ^oC and an ionic strength of 0.5 M. Such a lowering in rate constant in our measurements may be attributed to the possibility that, in our method multiple steps of hydrolysis such as dimerization, condensation, oligomerization and polymerization are involved in the H^+ release. Some of these steps may be slow, whereas in the previous study [108], the measurements were limited merely to the dimerization step which may be faster than other complicated agglomeration processes.

5.4 Kinetic studies of iron(III) hydrolysis in laboratory solutions using Raman spectroscopy technique

Using a Raman technique for kinetic studies in liquid aqueous solutions required relatively elevated concentrations of sample solution (about 0.25 M or higher) for a proper signal to noise in the spectra. As a result, 0.25 M of iron(III) perchlorate and iron(III) sulfate solutions with the appropriate amount of NaOH to obtain $[OH^-]/[Fe^{3+}]$ ratio about 1.0 were studied. On the other hand, kinetic information of 0.25 M of iron(III) in aqueous solutions at $[OH^-]/[Fe^{3+}]$ ratios more than 1.0 were not obtained because the perchlorate and sulfate signals were not observed. This may be attributed to scattering or absorption of the excitation light due to the dark colour of such concentrated solutions and presence of large solid particles.

The obtained Raman spectra are shown in figure 5.5a and 5.5b for iron(III) in perchlorate and sulfate media, respectively. Kinetic studies for Shilbottle solutions using Raman spectroscopy were also not possible due to the low iron concentrations which are less than 0.01 M. It is apparent from figure 5.5 that the Raman intensities of the symmetric stretching band (ν_1) at about 980 cm^{-1} increased with time after addition of an appropriate amount of NaOH to 0.25 M of iron(III) solution ($[OH^-]/[Fe^{3+}]$ ratio ≤ 1.0). Such increases may be ascribed to the fact that, the sulfate anions can form hydrogen-bonding and/or inner-sphere complexes with iron(III) clusters [34]. It has been found that the intensity of Raman signals of iron(II) sulfate increased with increasing temperature and sulfate concentration, and that was ascribed to the formation of sulfate inner-sphere complex [155]. Similar behaviour can be expected for perchlorate ligands with iron clusters.

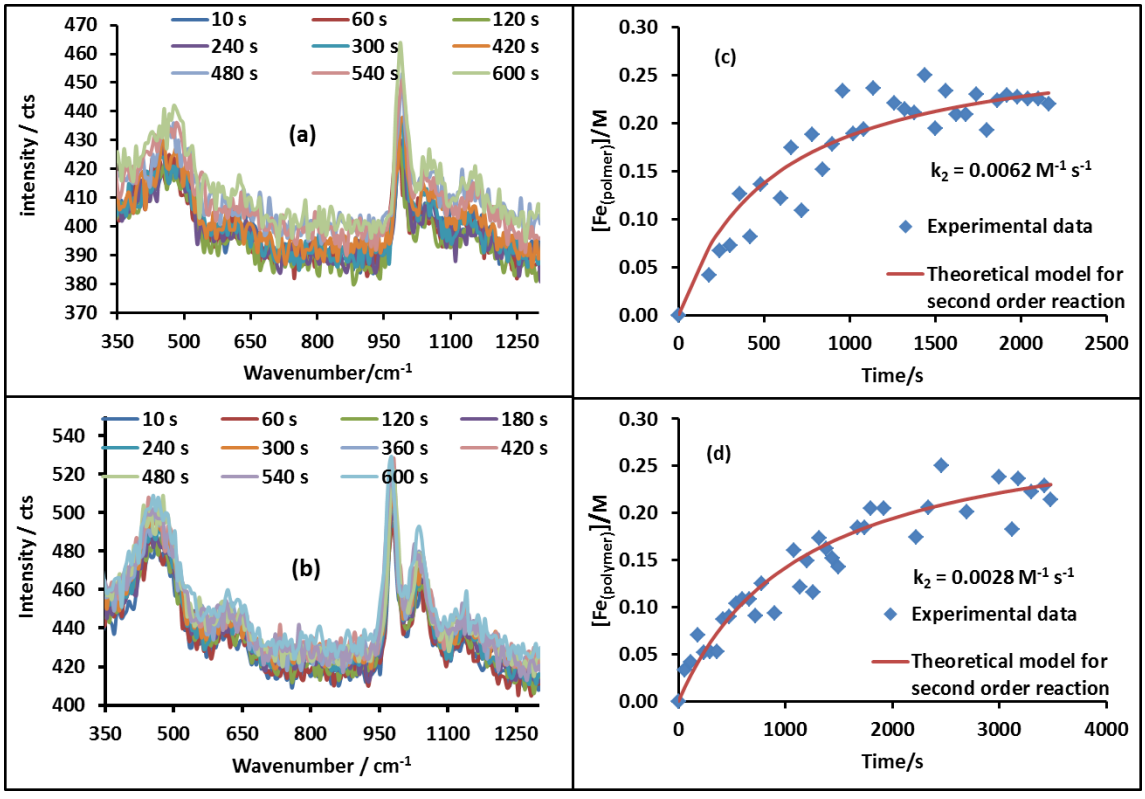

Figure 5.5: (a) and (b) are Raman spectra of 0.25 M of iron(III) in perchlorate and sulfate media, respectively at $[OH^-]/[Fe^{3+}]$ ratio 1.0; (c) and (d) theoretical model of simple second order reaction was fitted to the experimental data for iron(III) perchlorate and iron(III) sulfate, respectively.

Although perchlorate (ClO_4^-) anion is usually classified as a non-coordinating ligand or it can only form outer-sphere complexes, a large number of studies have discovered that ClO_4^- can be associated into inner-sphere complexes only when the competition with stronger Lewis bases was not involved in the solution. For example, the complexes of

nickel (II) and ethylenediamine with ClO_4^- $[Ni(en)_2(ClO_4)_2]$ and acetonitrile with nickel (II) perchlorate $[Ni(CH_3CN)_4(ClO_4)_2]$ have been prepared and characterized using vibrational analysis techniques (IR) [226, 227]. ClO_4^- in these complexes has been assigned to form bidentate and monodentate coordination complexes with ionic metals, respectively. Further, it has been established that the ClO_4^- can associate with iron(III) to form $[FeClO_4]^{2+}$ and the absolute stability constant (K) was evaluated using spectrophotometric measurements and mathematical treatments (K = 2.1) [228], while inner-sphere coordination of sulfate into iron(III) has been shown in several places [34, 38, 229].

Accordingly, the perchlorate and sulfate can be coordinated either as inner-sphere with iron(III) clusters which is less probable or bonded to iron(III) clusters via hydrogen bonding. Perchlorate and sulfate appear similar in the pattern vibration modes, because both exhibit fundamental tetrahedral vibration modes in Raman spectra. The relationship between formed complexes and the resulting Raman spectra are illustrated in figure 5.6.

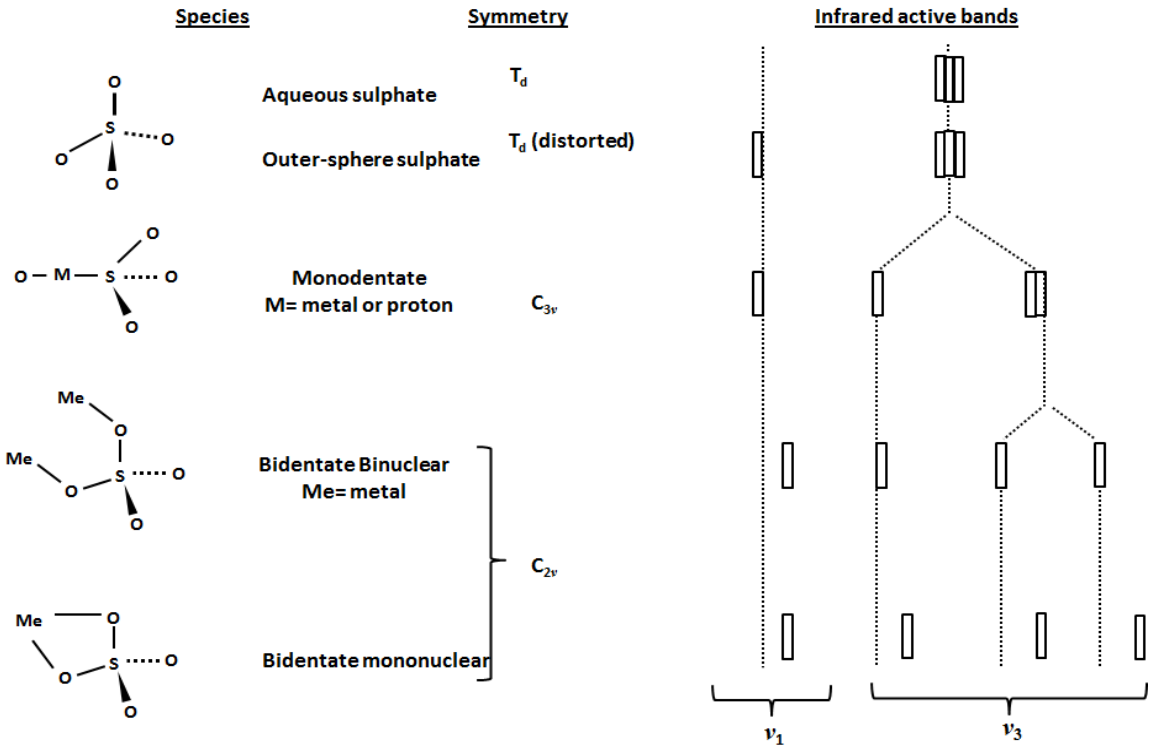

Figure 5.6: The relationship between the molecular symmetry of sulfate complexes and the observed infrared spectrum. Adapted from Ref.[230]

From figure 5.6, it is obvious that both sulfate and perchlorate ions exhibit high tetrahedral symmetry T_d and T_d distorted in free aqueous solution and outer-sphere

complexes, respectively. If the complexation of SO_4^{2-} and ClO_4^- with a metal ion takes place, the anion's symmetry will be lowered to (C_{3v} and/ or even C_{2v}), and degenerate vibrations of v_3 split into different wavenumbers depending on the bonding with metal ion whether it is monodentate, bidentate or bridged bidentate.

Accordingly, our findings appear to be consistent with a monodentate complex of sulfate with iron(III) clusters, as the v_3 band split into two bands at about 1046 and 1136 cm^{-1} (figure 5.5 b). While in the case of perchlorate, the v_3 modes were split into two very weak bands at about 1050 and 1145 cm^{-1} (figure 5.5 a), which indicates that monodentate bonds with iron(III) clusters may also occur. The two possible monodentate interactions of these ligands either by hydrogen bonding or inner-sphere with iron(III) clusters are illustrated in figure 5.7. It has been reported that the sulfate ions strongly interact with iron(III) to form soluble and solid complexes; these complexes are mainly hydrogen-bonded and less frequently in inner-sphere complexes [34].

These observations indicate that the hydrolysis of iron(III) occurred after addition of NaOH and condensation of iron(III) (probably dimers, trimers or high oligomers) formed and these oligomers and polymers coordinate with sulfate and perchlorate mostly by hydrogen-bonding and to a lesser extent by inner-sphere interactions. This is because the pHs of these solutions are about 1.8.

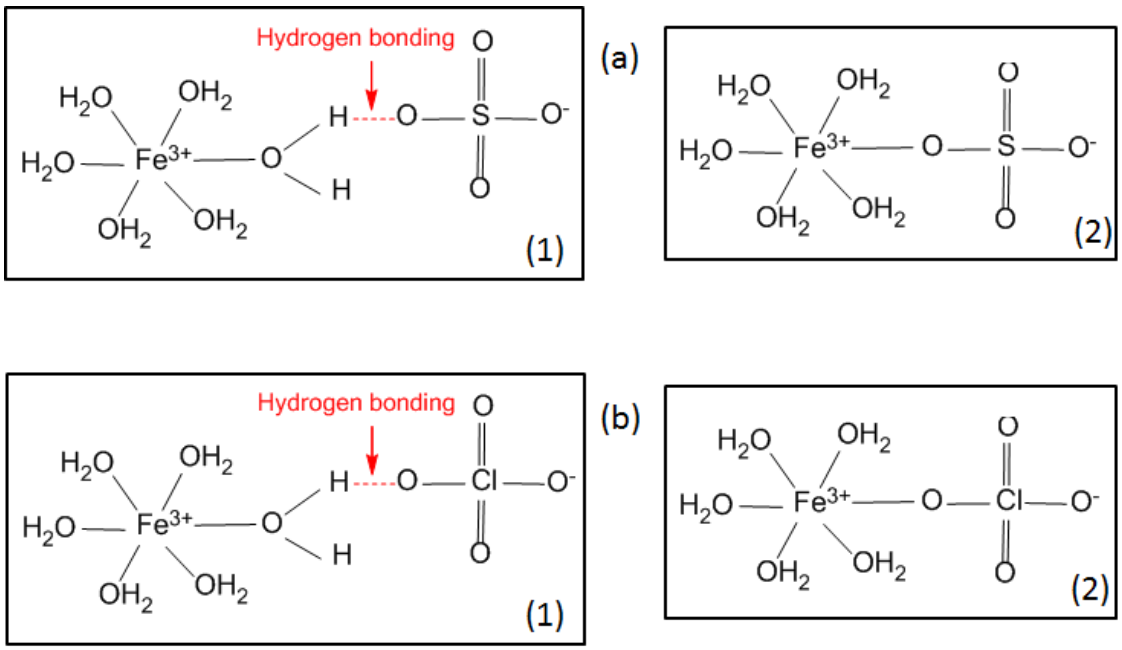

Figure 5.7: Showing the complexation of iron(III) with, (a) sulfate and (b) perchlorate (1) via hydrogen bonding, (2) inner-sphere coordination.

The change in Raman intensity (area under peak) of the symmetric stretching band (v_1) at about 980 cm^{-1}versus time was plotted (figure 5.5 c and 5.5 d). A theoretical model for a simple second order reaction was fitted to the obtained data, and they showed a good fit of theoretical curve to the data. Therefore, the hydrolysis of iron(III) in aqueous solution after addition NaOH is considered to be second order in respect to the iron. Due to the complexity of such hydrolysis processes, a proposed mechanism by which one can describe the process was not possible to provide. The rate constants calculated for both media (perchlorate and sulfate) are shown in table 5.3. The rate constants were close to each other in perchlorate and sulfate media. This indicates that the rate of monodentate coordination of ClO_4^- and SO_4^{2-} with iron(III) clusters is similar.

Solution	Iron(III) perchlorate	Iron(III) sulfate
Rate constant M^{-1} s^{-1}	6.2×10^{-3}	2.8×10^{-3}

Table 5.4: Rate constants of hydrolysis of 0.25 M iron(III) in two different media (perchlorate and sulfate) with $[OH^-]/[Fe^{3+}]$ ratio = 1.0 using Raman spectroscopy.

The changes (area under peak) of asymmetric stretching band (v_3 at 1080 cm^{-1}) and other two bending bands (v_2 at about 480 cm^{-1}) and (v_4 at about 645 cm^{-1}) with time were not observed in both iron(III) solutions (perchlorate and sulfate) figure 5.8. This indicates that the changes in the symmetric stretching band (v_1) in figure (5.5 a and 5.5 b) are due to chemical processes, and not simply the changes in intensity of the laser or changes in the detection of the light.

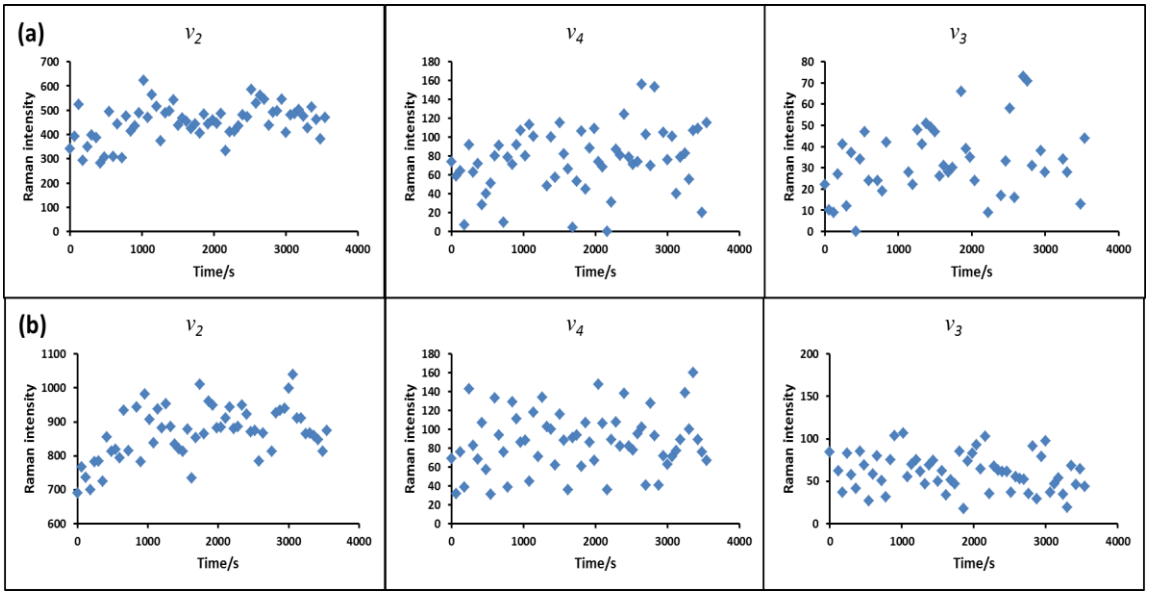

Figure 5.8: Raman intensities (area under peak) of asymmetric stretching band (v_3) and two bending bands (v_2) and (v_4) for (a) perchlorate, (b) sulfate in iron(III) solution.

5.5 Kinetic studies using Voltammetry

SWV was used to study the effects of sulfate ions (SO_4^{2-}) on the depletion of soluble species of iron(III) from aqueous solution, oligomerization of soluble iron(III) and the rate of oligomer formation.

5.6 Depletion of soluble species of iron(III)

Effects of sulfate ions (SO_4^{2-}) on the depletion of soluble species of iron(III) in aqueous solution were investigated, figure 5.9 a and 5.9 b illustrate the reduction peak of soluble complexes of iron(III) of 0.015 M of iron(III) in perchlorate and sulfate media, respectively. It is clear from the figure 5.9 that soluble species of iron(III) in sulfate solution (e. g. $FeSO_4^+$) stay dissolved in the solution longer than soluble species of iron(III) in perchlorate media (e.g. Fe^{3+}). This is shown by the disappearance of the reduction peak of soluble species of monomeric Fe(III)-sulfate only after addition of NaOH until the $[OH^-]/[Fe^{3+}]$ ratio exceeded 2.3. At a $[OH^-]/[Fe^{3+}]$ ratio of 2.4 the soluble species of monomeric iron(III) were entirely precipitated and depleted from the solution. In contrast, the soluble species of iron(III) in perchlorate were entirely precipitated and converted to the solid phase at an $[OH^-]/[Fe^{3+}]$ ratio of 2.1.

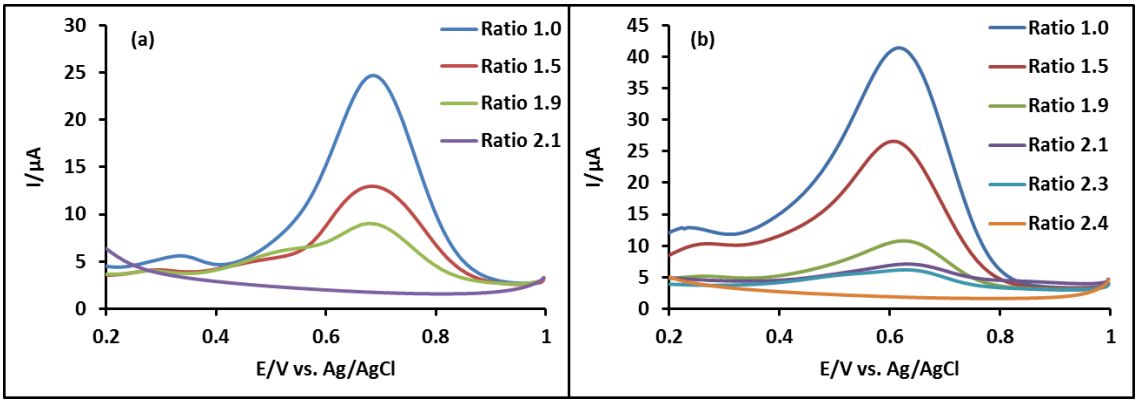

Figure 5.9: (a) and (b) are square wave voltammograms of 0.015 M iron(III) in (a) perchlorate and (b) sulfate media, respectively, with different ratios of $[OH^-]/[Fe^{3+}]$, (initial E = 1.0 V, low E = 0.2 V, amplitude = 0.025 V, frequency = 15 Hz, sample interval 0.004 V, quiet time = 2.0 s and sensitivity = 1.0×10^{-5} A/V), the working electrode was a 1 mm radius platinum electrode; the reference electrode was Ag/AgCl. The solution was not degassed.

The kinetic aspects of such variation in sulfate solution can be ascribed to the role of sulfate ions (SO_4^{2-}) in formation of $FeSO_4^+$ complexes with iron(III). Therefore, a possible interpretation of such behaviour can be ascribed to that p*K*a of $FeSO_4^+$ (which

we have calculated in this study chapter 4) is about 4.38 ± 0.16 which requires more NaOH to hydrolyse than soluble species of Fe^{3+} for which p*K*a is about 2.75.

5.7 Study of the effects of SO_4^{2-} on the hydrolysis process of iron(III) and rate of oligomerization using SWV

Several studies have demonstrated that hydrolysis and polymerization of iron(III) in aqueous solutions depend on number of parameters such pH, iron concentration, ageing time, temperature and anions [91, 99, 111, 126, 231-233]. The employed techniques were potentiometry (pH measurements), electron microscopy, ultracentrifugation, X-ray diffraction, infrared spectroscopy, light scattering using photon correlation spectroscopy and Mossbauer spectroscopy. Although, these methods and techniques have well characterized the composition, structure and morphology of the formed polymers and precipitates, these techniques did not provide kinetic information about soluble oligomers of iron(III).

In this work, electrochemical methods (using SWV) were developed to study the effects of sulfate ions on the hydrolysis of iron(III) and also kinetic aspects of the oligomerization. SWV (in chapter 3) was used to characterize soluble oligomer complexes of iron(III); it was shown that, the peak at about 0.20 V (vs. Ag/AgCl) is due to formation of soluble oligomer complexes (in this chapter labelled as $[Fe_{(oligmer)}]$). Monitoring the behaviour of this peak versus time provides useful kinetics information. In order to reveal the effects of sulfate on the hydrolysis process, two different media were used aqueous perchlorate and sulfate with iron(III).

5.7.1 Iron(III) perchlorate

Figure 5.10 shows the reduction peaks of iron(III) oligomer in perchlorate solution at around 0.2 V with an $[OH^-]/[Fe^{3+}]$ ratio of (a) 1.0 and (b) 1.5. It can be noted that the $Fe_{(oligomer)}$ reduction peak increases with time after addition NaOH to both ratios for more than 3 hours (180 min). Also the reduction peak of iron(III) monomer at about 0.730 V decreases. This indicates that condensation of low molecular weight species is continuous by forming high molecular weight polymers, and it also noted that the ClO_4^- has no effect on the oligomerization and polymerization processes.

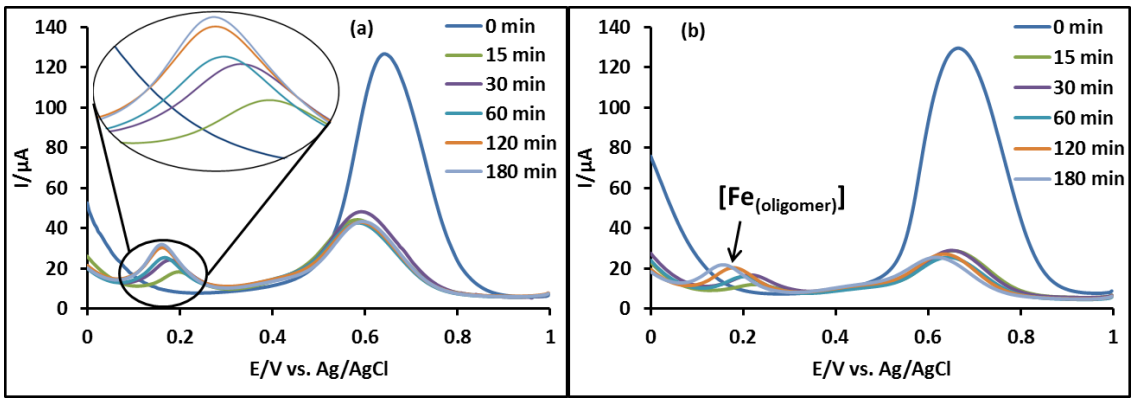

Figure 5.10: SWV voltammograms of 0.015 M of $Fe(ClO_4)_3.xH_2O$ after addition NaOH; (a) $[Fe^{3+}]/[OH^-]$ = 1.0 and (b) $[OH^-]/[Fe^{3+}]$ = 1.5, $[Fe_{(oligomer)}]$ represents iron(III) polymeric species, (initial E = 1.0 V, low E = 0.0 V, amplitude = 0.025 V, frequency = 15 Hz, sample interval 0.004 V, quiet time = 2.0 s and sensitivity = 1.0×10^{-5} A/V), the working electrode was a 1 mm radius platinum electrode; the reference electrode was Ag/AgCl. The solution was not degassed.

Moreover, it can be observed that the reduction peak of the oligomer (at around 0.2 V) shifted to the negative potential with increasing time; this can be ascribed to an increase of the oligomer mass (molecular weight) which become harder to reduce. Also, it is observed that the peak current (I_p) of soluble iron(III) oligomer [Fe $_{(oligomer)}$] increases which indicates that the soluble oligomer concentration increase as well.

The kinetic behaviour of oligomer formation was obtained by plotting peak current of formed oligomer (I_p) versus time, figure 5.11. It can be mentioned here that the same shape of the curve was acquired if the area under the peak of the formed oligomer (A_p) was plotted versus time. The theoretical model of simple second order reaction was fitted to obtained data, and rate constants were estimated at both ratios of $[OH^-]/[Fe^{3+}]$ (1.0 and 1.5), table 5.5.

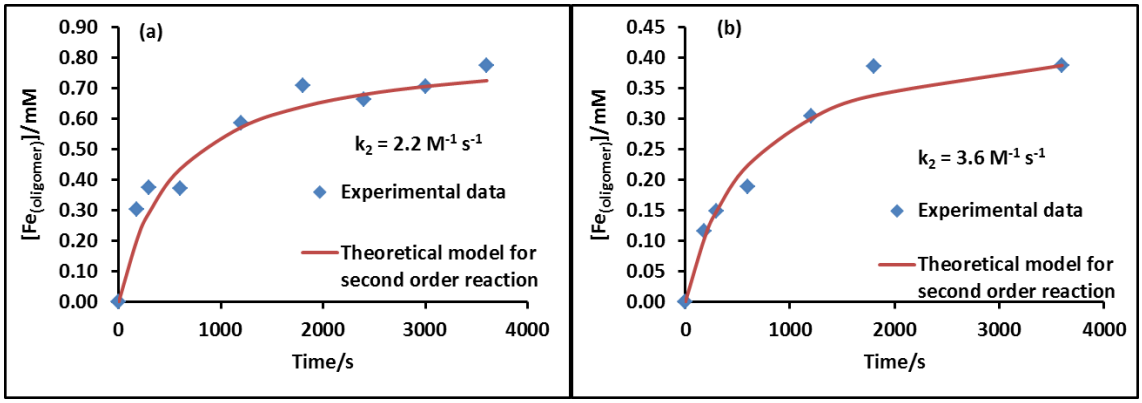

Figure 5.11: $[Fe_{(oligomer)}]$ vs. time curves of iron(III) in perchlorate solution at $[OH^-]/[Fe^{3+}]$ ratios (a) 1.0 and (b) 1.5; theoretical model of simple second order reaction was fitted to experimental data

5.7.2 Iron(III) sulfate

Figure 5.12 illustrates the reduction peak of the formed soluble iron(III) oilgomers at around 0.2 V at two different $[OH^-]/[Fe^{3+}]$ ratio (a) 1.0 and (b) 1.5 in sulfate solution. The behaviour of this peak is entirely different to that observed in perchlorate solution. From the figures 5.12, 5.13a and 13b), it is obvious that the soluble oligomer developed rapidly (in comparison to their counterparts in perchlorate) in first the 10 minutes. The soluble oligomers started to diminish with time up to nearly 180 minutes after which the soluble oligomer had disappeared from the solution. This is mainly attributed to role of SO_4^{2-} in catalysing a nucleation and formation solid phase processes which removes soluble iron(III) oligomers from the solution, and suppresses the formation of soluble high molecular weight polymers [111].

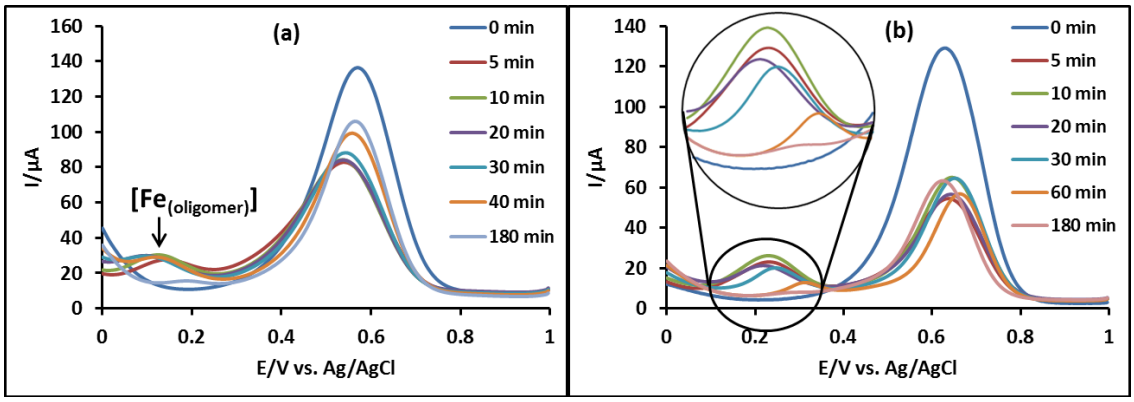

Figure 5.12: SWV voltammograms of 0.015 M of $Fe_2(SO_4)_3.5H_2O$ after addition NaOH; (a) $[Fe^{3+}]/[OH^-]$ = 1.0 and (b) $[OH^-]/[Fe^{3+}]$ = 1.5, $[Fe_{(oligomer)}]$ represents iron(III) oligomers peak, (initial E = 1.0 V, low E = 0.0 V, amplitude = 0.025 V, frequency = 15 Hz, sample interval 0.004 V, quiet time = 2.0 s and sensitivity = 1.0 × 10^{-5} A/V), the working electrode was a 1 mm radius platinum electrode; the reference electrode was Ag/AgCl. The solution was not degassed.

The rate of oligomerization process was studied by plotting the change in peak current of the formed soluble oligomers versus time figure 5.13. A theoretical model of a simple second order reaction was fitted to the obtained data and rate constants were measured for both $[OH^-]/[Fe^{3+}]$ ratios (1.0 and 1.5), table 5.5. The regression analysis was limited only to the hydrolysis process in the first 10 -15 minutes, as the fitting to theoretical model of second order was not possible in the case of sulfate due to the sharp decrease in the curve as a result of conversion of the soluble oligomers into solid phase after 15 minutes under SO_4^{2-} action.

Iron(III) salt	0.015 M $Fe(ClO_4)_3$	0.015 M $Fe_2(SO_4)_3$
$[OH^-]/[Fe^{3+}]$	Rate constant M^{-1} s^{-1}	
1.0	2.2	2.5
1.5	3.6	6.9

Table 5.5: Rate constants of oligomerization processes of 0.015 M of iron(III) in perchlorate and sulfate solutions at $[OH^-]/[Fe^{3+}]$ ratios 1.0 and 1.5.

The comparison between the rate constants of iron(III) in sulfate and perchlorate are not entirely satisfactory using this method because the duration of curve fitting was not equivalent in both cases, as it was only 10 minutes in the sulfate solution, whilst it extended to about 180 minutes in perchlorate solution. However, From table 5.5, it can be observed that, the rate of oligomerization processes increased with increasing the $[OH^-]/[Fe^{3+}]$ ratio in the first 10 minutes in sulfate solution, and in the all period of study (180 minutes) in perchlorate solution. Also it can be noted that, the rate of oligomers formation in sulfate solution seems to be slightly higher than formation of oligomers in perchlorate solution.

These observations can be confirmed from figures (5.10, 5.11a, 5.12 and 5.13a), as the oligomer reduction peak at about 0.2 V in sulfate media (figure 5.12) increased rapidly within the first 5 – 10 minutes, whereas the peak increased more slowly in iron(III) perchlorate solution (figure 5.10) for the same time (5 -10 minutes). This was mainly ascribed to the role of sulfate ions in promoting the formation of dimers and trimers followed by a rapid condensation process to form oligomer. However, after about 10 minutes of addition of NaOH, the reduction peak of soluble oligomers gradually diminished from the solution (this was observed from reduction peak at about 0.2 V), this may be due to rapid nucleation and solid formation step which was enhanced by sulfate.

Such sulfate effects were not observed in measured rate constants using chronopotentiometry (section 5.3). A possible reason we may suggest here is that, because all the hydrolysis steps take place simultaneously (dimerization, oligomerization, oligomerization and/or polymerization and nucleation), all these steps release H^+. Accordingly, the amount of H^+ ions released in this period of time (0 – 3 hours) may be equal in iron(III) perchlorate and sulfate solutions. It is well known that in sulfate solution some of these steps are suppressed and the rest are enhanced [111].

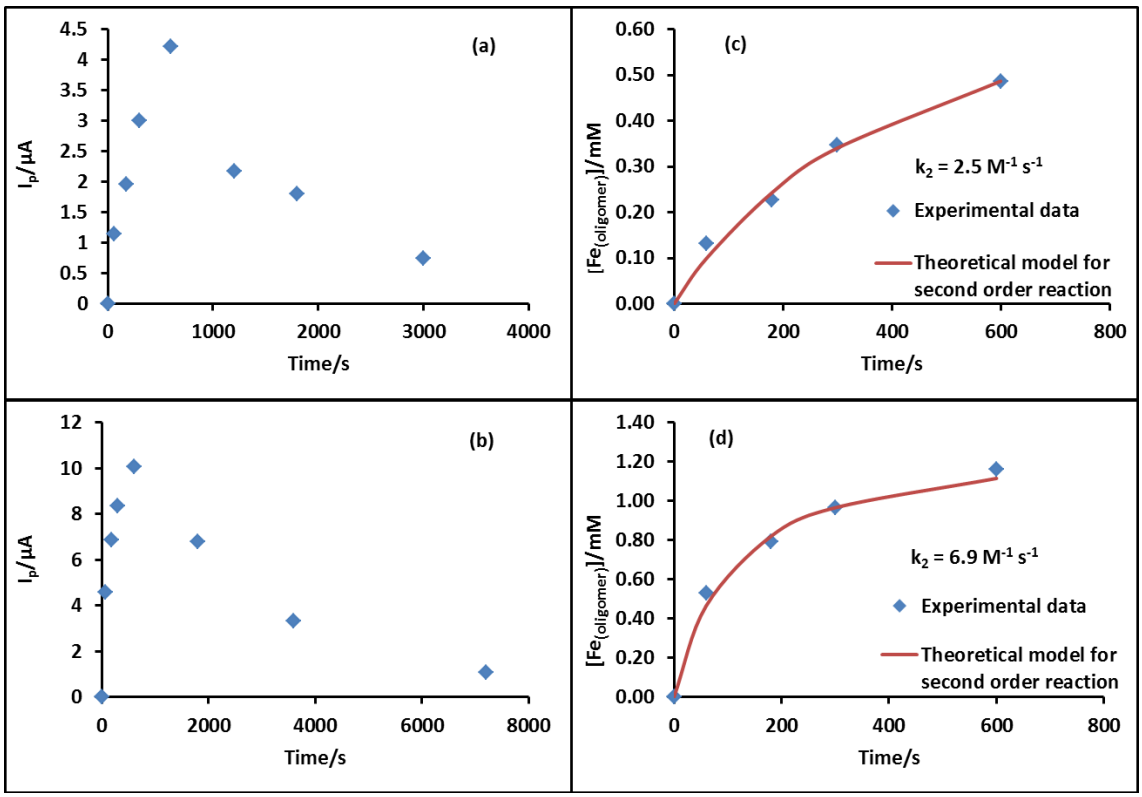

Figure 5.13: [$Fe_{(oligomer)}$] vs. time curves of iron(III) in sulfate solution at [OH^-]/[Fe^{3+}] ratios (a) 1.0 and (b) 1.5; theoretical model of simple second order reaction was fitted to experimental data (c) and (d) for [OH^-]/[Fe^{3+}] ratios (a) 1.0 and (b) 1.5, respectively.

It can be concluded from this chapter that, the kinetics of iron(III) hydrolysis in aqueous solution were studied by three methods. The first was a kinetic study of condensation of simple iron(III) species to form higher clusters and polymers of iron(III) based on monitoring of release of the H^+ using a chronopotentiometric technique, and related mechanism was proposed which was consistent with second order reaction in respect to soluble iron(III) species (equations 5.6 and 5.7). The second method was a kinetic study of coordination of sulfate and perchlorate into the inner-sphere and/or outer-sphere complexes by hydrogen bonding into iron(III) clusters using Raman spectroscopy. The third was a study of the rate of oligomerization of soluble iron(III) using a voltammetric technique. These methods showed that the effective rate constant which describes proton release is determined by the sum of several processes; hydrolysis (condensation, oligomerization and polymerization steps of iron(III) species using chronopotentiometric) is therefore larger than the rate constant for only the formation of soluble oligomers (voltammetry), which in turn is faster than coordination of perchlorate and sulfate into the inner-sphere iron(III) clusters determined by Raman spectroscopy.

In addition, it can be deduced that the rate of hydrolysis of iron(III) in respect to releasing hydrogen ions (H^+) was not highly influence by sulfate ions. Also the rate of coordination the sulphate and perchlorate into iron(III) clusters was similar. Whereas sulfate ions have slight effect on the rate of oligomerization process and depletion of soluble species of iron(III), this has mainly been attributed to the role of sulfate in suppression of formation of higher soluble polymers and catalysing formation of solid phases of basic iron(III) sulfate complexes and other solid precipitations. Due to the complexity of Shilbottle samples and its low content of soluble iron(III), the kinetic studies of such samples were limited to the chronopotentiometric method. As rate constants were measured, their values were slightly lower than obtained from laboratory samples by a factor of about 2. This may be due to that iron(III) concentration was low in compared to the iron(II), for this reason also the kinetic studies using SWV were not obtained. All these observations are summarised in the figure 5.14.

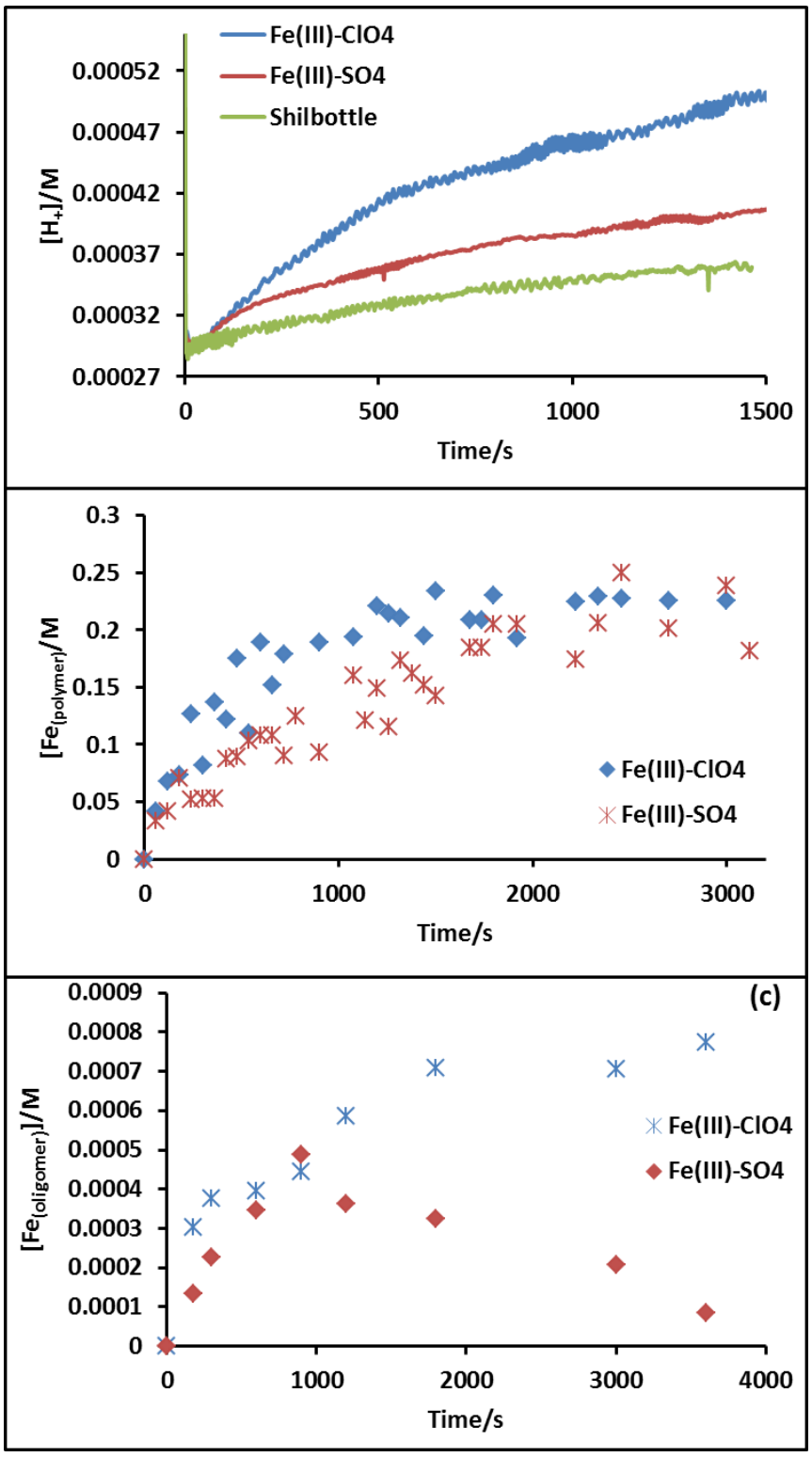

Figure 5.14: Showing comparison between the three kinetic methods used in this study and the effects of sulphate on the rate of hydrolysis, (a) chronopotentiometry, (b) Raman and (c) voltammetry (SWV)

Chapter 6: Conclusion and future work

6.1 Conclusion

This work was performed to investigate and explore in some details the chemistry of mine water pollution and kinetic aspects of the oligomerization of soluble iron(III) species of such waters in north east of England sites at Shilbottle, by which the environmental and geochemical researcher may try to improve and develop the remediation methods of such kind of environmental issues. The previous knowledge (and also in this work) about the composition of soluble components of this water shows that it is mainly iron and sulfate.

For this reason, the study was conducted in parallel manner for environmental and laboratory solutions ($Fe_2(SO_4)_3.5H_2O$ and $Fe(ClO_4)_3.xH_2O$), in order to carry out a comparison in respect of effects of ligands on the hydrolysis processes. The effects of two different ligands on the hydrolysis of iron(III) in aqueous solutions were investigated in laboratory solutions; these ligands were sulfate as strongly coordinated ligand and perchlorate as a weakly coordinated ligand. The behaviour of iron(III)-sulfate is significant for studying acid mine water solutions and perchlorate served as a control.

Various techniques were used in this study for characterization of soluble iron(III) complexes, determination of elemental concentrations and kinetic studies of iron(III) hydrolysis. Such techniques were spectroscopic and electrochemical; the former included inductively coupled plasma - optical atomic emission spectrometry (ICP-AES), Electrospray Ionization-Mass spectrometry (ESI – MS), Raman spectroscopy and diffraction technique X-Ray diffraction (XRD). The electrochemical ones include voltammetric (e. g. cyclic voltammetry (CV) and square wave voltammetry (SWV)) and potentiometric (e. g. ion selective electrode (ISE) methods and chronopotentiometric measurements). In addition a geochemical model (PHREEQC) was used to identify distribution of aqueous soluble species in acidic mine drainages in respect to the iron and sulfate.

Several measurements and characterization were made in this study, measuring kinetics of electron-solution interface in both laboratory and Shilbottle samples.

Characterizations of soluble species of iron(III) were performed using SWV, also dried solutions of both laboratory and Shilbottle samples were characterized via Raman spectroscopy. Also, solid samples of iron(III) perchlorate and iron(III) sulfate with certain amounts of NaOH were studied via XRD. Further electrochemical measurements such as pH and Eh and chloride concentrations for Shilbottle solutions were performed using potentiometry and voltammetry. Concentrations of some elements were determined via ICP-AES and also electrochemically (for soluble iron and sulfate), these measurements were used as inputs in a geochemical model PHREEQC. Finally, kinetic studies of the hydrolysis and soluble oligomerization processes of iron(III) in laboratory solutions and Shilbottle samples (only chronopotentiometry) were made using chronopotentiometric, voltammetric and Raman spectroscopy.

In chapter 3 electrochemical and spectroscopic techniques were used to characterize soluble and solid iron(III) complexes. It was shown that the electrode kinetics for Shilbottle samples were a simple one-electron reduction quasi-reversible behaviour and slightly different to iron(III)-sulfate in laboratory samples due to the complex composition of Shilbottle waters. Also Shilbottle solutions showed some unexpected variations such as the I_p^A/I_p^C ratio exceeds 1.0, the ratio varied between 1.29 and 1.45, and the current is non-zero at the beginning of the scan which indicate that there is substantial iron(II) present in these solutions. The laboratory solutions exhibited simple one-electron reduction quasi-reversible characteristics and the rate of electrode surface-solution in standard iron(III) in perchlorate solution was slightly faster than in iron(III)-sulfate solutions.

However, similar behaviour was observed for the reduction peak of monomeric species of iron(III)-sulfate complex in laboratory iron(III) sulfate and Shilbottle solutions using SWV. Also the reduction peak of iron(III) oligomers and also hydrogen ions were assigned using SWV. Raman studies have shown some similarity of dried samples of Shilbottle to iron(III)-sulfate rather than iron(III) perchlorate, and most vibration and stretching modes were ascribed to SO_4^{2-} in sulfate and Shilbottle samples and for ClO_4^- in perchlorate samples. Furthermore, there was similar behaviour for sulfate and Shilbottle solutions in mass spectra, as no signals were observed related to iron(III)-sulfate complexes, which is attributed to formation of neutral iron(III)-sulfate complexes. Whereas charged iron(III) clusters were observed in perchlorate media.

XRD data showed that, the crystallization of solid phase formed of iron(III) sulfate and iron(III) perchlorate with certain amount of NaOH was poor under our experimental conditions, with exception that formation of basic iron(III)-sulfate crystals as well as to crystals of $NaClO_4$ and Na_2SO_4 were assigned. Crystalline Fe oxides are not formed in the timescale of the experiments, but amorphous phases are more likely to exist in the Shilbottle samples.These conditions were chosen to be similar to kinetic studies performed using Raman spectroscopy in this work, the iron(III) concentration was 0.25 M, $[OH^-]/[Fe^{3+}]$ ratio ≤ 2.0 accordingly the pH ≤ 4, the temperature in range of 17 and 23 ^oC.

In chapter 4, in the study we developed electrochemical methods to measure soluble species of iron and sulfate in Shilbottle solutions using voltammetry. The methods have shown that soluble sulfate and iron concentration varied between (4630 and 7400 ppm) and between (182 and 355 ppm) for sulfate and iron, respectively. Also other electrochemical measurements such as potentiometry using ion selective electrodes were performed to determine $[H^+]$, $[Cl^-]$ and measuring Eh on inert electrode (e. g. Pt) and also voltammetry measurements to determinate Eh. The results showed that the pH of the environmental solution was about 3.6 ± 0.5, and the chloride concentration is low and does not exceed 3.0 ppm. There was a substantial difference between Eh and consequently pe values obtained by potentiometry and voltammetry; this was ascribed to a lack of redox equilibrium in the potentiometric measurement. Use of pe values from voltammetry in speciation models (PHREEQC) produced better agreement with UME determinations of the FeII/FeIII ratio. In addition, the AMD solutions are supersaturated with respect to goethite, hematite and therefore they are also out-of-equilibrium in this respect (PHREEQC results).

Numerous elements were measured using ICP-AES such as Fe, Mg, Ca, K, Mn, Al, Na, Cu, Pb, Sn, As, Hg, Zn, P and S. The obtained results were compared with electrochemical methods in respect of soluble iron and sulfate. The results showed some differences between two methods which has been ascribed to matrix effects in ICP-AES technique. Finally, the obtained electrochemical results were compared to the thermodynamic measurements (PHREEQC), and both methods showed that the predominant species of soluble iron (III) in acid mine drainages are $FeSO_4^+$.

In chapter 5, the study investigated the effects of sulfate on the hydrolysis and oligomerization of iron(III) solutions. Also, the study investigated the rate of iron(III)

hydrolysis, oligomerization in aqueous solutions by developed electrochemical methods, and rate of coordination of perchlorate and sulfate into iron(III) clusters using Raman spectroscopy. The studies using voltammetry found that soluble species of iron(III) sulfate ($FeSO_4^+$) required more NaOH to be removed from solution than required to remove soluble species of iron(III) in perchlorate media (Fe^{3+}). This was attributed mainly to the presence of $FeSO_4^+$, as its p*K*a value (which we estimated in this work) is about 4.38 ± 0.16. Therefore, the amount of NaOH required to push $FeSO_4^+$ to hydrolyse is more than that required for Fe^{3+} (pK_a= 2.77 ± 0.03). Also, the voltammetric method studied the rate of oligomerization of soluble iron(III) in sulfate and perchlorate solutions. The study found that the rate of iron(III) oligomerization was increased with increasing pH, and it is slightly faster in the presence of sulfate.

The chronopotentiometric studies have shown that the rate of iron hydrolysis depends mainly on the added amount of NaOH, and there are no marked sulfate effects on the release of H^+. This was ascribed to the fact that H^+ ions are produced as a result of multiple hydrolysis steps such as (dimerization, oligomerization, polymerization and nucleation) not only one step. These multiple hydrolysis steps occur simultaneously and some may not be markedly influenced by sulfate.

The kinetic studies using Raman concluded that the rate of coordination of sulfate and perchlorate to iron(III) clusters was fairly slow and it was similar for both ligands. Finally, voltammetric studies have shown that soluble species of iron(III) in presence of sulfate require more NaOH than those in perchlorate solution. This was attributed mainly to presence of $FeSO_4^+$. Furthermore, voltammetric studies have shown that sulfate catalyses oligomerization of soluble iron(III) and formation of basic sulfate complexes with assistance of $Fe(OH)^{2+}$.

6.2 Future work

Although this work has achieved its goals and aims to study kinetic processes of hydrolysis of iron(III) in both a pure laboratory and Shilbottle samples. Further studies are required for understanding additional information about voltammetric measurements. For example, the reduction peak of soluble oligomers which has been assigned on the square wave voltammogram in this work needs to be characterized using spectroscopic technique e. g. Mössbauer spectroscopy. This technique may provide structural information on such soluble oligomers. Also, extra kinetic studies can

be obtained using SWV by observing the changes in hydrogen reduction peak at about -0.18 V vs Ag/AgCl against time and the obtained results can be compared with chronopotentiometric measurements. Furthermore, it is well known that the oxidation of pyrite is the main source of AMD, therefore studying the oxidation of pyrite by means of Fe^{3+} is important; this could be achieved using scanning electrochemical microscopy SECM by local generation of Fe^{3+} at the tip and observation of the feedback produced by reduction at the pyrite. In addition, neutral soluble species formed in diluted (less than 1 mM) solutions of iron(III) in sulfate media need extra studies to find out their chemical structure.

7. References

1. Akcil, A. and S. Koldas, Acid Mine Drainage (AMD): causes, treatment and case studies. *Journal of Cleaner Production*, 2006. **14**(12-13): p. 1139-1145.
2. Egiebor, N.O. and B. Oni, Acid rock drainage formation and treatment: a review. *Asia-Pacific Journal of Chemical Engineering*, 2007. **2**(1): p. 47-62.
3. Azapagic, A., Developing a framework for sustainable development indicators for the mining and minerals industry. *Journal of Cleaner Production*, 2004. **12**(6): p. 639-662.
4. Abdalla, O.A.E., F.O. Suliman, H. Al-Ajmi, T. Al-Hosni, and H. Rollinson, Cyanide from gold mining and its effect on groundwater in arid areas, Yanqul mine of Oman. *Environmental Earth Sciences*, 2010. **60**(4): p. 885-892.
5. Zhuang, P., M.B. McBride, H.P. Xia, N.Y. Li, and Z.A. Lia, Health risk from heavy metals via consumption of food crops in the vicinity of Dabaoshan mine, South China. *Science of the Total Environment*, 2009. **407**(5): p. 1551-1561.
6. Kjeldsen, P., Behaviour of cyanides in soil and groundwater: A review. *Water Air and Soil Pollution*, 1999. **115**(1-4): p. 279-307.
7. Singer, P.C. and W. Stumm, Acidic mine drainage . rate-determining step. *Science*, 1970. **167**(3921): p. 1121-1123.
8. Benner, S.G., D.W. Blowes, W.D. Gould, R.B. Herbert, and C.J. Ptacek, Geochemistry of a permeable reactive barrier for metals and acid mine drainage. *Environmental Science & Technology*, 1999. **33**(16): p. 2793-2799.
9. Cruz Viggi, C., F. Pagnanelli, A. Cibati, D. Uccelletti, C. Palleschi, and L. Toro, Biotreatment and bioassessment of heavy metal removal by sulphate reducing bacteria in fixed bed reactors. *Water Research*, 2010. **44**(1): p. 151-158.
10. Dudka, S. and D.C. Adriano, Environmental impacts of metal ore mining and processing: A review. *Journal of Environmental Quality*, 1997. **26**(3): p. 590-602.
11. Akcil, A., First application of cyanidation process in Turkish gold mining and its environmental impacts. *Minerals Engineering*, 2002. **15**(9): p. 695-699.
12. Ochieng, G.M., E.S. Seanego, and O.I. Nkwonta, Impacts of mining on water resources in South Africa: A review. *Scientific Research and Essays*, 2010. **5**(22): p. 3351-3357.

13. Fu, S.S., P.J. Li, Q.A. Feng, X.J. Li, P. Li, Y.B. Sun, and Y. Chen, Soil quality degradation in a magnesite ining Area. *Pedosphere*, 2011. **21**(1): p. 98-106.
14. Donato, D.B., O. Nichols, H. Possingham, M. Moore, P.F. Ricci, and B.N. Noller, A critical review of the effects of gold cyanide-bearing tailings solutions on wildlife. *Environment International*, 2007. **33**(7): p. 974-984.
15. Chan, H.M., A.M. Scheuhammer, A. Ferran, C. Loupelle, J. Holloway, and S. Weech, Impacts of mercury on freshwater fish-eating wildlife and humans. *Human and Ecological Risk Assessment*, 2003. **9**(4): p. 867-883.
16. Sarmiento, A.M., A. DelValls, J.M. Nieto, M.J. Salamanca, and M.A. Caraballo, Toxicity and potential risk assessment of a river polluted by acid mine drainage in the Iberian Pyrite Belt (SW Spain). *Science of the Total Environment*, 2011. **409**(22): p. 4763-4771.
17. He, M., Z. Wang, and H. Tang, Spatial and temporal patterns of acidity and heavy metals in predicting the potential for ecological impact on the Le An river polluted by acid mine drainage. *Science of the Total Environment*, 1997. **206**(1): p. 67-77.
18. Jung, M.C., Heavy metal contamination of soils and waters in and around the Imcheon Au-Ag mine, Korea. *Applied Geochemistry*, 2001. **16**(11-12): p. 1369-1375.
19. Boularbah, A., C. Schwartz, G. Bitton, and J.L. Morel, Heavy metal contamination from mining sites in South Morocco: 1. Use of a biotest to assess metal toxicity of tailings and soils. *Chemosphere*, 2006. **63**(5): p. 802-810.
20. Rashed, M.N., Monitoring of contaminated toxic and heavy metals, from mine tailings through age accumulation, in soil and some wild plants at Southeast Egypt. *Journal of Hazardous Materials*, 2010. **178**(1-3): p. 739-746.
21. Jarvis, A.P., A. Moustafa, P.H.A. Orme, and P.L. Younger, Effective remediation of grossly polluted acidic, and metal-rich, spoil heap drainage using a novel, low-cost, permeable reactive barrier in Northumberland, UK. *Environmental Pollution*, 2006. **143**(2): p. 261-268.
22. Fuge, R., I.M.S. Laidlaw, W.T. Perkins, and K.P. Rogers, The influence of acidic mine and spoil drainage on water-quality in the mid-wales area. *Environmental Geochemistry and Health*, 1991. **13**(2): p. 70-75.
23. Neal, C., H.P. Jarvie, B.A. Whitton, and J. Gemmell, The water quality of the River Wear, North-East England. *Science of The Total Environment*, 2000. **251**: p. 153-172.

24. Palumbo-Roe, B. and B. Klinck, Bioaccessibility of arsenic in mine waste-contaminated soils: A case study from an abandoned arsenic mine in SW England (UK). *Journal of Environmental Science and Health Part a-Toxic/Hazardous Substances & Environmental Engineering*, 2007. **42**(9): p. 1251-1261.
25. Mayes, W.M., H.A.B. Potter, and A.P. Jarvis, Inventory of aquatic contaminant flux arising from historical metal mining in England and Wales. *Science of the Total Environment*, 2010. **408**(17): p. 3576-3583.
26. Isaacson, L.S., E.D. Burton, R.T. Bush, D.R.G. Mitchell, S.G. Johnston, B.C.T. Macdonald, . . . I. White, Iron(III) accumulations in inland saline waterways, Hunter Valley, Australia: Mineralogy, micromorphology and pore-water geochemistry. *Applied Geochemistry*, 2009. **24**(10): p. 1825-1834.
27. Banks, D., P.L. Younger, R.T. Arnesen, E.R. Iversen, and S.B. Banks, Mine-water chemistry: the good, the bad and the ugly. *Environmental Geology*, 1997. **32**(3): p. 157-174.
28. Colmer, A.R. and M.E. Hinkle, The Role of Microorganisms in Acid Mine Drainage: A Preliminary Report. *Science*, 1947. **106**(2751): p. 253-256.
29. Colmer, A.R., K.L. Temple, and M.E. Hinkle, An iron-oxidizing bacterium from the acid drainage of some bituminous coal mines. *Journal of bacteriology*, 1950. **59**(3): p. 317-328.
30. Leathen, W.W., S.A. Braley, Sr., and L.D. McIntyre, The role of bacteria in the formation of acid from certain sulfuritic constituents associated with bituminous coal. II. Ferrous iron oxidizing bacteria. *Applied microbiology*, 1953. **1**(2): p. 65-8.
31. Kleinmann, R.L.P., D.A. Crerar, and R.R. Pacelli, Biogeochemistry of acid mine drainage and a method to control acid formation. *Journal Name: Min. Eng.* (N.Y.); (United States); Journal Volume: 33:3, 1981: p. Medium: X; Size: Pages: 300-305.
32. Younger Puaul, B. Steven, and H. Robert, Mine Water Hydrology, Pollution, Remediation. Vol. 5. 2002, *The Netherlands and U. S. A.: Kluwer Academic*. 442.
33. Marini, L., G. Saldi, F. Cipolli, G. Ottonello, and M.V. Zuccolini, Geochemistry of water discharges from the Libiola mine, Italy. *Geochemical Journal*, 2003. **37**(2): p. 199-216.

34. Majzlan, J. and S.C.B. Myneni, Speciation of iron and sulfate in acid waters: Aqueous clusters to mineral precipitates. *Environmental Science & Technology,* 2005. **39**(1): p. 188-194.
35. Bigham, J.M., U. Schwertmann, S.J. Traina, R.L. Winland, and M. Wolf, Schwertmannite and the chemical modeling of iron in acid sulfate waters. *Geochimica Et Cosmochimica Acta,* 1996. **60**(12): p. 2111-2121.
36. Schwertmann, U. and E. Murad, Effect of pH on the formation of goethite and hematite from ferrihydrite. *Clays and Clay Minerals,* 1983. **31**(4): p. 277-284.
37. Regenspurg, S., A. Brand, and S. Peiffer, Formation and stability of schwertmannite in acidic mining lakes. *Geochimica Et Cosmochimica Acta*, 2004. **68**(6): p. 1185-1197.
38. Lazaroff, N., W. Sigal, and A. Wasserman, Iron oxidation and precipitation of ferric hydroxysulfates by resting thiobacillus-ferrooxidans cells. *Applied and Environmental Microbiology,* 1982. **43**(4): p. 924-938.
39. Bigham, J.M., U. Schwertmann, L. Carlson, and E. Murad, A poorly crystallized oxyhydroxysulfate of iron formed by bacterial oxidation of Fe(II) in acid-mine waters. *Geochimica Et Cosmochimica Acta,* 1990. **54**(10): p. 2743-2758.
40. Mycroft, J.R., G.M. Bancroft, N.S. McIntyre, J.W. Lorimer, and I.R. Hill, Detection of sulfur and polysulfides on electrochemically oxidized pyrite surfaces by x-ray photoelectron-spectroscopy and raman-spectroscopy. *Journal of Electroanalytical Chemistry*, 1990. **292**(1-2): p. 139-152.
41. Scaini, M.J., G.M. Bancroft, and S.W. Knipe, An XPS, AES, and SEM study of the interactions of gold and silver chloride species with PbS and FeS2: Comparison to natural samples. *Geochimica Et Cosmochimica Acta,* 1997. **61**(6): p. 1223-1231.
42. Eggleston, C.M., J.J. Ehrhardt, and W. Stumm, Surface structural controls on pyrite oxidation kinetics: An XPS-UPS, STM, and modeling study. *American Mineralogist,* 1996. **81**(9-10): p. 1036-1056.
43. Buckley, A.N. and R. Woods, The surface oxidation of pyrite. *Applied Surface Science,* 1987. **27**(4): p. 437-452.
44. Sasaki, K., Raman study of the microbially mediated dissolution of pyrite by Thiobacillus ferrooxidans. *Canadian Mineralogist*, 1997. **35**: p. 999-1008.
45. Chernyshova, I.V., An in situ FTIR study of galena and pyrite oxidation in aqueous solution. *Journal of Electroanalytical Chemistry*, 2003. **558**: p. 83-98.

46. Hamilton, I.C. and R. Woods, An investigation of surface oxidation of pyrite and pyrrhotite by linear potential sweep voltammetry. *Journal of Electroanalytical Chemistry*, 1981. **118**(FEB): p. 327-343.
47. Liu, R., A.L. Wolfe, D.A. Dzombak, C.P. Horwitz, B.W. Stewart, and R.C. Capo, Electrochemical study of hydrothermal and sedimentary pyrite dissolution. *Applied Geochemistry*, 2008. **23**(9): p. 2724-2734.
48. Tao, D.P., P.E. Richardson, G.H. Luttrell, and R.H. Yoon, Electrochemical studies of pyrite oxidation and reduction using freshly-fractured electrodes and rotating ring-disc electrodes. *Electrochimica Acta*, 2003. **48**(24): p. 3615-3623.
49. Rosso, K.M., U. Becker, and M.F. Hochella, The interaction of pyrite {100} surfaces with O-2 and H2O: Fundamental oxidation mechanisms. *American Mineralogist,* 1999. **84**(10): p. 1549-1561.
50. Rosso, K.M., U. Becker, and M.F. Hochella, Atomically resolved electronic structure of pyrite {100} surfaces: An experimental and theoretical investigation with implications for reactivity. *American Mineralogist,* 1999. **84**(10): p. 1535-1548.
51. Eggleston, C.M. and M.F. Hochella, Scanning tunneling microscopy of pyrite (100) - surface-structure and step reconstruction. *American Mineralogist*, 1992. **77**(1-2): p. 221-224.
52. Evangelou, V.P. and Y.L. Zhang, A review - pyrite oxidation mechanisms and acid-mine drainage prevention. *Critical Reviews in Environmental Science and Technology*, 1995. **25**(2): p. 141-199.
53. Keith, C.N. and D.J. Vaughan, Mechanisms and rates of sulphide oxidation in relation to the problems of acid rock (mine) drainage. *Environmental Mineralogy:* Microbial Interactions Anthropogenic Influences, Contaminated Land and Waste Management, ed. J.D. CotterHowells, et al. Vol. 9. 2000, London: Mineralogical Society Great Britain & Ireland. 117-139.
54. Bailey, L.K. and E. Peters, Decomposition of pyrite in acids by pressure leaching and anodization - case for an electrochemical mechanism. *Canadian Metallurgical Quarterly*, 1976. **15**(4): p. 333-344.
55. Temple, K.L. and A.R. Colmer, The autotrophic oxidation of iron by a new bacterium: thiobacillus ferrooxidans. *J. Bacteriol.,* 1951. **62**(5): p. 605-611.
56. Palencia, I., R.Y. Wan, and J.D. Miller, The electrochemical-behavior of a semiconducting natural pyrite in the presence of bacteria. *Metallurgical Transactions B-Process Metallurgy,* 1991. **22**(6): p. 765-774.

57. Konishi, Y., S. Asai, and H. Katoh, Bacterial dissolution of pyrite by thiobacillus-ferrooxidans. *Bioprocess Engineering*, 1990. **5**(5): p. 231-237.

58. Smith EE, S.R., The sulfide to sulfate reaction mechanism. 14010 *Federal Water Pollution Control*, 1970: p. 20.

59. Moses, C.O. and J.S. Herman, Pyrite oxidation at circumneutral pH. *Geochimica Et Cosmochimica Acta*, 1991. **55**(2): p. 471-482.

60. Goldhaber, M.B., Experimental-study of metastable sulfur oxyanion formation during pyrite oxidation at pH 6-9 and 30 ^{o}C. *American Journal of Science*, 1983. **283**(3): p. 193-217.

61. Moses, C.O., D.K. Nordstrom, J.S. Herman, and A.L. Mills, Aqueous pyrite oxidation by dissolved-oxygen and by ferric iron. *Geochimica Et Cosmochimica Acta*, 1987. **51**(6): p. 1561-1571.

62. Peters, E. and H. Majima, Electrochemical reactions of pyrite in acid perchlorate solutions. *Canadian Metallurgical Quarterly*, 1968. **7**(3): p. 111-117.

63. Stumm, W. and G.F. Lee, Oxygenation of Ferrous Iron. *Industrial & Engineering Chemistry*, 1961. **53**(2): p. 143-146.

64. Jönsson, J., J. Jönsson, and L. Lövgren, Precipitation of secondary Fe(III) minerals from acid mine drainage. *Applied Geochemistry*, 2006. **21**(3): p. 437-445.

65. Stipp, S.L., Speciation in the Fe(II)-Fe(III)-SO_4-H_2O system at 25 ^{o}C and low pH - sensitivity of an equilibrium-model to uncertainties. *Environmental Science & Technology*, 1990. **24**(5): p. 699-706.

66. Kobylin, P., T. Kaskiala, and J. Salminen, Modeling of H_2SO_4-$FeSO_4$-H_2O and H_2SO_4-$Fe_2(SO_4)_3$-H_2O systems for metallurgical applications. *Industrial & Engineering Chemistry Research*, 2007. **46**(8): p. 2601-2608.

67. Tosca, N.J., A. Smirnov, and S.M. McLennan, Application of the Pitzer ion interaction model to isopiestic data for the $Fe_2(SO_4)_3$-H_2SO_4-H_2O system at 298.15 and 323.15 K. *Geochimica Et Cosmochimica Acta*, 2007. **71**(11): p. 2680-2698.

68. Reardon, E.J. and R.D. Beckie, Modeling chemical-equilibria of acid mine-drainage - the $FeSO_4$-H_2SO_4-H_2O system. *Geochimica Et Cosmochimica Acta*, 1987. **51**(9): p. 2355-2368.

69. Casas, J.M., C. Paipa, I. Godoy, and T. Vargas, Solubility of sodium-jarosite and solution speciation in the system Fe(III)-Na-H_2SO_4-H_2O at 70 ^{o}C. *Journal of Geochemical Exploration*, 2007. **92**(2-3): p. 111-119.

70. Casas, J.M., G. Crisostomo, and L. Cifuentes, Speciation of the Fe(II)-Fe(III)-H_2SO_4-H_2O system at 25 and 50 ^oC. *Hydrometallurgy*, 2005. **80**(4): p. 254-264.
71. Sobron, P., F. Rull, F. Sobron, A. Sanz, J. Medina, and C.J. Nielsen, Modeling the physico-chemistry of acid sulfate waters through Raman spectroscopy of the system $FeSO_4$-H_2SO_4-H_2O. *Journal of Raman Spectroscopy*, 2007. **38**(9): p. 1127-1132.
72. Sobron, P., F. Rull, F. Sobron, A. Sanz, J. Medina, and C.J. Nielsen, Raman spectroscopy of the system. iron(III)-sulfuric acid-water: An approach to Tinto River's (Spain) hydrogeochemistry. *Spectrochimica Acta Part a-Molecular and Biomolecular Spectroscopy*, 2007. **68**(4): p. 1138-1142.
73. Bigham, J.M. and D.K. Nordstrom, Iron and aluminum hydroxysulfates from acid sulfate waters. *Sulfate Minerals - Crystallography, Geochemistry and Environmental Significance*, 2000. **40**: p. 351-403.
74. Bigham, J.M., L. Carlson, and E. Murad, Schwertmannite, a new iron oxyhydroxysulphate from pyhasalmi, finland, and other localities. *Mineralogical Magazine*, 1994. **58**(393): p. 641-648.
75. Kawano, M. and K. Tomita, Geochemical modeling of bacterially induced mineralization of schwertmannite and jarosite in sulfuric acid spring water. *American Mineralogist*, 2001. **86**(10): p. 1156-1165.
76. Equeenuddin, S.M., S. Tripathy, P.K. Sahoo, and M.K. Panigrahi, Geochemistry of ochreous precipitates from coal mine drainage in India. *Environmental Earth Sciences*, 2010. **61**(4): p. 723-731.
77. Randall, S.R., D.M. Sherman, and K.V. Ragnarsdottir, Sorption of As(V) on green rust ($Fe_4(II)Fe_2(III)(OH)_{12}SO_4$. $3H_2O$) and lepidocrocite (gamma-FeOOH): Surface complexes from EXAFS spectroscopy. Geochimica Et Cosmochimica Acta, 2001. **65**(7): p. 1015-1023.
78. Bibi, I., B. Singh, and E. Silvester, Akaganéite (β-FeOOH) precipitation in inland acid sulfate soils of south-western New South Wales (NSW), Australia. *Geochimica Et Cosmochimica Acta*, 2011. **75**(21): p. 6429-6438.
79. Hammarstrom, J.M., R.R. Seal, A.L. Meier, and J.M. Kornfeld, Secondary sulfate minerals associated with acid drainage in the eastern US: recycling of metals and acidity in surficial environments. *Chemical Geology*, 2005. **215**(1-4): p. 407-431.
80. Schwertmann, U. and L. Carlson, The pH-dependent transformation of schwertmannite to goethite at 25 ^oC. *Clay Minerals*, 2005. **40**(1): p. 63-66.

81. Jonsson, J., P. Persson, S. Sjoberg, and L. Lovgren, Schwertmannite precipitated from acid mine drainage: phase transformation, sulphate release and surface properties. *Applied Geochemistry*, 2005. **20**(1): p. 179-191.
82. Acero, P., C. Ayora, C. Torrento, and J.M. Nieto, The behavior of trace elements during schwertmannite precipitation and subsequent transformation into goethite and jarosite. *Geochimica Et Cosmochimica Acta*, 2006. **70**(16): p. 4130-4139.
83. Runkel, R.L., B.A. Kimball, D.M. McKnight, and K.E. Bencala, Reactive solute transport in streams: A surface complexation approach for trace metal sorption. *Water Resources Research*, 1999. **35**(12): p. 3829-3840.
84. Webster, J.G., P.J. Swedlund, and K.S. Webster, Trace Metal Adsorption onto an Acid Mine Drainage Iron(III) Oxy Hydroxy Sulfate. *Environmental Science & Technology*, 1998. **32**(10): p. 1361-1368.
85. Birus, M., N. Kujundzic, and M. Pribanic, Kinetics of complexation of iron(III) in aqueous-solution. *Progress in Reaction Kinetics*, 1993. **18**(3): p. 171-271.
86. Cornell, R.M., R. Giovanoli, and W. Schneider, Review of the hydrolysis of iron(III) and the crystallization of amorphous iron(III) hydroxide hydrate. *Journal of Chemical Technology and Biotechnology*, 1989. **46**(2): p. 115-134.
87. Jambor, J.L. and J.E. Dutrizac, Occurrence and constitution of natural and synthetic ferrihydrite, a widespread iron oxyhydroxide. *Chemical Reviews*, 1998. **98**(7): p. 2549-2585.
88. Voigt, B. and A. Gobler, Formation of pure hematite by hydrolysis of iron(III) salt-solutions under hydrothermal conditions. *Crystal Research and Technology*, 1986. **21**(9): p. 1177-1183.
89. Demopoulos, G.R., Aqueous precipitation and crystallization for the production of particulate solids with desired properties. *Hydrometallurgy*, 2009. **96**(3): p. 199-214.
90. Dousma, J. and P.L. De Bruyn, Hydrolysis-precipitation studies of iron solutions. I. Model for hydrolysis and precipitation from Fe(III) nitrate solutions. *Journal of Colloid and Interface Science*, 1976. **56**(3): p. 527-539.
91. Dousma, J. and P.L. Debruyn, Hydrolysis-precipitation studies of iron solutions .2. aging studies and model for precipitation from Fe(III) nitrate solutions. *Journal of Colloid and Interface Science*, 1978. **64**(1): p. 154-170.
92. Murphy, P.J., A.M. Posner, and J.P. Quirk, Characterization of partially neutralized ferric-chloride solutions. *Journal of Colloid and Interface Science*, 1976. **56**(2): p. 284-297.

93. Murphy, P.J., A.M. Posner, and J.P. Quirk, Chemistry of iron in soils - ferric hydrolysis products. *Australian Journal of Soil Research,* 1975. **13**(2): p. 189-201.

94. Hsu, P.H. and S.E. Ragone, *Aging of hydrolyzed iron (III) solutions. Journal of Soil Science,* 1972. **23**(1): p. 17-31.

95. Arnek, R.S., Kurt, Thermochemical Studies of Hydrolytic Reactions. 7. A Recalculation of Calorimeter Data on Iron(III) Hydrolysis. *Acta chemica Scandinavica* 1968. **22**(4): p. 1327.

96. Ciavatta, L. and M. Grimaldi, Hydrolysis of iron(III) ion, Fe^{3+}, in perchlorate media. *Journal of Inorganic & Nuclear Chemistry,* 1975. **37**(1): p. 163-169.

97. Knudsen, J.M., E. Larsen, J.E. Moreira, and O.F. Nielsen, Characterization of decaaqua-µ-oxodi-iron(III) by mossbauer and vibrational spectroscopy. *Acta Chemica Scandinavica Series a-Physical and Inorganic Chemistry*, 1975. **29**(9): p. 833-839.

98. Milburn, R.M. and W.C. Vosburgh, A Spectrophotometric Study of the Hydrolysis of Iron(III) Ion. II. Polynuclear Species1. *Journal of the American Chemical Society,* 1955. **77**(5): p. 1352-1355.

99. Dousma, J., T.J. Vandenhoven, and P.L. Debruyn, Influence of chloride-ions on formation of iron(III) oxyhydroxide. *Journal of Inorganic & Nuclear Chemistry*, 1978. **40**(6): p. 1089-1093.

100. Milburn, R.M., A Spectrophotometric Study of the Hydrolysis of Iron(III) Ion. III. Heats and Entropies of Hydrolysis. *Journal of the American Chemical Society,* 1957. **79**(3): p. 537-540.

101. Murphy, P.J., A.M. Posner, and J.P. Quirk, Characterization of hydrolyzed ferric ion solutions - comparison of effects of various anions on solutions. *Journal of Colloid and Interface Science,* 1976. **56**(2): p. 312-319.

102. Pykhteev, O.Y., A.A. Efimov, and L.N. Moskvin, Hydrolysis of iron(III) aqua complexes. *Russian Journal of Applied Chemistry,* 1999. **72**(1): p. 9-20.

103. Whiteker, R.A. and N. Davidson, Ion-Exchange and Spectrophotometric Investigation of Iron(III) Sulfate Complex Ions. *Journal of the American Chemical Society,* 1953. **75**(13): p. 3081-3085.

104. Lister, M.W. and D.E. Rivington, Ferric sulphate complexes, and ternary complexes with thiocyanate ions. *Canadian Journal of Chemistry,* 1955. **33**(10): p. 1591-1602.

105. Cavasino, F.P., Temperature-jump study of the kinetics of the formation of the monosulfato complex of iron(III). *The Journal of Physical Chemistry*, 1968. **72**(4): p. 1378-1384.
106. Davis, G.G. and W.M. Smith, The kinetics of the formation of the monosulphato complex of iron (III) in aqueous solution. *Canadian Journal of Chemistry*, 1962. **40**(9): p. 1836-1845.
107. Sapieszko, R.S., R.C. Patel, and E. Matijevic, Ferric hydrous oxide sols. 2. Thermodynamics of aqueous hydroxo and sulfato ferric complexes. *The Journal of Physical Chemistry*, 1977. **81**(11): p. 1061-1068.
108. Wendt, H., Schnelle Ionenreaktionen in Lösungen. III Die Kinetik der Bildung des binuklearen Eisen-III-hydroxokomplexes $Fe(OH)_2Fe^{4+}$. *Zeitschrift für Elektrochemie, Berichte der Bunsengesellschaft für physikalische Chemie*, 1962. **66**(3): p. 235-239.
109. Mattoo, B.N., Stability of Metal Complexes in Solution. *Zeitschrift für Physikalische Chemie*, 1959. **19**(3_4): p. 156-167.
110. Musić, S., A. Vértes, G.W. Simmons, I. Czakó-Nagy, and H. Leidheiser Jr, Mössbauer spectroscopic study of the formation of Fe(III) oxyhydroxides and oxides by hydrolysis of aqueous Fe(III) salt solutions. *Journal of Colloid and Interface Science*, 1982. **85**(1): p. 256-266.
111. Dousma, J., D.D. Ottelander, and P.L.D. Bruyn, Influence of sulfate-ions on the formation of iron(III) oxides. *Journal of Inorganic & Nuclear Chemistry*, 1979. **41**(11): p. 1565-1568.
112. Parida, K.M. and J. Das, Effect of sulfate ions on the formation and physico-chemical properties of ferric oxide hydroxides prepared by a homogeneous precipitation method .1. *Journal of Materials Science*, 1996. **31**(8): p. 2199-2205.
113. Younger, P.L., Passive in situ remediation of acidic mine waste leachates: progress and prospects. Land Reclamation: Extending the Boundaries, ed. H.M. Moore, H.R. Fox, and S. Elliott. 2003, Leiden: A a *Balkema Publishers*. 253-264.
114. Amos, P.W. and P.L. Younger, Substrate characterisation for a subsurface reactive barrier to treat colliery spoil leachate. *Water Research*, 2003. **37**(1): p. 108-120.
115. Allen J. Bard and L.R. Faulkner, Electrochemical Methods Fundamental and Application. Vol. Second Edition. 2001: *John Wiley*. 833.

116. Zoski, C.G., Handbook of Electrochemistry. Vol. First Edition. 2007: *Elsevier*. 891.
117. Wang, J., Analytical Electrochemistry. Vol. Third Edition. 2006, *New Jersey:* By John Wiley. 250.
118. Settle, F.A., Handbook of Instrumental Techniques of Analytical Chemistry. 1997, *New Jersey: By prentice Hall PTR.*
119. David, H., Modren Analytical Chemistry. 2000: *James M. Smith*. 798.
120. Bard, A.J., G. Inzelt, and F. Scholz, Electrochemical Dictionary. 2012: *Springer.*
121. Greef R., R. Peat, D. Pletcher, L. M. Petre, and J. Robinson, Instrumental Methods in Electrochemistry. 1985, *New York: Chichester.* 443.
122. Maloy, J.T., Factors affecting the shape of current-potential curves. *Journal of Chemical Education,* 1983. **60**(4): p. 285-289.
123. Christopher M. A. Brett and A.M.O. Brett, Electrochemistry Principles, Methods, and Applications. 1993, *United State, New York: Oxford University* Press. 444.
124. D. A. Skoog, F J. Holler, and T.A. Nieman, The principles of instrumental analysis. Vol. Fifth Edition. 1998: *Brooks/code Thomson Learning*. 849.
125. Bagotsky, V.S., Fundamentals of electrochemistry. Vol. Second Edition. 2006, New Jersey: *John Wiley*. 722.
126. Hsu, P.H., Appearance and stability of hydrolyzed $Fe(ClO_4)_3$ solutions. *Clays and Clay Minerals*, 1973. **21**(5): p. 267-277.
127. Pavia, D.L., G.M. Lampman, G.S. Kriz, and J.R. Vyvyan, Introduction to spectroscopy. Vol. fourth edition. 2009: *Brooks/ Cole, Cengage Learning.*
128. Pavia, D.L., G.M. Lampman, and G.S. Kriz, Introduction to spectroscopy. Vol. Third edition. 2001: *Brooks/code Thomson learning*. 579.
129. Christiane Fernandes, Leonardo M. Lube, A.H.J. Rafaela Oliveira Moreira, Bruno Szpoganicz, Stacy Sherrod, and D.H. Russell, Investigation of the interaction of iron(III) complexes with dAMP (2'-deoxyadenosine-5'-monophosphate) by ESI-MS, MALDI-MS and potentiometric titration: insights into synthetic nuclease behavior. *Dalton Transactions,* 2010. **39**(21): p. 5094-5100.
130. C. Vandecasteele and C.B. Block, Modren methods for trace element determination. 1993: *John Wiley.* 330.
131. Smith Ewen and D. Geoffrey, Modern Raman spectroscopy. 2005: *John Wiley*. 210.

132. Dieing Thomas, Hollricher Olaf, and T. Jan, Confocal Raman Microscopy. 2011, *New york: Springer*. 290.

133. Robinson James, Frame Eileen, and F. George, Undergraduate Instrumental Analysis. Vol. Sixth Eddition. 2005, *New York: Marcel Dekker*. 1079.

134. Willard Hobart. H., Merritt Lynne. L., Dean John, and F. Settoe, Instrumental Methods of Analysis. Vol. Seventh Edition. 1988, *California, USA: Wadsworth*. 895.

135. Khoe, G.H., P.L. Brown, R.N. Sylva, and R.G. Robins, The hydrolysis of metal-ions .9. iron(III) in perchlorate, nitrate, and chloride media (1 mol dm^{-3}). *Journal of the Chemical Society-Dalton Transactions*, 1986(9): p. 1901-1906.

136. Hellman, H., R.S. Laitinen, L. Kaila, J. Jalonen, V. Hietapelto, J. Jokela, . . . J. Ramo, Identification of hydrolysis products of FeCl3 center dot $6H_2O$ by ESI-MS. *Journal of Mass Spectrometry*, 2006. **41**(11): p. 1421-1429.

137. Sylva, R.N., The hydrolysis of iron (III). *Rev. Pure and Appl. Chem*., 1972. **22**.

138. Sommer, B.A. and D.W. Margerum, Kinetic study of hydroxoiron(III) dimer. *Inorganic Chemistry*, 1970. **9**(11): p. 2517-&.

139. Hemmes, P., L.D. Rich, D.L. Cole, and E.M. Eyring, Kinetics of hydrolysis of ferric ion in dilute aqueous solution. *Journal of Physical Chemistry*, 1971. **75**(7): p. 929-932.

140. Feitknecht, W. and W. Michaelis, Über die Hydrolyse von Eisen(III)-perchlorat-Lösungen. *Helvetica Chimica Acta*, 1962. **45**(1): p. 212-224.

141. Lente, G. and I. Fabian, New reaction path in the dissociation of the $Fe_2(\mu\text{-}OH)_2(H2O)_8^{4+}$ complex. *Inorganic Chemistry*, 1999. **38**(3): p. 603-605.

142. Flynn, C.M., Hydrolysis of inorganic iron(III) salts. *Chemical Reviews*, 1984. **84**(1): p. 31-41.

143. Gil, A.F., L. Salgado, L. Galicia, and I. Gonzalez, Predominance-zone diagrams of Fe(III) and Fe(II) sulfate complexes in acidic media - voltammetric and spectrophotometric studies, . *Talanta*, 1995. **42**(3): p. 407-414.

144. Mudashiru, L.K., A.C. Aplin, and B.R. Horrocks, Voltammetric methods for the speciation of dissolved iron and determination of Fe-containing nanoparticles in mine-water discharge. *Analytical Methods*, 2011. **3**(4): p. 927-936.

145. Angell, D.H. and Dickinso.T, Kinetics of ferrous/ferric and ferro/ferricyanide reactions at platinum and gold electrodes .1. kinetics at bare-metal surfaces. *Journal of Electroanalytical Chemistry*, 1972. **35**(NMAR): p. 55-72.

146. Weber, J., Z. Samec, and V. Marecek, Effect of anion adsorption on kinetics of Fe^{3+}-Fe^{2+} reaction on Pt and Au electrodes in $HClO_4$. *Journal of Electroanalytical Chemistry,* 1978. **89**(2): p. 271-288.

147. Samec, Z., Ultraslow kinetics of the ferric/ferrous electron transfer reaction on Au(110) electrode in perchloric acid solutions. *Journal of the Electrochemical Society,* 1999. **146**(9): p. 3349-3356.

148. Johnson, D.C. and E.W. Resnick, Electrocatalysis of reduction of iron(III) by halides adsorbed at platinum-electrodes in perchloric-acid solutions. *Analytical Chemistry,* 1977. **49**(13): p. 1918-1924.

149. Anson, F.C., Exchange Current Densities for Fe(II)-Fe(III) Solutions in Sulfuric Acid and Perchloric Acid. *Analytical Chemistry,* 1961. **33**(7): p. 939-942.

150. Gil, A.F., L. Galicia, and I. Gonzalez, Diffusion coefficients and electrode kinetic parameters of different Fe(III)-sulfate complexes. *Journal of Electroanalytical Chemistry,* 1996. **417**(1-2): p. 129-134.

151. Broadhurst, J.L. and J.G.H. du Perez, A thermodynamic study of the dissolution of gold in an acidic aqueous thiocyanate medium using iron (III) sulphate as an oxidant. *Hydrometallurgy,* 1993. **32**(3): p. 317-344.

152. Ling, Z.C. and A.L. Wang, A systematic spectroscopic study of eight hydrous ferric sulfates relevant to Mars. *Icarus,* 2010. **209**(2): p. 422-433.

153. Kazuo, N., Infrared and Raman Spectra of Inorganic and Coordination Compounds. 1986, New York: *Wiley*.

154. Frost, R.L., A Raman spectroscopic study of copiapites $Fe^{2+}Fe^{3+}(SO4)_6(OH)_2$. $20H_2O$: environmental implications. *Journal of Raman Spectroscopy*, 2011. **42**(5): p. 1130-1134.

155. Rudolph, W., M.H. Brooker, and P.R. Tremaine, Raman spectroscopic investigation of aqueous $FeSO_4$ in neutral and acidic solutions from 25 ^oC to 303 ^oC: Inner- and outer-sphere complexes. *Journal of Solution Chemistry*, 1997. **26**(8): p. 757-777.

156. Brill, T.B. and F. Goetz, Laser raman study of thermal-decomposition of solid NH_4ClO_4. *Journal of Chemical Physics,* 1976. **65**(3): p. 1217-1219.

157. Nakagawa, I. and T. Shimanouchi, Infrared absorption spectra of aquo complexes and the nature of co-ordination bonds. *Spectrochimica Acta,* 1964. **20**(3): p. 429-439.

158. Chiang, D.P., C.H. Peng, J.K. Mei, I.M. Jiang, S.C. Lin, Y.C. Chen, . . . W.S. Tse, Raman spectra of crystalline iron perchlorate hexahydrate. *Journal of Raman Spectroscopy*, 2008. **39**(3): p. 344-348.

159. Matijevic, E., R.S. Sapieszko, and J.B. Melville, Ferric hydrous oxide sols .1. monodispersed basic iron(III) sulfate particles. *Journal of Colloid and Interface Science*, 1975. **50**(3): p. 567-581.

160. Stefansson, A., Iron(III) hydrolysis and solubility at 25 ^{o}C. *Environmental Science & Technology*, 2007. **41**(17): p. 6117-6123.

161. Ciavatta, L., G. De Tommaso, and M. Iuliano, Hydroxo sulfate complexes of iron(III) in solution. *Annali Di Chimica*, 2002. **92**(7-8): p. 669-675.

162. Atkinson, R.J., A.M. Posner, and J.P. Quirk, Crystal nucleation in Fe(III) solutions and hydroxide gels. *Journal of Inorganic and Nuclear Chemistry*, 1968. **30**(9): p. 2371-2381.

163. Cornell, R.M., Effect of simple sugars on the alkaline transformation of ferrihydrite into goethite and hematite. *Clays and Clay Minerals*, 1985. **33**(3): p. 219-227.

164. Cornell, R.M. and R. Giovanoli, Effect of solution conditions on the proportion and morphology of goethite formed from ferrihydrite. *Clays and Clay Minerals*, 1985. **33**(5): p. 424-432.

165. Matijevic, E. and P. Scheiner, Ferric hydrous oxide sols .3. preparation of uniform particles by hydrolysis of Fe(III)-chloride, Fe(III)-nitrate, and Fe(III)-perchlorate solutions. *Journal of Colloid and Interface Science*, 1978. **63**(3): p. 509-524.

166. Atkinson, R.J., A.M. Posner, and J.P. Quirk, Crystal nucleation and growth in hydrolyzing iron(III) chloride solutions. *Clays and Clay Minerals*, 1977. **25**(1): p. 49-56.

167. Swanson, H.E. and S. United States. National Bureau of, Standard x-ray diffraction powder patterns. 1980, Washington, DC: U.S. Dept. of Commerce, *National Bureau of Standards* : For sale by the Supt. of Docs., U.S. G.P.O.

168. Swanson, H.E. and S. United States. National Bureau of. Standard x-ray diffraction powder patterns. 1957; Available from: http://books.google.com/books?id=gDjQAAAAMAAJ.

169. Tautkus, S., L. Steponeniene, and R. Kazlauskas, Determination of iron in natural and mineral waters by flame atomic absorption spectrometry. *Journal of the Serbian Chemical Society*, 2004. **69**(5): p. 393-402.

170. To, T.B., D.K. Nordstrom, K.M. Cunningham, J.W. Ball, and R.B. McCleskey, New method for the direct determination of dissolved Fe(III) concentration in acid mine waters. *Environmental Science & Technology*, 1999. **33**(5): p. 807-813.

171. Grotti, M., M.L. Abelmoschi, F. Soggia, and R. Frache, Determination of ultratrace elements in natural waters by solid-phase extraction and atomic spectrometry methods. *Analytical and Bioanalytical Chemistry*, 2003. **375**(2): p. 242-247.

172. Wu, J.F. and E.A. Boyle, Determination of iron in seawater by high-resolution isotope dilution inductively coupled plasma mass spectrometry after $Mg(OH)_2$ coprecipitation. *Analytica Chimica Acta*, 1998. **367**(1-3): p. 183-191.

173. Lattuada, R.M., C.T.B. Menezes, P.T. Pavei, M.C.R. Peralba, and J.H.Z. Dos Santos, Determination of metals by total reflection X-ray fluorescence and evaluation of toxicity of a river impacted by coal mining in the south of Brazil. *Journal of Hazardous Materials*, 2009. **163**(2-3): p. 531-537.

174. Karamanev, D.G., L.N. Nikolov, and V. Mamatarkova, Rapid simultaneous quantitative determination of ferric and ferrous ions in drainage waters and similar solutions. *Minerals Engineering*, 2002. **15**(5): p. 341-346.

175. Bertolacini, R.J. and J.E. Barney, Colorimetric Determination of Sulfate with Barium Chloranilate. *Analytical Chemistry*, 1957. **29**(2): p. 281-283.

176. Popoff, S. and E.W. Neuman, Microscopic examination of precipitates as an aid to precise analysis I-Estimation of Sulfates as Barium Sulfate. *Industrial & Engineering Chemistry Analytical Edition*, 1930. **2**(1): p. 45-54.

177. Reisman, D.J., V. Sundaram, S.R. Al-Abed, and D. Allen, Statistical validation of sulfate quantification methods used for analysis of acid mine drainage. *Talanta*, 2007. **71**(1): p. 303-311.

178. Elenkova, N.G., R.A. Tsoneva, and T.K. Nedelcheva, New turbidimetric method for determination of sulfate. *Talanta*, 1980. **27**(1): p. 67-68.

179. Morales, J.A., L.S. de Graterol, and J. Mesa, Determination of chloride, sulfate and nitrate in groundwater samples by ion chromatography. *Journal of Chromatography A*, 2000. **884**(1-2): p. 185-190.

180. Budic, B., Matrix interferences in the determination of trace elements in waste waters by inductively coupled plasma atomic emission spectrometry with ultrasonic nebulization. *Fresenius Journal of Analytical Chemistry*, 2000. **368**(4): p. 371-377.

181. Robinson, J.W., Undergraduate Instrumental Analysis. 1995, New York: *MARCEL DEKKER, INC*. 858.
182. Power, G.P. and I.M. Ritchie, Mixed potentials - experimental illustrations of an important concept in practical electrochemistry. *Journal of Chemical Education*, 1983. **60**(12): p. 1022-1026.
183. Grundl, T., Redox inactivity of colloidal ferric oxyhydroxide solids. *Journal of Contaminant Hydrology*, 1992. **9**(4): p. 369-377.
184. Jackson, R.E. and R.J. Patterson, Interpretation of ph and eh trends in a fluvial-sand aquifer system. *Water Resources Research*, 1982. **18**(4): p. 1255-1268.
185. Hostettler, J.D., Electrode electrons, aqueous electrons, and redox potentials in natural-waters. *American Journal of Science*, 1984. **284**(6): p. 734-759.
186. Auque, L., M.J. Gimeno, J. Gomez, and A.C. Nilsson, Potentiometrically measured Eh in groundwaters from the Scandinavian Shield. *Applied Geochemistry*, 2008. **23**(7): p. 1820-1833.
187. Langmuir, D. and Whittemo.Do, Variations in stability of precipitated ferric oxyhydroxides. *Advances in Chemistry Series*, 1971(106): p. 209-&.
188. Grundl, T.J. and D.L. Macalady, Electrode measurement of redox potential in anaerobic ferric/ferrous chloride systems. *Journal of Contaminant Hydrology*, 1990. **5**(1): p. 97-117.
189. Miles, D.L. and J.M. Cook, The determination of sulfate in natural-waters by inductively-coupled plasma emission-spectrometry. *Analytica Chimica Acta*, 1982. **141**(SEP): p. 207-212.
190. Appelo, C.J. and P. Dieke, Geochemistry Groundwater and Pollution 2nd Edition. 2005: *Taylor & Francis Group*.
191. Balintova, M. and A. Petrilakova, Study of pH Influence on Selective Precipitation of Heavy Metals from Acid Mine Drainage, in *Pres 2011: 14th International Conference on Process Integration, Modelling and Optimisation for Energy Saving and Pollution Reduction, Pts 1 and 2*, J.J. Klemes, P.S. Varbanov, and H.L. Lam, Editors. 2011, Aidic Servizi Srl: Milano. p. 345-350.
192. John, W.W., Handbook of Anion Determination. 1979: *Butterworth-Heinemann Ltd* 768.
193. van Staden, J.F. and S.I. Tlowana, Spectrophotometric determination of chloride in mineral and drinking waters using sequential injection analysis. *Fresenius Journal of Analytical Chemistry*, 2001. **371**(3): p. 396-399.

194. Demkowska, I., Z. Polkowska, and J. Namiesnik, Application of ion chromatography for the determination of inorganic ions, especially thiocyanates in human saliva samples as biomarkers of environmental tobacco smoke exposure. *Journal of Chromatography B-Analytical Technologies in the Biomedical and Life Sciences,* 2008. **875**(2): p. 419-426.

195. Jimenez, P.M., M. Gallego, and M. Valcarcel, Indirect atomic-absorption determination of chloride by continuous precipitation of silver-chloride in a flow-injection system. *Journal of Analytical Atomic Spectrometry*, 1987. **2**(2): p. 211-215.

196. Teixeira, L.S.G., T.J. Chaves, P.R.B. Guimaraes, L.A.M. Pontes, and J.S.R. Teixeira, Indirect determination of chloride and sulfate ions in ethanol fuel by X-ray fluorescence after a precipitation procedure. *Analytica Chimica Acta,* 2009. **640**(1-2): p. 29-32.

197. Gamlen, G.A. and D.O. Jordan, *295.* A spectrophotometric study of the iron(III) chloro-complexes. *Journal of the Chemical Society* (Resumed), 1953: p. 1435-1443.

198. Rabinowitch, E. and W.H. Stockmayer, Association of Ferric Ions with Chloride, Bromide and Hydroxyl Ions (A Spectroscopic Study). *Journal of the American Chemical Society*, 1942. **64**(2): p. 335-347.

199. Charlton, S.R. and D.L. Parkhurst, Modules based on the geochemical model PHREEQC for use in scripting and programming languages. *Computers & Geosciences*, 2011. **37**(10): p. 1653-1663.

200. Malmstrom, M.E., G. Destouni, and P. Martinet, Modeling expected solute concentration in randomly heterogeneous flow systems with multicomponent reactions. *Environmental Science & Technology,* 2004. **38**(9): p. 2673-2679.

201. Melchior, D.C. and R.L. Bassett, Chemical modeling of aqueous systems 2. 1989. Medium: X; Size: Pages: (vp.).

202. Grundl, T.J. and D.L. Macalady, Electrode measurement of redox potential in anaerobic ferric/ferrous chloride systems. *Journal of Contaminant Hydrology,* 1989. **5**(1): p. 97-117.

203. Byrne, R.H., Y.R. Luo, and R.W. Young, Iron hydrolysis and solubility revisited: observations and comments on iron hydrolysis characterizations. *Marine Chemistry,* 2000. **70**(1-3): p. 23-35.

204. Feng, W. and D. Nansheng, Photochemistry of hydrolytic iron (III) species and photoinduced degradation of organic compounds. A minireview. *Chemosphere,* 2000. **41**(8).

205. Jolivet, J.P., C. Chaneac, and E. Tronc, Iron oxide chemistry. From molecular clusters to extended solid networks. *Chemical Communications*, 2004(5): p. 481-487.

206. Martin, J.H. and S.E. Fitzwater, Iron-deficiency limits phytoplankton growth in the northeast pacific subarctic. *Nature*, 1988. **331**(6154): p. 341-343.

207. Gruber, B. and H. Kosegarten, Depressed growth of non-chlorotic vine grown in calcareous soil is an iron deficiency symptom prior to leaf chlorosis. *Journal of Plant Nutrition and Soil Science-Zeitschrift Fur Pflanzenernahrung Und Bodenkunde*, 2002. **165**(1): p. 111-117.

208. Crichton, R., Inorganic Biochemistry of Iron Metabolism: From Molecular Mechanisms to Clinical Consequences. 2001: *Wiley.*

209. Johnson, D.B. and K.B. Hallberg, Acid mine drainage remediation options: a review. *Science of The Total Environment*, 2005. **338**(1–2): p. 3-14.

210. Millero, F.J., W.S. Yao, and J. Aicher, The speciation of Fe(II) and Fe(III) in natural-waters. *Marine Chemistry*, 1995. **50**(1-4): p. 21-39.

211. Meinrath, G. and P.M. May, Thermodynamic Prediction in the Mine Water Environment. *Mine Water and the Environment*, 2002. **21**(1): p. 24-35.

212. Meinrath, G., B. Merkel, A. Odegaard-Jensen, and C. Ekberg, Sorption of iron on surfaces: Modelling data evaluation, and measurement uncertainty. *Acta Hydrochimica Et Hydrobiologica*, 2004. **32**(2): p. 154-160.

213. Kirk Nordstrom, D., Trace metal speciation in natural waters: Computational vs. analytical. *Water, Air, & Soil Pollution*, 1996. **90**(1): p. 257-267.

214. Harvie, C.E., N. Moller, and J.H. Weare, The prediction of mineral solubilities in natural-waters - the Na-K-Mg-Ca-H-Cl-SO_4-OH-HCO_3-CO_3-CO_2-H_2O system to high ionic strengths at 25 ^{o}C. . *Geochimica Et Cosmochimica Acta*, 1984. **48**(4): p. 723-751.

215. Harvie, C.E. and J.H. Weare, The prediction of mineral solubilities in natural-waters - the Na-K-Mg-Ca-Cl-SO_4-H_2O system from zero to high-concentration at 25 ^{o}C. *Geochimica Et Cosmochimica Acta*, 1980. **44**(7): p. 981-997.

216. Rose, A.L. and T.D. Waite, Kinetics of hydrolysis and precipitation of ferric iron in seawater. *Environmental Science & Technology*, 2003. **37**(17): p. 3897-3903.

217. Cuculic, V. and I. Pizeta, Kinetics of iron(III) hydrolysis and precipitation in aqueous glycine solutions assessed by voltammetry. *Collection of Czechoslovak Chemical Communications*, 2009. **74**(10): p. 1531-1542.

218. Pham, A.N., A.L. Rose, A.J. Feitz, and T.D. Waite, Kinetics of Fe(III) precipitation in aqueous solutions at pH 6.0-9.5 and 25 ^{o}C. *Geochimica Et Cosmochimica Acta*, 2006. **70**(3): p. 640-650.

219. Grundl, T. and J. Delwiche, Kinetics of ferric oxyhydroxide precipitation. *Journal of Contaminant Hydrology*, 1993. **14**(1): p. 71-87.

220. Baker, F.L. and W.M. Smith, Acid dependence and ion pairing in the anation reactions yielding iron(III) monosulfate. *Canadian Journal of Chemistry*, 1970. **48**(19): p. 3100-3103.

221. Wendt, H. and H. Strehlow, Schnelle Ionenreaktionen in Lösungen. II Die Bildung einiger einfacher Komplexe des Eisen-III-ions [la]. *Zeitschrift für Elektrochemie, Berichte der Bunsengesellschaft für physikalische Chemie*, 1962. **66**(3): p. 228-234.

222. Diz, H., J. Novak, and J. Rimstidt, Iron precipitation kinetics in synthetic acid mine drainage. *Mine Water and the Environment*, 1999. **18**(1): p. 1-14.

223. Zinck, J.M., An investigation into the hydrolytic precipitation of iron(III) from sulphate-bearing effluents. 1994, *National Library of Canada = Bibliothèque nationale du Canada: Ottawa.*

224. Tobe, M.L. and B. John, Inorganic Reaction Mechanisms. 1999: *Longman*.

225. Guimaraes, L., H.A. de Abreu, and H.A. Duarte, Fe(II) hydrolysis in aqueous solution: A DFT study. *Chemical Physics*, 2007. **333**(1): p. 10-17.

226. Farago, M.E., J.M. James, and V.C.G. Trew, Complexes of nickel(II) with ethylenediamine and perchlorate or tetraphenylborate. *Journal of the Chemical Society A: Inorganic, Physical, Theoretical*, 1967: p. 820-824.

227. Wickenden, A.E. and R.A. Krause, Complexes of Nickel(II) with Acetonitrile. Coordination of Perchlorate. *Inorganic Chemistry*, 1965. **4**(3): p. 404-407.

228. Feng, Q. and H. Waki, Evaluation of absolute stability-constants of complexes .1. theory and applications to the inorganic one-to-one complexes of iron(III) in perchlorate-media. *Polyhedron*, 1988. **7**(4): p. 291-295.

229. Magini, M., Solute structuring in aqueous iron(III) sulfate-solutions - evidence for the formation of iron(III)-sulfate complexes. *Journal of Chemical Physics*, 1979. **70**(1): p. 317-324.

230. Hug, S.J., In situ Fourier transform infrared measurements of sulfate adsorption on hematite in aqueous solutions. *Journal of Colloid and Interface Science,* 1997. **188**(2): p. 415-422.
231. Noerlund, C.A., Hydrothermal preparation of goethite and hematite from amorphous iron(III) hydroxide. *Acta Chem. Scand.,* 1968. **22**(Copyright (C) 2012 American Chemical Society (ACS). All Rights Reserved.): p. 1487-90.
232. Bottero, J.Y., D. Tchoubar, M. Arnaud, and P. Quienne, Partial hydrolysis of ferric nitrate salt - structural investigation by dynamic light-scattering and small-angle x-ray-scattering. *Langmuir,* 1991. **7**(7): p. 1365-1369.
233. Tchoubar, D., J.Y. Bottero, P. Quienne, and M. Arnaud, Partial hydrolysis of ferric-chloride salt - structural investigation by photon-correlation spectroscopy and small-angle x-ray-scattering. *Langmuir,* 1991. **7**(2): p. 398-402.